

Arbeitsbericht NAB 22-02

**TBO Stadel-2-1:
Data Report
Dossier V
Structural Geology**

September 2022

A. Ebert, S. Cioldi, E. Hägerstedt &
H.P. Weber

**National Cooperative
for the Disposal of
Radioactive Waste**

Hardstrasse 73
P.O. Box
5430 Wettingen
Switzerland
Tel. +41 56 437 11 11

nagra.ch

Arbeitsbericht NAB 22-02

**TBO Stadel-2-1:
Data Report
Dossier V
Structural Geology**

September 2022

A. Ebert¹, S. Cioldi¹ & E. Hägerstedt¹ &
H.P. Weber²

¹Geologiegemeinschaft Strukturgeologie-Experten
Nagra Tiefbohrungen

²Nagra

Keywords:

STA2-1, Nördlich Lägern, TBO, deep drilling campaign,
structural geology, goniometry, drill cores

**National Cooperative
for the Disposal of
Radioactive Waste**

Hardstrasse 73
P.O. Box
5430 Wettingen
Switzerland
Tel. +41 56 437 11 11

nagra.ch

Nagra Arbeitsberichte ("Working Reports") present the results of work in progress that have not necessarily been subject to a comprehensive review. They are intended to provide rapid dissemination of current information.

This NAB aims at reporting drilling results at an early stage. Additional borehole-specific data will be published elsewhere.

In the event of inconsistencies between dossiers of this NAB, the dossier addressing the specific topic takes priority. In the event of discrepancies between Nagra reports, the chronologically later report is generally considered to be correct. Data sets and interpretations laid out in this NAB may be revised in subsequent reports. The reasoning leading to these revisions will be detailed there.

This report was finalised in June 2023.

This Dossier was prepared by a project team consisting of:

A. Ebert (core description, core photograph picking, core goniometry, writing and QC)

S. Cioldi (core description, core photograph picking and core goniometry)

E. Hägerstedt (core description, core photograph picking and core goniometry)

K. Decker (QC)

M. Gysi (conceptualisation)

H.P. Weber (project management and QC)

Editorial work: Geomecon, P. Blaser and M. Unger

The Dossier has greatly benefitted from technical discussions with, and reviews by, external and internal experts. Their input and work are very much appreciated.

Copyright © 2022 by Nagra, Wettingen (Switzerland) / All rights reserved.

All parts of this work are protected by copyright. Any utilisation outwith the remit of the copyright law is unlawful and liable to prosecution. This applies in particular to translations, storage and processing in electronic systems and programs, microfilms, reproductions, etc.

Table of Contents

Table of Contents	I
List of Tables.....	III
List of Figures	III
List of Appendices	IX
1 Introduction	1
1.1 Context.....	1
1.2 Location and specifications of the borehole	2
1.3 Documentation structure for the STA2-1 borehole	6
1.4 Scope and objectives of this dossier	7
1.5 Petrophysical logs and preliminary log analysis available	7
1.6 Borehole deviation.....	8
2 Methodology	9
2.1 Core goniometry	9
2.1.1 Introduction	9
2.1.2 Workflow.....	9
2.1.3 Dip picking and dip type classification	11
2.1.4 Dip data for non-oriented and missing cores	14
2.1.5 Goniometry confidence assessment and uncertainties.....	16
2.2 Structural work	19
2.3 Geo-statistical evaluation.....	26
3 Inventory of structure types	27
3.1 Examples of fault planes.....	27
3.2 Examples of fault zones.....	34
3.3 Examples of joints	35
3.4 Examples of veins / tension gashes.....	36
3.5 Examples of stylolites.....	39
3.6 Examples of open pores.....	41
3.7 Examples of drilling-induced fractures.....	43
3.8 Examples of folding.....	46
4 Geo-statistical evaluation: results	47
4.1 Entire cored borehole section (470.00 m to 1'288.87 m MD log depth)	47
4.1.1 Basic structural dip evaluation.....	47
4.1.2 Natural structural discontinuities	51
4.1.3 Fracture density (P10 and P32) and distribution	61
4.1.4 Kinematic indicators.....	61

4.2	Malm.....	66
4.2.1	«Felsenkalke» + «Massenkalk».....	67
4.2.2	Schwarzbach Formation	74
4.2.3	Villigen Formation.....	80
4.2.4	Wildegg Formation.....	87
4.3	Dogger	94
4.3.1	«Brauner Dogger» (Wutach Formation to «Murchisonae-Oolith Formation»).....	94
4.3.2	Opalinus Clay	101
4.4	Lias (Staffelegg Formation).....	107
4.5	Keuper	113
4.5.1	Klettgau Formation.....	113
4.5.2	Bänkerjoch Formation	117
4.6	Muschelkalk.....	123
4.6.1	Schinznach Formation	123
4.6.2	Zeglingen Formation	129
4.6.3	Kaiseraugst Formation.....	136
4.7	Dinkelberg Formation and Weitenau Formation	141
5	Main structural findings	145
5.1	Deformed interval in the Opalinus Clay between 883.78 m and 890.19 m MD (log depth)	145
5.2	Deformed salt in the Zeglingen Formation from 1'152.02 m to 1'179.58 m MD (log depth)	151
6	References.....	159

List of Tables

Tab. 1-1:	General information about the STA2-1 borehole	2
Tab. 1-2:	Core and log depth for the main lithostratigraphic boundaries in the STA2-1 borehole.....	5
Tab. 1-3:	List of dossiers included in NAB 22-02	6
Tab. 2-1:	Core goniometry confidence assessment of the analysed interval.....	16
Tab. 2-2:	Types of structural discontinuities identified in this study	20
Tab. 2-3:	Systematically recorded parameters for the investigated structures	23
Tab. 4-1:	Vector means of orientation values for bedding planes and structural discontinuities.....	47
Tab. 4-2:	List of interpreted fault zones, mirror-like fault planes (MirFP), fault planes (FP), Salt shear bands (SB) and the associated FDC	53
Tab. 4-3:	List of all kinematic indicators in oriented and non-oriented cores.....	62

List of Figures

Fig. 1-1:	Tectonic overview map with the three siting regions under investigation	1
Fig. 1-2:	Overview map of the investigation area in the Nördlich Lägern siting region with the location of the STA2-1 borehole in relation to the boreholes Weiach-1, BUL1-1, STA3-1 and BAC1-1	3
Fig. 1-3:	Lithostratigraphic profile and casing scheme for the STA2-1 borehole.....	4
Fig. 1-4:	Borehole deviation within the cored section.....	8
Fig. 2-1:	Using a goniometer to determine kinematic indicators along faults.....	11
Fig. 2-2:	Symbols for dip types, fracture density classes and kinematic data used for this study.....	12
Fig. 2-3:	Mirror-like fault planes identified within the drill core at 951.95 m and 951.98 m MD (log depth) in the Staffelegg Formation	13
Fig. 2-4:	Example of dip data in a non-oriented core interval.....	14
Fig. 2-5:	Interval without 360° core photographs from 1'220.42 m to 1'220.62 m MD (log depth) in the Kaiseraugst Formation	15
Fig. 2-6:	Core – FMI / UBI correlation for a fault plane at 710.26 m MD (log depth) in the Wildeggen Formation	17
Fig. 2-7:	Core – FMI / UBI correlation from 909.05 m to 910.15 m MD (log depth) in the Staffelegg Formation	17
Fig. 2-8:	Core – FMI / UBI correlation for subhorizontal to shallow dipping bedding	18
Fig. 2-9:	The five main groups of structural discontinuities	20

Fig. 2-10:	Completed DIN A3 sheet of primary record of the detailed structural core analysis	25
Fig. 3-1:	Fault plane	27
Fig. 3-2:	Fault plane	28
Fig. 3-3:	Fault plane	29
Fig. 3-4:	Mirror-like fault plane	30
Fig. 3-5:	Mirror-like fault plane	31
Fig. 3-6:	Stylolitic fault plane.....	32
Fig. 3-7:	Stylolitic fault plane.....	33
Fig. 3-8:	Fault zone	34
Fig. 3-9:	Joint	35
Fig. 3-10:	Joint	35
Fig. 3-11:	Vein / tension gash.....	36
Fig. 3-12:	Vein / tension gash.....	36
Fig. 3-13:	Vein / tension gash.....	37
Fig. 3-14:	Vein / tension gash.....	38
Fig. 3-15:	Stylolite.....	39
Fig. 3-16:	Stylolite.....	39
Fig. 3-17:	Stylolite.....	40
Fig. 3-18:	Open pores.....	41
Fig. 3-19:	Open pores.....	42
Fig. 3-20:	Petal fractures	43
Fig. 3-21:	Discing.....	44
Fig. 3-22:	Discing.....	45
Fig. 3-23:	Folding.....	46
Fig. 4-1:	Stereogram and depth plot for bedding planes (n = 326) for the entire cored borehole section.....	48
Fig. 4-2:	Dip azimuth rose diagram, dip histogram and depth plot for bedding planes (n = 326) for the entire cored borehole section.....	49
Fig. 4-3:	Vector azimuth (or walkout) plot with bedding dips (n = 326) in oriented cores picked on oriented 360° core photographs	50
Fig. 4-4:	Overview plot showing P32 densities for fractures and stylolites along the STA2-1 borehole.....	52
Fig. 4-5:	Stereogram and depth plot of fault planes for the entire cored interval.....	54
Fig. 4-6:	Dip azimuth rose diagram, dip histogram and depth plot for fault planes in the entire cored interval	55
Fig. 4-7:	Stereogram and depth plot for tension gashes / veins, unassigned fractures and joints in the entire cored interval	57

Fig. 4-8:	Dip azimuth rose diagram of tension gashes / veins, unassigned fractures and joints in the entire cored interval	58
Fig. 4-9:	Stereogram and depth plot for stylolites (n = 845) along the cored STA2-1 borehole	59
Fig. 4-10:	Dip azimuth rose diagram and depth plot for stylolites in the entire cored interval	60
Fig. 4-11:	Plunge azimuth of striations along fault planes in the entire cored interval	62
Fig. 4-12:	Stereogram of striations on all oriented fault planes (including multiple lineations on a single fault plane) and associated kinematic data	63
Fig. 4-13:	Stereogram with all striations on oriented thrust / reverse fault planes (including multiple lineations on a single fault plane)	63
Fig. 4-14:	Stereogram with all striations on oriented normal fault planes (including multiple lineations on a single fault plane)	64
Fig. 4-15:	Stereogram with all striations on oriented strike-slip fault planes (including multiple lineations on a single fault plane)	64
Fig. 4-16:	Stereogram with all striations on oriented fault planes with unknown shear sense (including multiple lineations on a single fault plane)	65
Fig. 4-17:	Stereogram and depth plot of fault planes («Felsenkalke» + «Massenkalk»)	67
Fig. 4-18:	Dip azimuth rose diagram, dip histogram and depth plot of fault planes («Felsenkalke» + «Massenkalk»)	68
Fig. 4-19:	Stereogram and depth plot of tension gashes / veins and unassigned fractures («Felsenkalke» + «Massenkalk»)	69
Fig. 4-20:	Dip azimuth rose diagram, dip histogram and depth plot of tension gashes / veins, joints and unassigned fractures («Felsenkalke» + «Massenkalk»)	70
Fig. 4-21:	Stereogram and depth plot of stylolites («Felsenkalke» + «Massenkalk»; n = 277)	71
Fig. 4-22:	Dip azimuth rose diagram, dip histogram and depth plot of stylolites («Felsenkalke» + «Massenkalk»; n = 277)	72
Fig. 4-23:	Stereogram with striations on fault planes, including multiple lineations on a single fault plane («Felsenkalke» + «Massenkalk»; n = 60)	73
Fig. 4-24:	Stereogram and depth plot of fault planes (Schwarzbach Formation)	74
Fig. 4-25:	Dip azimuth rose diagram, dip histogram and depth plot of fault planes (Schwarzbach Formation)	75
Fig. 4-26:	Stereogram and depth plot of tension gashes / veins and unassigned fractures (Schwarzbach Formation)	76
Fig. 4-27:	Stereogram and depth plot of stylolites (Schwarzbach Formation; n = 38)	77
Fig. 4-28:	Dip azimuth rose diagram, dip histogram and depth plot of stylolites (Schwarzbach Formation; n = 38)	78
Fig. 4-29:	Stereogram of striations on fault planes, including multiple lineations on a single fault plane (Schwarzbach Formation; n = 16)	79
Fig. 4-30:	Stereogram and depth plot of fault planes (Villigen Formation)	80

Fig. 4-31:	Dip azimuth rose diagram, dip histogram and depth plot of fault planes (Villigen Formation).....	81
Fig. 4-32:	Stereogram and depth plot of tension gashes / veins and unassigned fractures (Villigen Formation).....	82
Fig. 4-33:	Dip azimuth rose diagram, dip histogram and depth plot of tension gashes / veins, joints and unassigned fractures (Villigen Formation).....	83
Fig. 4-34:	Stereogram and depth plot of stylolites (Villigen Formation; n = 254).....	84
Fig. 4-35:	Dip azimuth rose diagram, dip histogram and depth plot of stylolites (Villigen Formation; n = 254).....	85
Fig. 4-36:	Stereogram of striations on fault planes (including multiple lineations on a single fault plane) (Villigen Formation; n = 82).....	86
Fig. 4-37:	Stereogram and depth plot of fault planes (Wildegge Formation).....	87
Fig. 4-38:	Dip azimuth rose diagram, dip histogram and depth plot of fault planes (Wildegge Formation).....	88
Fig. 4-39:	Stereogram and depth plot of tension gashes / veins and unassigned fractures (Wildegge Formation).....	89
Fig. 4-40:	Dip azimuth rose diagram, dip histogram and depth plot of tension gashes / veins, joints and unassigned fractures (Wildegge Formation).....	90
Fig. 4-41:	Stereogram and depth plot of stylolites (Wildegge Formation; n = 40).....	91
Fig. 4-42:	Dip azimuth rose diagram, dip histogram and depth plot of stylolites (Wildegge Formation; n = 40).....	92
Fig. 4-43:	Stereogram of striations on fault planes, including multiple lineations on a single fault plane (Wildegge Formation; n = 26).....	93
Fig. 4-44:	Stereogram and depth plot of fault planes («Brauner Dogger»).....	94
Fig. 4-45:	Dip azimuth rose diagram, dip histogram and depth plot of fault planes («Brauner Dogger»).....	95
Fig. 4-46:	Stereogram and depth plot of tension gashes / veins, joints and unassigned fractures («Brauner Dogger»).....	96
Fig. 4-47:	Dip azimuth rose diagram, dip histogram and depth plot of tension gashes / veins, joints and unassigned fractures («Brauner Dogger»).....	97
Fig. 4-48:	Stereogram and depth plot of stylolites («Brauner Dogger»; n = 13).....	98
Fig. 4-49:	Dip azimuth rose diagram, dip histogram and depth plot of stylolites («Brauner Dogger»; n = 13).....	99
Fig. 4-50:	Stereogram of striations on fault planes, including multiple lineations on a single fault plane («Brauner Dogger»; n = 26).....	100
Fig. 4-51:	Stereogram and depth plot of fault planes (Opalinus Clay).....	101
Fig. 4-52:	Dip azimuth rose diagram, dip histogram and depth plot of fault planes (Opalinus Clay).....	102
Fig. 4-53:	Stereogram and depth plot of tension gashes / veins, joints and unassigned fractures (Opalinus Clay).....	103

Fig. 4-54:	Dip azimuth rose diagram, dip histogram and depth plot of tension gashes / veins, joints and unassigned fractures (Opalinus Clay).....	104
Fig. 4-55:	Stereogram and depth plot of stylolites (Opalinus Clay; n = 2)	105
Fig. 4-56:	Stereogram of striations on fault planes, including multiple lineations on a single fault plane (Opalinus Clay; n = 30).....	106
Fig. 4-57:	Stereogram and depth plot of fault planes (Lias).....	107
Fig. 4-58:	Dip azimuth rose diagram, dip histogram and depth plot of fault planes (Lias)...	108
Fig. 4-59:	Stereogram and depth plot of tension gashes / veins, joints and unassigned fractures (Lias).....	109
Fig. 4-60:	Dip azimuth rose diagram, dip histogram and depth plot of tension gashes / veins, joints and unassigned fractures (Lias).....	110
Fig. 4-61:	Stereogram and depth plot of stylolites (Lias; n = 7)	111
Fig. 4-62:	Stereogram of striations on fault planes, including multiple lineations on a single fault plane (Lias; n = 14).....	112
Fig. 4-63:	Stereogram and depth plot of faults (Klettgau Formation).....	113
Fig. 4-64:	Dip azimuth rose diagram, dip histogram and depth plot of faults (Klettgau Formation)	114
Fig. 4-65:	Stereogram and depth plot of tension gashes / veins, joints and unassigned fractures (Klettgau Formation)	115
Fig. 4-66:	Stereogram of striations on fault planes, including multiple lineations on a single fault plane (Klettgau Formation; n = 39).....	116
Fig. 4-67:	Stereogram and depth plot of faults (Bänkerjoch Formation)	117
Fig. 4-68:	Dip azimuth rose diagram, dip histogram and depth plot of faults (Bänkerjoch Formation).....	118
Fig. 4-69:	Stereogram and depth plot of tension gashes / veins, joints and unassigned fractures (Bänkerjoch Formation).....	119
Fig. 4-70:	Dip azimuth rose diagram, dip histogram and depth plot of tension gashes / veins, joints and unassigned fractures (Bänkerjoch Formation).....	120
Fig. 4-71:	Stereogram and depth plot of stylolites (Bänkerjoch Formation; n = 2)	121
Fig. 4-72:	Stereogram of striations on fault planes, including multiple lineations on a single fault plane (Bänkerjoch Formation; n = 107).....	122
Fig. 4-73:	Stereogram and depth plot of fault planes (Schinznach Formation).....	123
Fig. 4-74:	Stereogram and depth plot of tension gashes / veins, joints and unassigned fractures (Schinznach Formation).....	124
Fig. 4-75:	Dip azimuth rose diagram, dip histogram and depth plot of tension gashes / veins, joints and unassigned fractures (Schinznach Formation).....	125
Fig. 4-76:	Stereogram and depth plot of stylolites (Schinznach Formation; n = 200)	126
Fig. 4-77:	Dip azimuth rose diagram, dip histogram and depth plot of stylolites (Schinznach Formation; n = 200)	127
Fig. 4-78:	Stereogram of striations on fault planes, including multiple lineations on a single fault plane (Schinznach Formation; n = 5).....	128

Fig. 4-79:	Stereogram and depth plot of fault planes (Zeglingen Formation).....	129
Fig. 4-80:	Dip azimuth rose diagram, dip histogram and depth plot of fault planes (Zeglingen Formation).....	130
Fig. 4-81:	Stereogram and depth plot of tension gashes / veins, joints and unassigned fractures (Zeglingen Formation).....	131
Fig. 4-82:	Dip azimuth rose diagram, dip histogram and depth plot of tension gashes / veins, joints and unassigned fractures (Zeglingen Formation).....	132
Fig. 4-83:	Stereogram and depth plot of stylolites (Zeglingen Formation; n = 10).....	133
Fig. 4-84:	Dip azimuth rose diagram, dip histogram and depth plot of stylolites (Zeglingen Formation; n = 10)	134
Fig. 4-85:	Stereogram of striations on fault planes, including multiple lineations on a single fault plane (Zeglingen Formation; n = 35)	135
Fig. 4-86:	Stereogram and depth plot of fault planes (Kaiseraugst Formation)	136
Fig. 4-87:	Dip azimuth rose diagram, dip histogram and depth plot of fault planes (Kaiseraugst Formation)	137
Fig. 4-88:	Stereogram and depth plot of tension gashes / veins, joints and unassigned fractures (Kaiseraugst Formation)	138
Fig. 4-89:	Stereogram and depth plot of stylolites (Kaiseraugst Formation; n = 2).....	139
Fig. 4-90:	Stereogram of striations on fault planes, including multiple lineations on a single fault plane (Kaiseraugst Formation; n = 27).....	140
Fig. 4-91:	Stereogram and depth plot of fault planes (Dinkelberg Formation and Weitenau Formation).....	141
Fig. 4-92:	Dip azimuth rose diagram, dip histogram and depth plot of fault planes (Dinkelberg Formation and Weitenau Formation)	142
Fig. 4-93:	Stereogram of striations on fault planes, including multiple lineations on a single fault plane (Dinkelberg Formation and Weitenau Formation; n = 73).....	143
Fig. 5-1:	Overview plot of the Opalinus Clay with the deformation interval from 883.78 m to 890.19 m MD (log depth)	146
Fig. 5-2:	Stereogram and depth plot of fault planes and bedding planes from the depth interval from 883.78 m to 890.19 m MD (log depth)	147
Fig. 5-3:	Dip azimuth rose diagrams and depth plot of bedding planes (left) and fault planes (right) from the depth interval from 883.78 m to 890.19 m MD (log depth).....	148
Fig. 5-4:	Stereogram of striations on fault planes within the deformation interval.....	149
Fig. 5-5:	Example of a fault plane, depth 855.61 m MD (log depth)	150
Fig. 5-6:	Fault planes and tension gashes / veins in the interval from 885.93 m to 886.33 m MD (log depth)	150
Fig. 5-7:	Tension gashes / veins in the interval from 885.38 m to 885.64 m MD (log depth).....	151
Fig. 5-8:	Example of recrystallised halite.....	152

Fig. 5-9:	Plunge rose diagram of shape preferred orientation of the long axes of recrystallised salt grains.....	153
Fig. 5-10:	Thin stretched dolomitic layer forming boudins in anhydrite	154
Fig. 5-11:	Thin dolomitic layer with a fabric characterised by boudins and tension gashes /veins in an en-echelon arrangement	155
Fig. 5-12:	Stereogram of stretching lineations and shear directions indicated within thin dolomitic layers	156
Fig. 5-13:	Stereogram and depth plot of bedding.....	157

List of Appendices

App. A:	Lithostratigraphy profile Stadel-2-1, 1:2'500, 0.00 m to 1'288.12 m MD core depth
App. B:	Structural geology profile Stadel-2-1, 1:1'000, 450.00 m to 1'288.87 m MD log depth
App. C-1:	Structural geology profile Stadel-2-1, 1:100, 465.00 m to 740.00 m MD log depth
App. C-2:	Structural geology profile Stadel-2-1, 1:100, 715.00 m to 990.00 m MD log depth
App. C-3:	Structural geology profile Stadel-2-1, 1:100, 965.00 m to 1'240.00 m MD log depth
App. C-4:	Structural geology profile Stadel-2-1, 1:100, 1'215.00 m to 1'288.87 m MD log depth
App. D-1:	Overview plot of stereograms and rose diagrams: «Felsenkalke» + «Massenkalk» to Staffelegg Fm.
App. D-2:	Overview plot of stereograms and rose diagrams: Klettgau to Weitenau Fm.
App. E-1:	Core goniometry depth shift table
App. E-2:	Core goniometry rotation angle table
App. F:	Lithostratigraphy patterns, colours, weathering index and symbols for lithostratigraphy

Note: In the digital version of this report the appendices can be found under the paper clip symbol.

1 Introduction

1.1 Context

To provide input for site selection and the safety case for deep geological repositories for radioactive waste, Nagra has drilled a series of deep boreholes ("Tiefbohrungen", TBO) in Northern Switzerland. The aim of the drilling campaign is to characterise the deep underground of the three remaining siting regions located at the edge of the Northern Alpine Molasse Basin (Fig. 1-1).

In this report, we present the results from the Stadel-2-1 borehole.

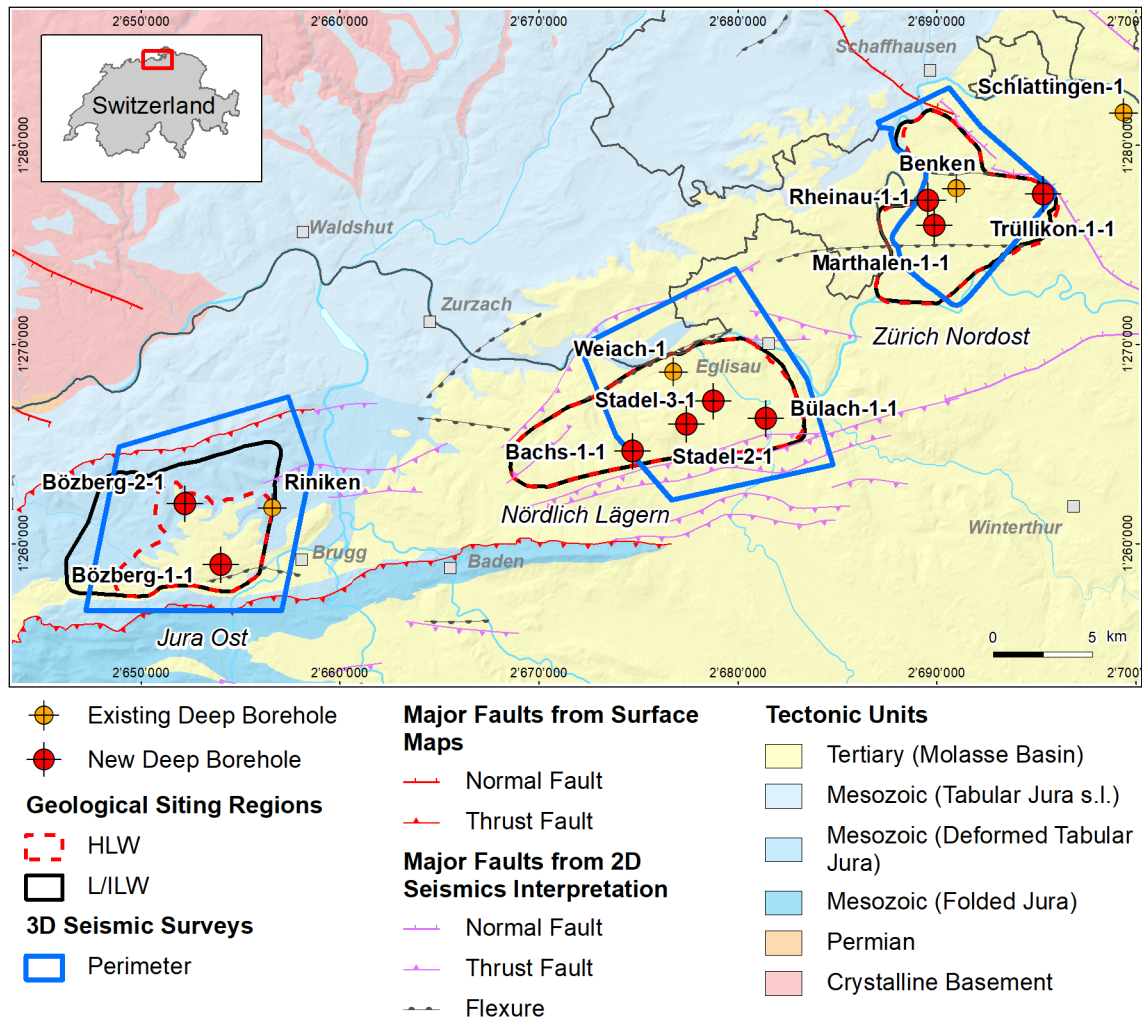


Fig. 1-1: Tectonic overview map with the three siting regions under investigation

1.2 Location and specifications of the borehole

The Stadel-2-1 (STA2-1) exploratory borehole is the seventh borehole drilled within the framework of the TBO project. The drill site is located in the central part of the Nördlich Lägern siting region (Fig. 1-2). The vertical borehole reached a final depth of 1'288.12 m (MD)¹. The borehole specifications are provided in Tab. 1-1.

Tab. 1-1: General information about the STA2-1 borehole

Siting region	Nördlich Lägern
Municipality	Stadel (Canton Zürich / ZH), Switzerland
Drill site	Stadel-2 (STA2)
Borehole	Stadel-2-1 (STA2-1)
Coordinates	LV95: 2'677'447.617 / 1'265'987.019
Elevation	Ground level = top of rig cellar: 417.977 m above sea level (asl)
Borehole depth	1'288.12 m measured depth (MD) below ground level (bgl)
Drilling period	25th January – 8th July 2021 (spud date to end of rig release)
Drilling company	Daldrup & Söhne AG
Drilling rig	Wirth B 152t
Drilling fluid	Water-based mud with various amounts of different components such as ² : 0 – 670 m: Bentonite & polymers 670 – 1'051 m: Potassium silicate & polymers 1'051 – 1'117 m: Water & polymers 1'117 – 1'288.12 m: Sodium chloride brine & polymers

The lithostratigraphic profile and the casing scheme are shown in Fig. 1-3. The comparison of the core versus log depth³ of the main lithostratigraphic boundaries in the STA2-1 borehole is shown in Tab. 1-2.

¹ Measured depth (MD) refers to the position along the borehole trajectory, starting at ground level, which for this borehole is the top of the rig cellar. For a perfectly vertical borehole, MD below ground level (bgl) and true vertical depth (TVD) are the same. In all Dossiers depth refers to MD unless stated otherwise.

² For detailed information see Dossier I.

³ Core depth refers to the depth marked on the drill cores. Log depth results from the depth observed during geophysical wireline logging. Note that the petrophysical logs have not been shifted to core depth, hence log depth differs from core depth.

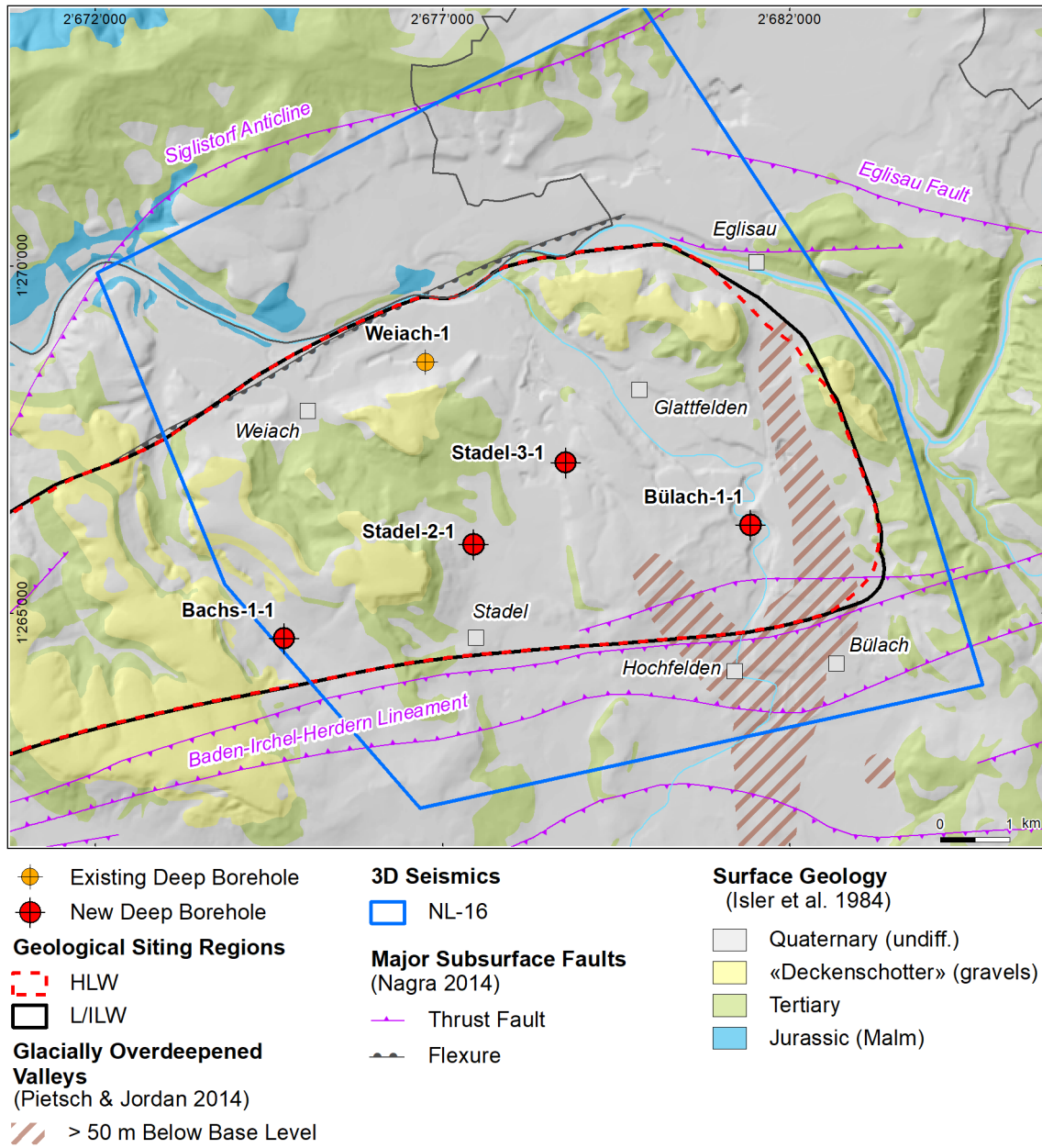


Fig. 1-2: Overview map of the investigation area in the Nördlich Lägern siting region with the location of the STA2-1 borehole in relation to the boreholes Weiach-1, BUL1-1, STA3-1 and BAC1-1

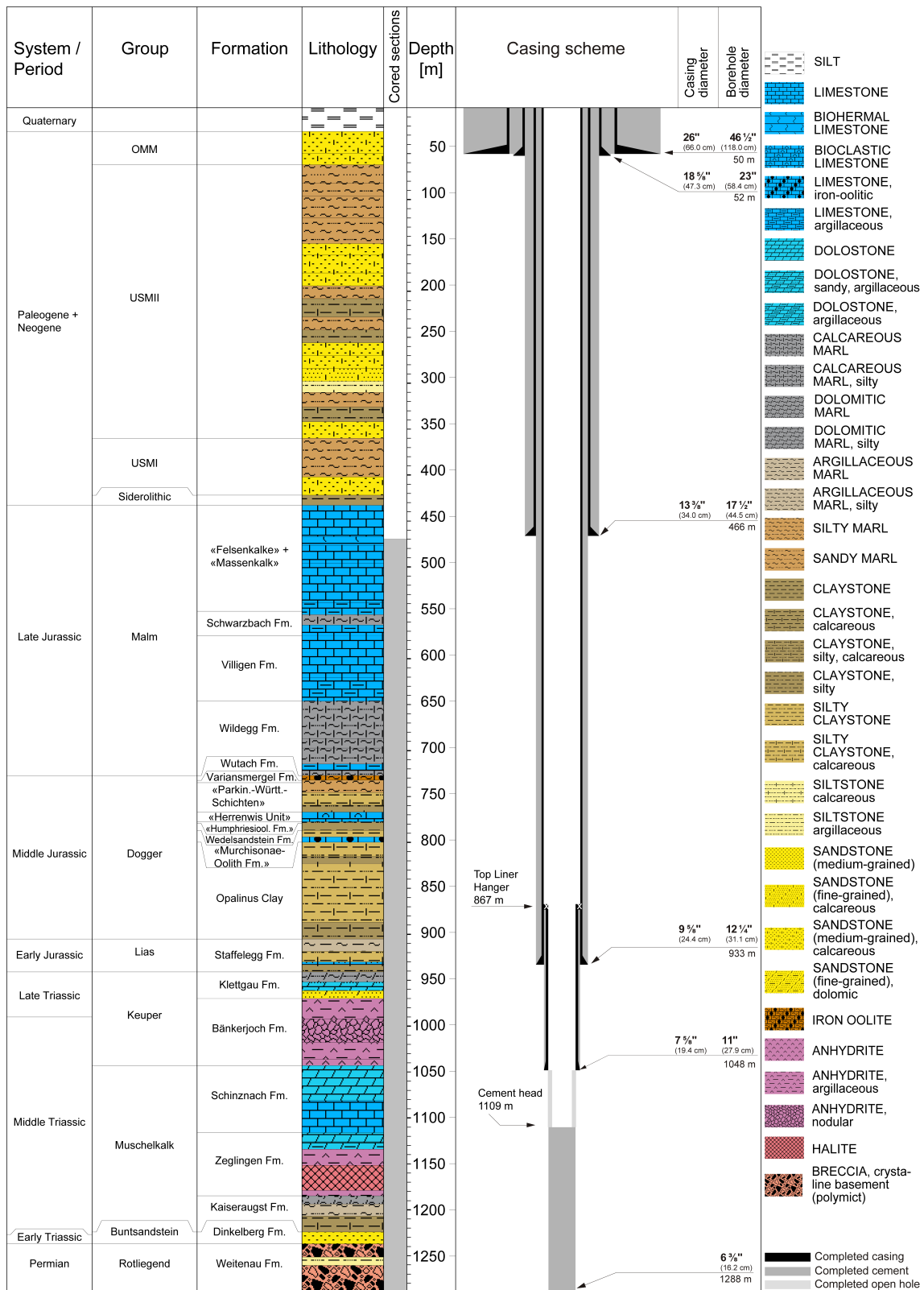


Fig. 1-3: Lithostratigraphic profile and casing scheme for the STA2-1 borehole⁴

⁴ For detailed information see Dossier I and III.

Tab. 1-2: Core and log depth for the main lithostratigraphic boundaries in the STA2-1 borehole⁵

System / Period	Group	Formation	Core depth in m (MD)	Log	
Quaternary			26.0	—	
Paleogene + Neogene	OMM		62.0	—	
	USM		422.0	—	
	Siderolithic		433.0	—	
Jurassic	Malm	«Felsenkalk» + «Massenkalk»	548.35	548.62 —	
		Schwarzbach Formation	575.08	575.45 —	
		Villigen Formation	646.23	646.63 —	
		Wildeggen Formation	727.18	728.20 —	
	Dogger	Wutach Formation	732.16	733.25 —	
		Variansmergel Formation	734.92	735.95 —	
		«Parkinsoni-Württembergica-Schichten»	767.02	768.05 —	
		«Herrenwis Unit»	777.54	778.47 —	
		«Humphriesiolith Formation»	779.34	780.27 —	
		Wedelsandstein Formation	786.85	787.79 —	
	Lias	«Murchisonae-Oolith Formation»	799.67	800.67 —	
		Opalinus Clay	905.20	906.87 —	
				940.89	941.42 —
	Triassic	Keuper	Klettgau Formation	969.87	970.52 —
Bänkerjoch Formation			1043.07	1043.62 —	
Muschelkalk		Schinznach Formation	1116.01	1116.69 —	
		Zeglingen Formation	1184.72	1185.42 —	
		Kaiseraugst Formation	1224.20	1225.07 —	
Buntsandstein	Dinkelberg Formation		1237.01 1237.94 —		
Permian	Rotliegend	Weitenau Formation	<small>final depth</small> 1288.12	1288.87	

⁵ For details regarding lithostratigraphic boundaries see Dossier III and IV; for details about depth shifts (core goniometry) see Section 2.1.

1.3 Documentation structure for the STA2-1 borehole

NAB 22-02 documents the majority of the investigations carried out in the STA2-1 borehole, including laboratory investigations on core material. The NAB comprises a series of stand-alone dossiers addressing individual topics and a final dossier with a summary composite plot (Tab. 1-3).

This documentation aims at early publication of the data collected in the STA2-1 borehole. It includes most of the data available approximately one year after completion of the borehole. Some analyses are still ongoing (e.g. diffusion experiments, analysis of veins, hydrochemical interpretation of water samples) and results will be published in separate reports.

The current borehole report will provide an important basis for the integration of datasets from different boreholes. The integration and interpretation of the results in the wider geological context will be documented later in separate geoscientific reports.

Tab. 1-3: List of dossiers included in NAB 22-02

Black indicates the dossier at hand.

Dossier	Title	Authors
I	TBO Stadel-2-1: Drilling	P. Hinterholzer-Reisegger
II	TBO Stadel-2-1: Core Photography	D. Kaehr & M. Gysi
III	TBO Stadel-2-1: Lithostratigraphy	P. Jordan, P. Schürch, H. Naef, M. Schwarz, R. Felber, T. Ibele & H.P. Weber
IV	TBO Stadel-2-1: Microfacies, Bio- and Chemostratigraphic Analyses	S. Wohlwend, H.R. Bläsi, S. Feist-Burkhardt, B. Hostettler, U. Menkveld-Gfeller, V. Dietze & G. Deplazes
V	TBO Stadel-2-1: Structural Geology	A. Ebert, S. Cioldi, E. Hägerstedt & H.P. Weber
VI	TBO Stadel-2-1: Wireline Logging, Micro-hydraulic Fracturing and Pressure-meter Testing	J. Gonus, E. Bailey, J. Desroches & R. Garrard
VII	TBO Stadel-2-1: Hydraulic Packer Testing	R. Schwarz, R. Beauhiem, S.M.L. Hardie & A. Pechstein
VIII	TBO Stadel-2-1: Rock Properties, Porewater Characterisation and Natural Tracer Profiles	C. Zwahlen, L. Aschwanden, E. Gaucher, T. Gimmi, A. Jenni, M. Kiczka, U. Mäder, M. Mazurek, D. Roos, D. Rufer, H.N. Waber, P. Wersin & D. Traber
IX	TBO Stadel-2-1: Rock-mechanical and Geomechanical Laboratory Testing	E. Crisci, L. Laloui & S. Giger
X	TBO Stadel-2-1: Petrophysical Log Analysis	S. Marnat & J.K. Becker
	TBO Stadel-2-1: Summary Plot	Nagra

1.4 Scope and objectives of this dossier

The dossier at hand (Dossier V) documents the work of the structural geology experts. The objectives of the report are:

- core goniometry to reset drill cores to the correct depth and original orientation based on high resolution borehole images and high resolution 360° core photographs (Appendices E-1 and E-2)
- structural discontinuities identification on high resolution 360° core photographs and drill cores
- true dip and dip azimuth analysis of structures and bedding planes on high resolution 360° photographs in TerraStation II and/or manual measurements with a geological compass on drill cores
- documentation of recorded structures and their relevant parameters
- visualisation of structural geology data as profiles and overview plots:
 - profile 1:1'000: Appendix B
 - profile 1:100: Appendices C-1 to C-4
 - overview plot of stereograms and rose diagrams: Appendices D-1 and D-2

The level of detail in this dossier is limited by the data availability at data cut-off two months after the end of drilling operations. The lithostratigraphic subdivision used in this report is in line with the finding in Dossier III.

1.5 Petrophysical logs and preliminary log analysis available

The petrophysical logs and preliminary log analysis listed below were available at the data-freeze and considered as a supplementary source of information for this report (for more details, see Dossier VI):

- total natural gamma ray borehole and potassium corrected (GR)
- caliper / radius (RD1 to RD6)
- near / array corrected limestone porosity (APLC)
- high resolution formation density (RHO8)
- high resolution formation photoelectric factor (PEF8)
- array laterolog apparent resistivity from computed focusing mode 0 to 5 (RLA1 to RLA5)
- formation micro imager (FMI)
- ultrasonic borehole image (UBI)
- borehole breakouts and centreline fractures analysis based on FMI and UBI images

1.6 Borehole deviation

The cored section of STA2-1 is almost vertical with a slight average deviation towards SE. At around 1'030 m MD (log depth), the deviation changes gradually from SE to N. The maximum horizontal deviation over the total length of the cored section at 1'196.60 m MD (log depth) is 3.28 m towards SE (Fig. 1-4).

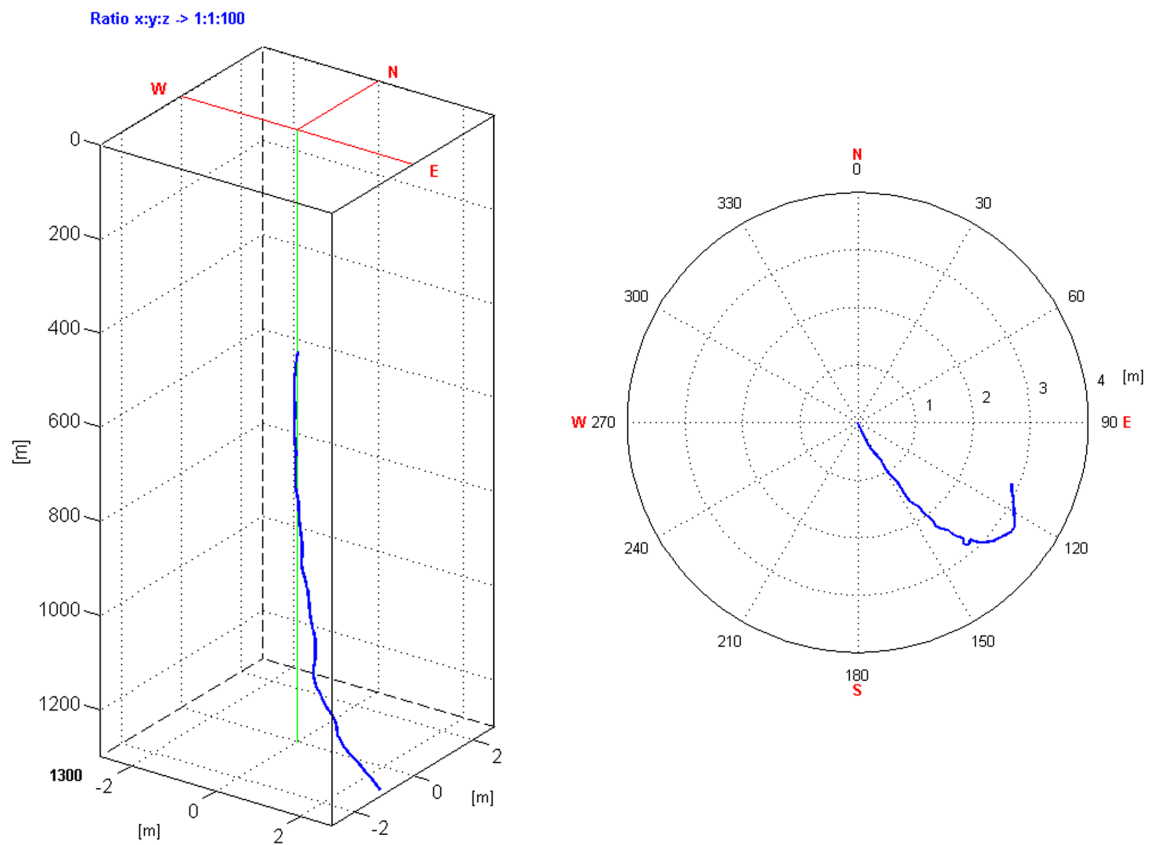


Fig. 1-4: Borehole deviation within the cored section

The left image visualises the borehole path in 3D with a compressed z-axis compared to the x- and y-axis. The borehole azimuth is shown on the right.

2 Methodology

2.1 Core goniometry

2.1.1 Introduction

A structural analysis was performed on drill cores along with circumferential and planar drill core photographs. Using the reference line on the core surface, positioned at an azimuth of 0° during core photography, most drill cores could be oriented using borehole image logs.

For this study, high-resolution 360° and planar photographs were available for most of the cored interval from 470.00 m to 1'288.12 m MD (core depth). The data were delivered as 1'311 circumferential and 1'366 planar photographs in TIF format. However, the original photographs with a resolution of 10 pixels/mm were too large to be handled with TerraStation II (TERRASCIENCES Inc.). Therefore, the original photographs were compressed by 25% and exported with a resolution of 300 dpi. In addition, FMI and UBI logs were available. Both were of good to excellent quality. Further relevant data included auxiliary borehole data, core orientation line and core section listings, lithostratigraphic boundaries and petrophysical logs.

2.1.2 Workflow

This section describes the methodology used for extracting the directional information from 360° core photographs. The following steps were tailored for efficient core goniometry using the TerraStation II software:

1. Quality control of core photographs:

Prior to loading the data, it was ensured that the core orientation line (red) on the 360° core photographs was set to 0° .

Note: the core orientation line (COL) represents a continuous reference line set to an azimuth of 0° to fix the relative orientation of drill cores. The COL was drawn on the core surface immediately after core retrieval at the drill site. The line lengths vary widely from a few centimetres up to several metres and therefore sometimes continue over several core sections depending on whether each individual core section could be fitted together along the core edges or not. If core sections could not be merged, a new COL was determined. The coherent COL was then used to orient the drill core using borehole image logs.

2. Data loading:

All 360° core photographs were loaded as mirrored images in order to simulate the borehole image log looking from the inside of the borehole. A constant value of 95 mm (3.74") was added as image diameter.

The processed FMI and UBI logs as well as the auxiliary petrophysical logs were imported into TerraStation II. It was checked that the depth of the petrophysical logs, especially the first GR (gamma ray) run, matched the depth of the FMI data.

3. Depth shifting:

The 360° core photographs were shifted to FMI logs using distinct, correlated planar and/or non-planar features. For the purpose of simplicity and consistency, only one shift value was applied for each individual core section (generally 3 m per section). This resulted in minor data gaps and/or overlaps at core section boundaries of a few centimetres maximum. In total, 279 distinct depth shift values were applied for the core sections of the entire cored borehole; these varied from 0.00 m to + 1.67 m. The defined values are listed in Appendix E-1.

4. Core orientation:

The core was oriented using correlated geological features (e.g. faults / fractures, inclined / deformed bedding, nodules, etc.) which were matched with the orientation on the FMI by rotating the 360° core photographs clockwise around the borehole axis.

The obtained angle of rotation was then applied to the entire core section with a continuous COL. Simultaneously, the validity across other geological features was checked. Note that the length of a linked COL segment was highly variable and could continue across several core sections. All COLs and the applied angles of rotation of the individual COLs are listed in Appendix E-2. To highlight the uncertainties related to core orientation, an uncertainty assessment was carried out and visualised using three confidence classes.

5. Quality control of core goniometry:

Prior to the structural recording of the drill cores, the depth shifts, the core correlation with the FMI / UBI image logs and the core orientations were reviewed.

The following steps do not belong to classical core goniometry. However, they played a key role in the coherent workflow of the structural core analysis and are thus mentioned here:

6. Dip picking on oriented 360° core photographs:

Bedding-related planes were picked manually for a structural dip evaluation.

Structural elements on drill cores were picked manually and characterised in detail with respect to relevant parameters.

7. Recording of kinematic features:

Kinematic indicators along fault planes such as slickensides, striations, shear sense indicators and (fault) offsets were identified and measured on the cores. To determine the lineation plunge azimuth and plunge and/or planes not visible in the photographs, a goniometer constructed by Geo Explorers was used. The drill core was placed in the goniometer facing up-hole and rotated around the vertical axis by the angle of rotation determined from the COL. Subsequently, the plunge azimuth and plunge of the striation were measured using a geological compass (see Fig. 2-1).

8. Examination of angular differences:

Using the TectonicsFP software, the angular differences between the striation plunge azimuths / plunges and the orientation of associated fault planes were checked. If the angular offset exceeded 15°, the fault plane and lineation were remeasured.

9. Quality control:

A final quality control was performed, with the main focus on consistency (between TerraStation II, primary records of structural core analysis and the structural inventory metadata), completeness of records and the accurate characterisation of the recorded tectonic features.

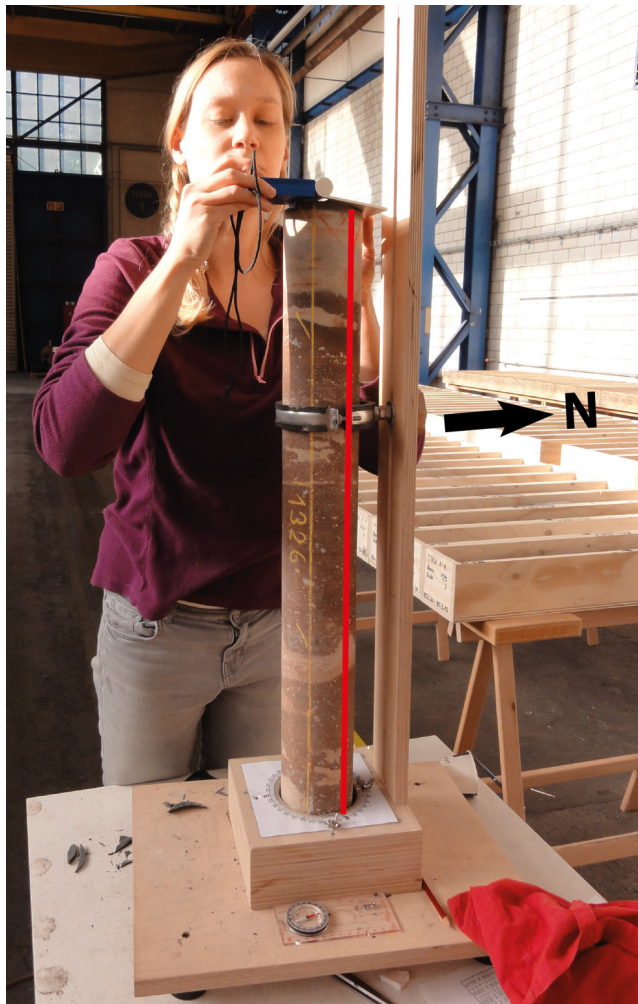

















Fig. 2-1: Using a goniometer to determine kinematic indicators along faults
Note the red core orientation line defining the position of the drill core in the goniometer.

2.1.3 Dip picking and dip type classification

Due to higher accuracy and reliability compared to automated methods, a manual sinusoid method and a point-to-point method were used to pick all relevant features on the 360° core photographs. In a cylindrical borehole, a perfect plane will appear as a sine wave on the circumferential core photograph and its amplitude reflects the dip relative to the borehole axis.

Different dip classes were defined for the different structure types. For this study, a total of 15 different dip types were defined in TerraStation II (Fig. 2-2).

Dip Types

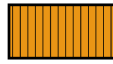
	Fault plane		Undifferentiated bedding		Drilling-induced fracture
	Mirror-like fault plane		Cross-bedding		Borehole breakout
	Stylolitic fault plane		Deformed bedding		Centreline fracture
	Unassigned fracture		Stylolite		
	Joint		Fold axis		
	Tension gash / vein		Open pore		

Fracture density classes

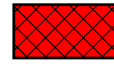
FDC2: 20 to 60 m²/m³



FDC3: 60 to 200 m²/m³







FDC3: > 200 m²/m³



TectonicsFP symbols

Shear sense:

	up / down - direction indicated by arrow in relation to fault plane
	dextral - direction indicated by arrows
	sinistral - direction indicated by arrows
	unknown

Shear sense quality:




good	
moderate	
poor	

Fig. 2-2: Symbols for dip types, fracture density classes and kinematic data used for this study

Some structures were only visible on planes not outcropping at the rim of the core and were not visible on the 360° core photographs. The orientation of these structures was obtained with a geological compass, as described above, and the data were subsequently imported into the digital dip dataset. Consequently, the associated dip sine waves did not fit with any visible traces and/or were simply not visible at this depth level, as exemplified in Fig. 2-3.

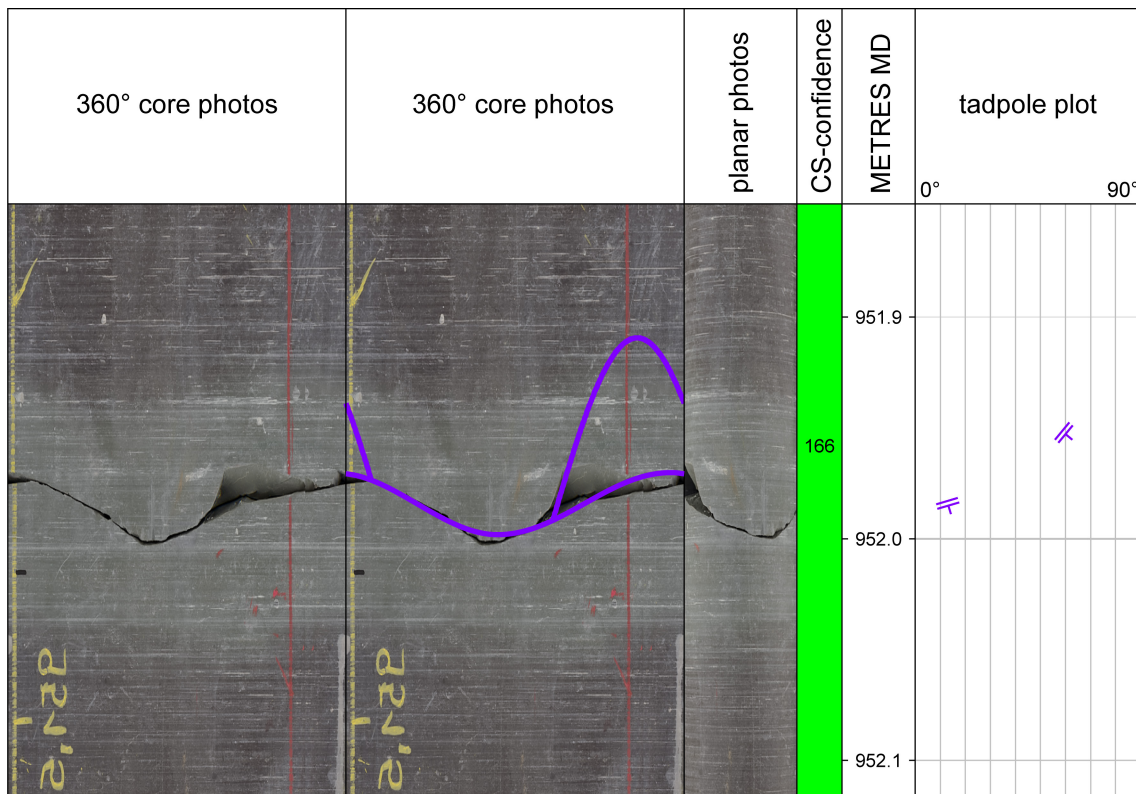


Fig. 2-3: Mirror-like fault planes identified within the drill core at 951.95 m and 951.98 m MD (log depth) in the Staffelegg Formation

From left to right: shifted and oriented 360° core photograph without (left) and with (right) picked sine waves, followed by depth-shifted planar core photographs, core section numbering in the coloured bar displaying the goniometry confidence ranking, depth track showing the position and length of the currently displayed window, tadpole plot. Note that the displayed sine wave of the structure at 951.95 m MD (log depth) is not visible on the 360° core photograph. The mirror-like fault plane was therefore implemented from the core analysis and the orientation was obtained from a compass measurement.

2.1.4 Dip data for non-oriented and missing cores

Due to a lack of correlated features, poor data quality or missing image log data, 65.13 m of the available drill cores remained non-oriented. Within these non-oriented drill cores, a total of one bedding plane and 46 tectonic / drilling-induced discontinuities could be observed and picked. The structural planes were nevertheless measured manually with a geological compass and included in TerraStation II, or picked digitally on 360° core photographs. For non-oriented drill cores and core photographs, the red COL was set to 0°. Because the dip angle measurements of these features are correct, however, the dip azimuth measurements are affected by the lack of orientation, the non-oriented dataset can only be used for fracture density calculations.

To highlight incorrect dip azimuth measurements of these features, a quality indicator of 0 was assigned and open tadpoles were used for visualisation (Fig. 2-4). A quality indicator of 1 was assigned to all correctly oriented features.

For intervals with missing 360° core photographs, short drill core sections could still be oriented using the coherent core orientation line, which sometimes continued across several cores. The depth and orientation of the structures were then measured on the core and the dip data were subsequently imported into the digital database of TerraStation II (see Fig. 3-5).

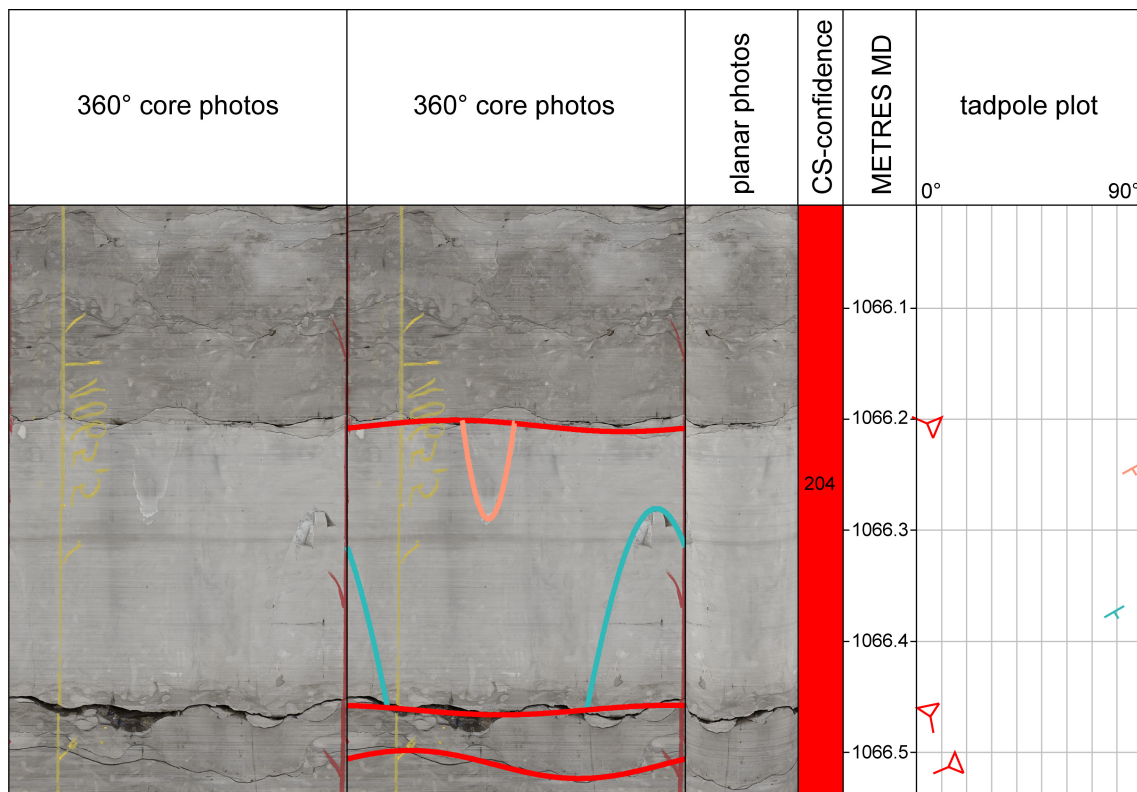


Fig. 2-4: Example of dip data in a non-oriented core interval

The goniometry confidence is set to "core not oriented" ("CS-confidence" column, red). Example from the Schinznach Formation from 1'066.0 m to 1'066.53 m MD (log depth).

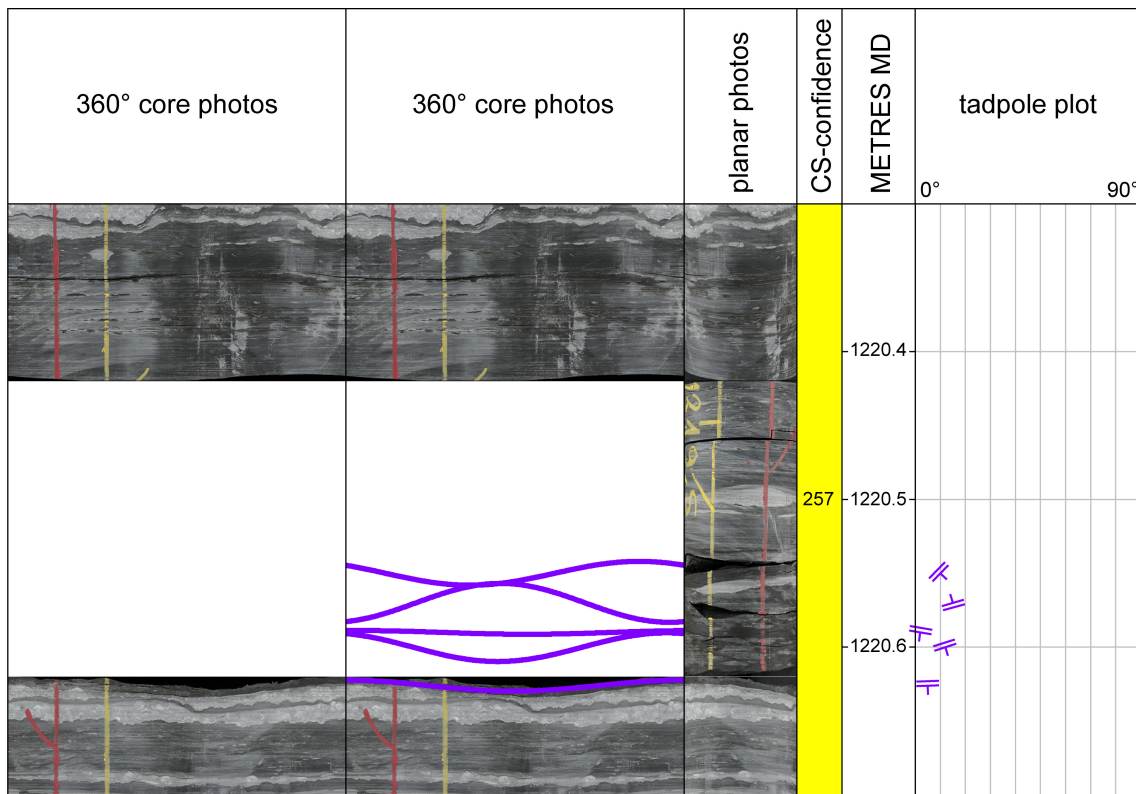


Fig. 2-5: Interval without 360° core photographs from 1'220.42 m to 1'220.62 m MD (log depth) in the Kaiseraugst Formation

In this example, the core goniometry and structural analysis were performed directly on the drill core. The orientation data were determined with a geological compass and subsequently imported into the digital dip database of TerraStation II. The goniometry confidence for this core section is moderate ("CS-confidence" column, yellow).

2.1.5 Goniometry confidence assessment and uncertainties

Goniometry confidence ranking

To visualise the uncertainties related to the core goniometry, the reliability of the core orientation was classified using a confidence ranking scheme. The assessment was carried out for each connected COL and depended particularly on the number of reliably correlated features within these intervals. Features with a moderate to steep (> 15°) dip generally provided a higher confidence and resulted in lower angular uncertainties than e.g. shallow structures (< 15°). The features used for the core goniometry are listed in Appendix E along with the coherent COLs. Examples of the correlated features between the FMI and the core are presented in Figs. 2-6, 2-7 and 2-8.

There are three confidence levels for the goniometry illustrated as coloured fields in the structural composite plots (Appendix A). The confidence level depends on the number of evident structures found within each coherent COL:

- **high** is defined by three or more distinct, preferably moderately inclined to steep (> 15°) planar and/or non-planar features (Fig. 2-6), resulting in a high angular accuracy.
- **moderate** is associated with one or two correlated (non-) planar structures with shallow to moderate dip angles (< 15°; Figs. 2-7 and 2-8). Thus, the core orientation contains some uncertainty and is less accurate.
- **not oriented** is characterised by a lack of obvious indicators for the core orientation; these cores are not oriented.

Tab. 2-1 gives an overview of the core goniometry confidence assessment. The procedure described in Section 2.1.2 resulted in a successful orientation of 745.97 m out of the total 811.10 m drill cores (92%).

Tab. 2-1: Core goniometry confidence assessment of the analysed interval

Borehole interval			Goniometry confidence								
Top	Bottom	Length	High			Moderate			Not oriented		
[m MD core depth]			[m]	[%]	No. of COLs	[m]	[%]	No. of COLs	[m]	[%]	No. of COLs
470.00	1'288.12	818.12	335.26	41	35	410.71	51	53	65.13	8	87

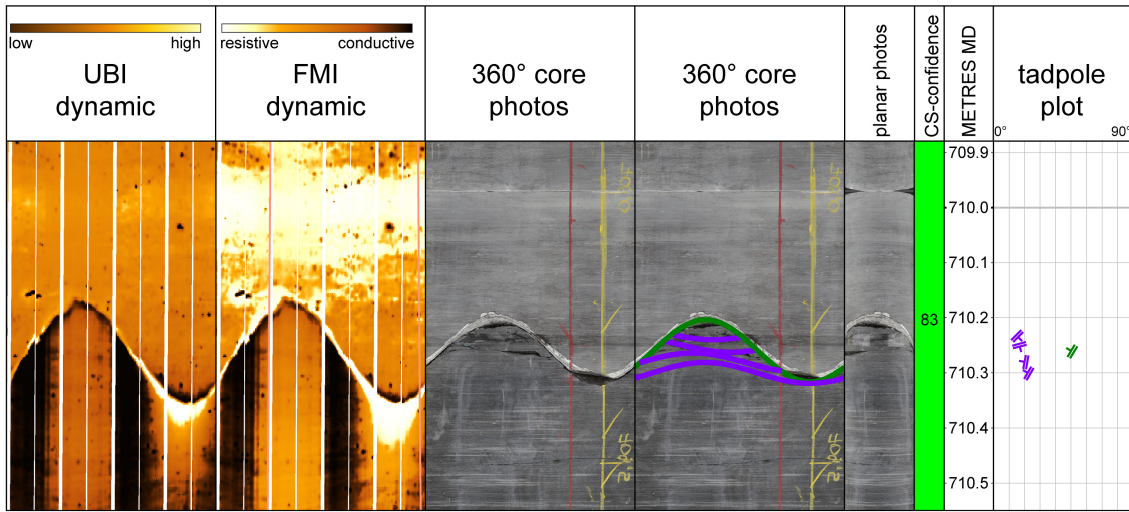


Fig. 2-6: Core – FMI / UBI correlation for a fault plane at 710.26 m MD (log depth) in the Wildegg Formation

This prominent NW-dipping fault plane was unequivocally correlated across the UBI and FMI logs and the core photographs, and therefore represents a high-confidence indicator for the core orientation. From left to right: acoustic UBI image log, dynamic normalised FMI images, shifted and oriented 360° core photographs without (left) and with (right) sine waves, followed by shifted planar core photographs. The core section numbering is shown in the coloured bar displaying the goniometry confidence ranking ("CS-confidence" column, high – green in this case). The depth track shows the position and length of the currently displayed window (about 65 cm). A tadpole plot with true orientations of manually picked mirror-like fault planes (shown in purple) is also displayed.

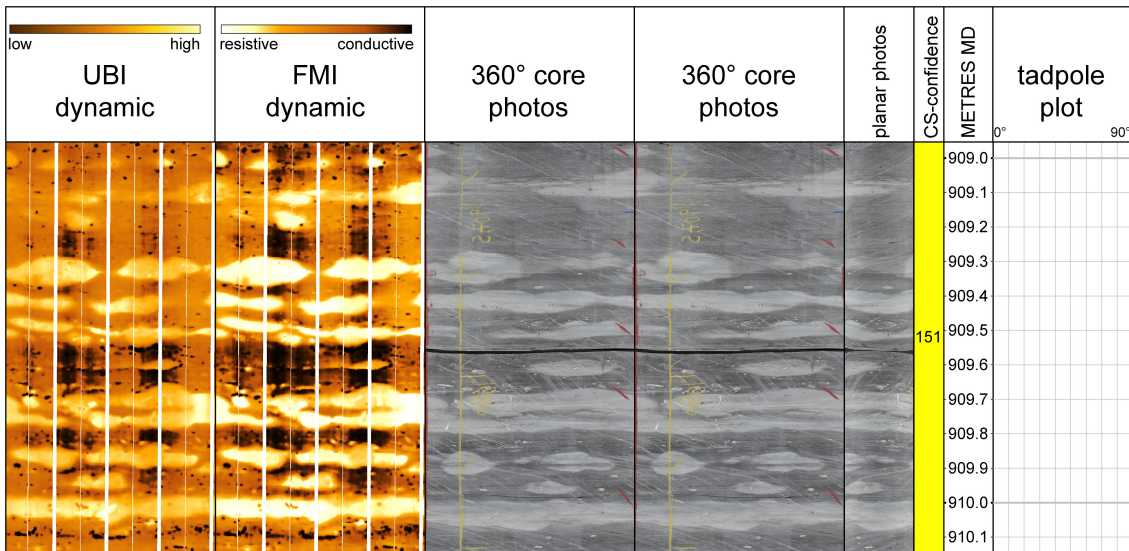


Fig. 2-7: Core – FMI / UBI correlation from 909.05 m to 910.15 m MD (log depth) in the Stafflegg Formation

These unique structures represent nodules which appear bright on the UBI (high amplitude) and on the FMI (high resistivity) images. They were used to shift and orient core section 151. Due to their heterogeneous nature, they are considered as indicators of limited quality for the core goniometry and assigned a moderate confidence level ("CS-confidence" column, yellow).

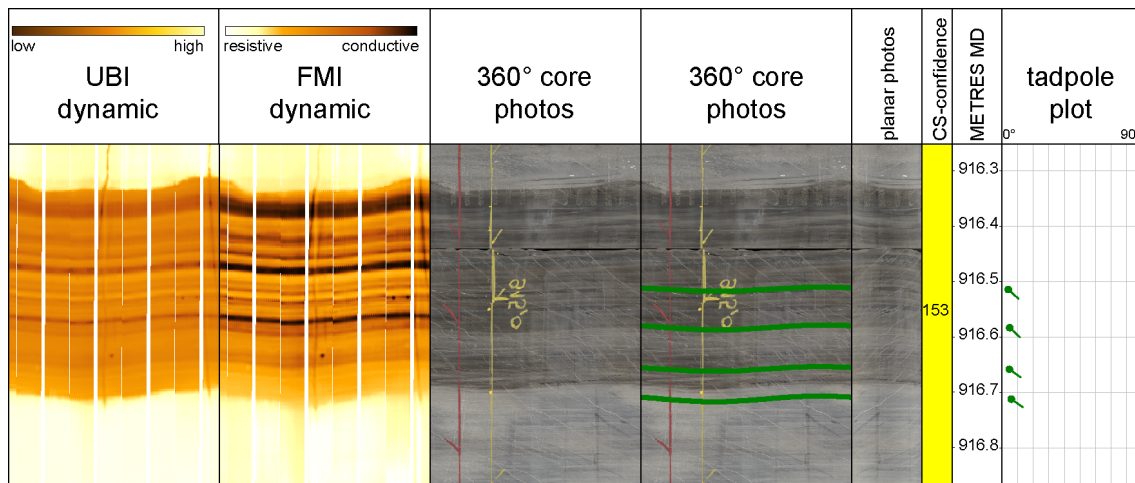


Fig. 2-8: Core – FMI / UBI correlation for subhorizontal to shallow dipping bedding

The FMI and the core photograph match within the well-bedded strata in the Staffelegg Formation from 916.35 m to 916.70 m MD (log depth). Although the bedding planes are clearly visible on the FMI and core photographs, the relatively low dip angles ($< 10^\circ$) imply some angular uncertainty and are therefore considered as moderate indicators for core goniometry ("CS-confidence" column, yellow).

Project-specific uncertainties

A number of unavoidable limitations and uncertainties were associated with the work performed and may have affected the accuracy of the results. These factors are evaluated below:

- Angular uncertainty is associated with the core goniometry and is reflected by the confidence scheme. It implies in particular an angular error for the azimuth.
- Errors related to compass measurements on drill cores: to explore the measurement-related error, multiple measurements of the same structure were performed by different users. The reproducibility was 5° for the dip magnitudes and 5° to 10° for the dip azimuths. Considering that most geological compasses have an error margin within 2° for dip azimuth and magnitude, it can be concluded that the above-mentioned goniometer has an acceptable error margin and can safely be used for accurate structural core analysis.
- Dip picking on 360° photographs: the pixel resolution of the screen defines the angular uncertainty of the dip picks in 3D space and is 1° to 2° for the dip angle and 2° to 4° for the dip azimuth.
- Core photographs: although the derived 360° core photographs covered almost the entire studied interval (470.00 m to 1'288.12 m MD core depth), some data gaps occurred, e.g. from 474.45 m to 475.50 m MD (core depth), from 934.95 m to 938.60 m MD (core depth), from 941.10 m to 942.09 m MD (core depth), from 945.30 m to 946.15 m MD (core depth), from 961.50 m to 962.66 m MD (core depth), from 973.69 m to 974.65 m MD (core depth), from 997.10 m to 997.40 m MD (core depth), from 1'051.04 m to 1'053.00 m MD (core depth), from 1'061.13 m to 1'061.63 m MD (core depth), from 1'207.05 m to 1'209.91 m MD (core depth) and from 1'216.52 m to 1'216.99 m MD (core depth). These gaps, all larger than 30 cm, are mainly related to disintegrated and/or highly fractured drill cores, which were not suitable for circumferential photography, or to data gaps between core sections.

- In some core intervals the core orientation line was discontinuous. This was mainly related to uncertainties in assembling individual core pieces / sections at the drill site. In such cases, the non-coherent core sections were treated separately (see Appendix E-2)
- Due to the presence of steel in the Nagra core storage facility in Würenlingen, a site-specific magnetic field disturbance was recognised. Consequently, the goniometer needed to be carefully aligned towards relative north to obtain the correct orientations of the geological features (mainly lineations) measured with a compass. This always had to be kept in mind when moving the equipment across the core store

2.2 Structural work

This section describes (A) how the structural recording and characterisation of drill cores was carried out, (B) which structure types were distinguished, and (C) which structure parameters were defined. Details with regard to the structural core analysis are given in the structural analysis manual and enclosed factsheets and templates (Ebert & Decker 2019).

- A) After the core goniometry was finalised, all deformation structures were recorded on the drill cores. The recording was usually finalised within a few weeks.

The overall core quality was excellent. Only cores from clay-rich lithologies (particularly the Dogger) were affected by progressive discing but were still suitable for structural analysis. Due to 370 samples with lengths of up to 50 cm being taken at the drill site (e.g. for porewater or geomechanical analyses), there were gaps within the core sections. Samplers were strictly advised not to sample core intervals containing tectonic structures. The completeness of the structural record is therefore not biased or limited by sampling. Furthermore, it can be assumed that the complete structural inventory was recorded because high-resolution core photographs were taken from all cores, including the sampled core sections.

Most of the structural work was performed by two people. A structural geology expert defined all visible structure types along with their relevant parameters for each core section, which was usually 3 m long. At the same time, the other colleague manually picked the structures on the 360° core photographs in TerraStation II. The structures and their parameters such as mineralisation, thickness or shear sense were documented on a DIN A3 template with content previously defined in Ebert & Decker (2019). The log depth was determined in metres MD along with the true orientation of the structures on oriented 360° core photographs. The difference in depth between the core and log depth mostly varied by only a few centimetres and depended on the dynamic depth shift of the core photographs with regard to the FMI used as the main depth reference data. Striations on slickensides recognised on surfaces of broken cores were measured with a geological compass (Fig. 2-1). As soon as a core section was completely analysed, all entries from the DIN A3 template were digitised, and data QC was carried out.

- B) Depending on rock rheology and the type and degree of deformation, different types of structural discontinuities may develop. Based on this, the structures were subdivided into five main groups of discontinuities (Fig. 2-9). In total, 11 types of structures were distinguished in this study (Tab. 2-2) and are illustrated with numerous examples in Chapter 3. Detailed definitions and information on the origin of the structures can be found in the structural manual of Ebert & Decker (2019).
- C) Additionally, parameters such as mineralisation, shear sense and thickness (listed in Tab. 2-3) were determined and documented for each individual structure on the DIN A3 template (Fig. 2-10). In addition, each structure was sketched and labelled with a consecutive number on the designed grid with a scale of 1:10.




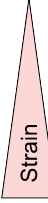
Mohr-Coulomb type brittle failure			Viscous (ductile) deformation	
Fractures			Without cohesion loss	
Drilling-induced	Extensional	Shear	Carbonate solution	Ductile shear
 <p>Centreline fracture Petal fracture Core discing</p>	 <p>Joint Vein (Tension gash)</p>	 <p>Fault plane Fault zone</p>	<p>Stylolite / Dissolution seam Stylobreccia</p>	 <p>Shear band Mylonite</p>

Fig. 2-9: The five main groups of structural discontinuities

Tab. 2-2: Types of structural discontinuities identified in this study

For more details see Ebert & Decker (2019).

Discontinuity group	Structure type	Characteristics
Brittle structures with shear indications	Fault plane	Planes of shear failure, i.e. planes along which there has been movement parallel to the plane (Peacock et al. 2016). Single, thin, planar and sharp structural discontinuities with shear indications (e.g. striation or slickenfibres).
	Mirror-like fault plane	A fault plane with a smoothed, polished or shiny slip surface.
	Stylolitic fault plane	A fault plane with dissolution seams and stylolite-bearing columns which are oblique or parallel to the plane (modified from Hancock 1985).
	Fault zone	A fault zone is defined as a zone with a volume which includes interacting and linked fault segments, densely fractured rock and/or fault rocks; zones are typically bounded by sub-parallel margins or fault planes (modified from Peacock et al. 2016).

Tab. 2-2: continued

Discontinuity group	Structure type	Characteristics
Brittle structures without shear or slip indications	Joint	A barren, closed fracture on which there is no measurable slip or dilatation at the scale of observation. If any mineral fill, including crystal growth fibres, is visible, the structure is better called a vein (Hancock 1985).
	Vein	Extensional fracture filled by secondary mineral crystallisation.
	Tension gash	Vein formed by dilatation; tension gashes may be fully cemented (vein), partly cemented (partly open) or open (Passchier & Trouw 1996).
Structure without preserved evidence for the mode of fracturing	Unassigned fracture	General term for a structure without preserved evidence for the mode of fracturing, i.e. it is applicable to structures formed by extension or shear; fractures can include close-to-planar discontinuities such as dykes, faults, joints and veins (Peacock et al. 2016).
Structures caused by dissolution	Stylolites	Stylolites are irregular seams of insoluble residues with dark, "mountainous" rough teeth formed by pressure solution (Passchier & Trouw 1996).
	Open pores	Isolated open volumes in the rock mass, resulting e.g. from incomplete cementation of veins, dissolution or preserved cavities in fossils.
	Karst	Open networks resulting from dissolution of carbonates. These cm- to m-wide cavities may have been refilled later.
Fabrics without cohesion loss, e.g. caused by ductile deformation	Shear bands	Minor planar shear zones in which the progressive deformation is non-coaxial (Passchier & Trouw 1996).
	Mylonites	Strongly deformed rock from a ductile shear zone with a planar foliation and usually with a stretching lineation (Passchier & Trouw 1996).
	Schistosity	Secondary foliation defined by preferred orientation of equant fabric elements in a medium- to coarse-grained rock. Individual foliation-defining elements (e.g. micas) are visible with the naked eye (Passchier & Trouw 1996).
	Dynamic recrystallisation	Dynamically recrystallised, smaller and elongated crystals.

Tab. 2-2: continued

Discontinuity group	Structure type	Characteristics
Drilling-induced fractures (DIF)	Drilling-induced fractures	Collective term for fractures created by forces associated with drilling and coring procedures. Depending on load on drill bit, mud weight and rock properties, drilling-induced fractures develop during drilling or shortly thereafter. Based on the aperture, fracture surface and geometric relationships, drilling-induced fractures can be distinguished from natural fractures. Drilling-induced fractures are always open and never mineralised.
	Petal fracture	Drilling-induced fracture with convex-up geometry cutting a core downwards starting from its perimeter. Petal fractures form immediately ahead of the drill bit as a result of excessive bit weight during coring. They propagate downhole.
	Centreline fracture	Drilling-induced fracture that typically splits a core approximately in half.
	Core discing	The formation of discs of relatively uniform thickness which fracture on surfaces approximately normal to the axis of the core.
Additional features / dip types	Undifferentiated bedding	Planar surface representing either the boundary between two different lithological units or internal bedding. Thought to reflect original horizontal and planar surfaces.
	Deformed bedding	Bedding planes occurring in narrow zones in any lithology with moderate to steep dip angles (> 15°) which differ from the general structural dip. They have been subject to deformation due to faulting and/or folding.
	Cross-bedding	Inclined foreset surfaces in sandstone occurring in sets and bounded by set boundaries. These sedimentary features may be used as paleocurrent indicators. Upper truncation by the next set is diagnostic.
	Fold (axis)	One or a stack of originally flat and planar surfaces, such as sedimentary rocks, that are bent or curved due to applied external stress. Folds appear in various scales and shapes.

Tab. 2-3: Systematically recorded parameters for the investigated structures

Parameter	Definition of parameters and procedure for defining parameters
Depth	<p>All types of structures are recorded quantitatively along the scanline of the core axis. The depth of the structure is measured at the point where it cuts the core axis. For steeply dipping planes, the depth should be determined halfway between the top and the base of the intersection ellipse of the structure.</p> <p>If a zone is recorded (e.g. fault zone, shear band, fracture density class), the top (Top MD) and the base (Bottom MD) of the zone are specified in the corresponding columns.</p>
Core orientation line number	<p>After extraction of the core from the inner tube, the core pieces are juxtaposed whenever possible. Continuous sections without drilling breaks, demarcated by grinding, crushed or core loss zones, are marked with a core orientation line and denoted with a consecutive number. This number enables linking of the recorded structure with the key structure of this orientation line section that was identified on the borehole image.</p>
Depth shift between core and FMI	<p>The depth shift is defined using correlated structures visible on both the FMI and core.</p>
Correlation with log	<p>Assessment of whether each individual structure can be clearly identified on FMI / UBI and core. "yes" indicates that the structure can be correlated with the image log and "no" indicates structures which cannot be correlated, or which are not shown by the image log. In addition, a correlation quality ranking is carried out (1 – good, 2 – moderate, 3 – no correlation).</p>
Dip direction and dip angle	<p>Measured dip direction and dip angle of the structure.</p>
Structure type	<p>The abbreviations for structure types according to Tab. 3-2 are entered into the paper template.</p>
Length of structure	<p>The length of the long axis of the intersection ellipse is measured for structures which cut the core axis at acute angles (dipping with more than about 70°) and structures which do not cut through the entire core diameter. The measured length will be used for the calculation of fracture density P32. Measurements are required to reduce the inaccuracy resulting from calculating fracture areas solely from the angle between the structure and the core axis.</p>
Azimuth and plunge of lineations	<p>Measured plunge azimuth and plunge of the lineation observed on the measured plane.</p>
Shear sense and quality	<p>Shear sense of fault planes and shear bands using up (reverse fault), down (normal fault), dex (dextral strike slip) or sin (sinistral strike slip), and reliability indicators (good, fair, poor) of the shear sense observation.</p>
Mineralisation / fault rock type	<p>Any type of filling, mineralisation or fault rock associated with the structure (e.g. CC for calcite of a vein filling, synCC for mineralisation of slicken-fibres).</p>

Tab. 2-3: continued

Parameter	Definition of parameters and procedure for defining parameters
Open / closed and width / length of open structures	Information on whether a tension gash / vein is open (displaying a continuous aperture), partly open (displaying a discontinuous aperture) or closed at the observation scale (i.e. the naked eye), including the width of the aperture and the observed lengths of open streaks for partly open structures.
Roughness	Roughness classification of a structure using the joint roughness coefficient (JRC). The JRC gives a picture of the classification of fracture smoothness and waviness (planarity) along 10 cm length of the fracture (Barton 1976, Barton & Choubey 1977). The scale of the JRC is from 0 (very smooth and planar) to 20 (very rough and wavy).
Fracture condition	Specifies whether the core is broken naturally or artificially at the structure under consideration or intact. If it cannot be specified whether the fracture occurred naturally or artificially, broken should be used.
Fracture density	Numerical value that reflects a quantitative measure of the abundance of fractures in a rock mass (e.g. fractures per metre, fracture area per rock volume).
Fracture density class (FDC)	In cases where cores or parts of a core are heavily disintegrated and order cannot be restored, the density of natural fractures cannot be assessed accurately. Fracture density should be estimated using the classification scheme of Bauer et al. (2016): fracture density class 2 (spacing of fractures = 5 cm to 10 cm), fracture density class 3 (spacing of fractures = 1 cm to 5 cm) or fracture density class 4 (spacing of fractures < 1 cm).
Additional remarks	Offsets or displacements as well as crosscutting relations are documented under "remarks". Further remarks are e.g. karstification, the shape and length of the teeth of stylolites, alterations, recrystallisation phenomena or whether a structure is likely of syndimentary origin.

2.3 Geo-statistical evaluation

For the geo-statistical evaluation presented in Chapter 4, different structural tools and techniques were applied to analyse the available dip dataset. Most of the work was performed with TerraStation II. This provides several advanced modules for the import, processing, visualisation and analysis of all types of available borehole data such as petrophysical logs, borehole images, core data and stratigraphic information.

For the structural evaluation of the different lithostratigraphic units and the different types of structural discontinuities, a series of figures was compiled:

- Stereograms (Schmidt projection, lower hemisphere)
 - Poles of the planes were displayed to examine the spatial orientation of bedding and structural planes
 - Dip azimuth rose diagrams were compiled for planar features (bedding, fractures and stylolites). The diagrams show the dip azimuth of the planes under consideration. The rose diagram is a circular histogram summarising orientation measurements. The radius of each segment of a rose diagram is proportional to the number of observations that occur within the angular range of that segment. Dip azimuth rose diagrams are displayed with cumulative petals, resulting in stacked petals for different dip categories. For the directional statistics in Chapter 4 a minimum threshold of ten structures was set for the rose diagrams
- Dip histograms visualise the dip angle distribution and clustering for a given dip dataset
- Vector means for representative clusters of the different structure types were calculated in stereograms
- The vector azimuth plot (dip walkout plot) reflects the along-borehole dip azimuth variations and was compiled for bedding-related dips only (deformed dips and crossbedding were excluded). Here, the azimuth of the bedding was plotted in a nose-to-tail fashion pointing in the direction of dip. The length of an interval is related to the number of dips and not to the thickness of lithostratigraphic units
- Fracture density (P32 curves) reflects the fracture area per unit of rock volume (m^2/m^3). The algorithm computes the area of each fracture and creates a sum of the areas across the defined window of 1 m core length and steps of 0.1524 m. The lengths of subvertical fractures are incorporated whereas truncated parts of fractures are discarded. The computation of the area accounts for borehole ellipticity. The total area of fractures is then divided by the borehole volume (or volume of the rock mass) of the selected window. See Ebert & Decker (2019) and the literature therein for a more detailed discussion on P32 fracture density calculation. For this study, P32 fracture densities were calculated for all structural discontinuities as well as for each individual group:
 - fault planes, mirror-like fault planes and stylolitic fault planes
 - unassigned fractures, joints and tension gashes / veins
 - stylolites

The recorded kinematic indicators were analysed using the TectonicsFP software. The available fault and kinematic data were plotted in the stereographic Angelier projection, with the symbols and colours reflecting the different shear senses (up, down, sinistral or dextral) and the observed shear sense reliability (good, moderate, poor). All Angelier plots in this report show corrected datasets, in which the data points of the lineations are projected onto the great circle of the corresponding fault plane, even if they have an angular offset $< 15^\circ$.

3 Inventory of structure types

The different structure types identified in the drill cores from STA2-1 and their relevant characteristics were described in Section 2.2. In this chapter, these structures are visualised with examples. The diameter of the cores in the following figures (Figs. 3-1 to 3-23) is 95 mm.

3.1 Examples of fault planes



Fig. 3-1: Fault plane

Characteristics: Example of a fault plane with striation and mm-thick synkinematic calcite fibres. Shear sense is top up (reverse fault).

Formation: Villigen Formation, depth: 671.53 m MD (core depth)



Fig. 3-2: Fault plane

Characteristics: Example of a subhorizontal fault plane with striation.

Formation: Wildegg Formation, depth: 654.37 m MD (core depth)



Fig. 3-3: Fault plane

Characteristics: Example of a strike-slip fault. The striation and synkinematic calcite fibres are subhorizontal. Shear sense is sinistral. The photograph depicts the foot-wall of the fault.

Formation: Wildegge Formation, depth: 719.97 m MD (core depth)



Fig. 3-4: Mirror-like fault plane

Characteristics: A shallow-dipping non-planar fault plane with a polished, mirror-like slip surface and striation.

Formation: Opalinus Clay, depth: 821.92 m MD (core depth)



Fig. 3-5: Mirror-like fault plane

Characteristics: Example of a fault plane with a smooth mirror-like slip surface and striation.

Formation: Opalinus Clay, depth: 842.45 m MD (core depth)

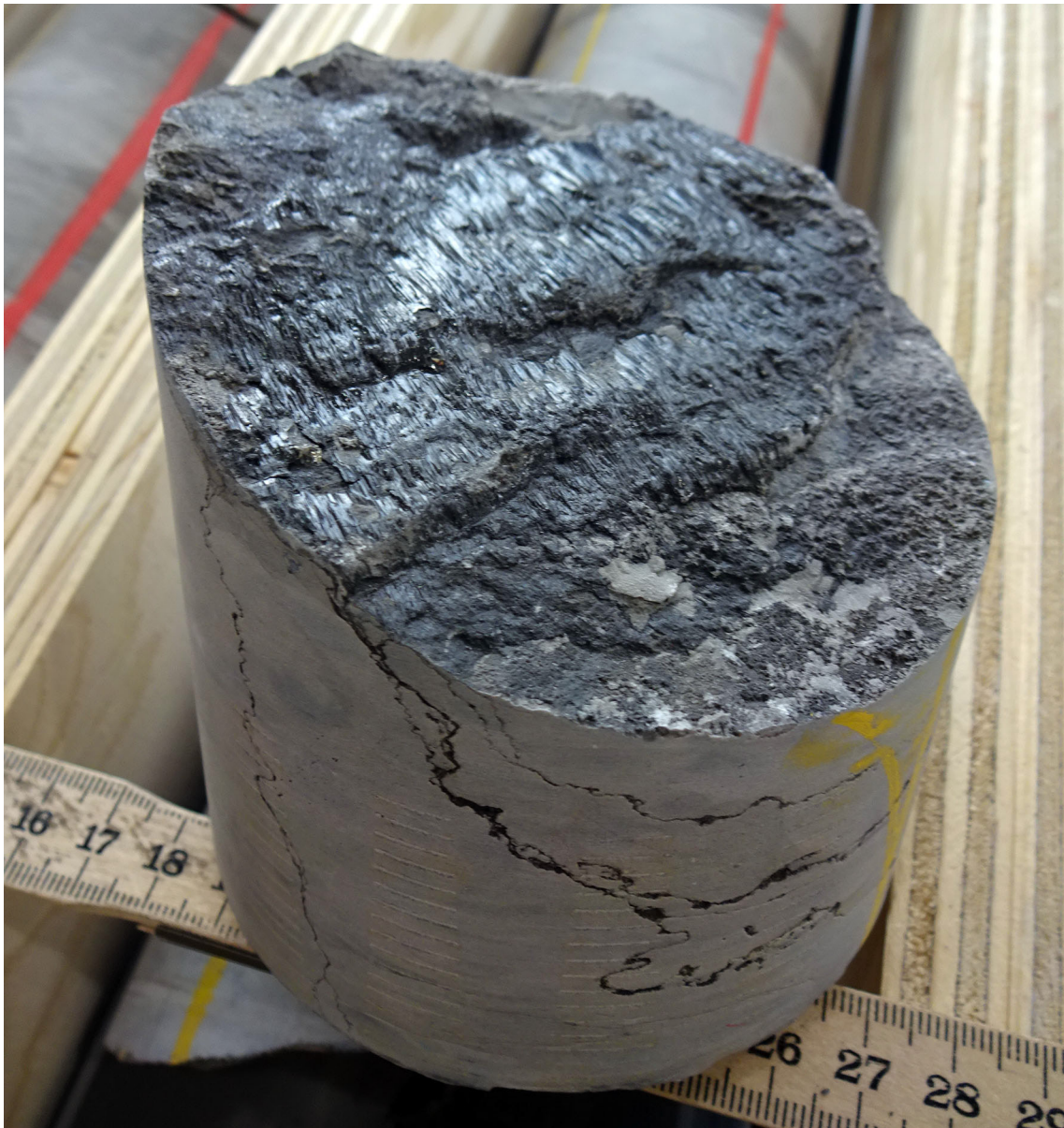


Fig. 3-6: Stylolitic fault plane

Characteristics: Example of a stylolitic fault plane with striation generated by carbonate dissolution and displacement sub-parallel to the plane.

Formation: Villigen Formation, depth: 636.79 m MD (core depth)

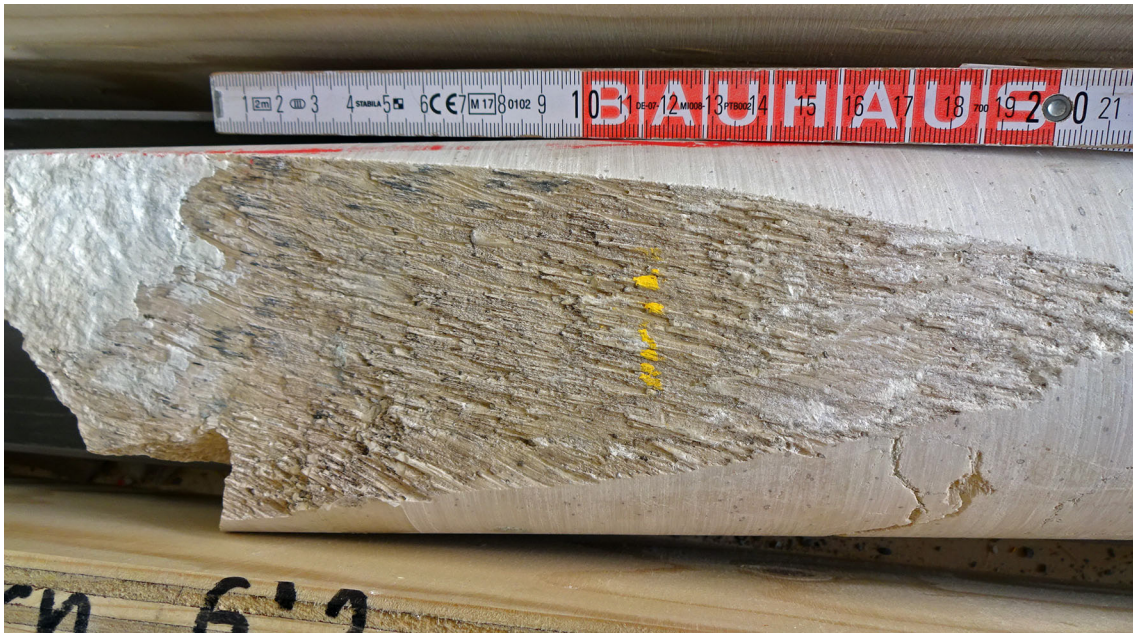


Fig. 3-7: Stylolitic fault plane

Characteristics: Example of a steeply dipping stylolitic fault plane with subvertical striation generated by carbonate dissolution and displacement sub-parallel to the fault plane.

Formation: «Felsenkalke» + «Massenkalk», depth: 481.89 m MD (core depth)

3.2 Examples of fault zones

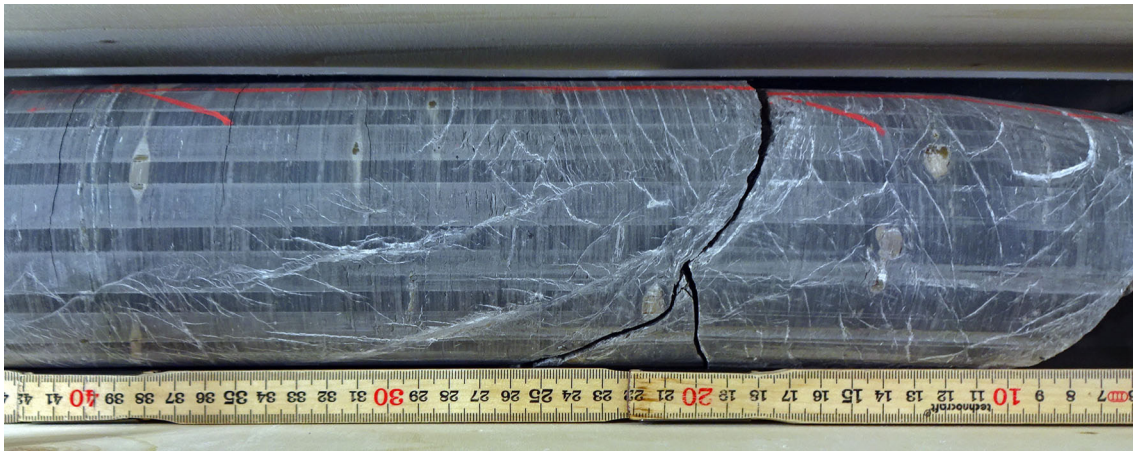


Fig. 3-8: Fault zone

Characteristics: Example of a fault zone with a network of numerous fault planes with syn-kinematic calcite mineralisation and tension gashes. The core disintegration level corresponds to fracture density class 3. The fault zone shows an orientation of 280/67.

Formation: Opalinus Clay, depth: 884.92 m to 885.60 m MD (core depth)

3.3 Examples of joints

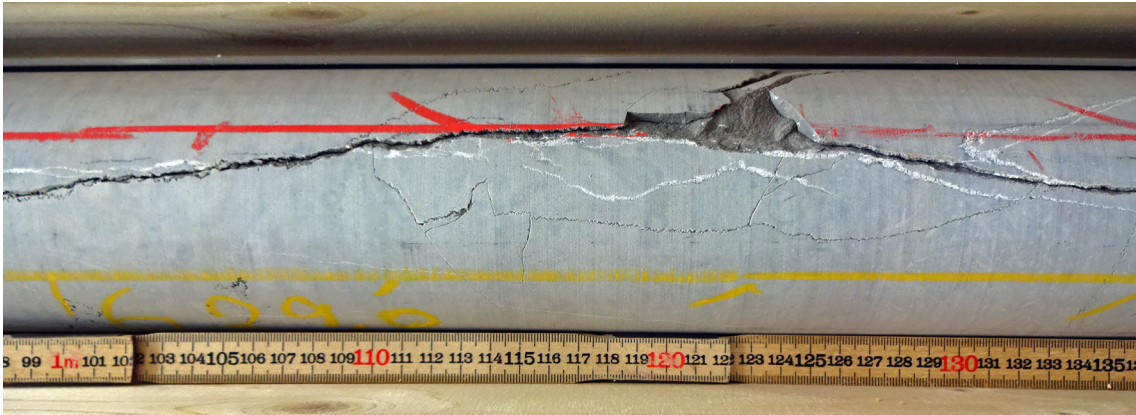


Fig. 3-9: Joint

Characteristics: A 54 cm long, subvertical joint characterised by a rough surface and the absence of slip indications.

Formation: Villigen Formation, depth: 626.11 m MD (core depth)

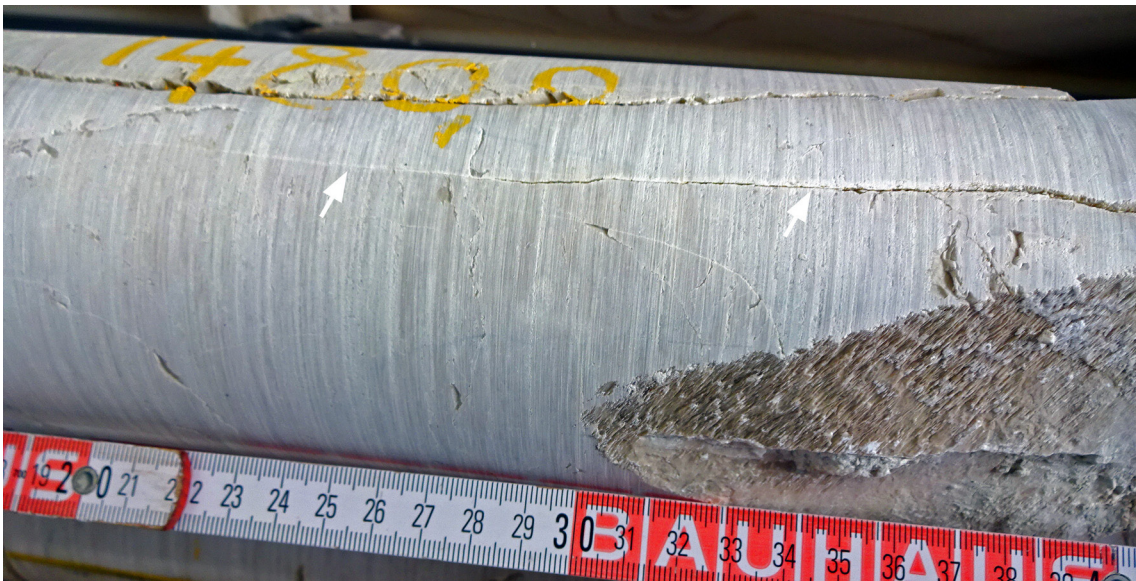


Fig. 3-10: Joint

Characteristics: A 26 cm long, subvertical joint characterised by the absence of slip indications and a thin bleaching rim (marked with white arrows).

Formation: «Felsenkalke» + «Massenkalk», depth: 480.15 m MD (core depth)

3.4 Examples of veins / tension gashes

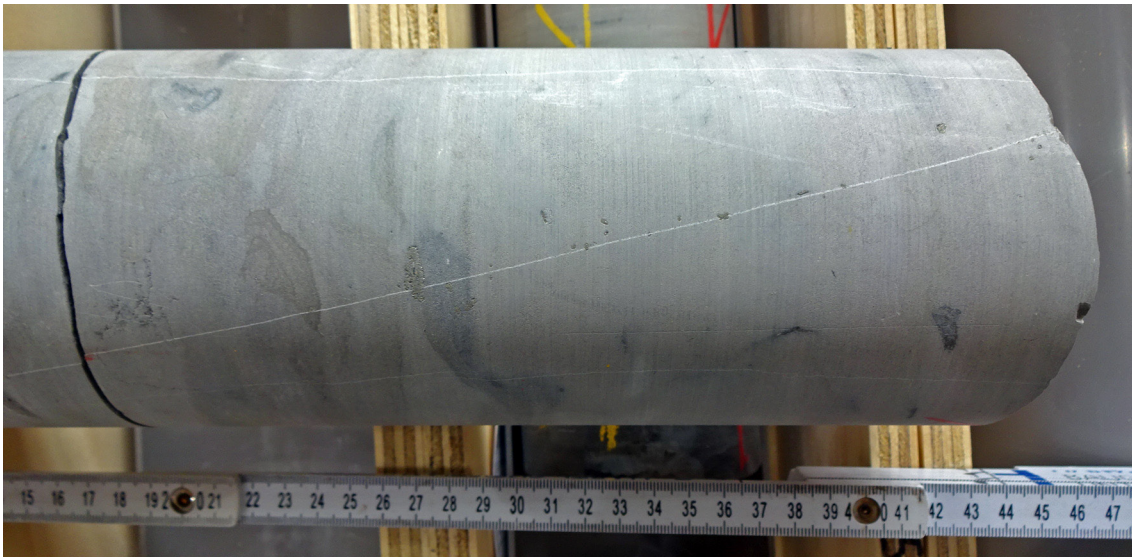


Fig. 3-11: Vein / tension gash

Characteristics: Example of a thin, steeply dipping calcite-filled tension gash.

Formation: Wildegg Formation, depth: 651.40 m MD (core depth)

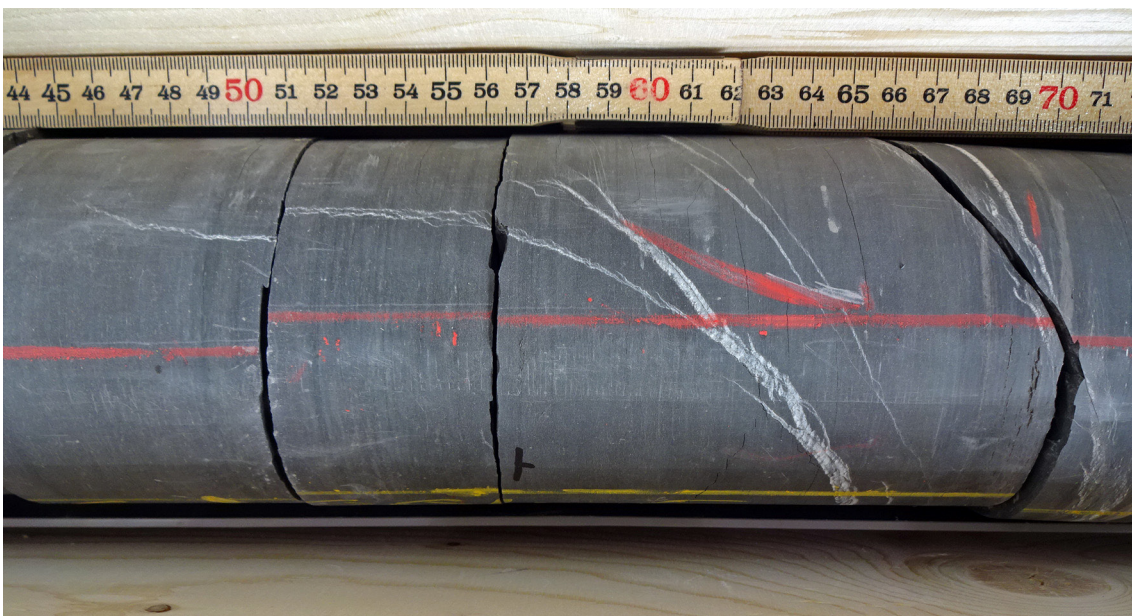


Fig. 3-12: Vein / tension gash

Characteristics: Example of several mm-thick and calcite-filled tension gashes.

Formation: Opalinus Clay, depth: 884.46 m to 884.70 m MD (core depth)

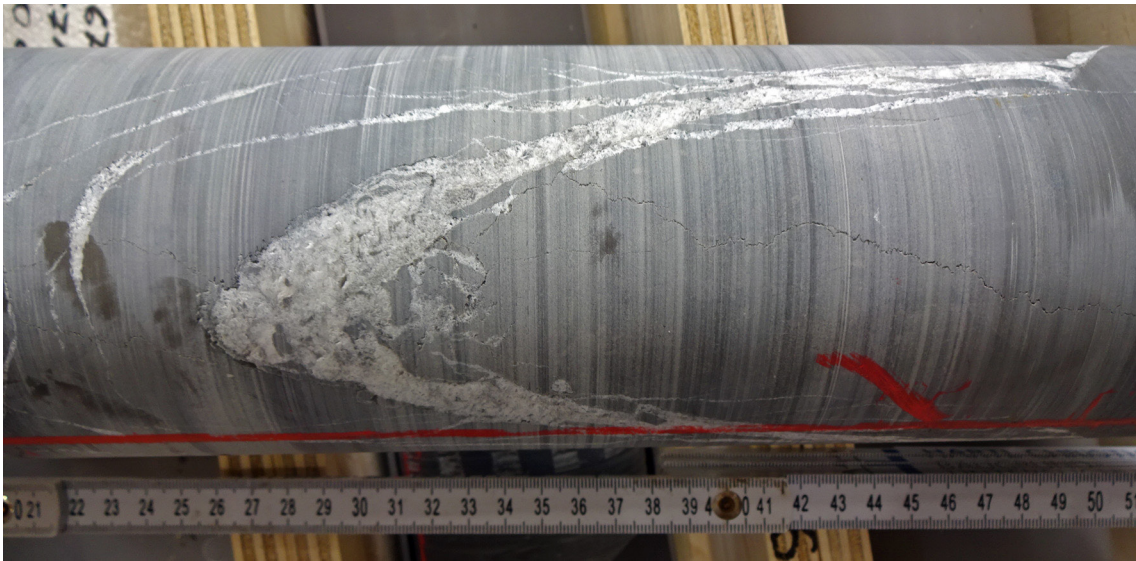


Fig. 3-13: Vein / tension gash

Characteristics: Example of a cm-thick tension gash filled with calcite.

Formation: Wildegg Formation, depth: 671.40 m MD (core depth)

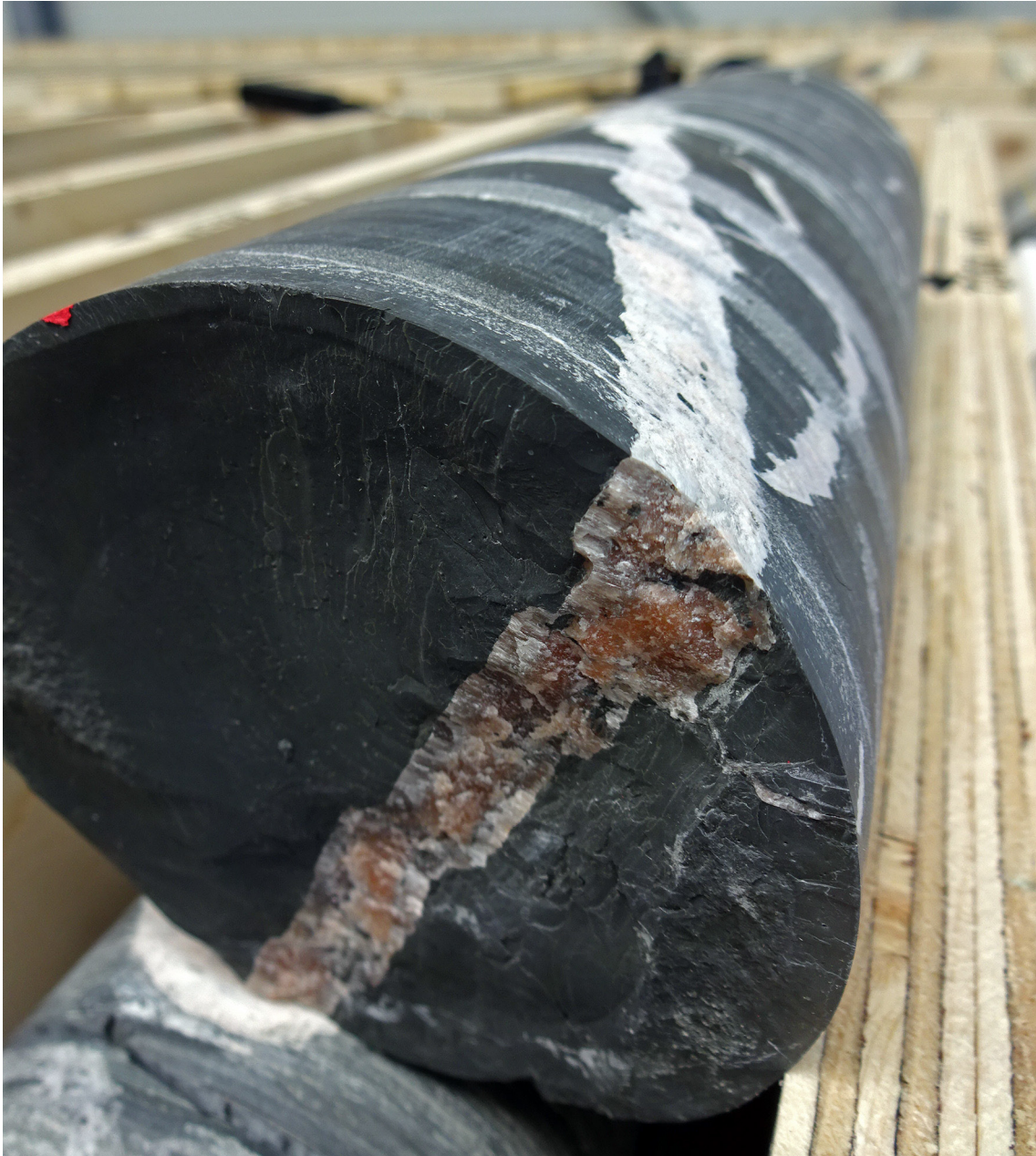


Fig. 3-14: Vein / tension gash

Characteristics: Example of a subvertical, anhydrite-filled tension gash, typical for the Bänkerjoch Formation. Two generations of mineralisation can be distinguished, with fibrous anhydrite at the rock wall and blocky to fine-grained anhydrite in the middle of the vein.

Formation: Bänkerjoch Formation, depth: 1'021.43 m MD (core depth)

3.5 Examples of stylolites

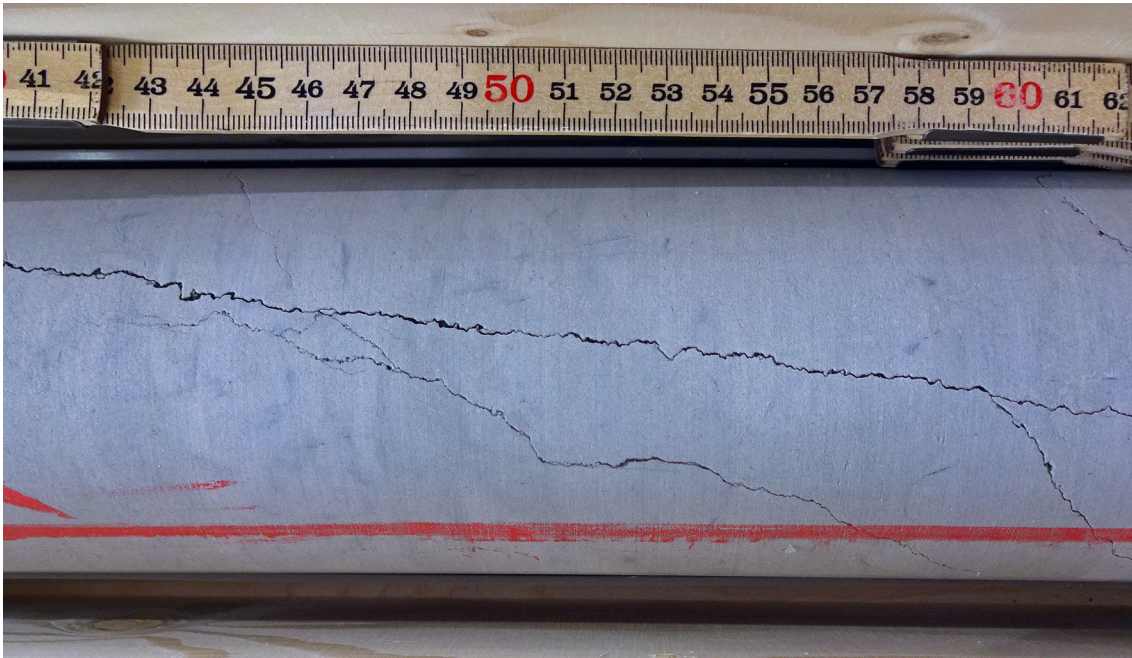


Fig. 3-15: Stylolite

Characteristics: Example of a subvertical stylolite with subhorizontal teeth.

Formation: Villigen Formation, depth: 638.59 m MD (core depth)



Fig. 3-16: Stylolite

Characteristics: Example of a subvertical stylolite confined to a calcareous layer.

Formation: Wildegg Formation, depth: 650.15 m MD (core depth)

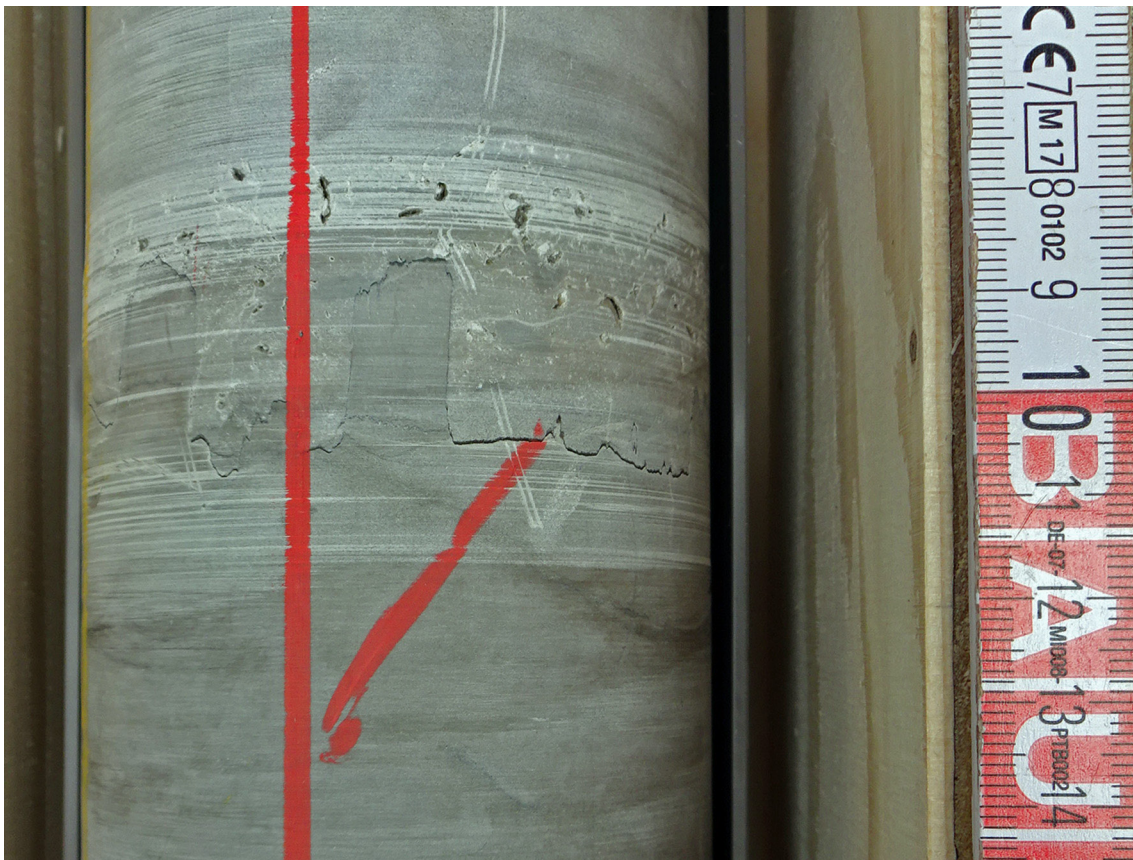


Fig. 3-17: Stylolite

Characteristics: Example of a subhorizontal stylolite with cm-long subvertical teeth.

Formation: Schinznach Formation, depth: 1'096.10 m MD (core depth)

3.6 Examples of open pores

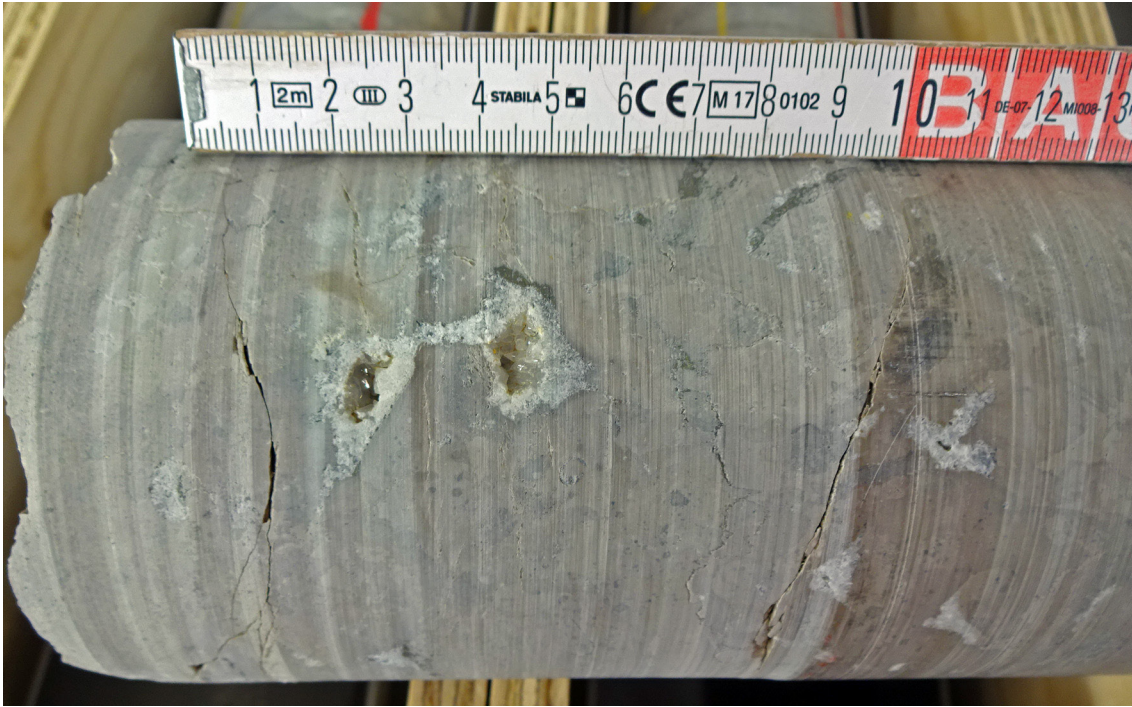


Fig. 3-18: Open pores

Characteristics: Example of two large druse-like open pores with idiomorphic calcite crystals.

Formation: Villigen Formation, depth: 547.80 m MD (core depth)

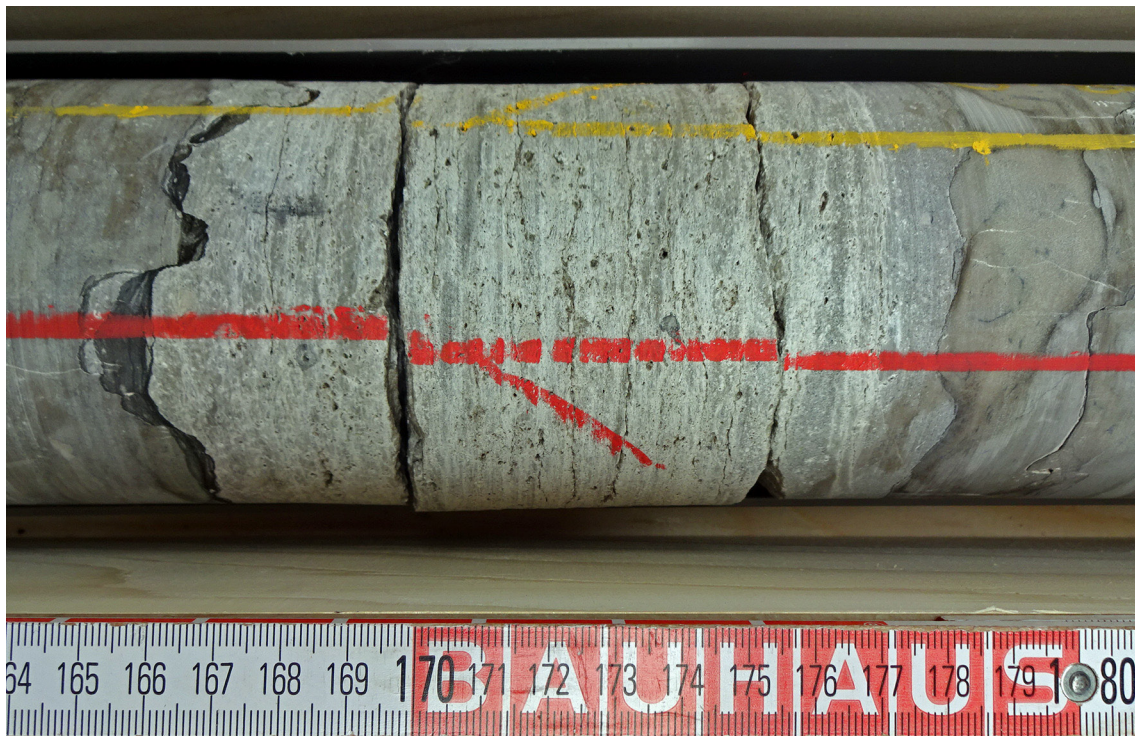


Fig. 3-19: Open pores

Characteristics: Example of open pores typically found in bioclastic-rich layers with a dense network of mm-sized open pores either with thin mineral coatings or without mineralisation. The bottom of this layer is formed by a stylolite.

Formation: Schinznach Formation, depth: 1'098.63 m to 1'098.75 m MD (core depth)

3.7 Examples of drilling-induced fractures



Fig. 3-20: Petal fractures

Characteristics: Example of a sequence of petal fractures with dip azimuth to the WSW.

Formation: Schinznach Formation, depth: 477.76 m to 477.89 m MD (core depth)



Fig. 3-21: Discing

Characteristics: Example of discing in clay-rich sediments, splitting the core into discs with typical parallel fractures. Discs are oriented perpendicular to the core axis and (sub-) parallel to the bedding.

Formation: Opalinus Clay, depth: 886.68 m MD (core depth)



Fig. 3-22: Discing

Characteristics: Example of discing in a claystone, splitting the core into several discs with typical parallel fractures. Discs are oriented perpendicular to the core axis and (sub-) parallel to the bedding. Here, fracturing nucleated from the shell in the centre of the core as indicated by the plumose structure.

Formation: Opalinus Clay, depth: 825.04 m MD (core depth)

3.8 Examples of folding

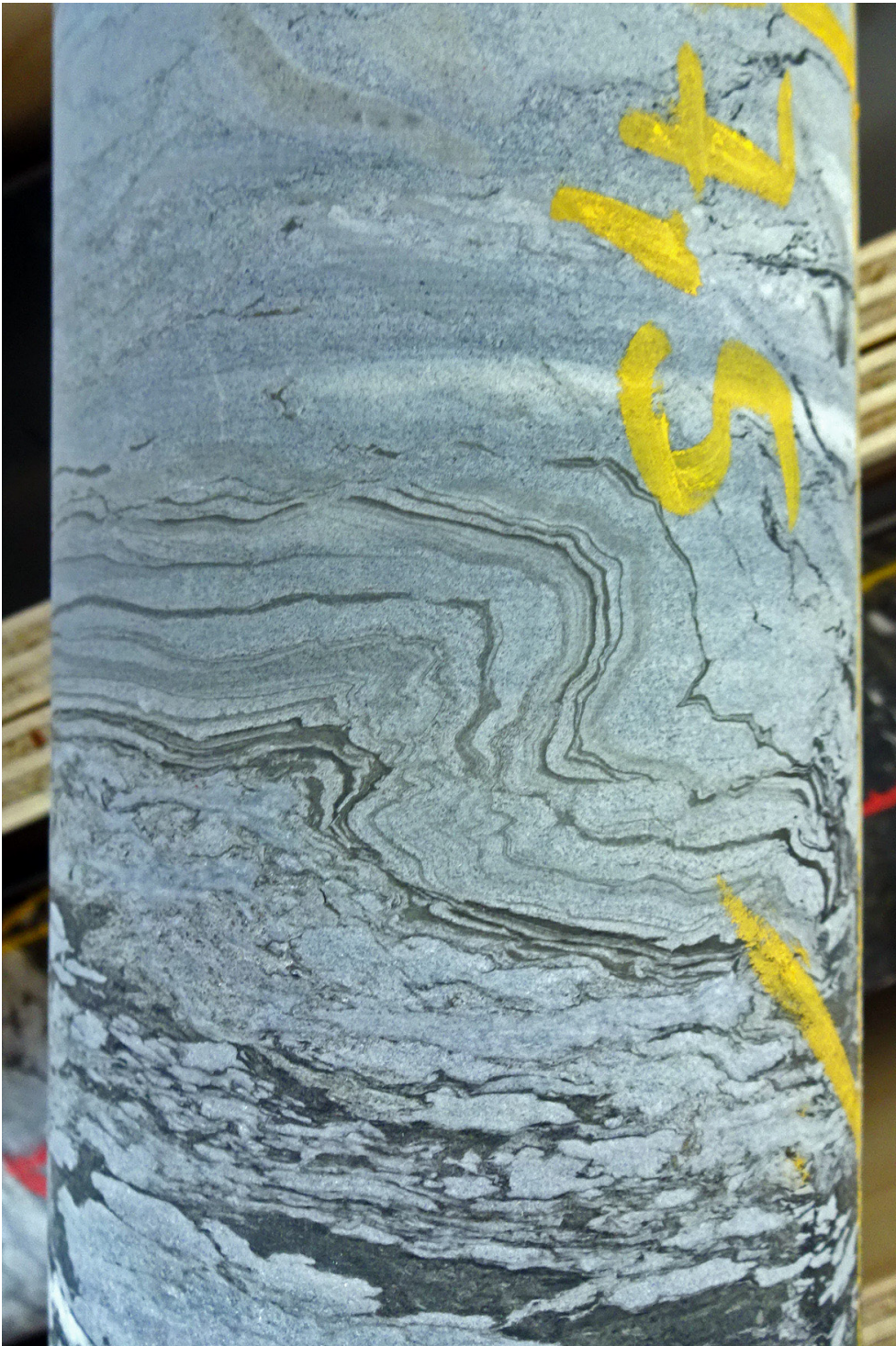


Fig. 3-23: Folding

Characteristics: Example of folded anhydrite and dolomitic marl layers, most likely of syn-sedimentary origin (folded layers show varying thickness and are eroded on top).

Formation: Zeglingen Formation, depth: 1'147.57 m MD (core depth)

4 Geo-statistical evaluation: results

Vector means of orientation values (dip direction and dip angle) of bedding planes and planar structural discontinuities were calculated for different data clusters in a stereogram projection (see Tab. 4-1). Bedding dips and structural discontinuities recorded in non-oriented cores (n = 98) were excluded from the following stereographic evaluation unless otherwise specified. However, they were included in the fracture density calculations (P32 curves) presented in Section 4.1.3 and in Tab. 4-1.

Tab. 4-1: Vector means of orientation values for bedding planes and structural discontinuities
Azim: azimuth

	Cluster 1 (main)			Cluster 2 (subordinate)			Cluster 3 (subordinate)		
	Azim	Dip	No.	Azim	Dip	No.	Azim	Dip	No.
Bedding	145	04	291						
Faults	163	05	432						
Tension gashes, joints, unassigned fractures	290	81	130						
Stylolites	169	05	394	7	78	125	191	72	247

4.1 Entire cored borehole section (470.00 m to 1'288.87 m MD log depth)

A total of 2'843 individual planar and non-planar features were identified during the core analysis and manual dip picking of the 818.87 m of core material. They are visualised in different scales in the structural composite plots of Appendices B and C-1 – C-4 and are evaluated briefly below.

4.1.1 Basic structural dip evaluation

Bedding dips, particularly in lithologies with planar bedding planes such as in claystone, marl and siltstone sequences, are the best indicators for structural dip and its variation with depth. The dip variations along the current borehole are well reflected in the stereograms of Figs. 4-1 and 4-2 and in the vector azimuth plot in Fig. 4-3.

The studied borehole interval (470.00 m to 1'288.87 m MD log depth) ranging from the Malm to the Permian Weitenau Formation reveals a subhorizontal to shallow (1° to 10°) structural dip towards the SE that is consistent throughout the studied section down to the Kaiseraugst Formation. The overall mean structural dip 145/04 [dip azimuth/dip angle] (n = 291; see Cluster 1 in Tab. 4-1). However, a few abrupt local changes in dip orientation were associated with evident faults / fault zones or with soft-sediment deformation. Within the Weitenau Formation, the dip direction changes towards the NNE indicating an angular unconformity at the top of the Permian at 1'237.94 m MD (log depth). However, this observation is based on only four representative bedding dips within the Weitenau Formation. These dip changes are highlighted in the dip vector azimuth plot of Fig. 4-3.

Dip anomalies were observed in the Opalinus Clay from 840.4 m to 840.9 m MD (log depth) and from 879.5 m to 886.6 m MD (log depth). These borehole intervals are partly characterised by bedding dips ranging from subhorizontal to about 25° and by variable dip directions. Dip changes are most likely linked to faulting and/or soft-sediment deformation. However, a more detailed structural dip evaluation is beyond the scope of this study.

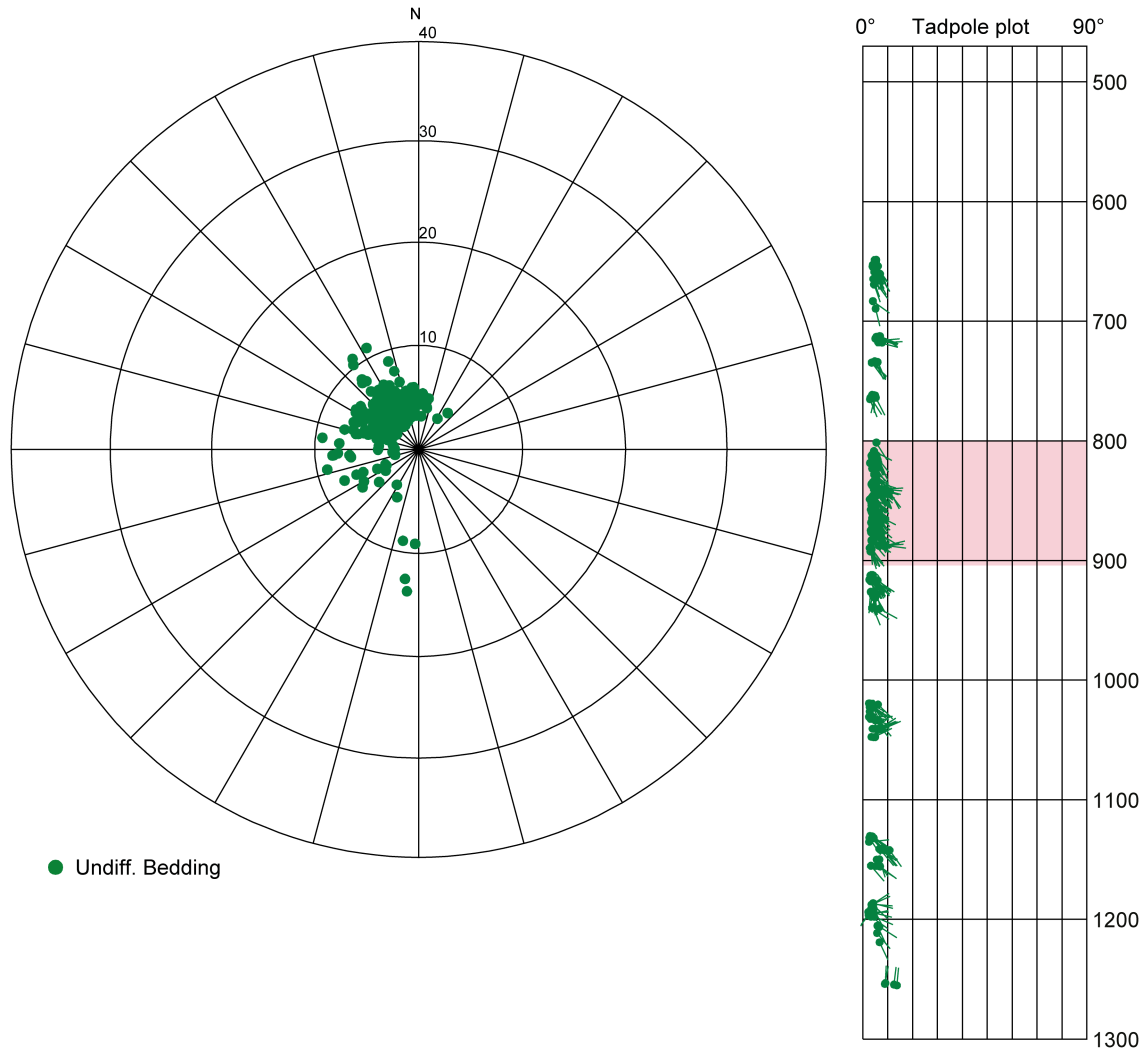


Fig. 4-1: Stereogram and depth plot for bedding planes (n = 326) for the entire cored borehole section

Note the predominance of 0° to 10° SE-directed dips with an overall mean of 145/04 (selected cluster of n = 291). Depth range is 470.00 m to 1'288.87 m MD (log depth). The Opalinus Clay interval is indicated by a red bar in the tadpole plot. The perimeter of the stereogram corresponds to 40° dip.

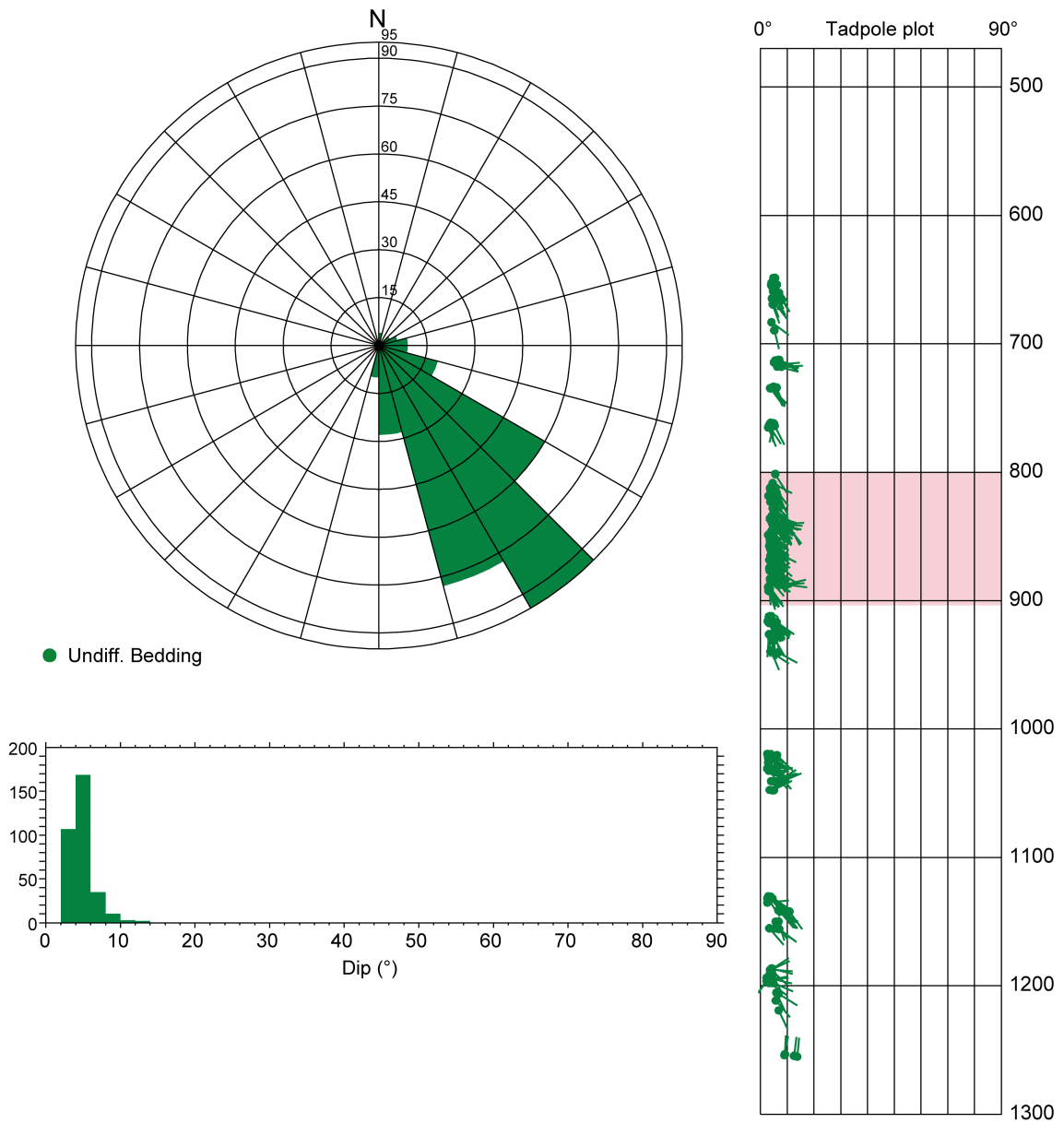


Fig. 4-2: Dip azimuth rose diagram, dip histogram and depth plot for bedding planes (n = 326) for the entire cored borehole section

Note the predominance of dip directions towards the SE. Depth range is 470.00 m to 1'288.87 m MD (log depth). The Opalinus Clay interval is indicated by a red bar in the tadpole plot.

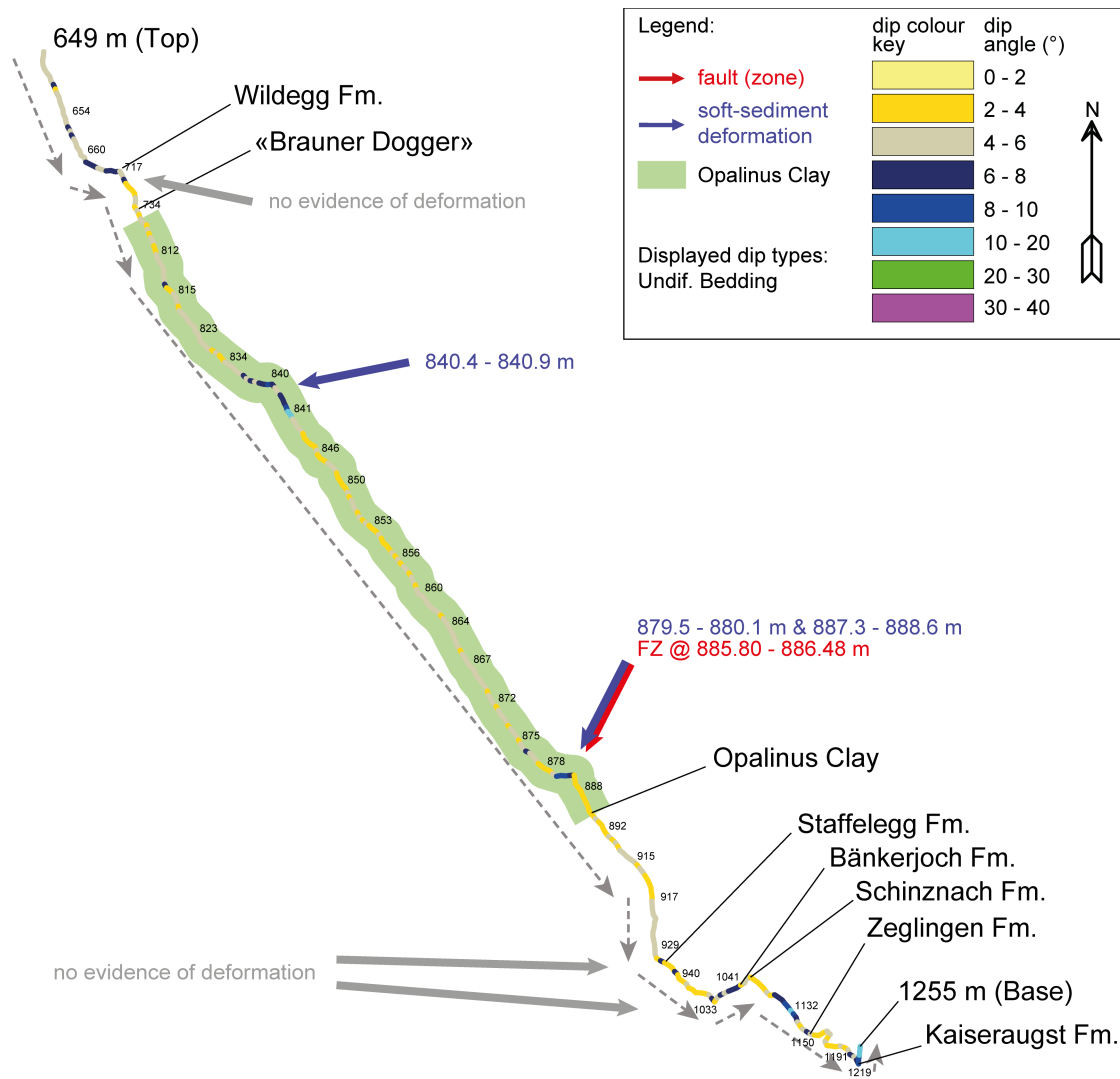


Fig. 4-3: Vector azimuth (or walkout) plot with bedding dips (n = 326) in oriented cores picked on oriented 360° core photographs

The colour-coding reflects the dip angle. The horizontal distance has no particular meaning and only visualises the bedding pick frequency. Grey dashed arrows point in the direction of the overall dip direction. Lithostratigraphic formation boundaries (bottoms) are indicated as well as faults / fault zones (red arrows) and zones with possible soft-sediment deformation (blue arrows). The Opalinus Clay interval is shaded in green. Steeply dipping, deformed bedding planes and those from non-oriented cores are excluded from this plot. Additionally, there are long intervals with no bedding picks, which sometimes correlate well with azimuth changes, even though no abrupt changes in bedding orientation, e.g. due to fault zones, were detected. Depths are given in metres MD (log depth).

4.1.2 Natural structural discontinuities

Fault planes

In total, 690 individual faults were recorded in the STA2-1 borehole. Faults are planes of shear failure, i.e. planes with plane-parallel movement (Ebert & Decker 2019). Depending on their appearance in the drill core, three types were distinguished: (1) fault planes ($n = 270$), (2) mirror-like fault planes ($n = 325$) and (3) stylolitic fault planes ($n = 95$). Out of all recorded faults, 674 (96%) were detected in oriented cores and are included in this evaluation.

Several structurally complex intervals along the borehole were interpreted as fault zones. They are commonly associated with intense fracturing and high fracture densities. The latter correspond to the different fracture density classes (FDC) defined by Ebert & Decker (2019). In total, 5 individual fault zones were defined for the entire cored interval along with their FDC in some zones (see Tab. 4-2). Additionally, 22 zones with closely spaced fault planes, mirror-like fault planes or shear bands were distinguished. Not all structures within these zones could be recorded individually.

Faults are unevenly distributed along the borehole as shown in Fig. 4-4 and are discussed in more detail in Section 4.1.4. At certain depths faults are absent, whereas at other depths they occur as swarms with a large number of individual fault planes causing heavily fractured and disintegrated rock. Such fault zones and core intervals are described using FDC.

The orientations of all recorded faults are displayed in the stereograms of Figs. 4-5 and 4-6. Faults show a scattered orientation with variable dip directions and dip angles ranging from horizontal to subvertical (1° to 85°). However, there is a predominance of bedding-sub-parallel SSE-dipping faults with an overall mean of 163/05 ($n = 432$; mean of selected cluster). Associated kinematic data could be defined on 540 fault planes out of 690 and are further evaluated in Section 4.1.4.

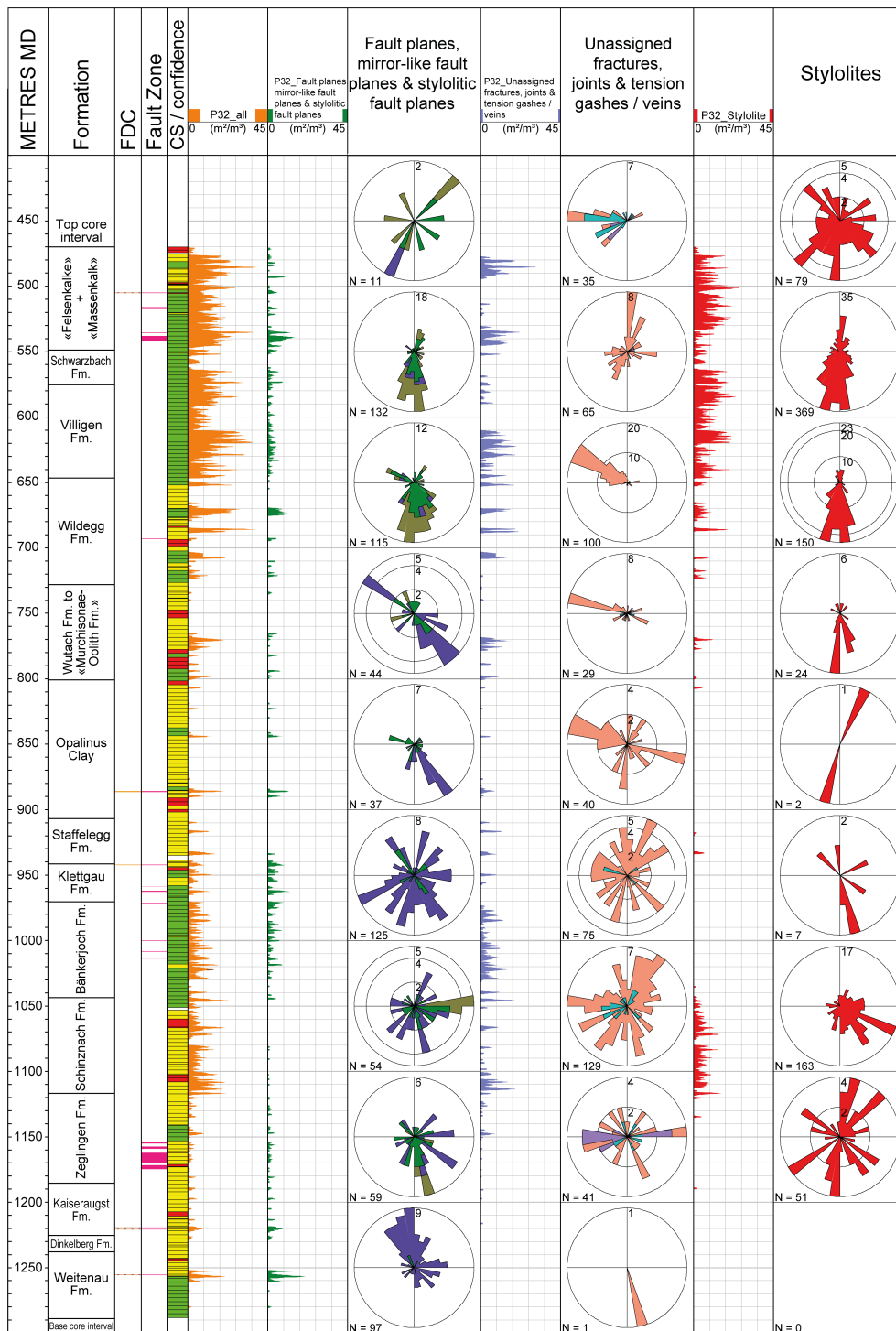


Fig. 4-4: Overview plot showing P32 densities for fractures and stylolites along the STA2-1 borehole

In addition, a lithostratigraphic subdivision, core sections and goniometry confidence as well as fault zones associated with intense fracturing (described by FDC; see Tab. 4-2 below) are shown. Rose diagrams with the respective number of planes are displayed for 100 m intervals, except for the top- and bottommost diagrams which cover thickness intervals of 30 m and 89 m, respectively.

Tab. 4-2: List of interpreted fault zones, mirror-like fault planes (MirFP), fault planes (FP), Salt shear bands (SB) and the associated FDC

Fault zones				FDC
Top (m MD log depth)	Bottom (m MD log depth)	Thickness (m)	Type	Type
504.98	505.14	0.16	MirFP zone	FDC 3
516.06	516.24	0.18	Fault zone	
517.17	517.25	0.08	MirFP zone	
535.46	535.71	0.25	Fault zone	
538.14	542.21	4.07	FP zone	
692.90	693.09	0.19	FP zone	
885.80	886.48	0.68	Fault zone	FDC 3
941.94	942.37	0.43	MirFP zone	FDC 2
958.60	958.70	0.10	MirFP zone	FDC 4
958.88	959.10	0.22	MirFP zone	FDC 4
962.13	962.55	0.42	MirFP zone	FDC 4
971.18	971.38	0.20	MirFP zone	FDC 4
999.83	1'000.34	0.51	MirFP zone	FDC 2
1'008.07	1'008.26	0.19	MirFP zone	FDC 2
1'014.11	1'014.14	0.03	Fault zone	
1'154.06	1'154.26	0.20	Salt SB zone	
1'154.51	1'154.90	0.39	Salt SB zone	
1'157.13	1'159.27	2.14	Salt SB zone	
1'162.52	1'166.70	4.20	Salt SB zone	
1'166.70	1'168.69	1.99	Salt SB zone	
1'168.73	1'170.07	0,62	Salt SB zone	
1'173.83	1'174.68	0.87	Salt SB zone	
1'219.07	1'219.09	0.02	MirFP zone	FDC 4
1'220.55	1'220.63	0.08	MirFP zone	FDC 3
1'255.41	1'255.48	0.07	MirFP zone	FDC 3

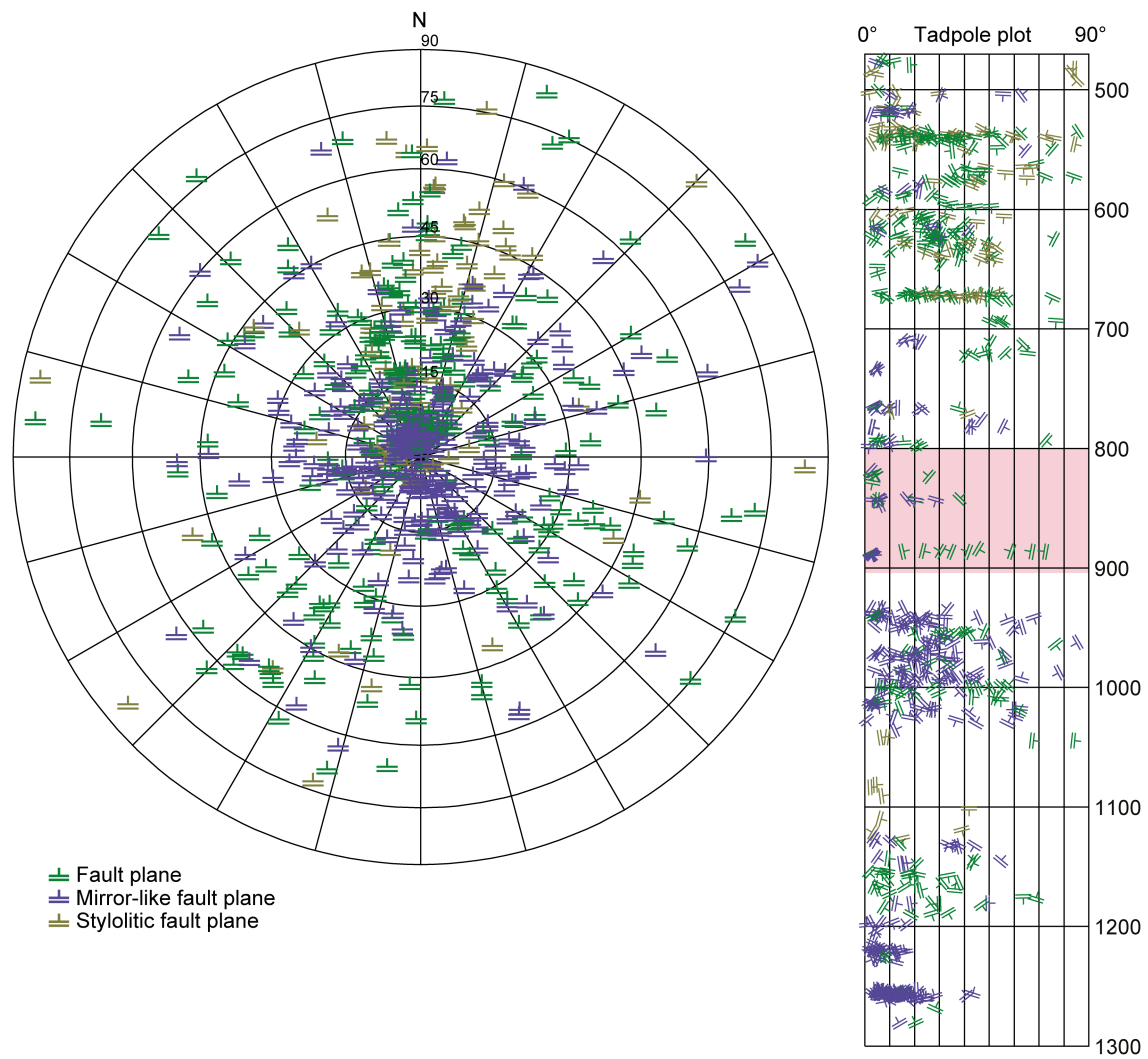


Fig. 4-5: Stereogram and depth plot of fault planes for the entire cored interval

A total of 674 fault planes in oriented cores are plotted: fault planes (n = 269), mirror-like fault planes (n = 313) and stylolitic fault planes (n = 92). Depth range is 470.00 m to 1'288.87 m MD (log depth). In the tadpole plot, the Opalinus Clay interval is indicated by a red bar.

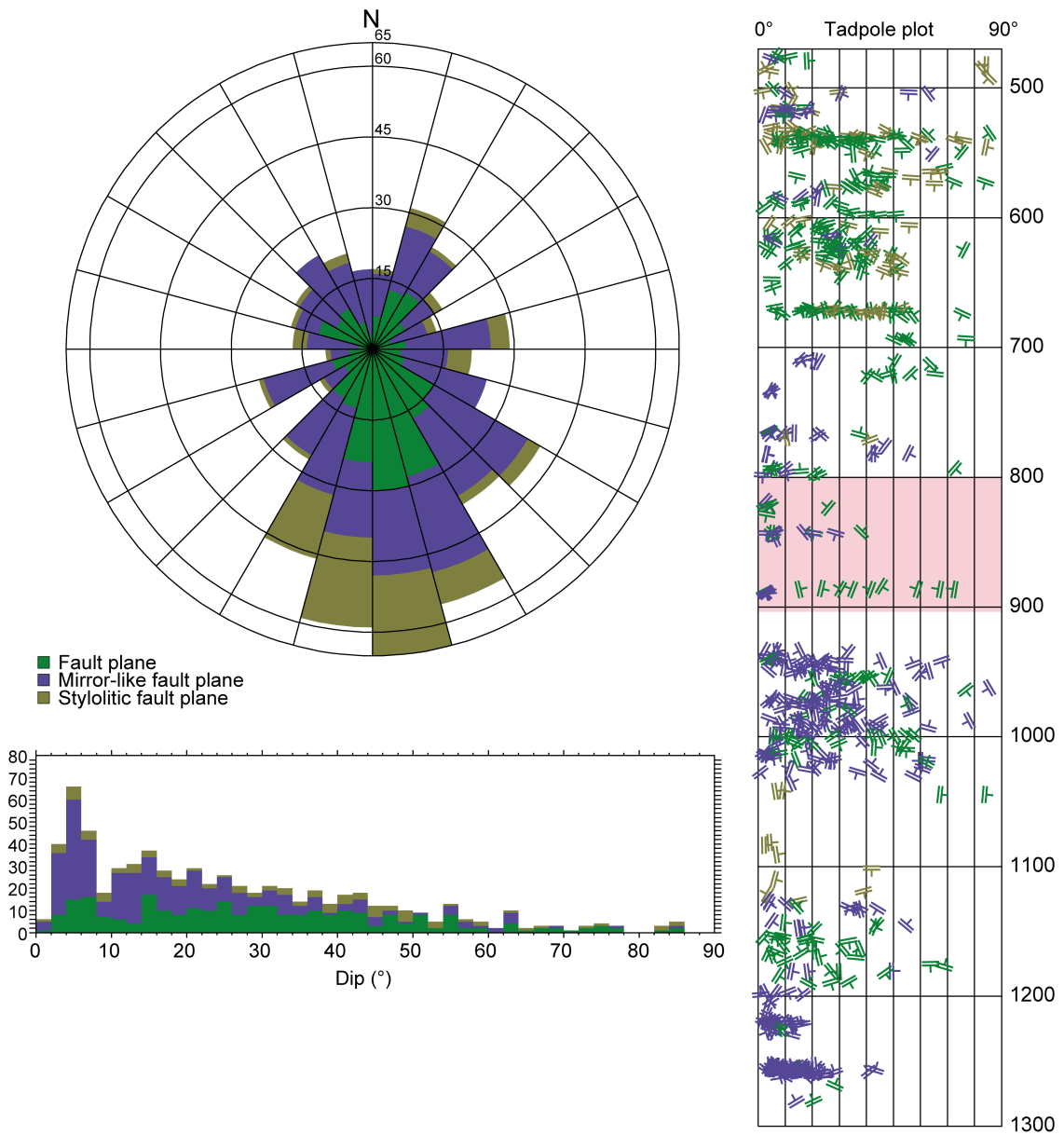


Fig. 4-6: Dip azimuth rose diagram, dip histogram and depth plot for fault planes in the entire cored interval

A total of 674 fault planes in oriented cores are plotted: fault planes (n = 269), mirror-like fault planes (n = 313) and stylolitic fault planes (n = 92). Depth range is 470.00 m to 1'288.87 m MD (log depth). In the tadpole plot, the Opalinus Clay interval is indicated by a red bar.

Tension gashes / veins, joints and unassigned fractures

This group of structures represents extensional features without shear indicators and comprises tension gashes / veins (n = 433) and joints (n = 30). Unassigned fractures (n = 62) which could not be assigned to a specific class of structure are also included. Additionally, a few zones rich in tension gashes (n = 26), joints (n = 2) and unassigned fractures (n = 1) were identified. With a total of 525 individual structures, they represent a smaller group of structural discontinuities than the fault planes. Out of these 525 structures, 515 (98.1%) planes were recorded in oriented cores.

The spatial distribution of tension gashes / veins, joints and unassigned fractures along the STA2-1 borehole is presented in Fig. 4-4 and discussed in Section 4.1.4. Compared to faults, they reveal a considerable orientation scatter as shown in Figs. 4-7 and 4-8. However, one orientation cluster can be distinguished (see Tab. 4-1). It represents a steeply dipping to subvertical cluster (75° to 90°) characterised by WNW-dipping planes (overall mean: 290/81; n = 129).

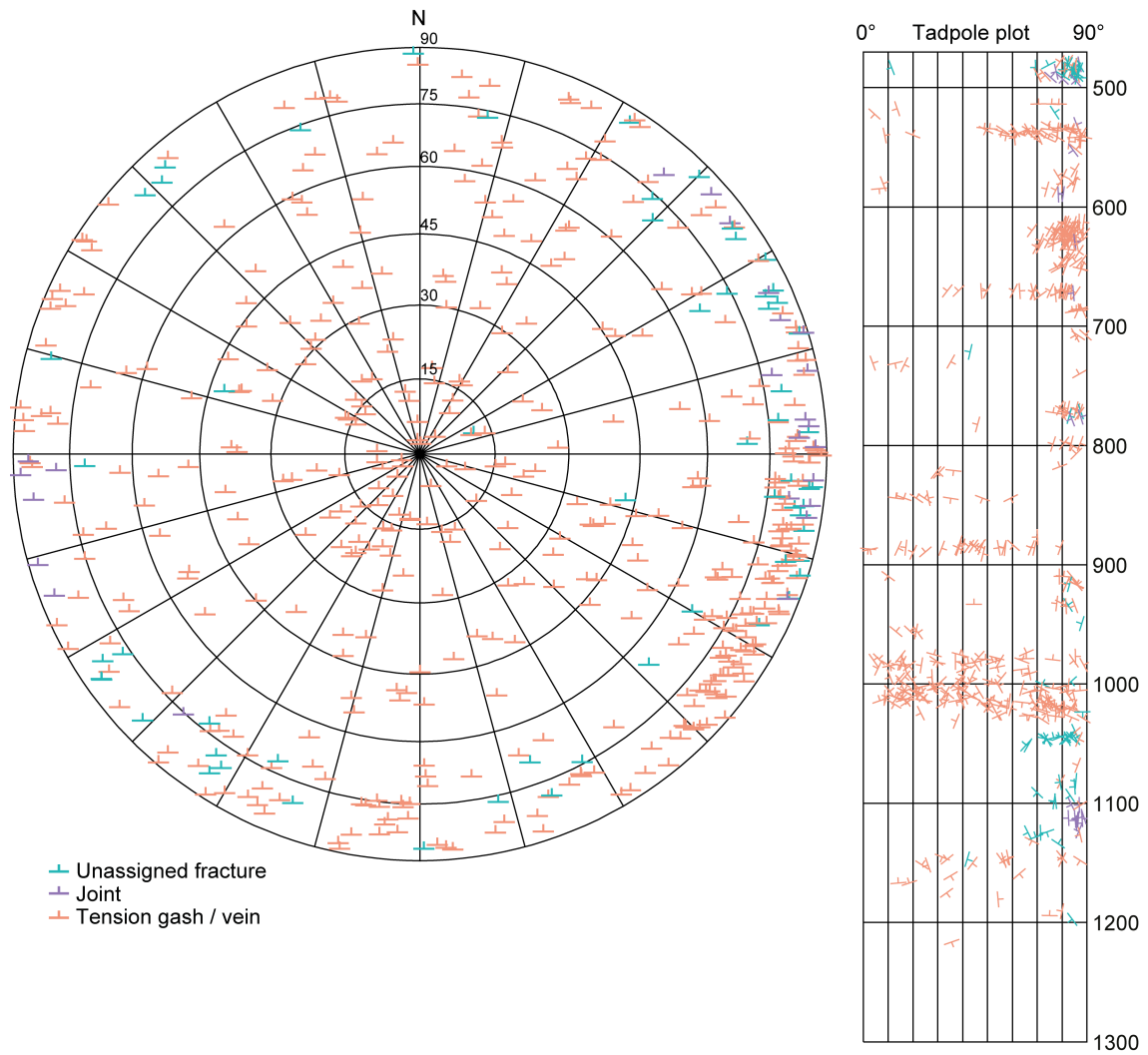


Fig. 4-7: Stereogram and depth plot for tension gashes / veins, unassigned fractures and joints in the entire cored interval

A total of 515 structures are displayed: tension gashes / veins (n = 431), joints (n = 24) and unassigned fractures (n = 60). Depth range is 470.00 m to 1'288.87 m MD (log depth). In the tadpole plot, the Opalinus Clay interval is indicated by a red bar.

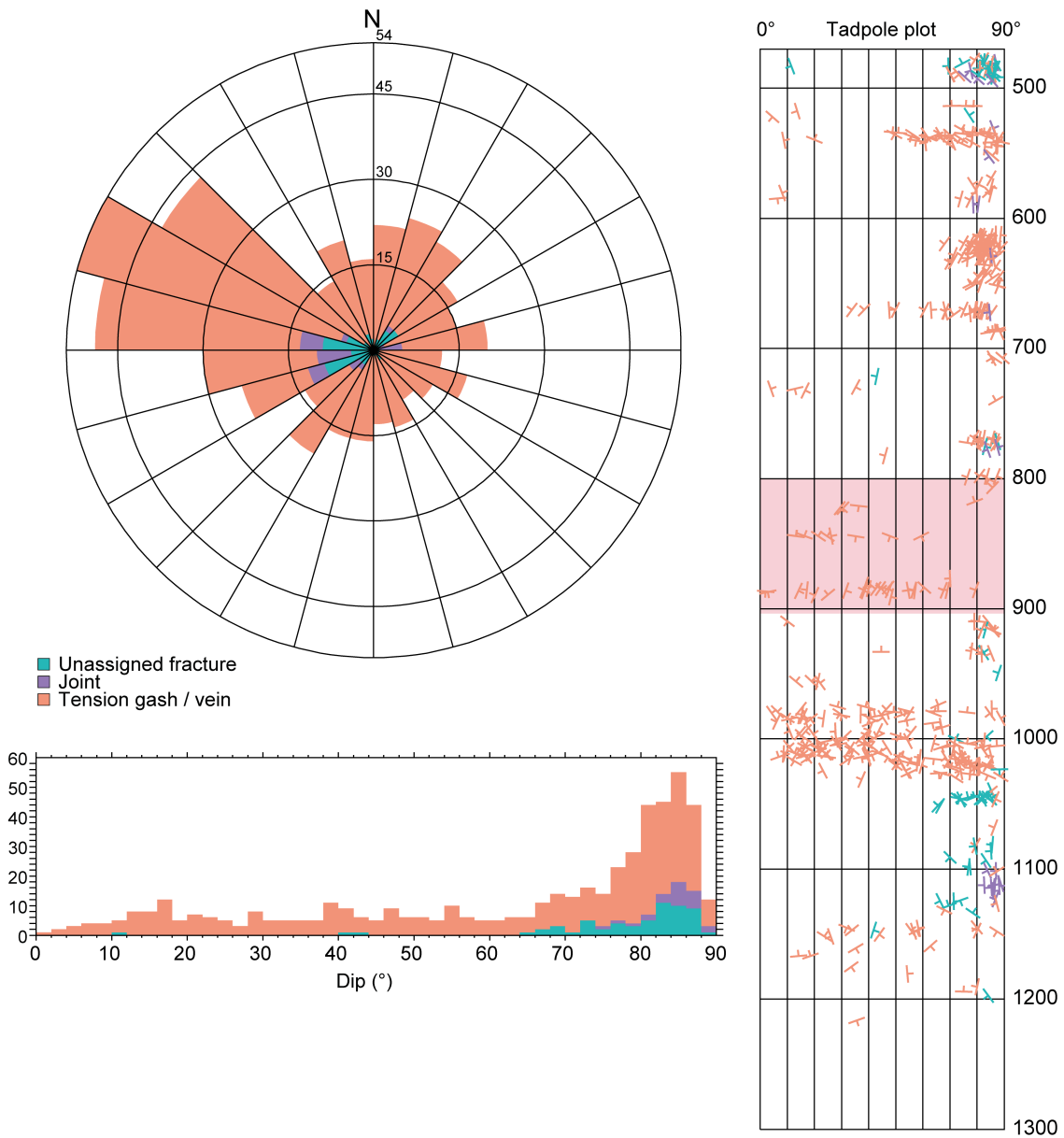


Fig. 4-8: Dip azimuth rose diagram of tension gashes / veins, unassigned fractures and joints in the entire cored interval

A total of 515 structures are displayed: tension gashes / veins (n = 431), joints (n = 24) and unassigned fractures (n = 60). Depth range is 470.00 m to 1'288.87 m MD (log depth). In the tadpole plot, the Opalinus Clay interval is indicated by a red bar.

Stylolites

A total of 917 stylolites and 5 stylolite-rich zones were identified in the STA2-1 borehole. Out of these, 845 (98%) were recorded in oriented cores. Particularly in stylolite-rich intervals such as the Malm and the Schinznach Formation (see Fig. 4-9), not all individual stylolites could be picked or documented and only dominant ones which could be clearly observed in core photographs were recorded and categorised. Intervals with high densities of stylolites were defined as stylolitic zones.

Stylolites show one well-developed and two subordinate orientation clusters (Figs. 4-9, 4-10 and Tab. 4-1): a subhorizontal to shallow (1° to 25°) SE-dipping cluster (overall mean: $169/05$; $n = 394$) and two steep to subvertical (50° to 90°) clusters with dip directions towards the NNE and the SSW (overall means: $7/78$; $n = 125$ and $191/72$; $n = 247$).

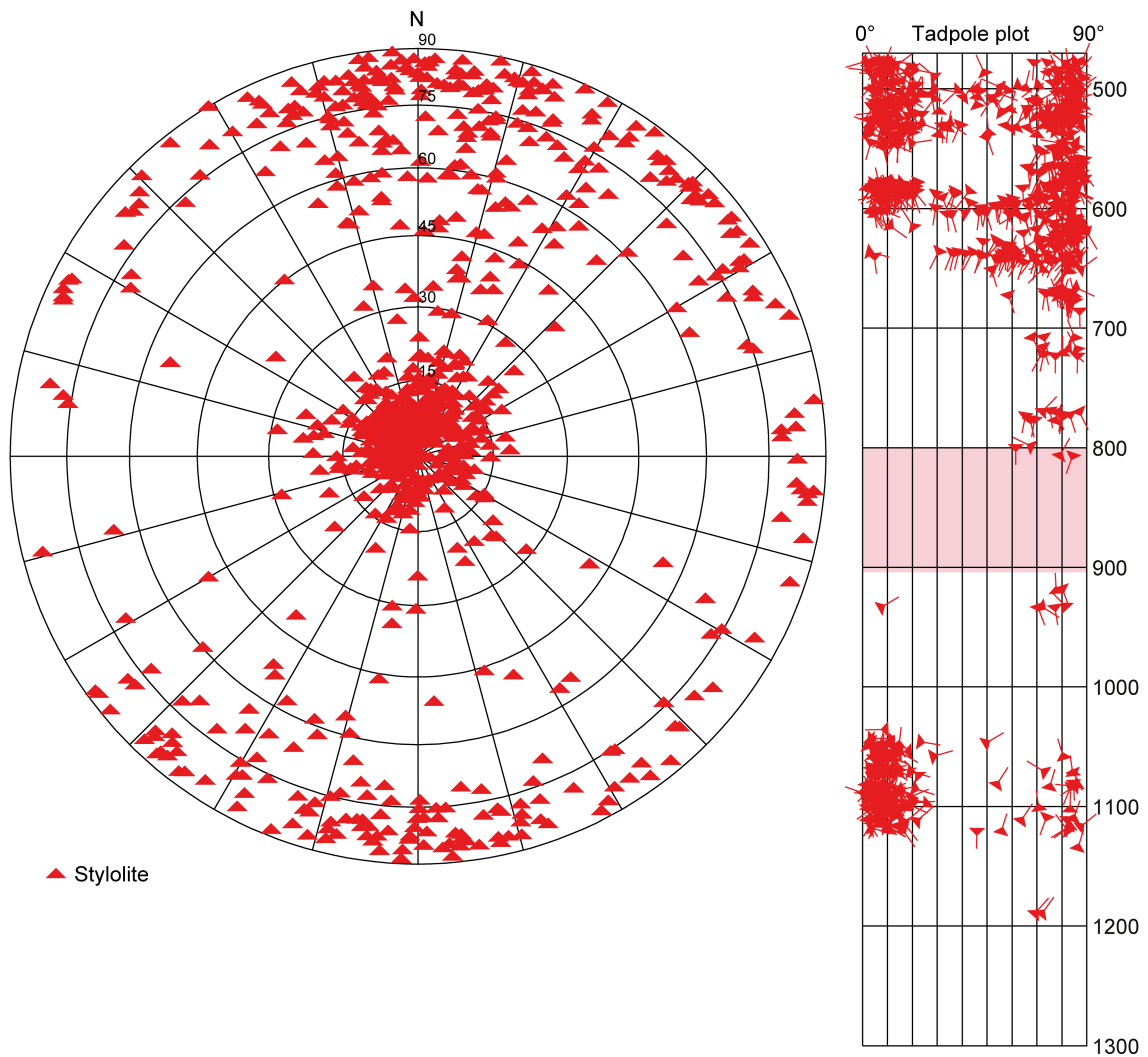


Fig. 4-9: Stereogram and depth plot for stylolites ($n = 845$) along the cored STA2-1 borehole. Depth range is 470.00 m to 1'288.87 m MD (log depth). In the tadpole plot, the Opalinus Clay interval is indicated by a red bar.

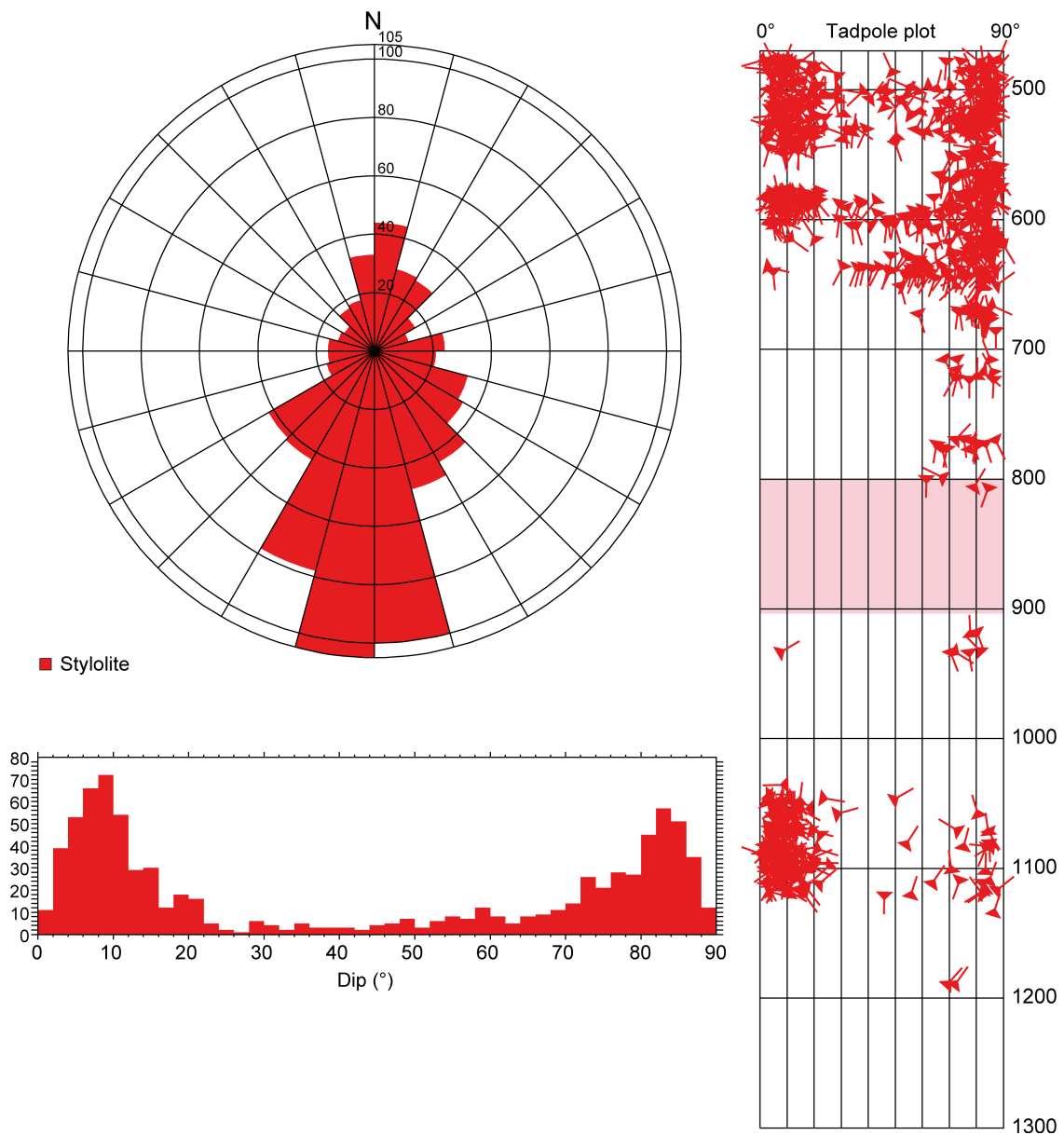


Fig. 4-10: Dip azimuth rose diagram and depth plot for stylolites in the entire cored interval
 Depth range is 470.00 m to 1'288.87 m MD (log depth), n = 845. In the tadpole plot, the Opalinus Clay interval is indicated by a red bar.

4.1.3 Fracture density (P10 and P32) and distribution

Density histograms were calculated in order to evaluate the spatial distribution of fractures and stylolites (see Fig. 4-4). As mentioned above, structures recorded in non-oriented cores (n = 98) were considered in the fracture density calculations.

Fault planes were unevenly distributed along the cored interval. Higher fault counts with > 10 faults per metre occurred within the borehole intervals from 538.00 m to 540.00 m MD (log depth) in the «Felsenkalke» + «Massenkalk» and from 1'252.00 m to 1'258.00 m MD (log depth) within the Weitenau Formation. The highest density of fault planes with up to 23 planes per metre was observed within the fault zone in the Weitenau Formation. Abundant faults commonly form prominent fault zones associated with intensely fractured and partly disintegrated drill cores (FDC 2 – 3; see Tab. 4-2 and Fig. 4-4). The average density of fault planes for the entire cored borehole section was 0.9 planes per metre.

Tension gashes / veins, joints and unassigned fractures (with a fracture count of up to 10 / m to 13 / m) are particularly abundant within the Malm and the Bänkerjoch Formation (see Fig. 4-4). The highest fracture density (with up to 13 fractures per metre) was encountered within the Wildegg Formation at approximately 670 m MD. However, the average density for the entire cored borehole section was about 0.7 fractures per metre.

Stylolites revealed an uneven distribution along the borehole and occurred predominantly within the carbonate-rich lithologies of the Malm from approximately 470.0 m to 728.2 m MD (log depth), in the «Herrenwis Unit» from 768.05 m to 778.47 m MD (log depth) and in the Schinznach Formation from 1'043.62m to 1'116.69 m MD (log depth). The highest density, with up to 13 stylolites per metre, occurred within the Villigen Formation at approximately 582 m MD (log depth). However, the average density for the whole borehole section was about 1.2 stylolites per metre.

4.1.4 Kinematic indicators

Striations could be measured on 556 fault planes. In total, 97% of the striations (n = 540) were observed in oriented cores. The orientations of the striations in oriented cores are given in Figs. 4-11 to 4-16. There is a clear predominance of S-dipping striations. The plunge of striations varies between subhorizontal to steep (1° to 40°). However, the vast majority does not exceed 20°.

Three different shear senses were distinguished for the analysed drill cores:

- up = thrusting / reverse faulting
- down = normal faulting
- dextral / sinistral = strike-slip faulting

A total of 160 shear indicators were identified as thrusts / reverse faults (Tab. 4-3). In contrast, the number of faults classified as normal faults (n = 30) or strike-slip faults (n = 10) is much lower (Tab. 4-3). However, the shear sense of most fault planes (n = 356) was uncertain or not observable (Tab. 4-3).

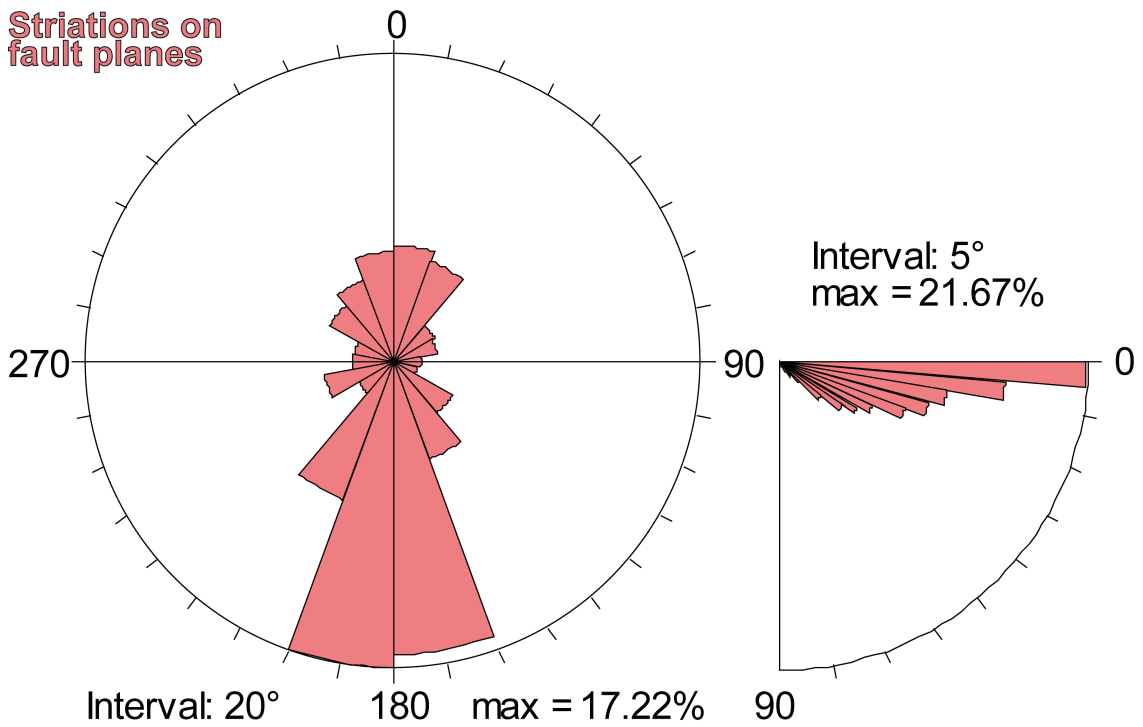


Fig. 4-11: Plunge azimuth of striations along fault planes in the entire cored interval
 The striations (n = 540) from oriented cores of the entire cored interval from the Malm to the Permian are presented. Left: plunge azimuth rose diagram, right: plunge histogram. Depth range is 470.00 m to 1'288.87 m MD (log depth).

Tab. 4-3: List of all kinematic indicators in oriented and non-oriented cores

Shear sense	Number
Up	160
Down	30
Sinistral	5
Dextral	5
Unknown	356
In oriented cores	540
In non-oriented cores	16
Total measured lineations	556

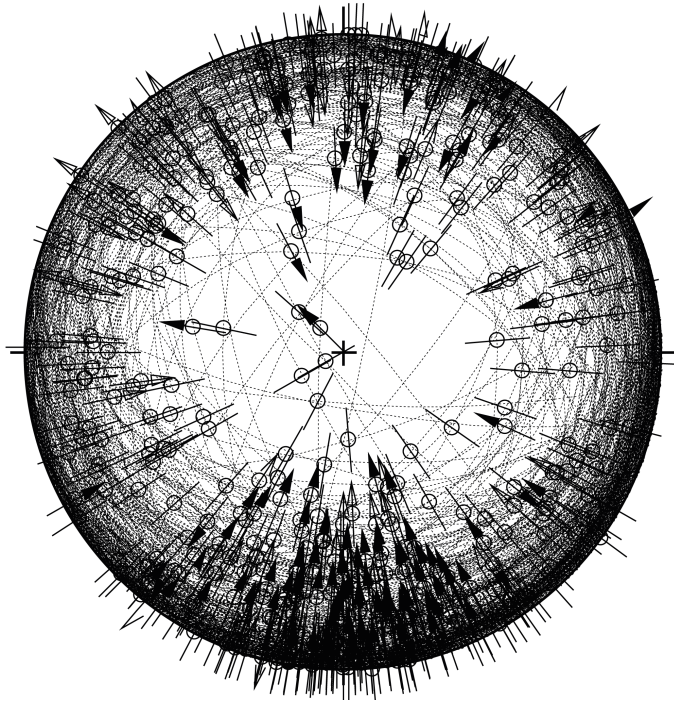


Fig. 4-12: Stereogram of striations on all oriented fault planes (including multiple lineations on a single fault plane) and associated kinematic data

Shear sense up (n = 160), down (n = 28), dextral (n = 5), sinistral (n = 5) and unknown (n = 342). Depth range is 470.00 m to 1'288.87 m MD (log depth).

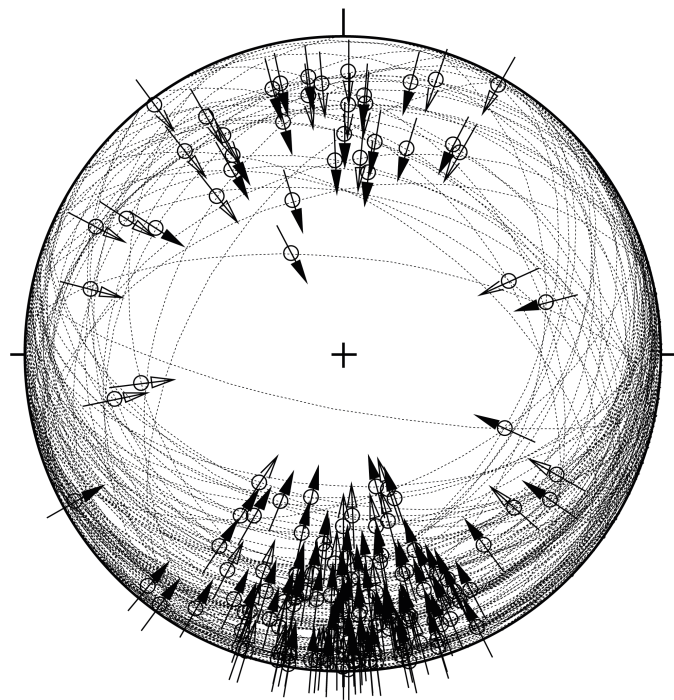


Fig. 4-13: Stereogram with all striations on oriented thrust / reverse fault planes (including multiple lineations on a single fault plane)

Shear sense up (n = 160). Depth range is 470.00 m to 1'288.87 m MD (log depth).

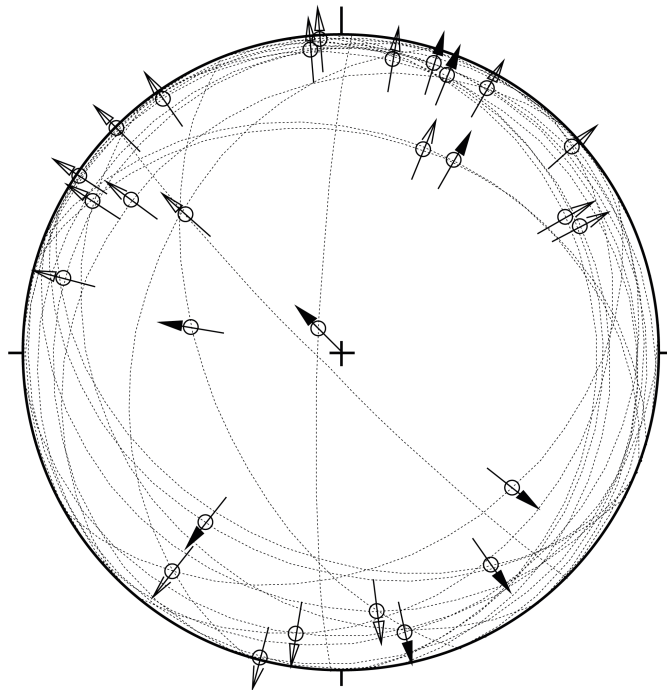


Fig. 4-14: Stereogram with all striations on oriented normal fault planes (including multiple lineations on a single fault plane)

Shear sense down ($n = 28$). Depth range is 470.00 m to 1'288.87 m MD (log depth).

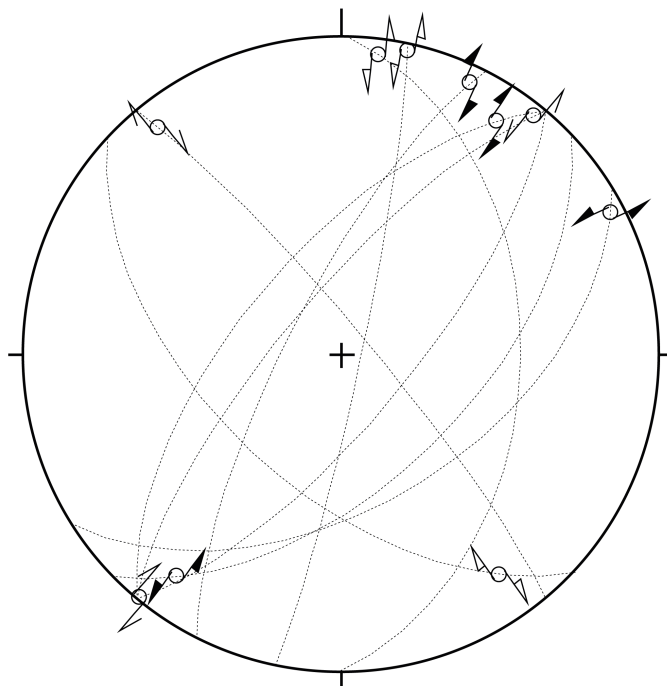


Fig. 4-15: Stereogram with all striations on oriented strike-slip fault planes (including multiple lineations on a single fault plane)

Shear sense dextral ($n = 5$) and sinistral ($n = 5$). Depth range is 470.00 m to 1'288.87 m MD (log depth).

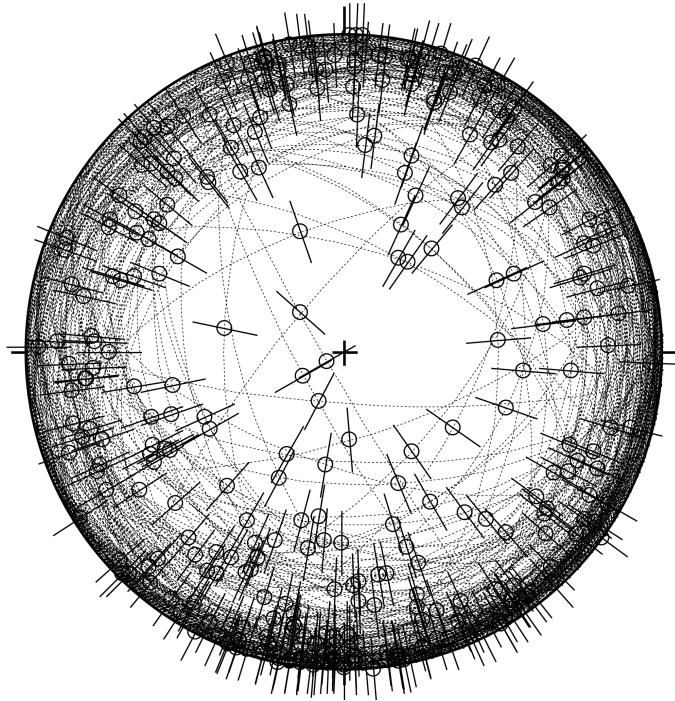


Fig. 4-16: Stereogram with all striations on oriented fault planes with unknown shear sense (including multiple lineations on a single fault plane)

Shear sense unknown (n = 342). Depth range is 470.00 m to 1'288.87 m MD (log depth).

4.2 Malm

The cored Malm covers the interval from 470.00 m to 728.20 m MD (log depth). The Malm shows a high density of all structure types. One third of all structures are stylolites. Further dominant structures are tension gashes and fault planes. They are more or less homogeneously distributed over the entire Malm interval. Mirror-like fault planes, joints and unassigned fractures are rare.

Fault planes and stylolitic fault planes preferably dip towards SSE to SSW in all the formations of the Malm interval. The plunge azimuth of striations is scattered with a majority dipping towards the south. Reverse faulting dominates, but normal faulting has also been observed in the «Felsenkalke» + «Massenkalk».

Tension gashes are mostly steeply dipping to subvertical. In the «Felsenkalke» + «Massenkalk» they dip to the N and to the SW to W. In the Villigen Formation and the Wildegg Formation they show a preferred dip direction to the WNW and NW. Tension gashes are rare in the Schwarzbach Formation.

Stylolites are dipping either subhorizontal to shallow or steep to subvertical. Flat stylolites are rare in the marly layers. In the interval from the Wildegg Formation to the Schwarzbach Formation, stylolites show a clear preferred orientation towards the south. In the «Felsenkalke» + «Massenkalk», on the other hand, the orientation varies with a slight preferred orientation towards the N and SW.

For the detailed stereographic evaluation, four lithostratigraphic units were defined within the Malm interval. Only the data from oriented cores are presented.

4.2.1 «Felsenkalke» + «Massenkalk»

The orientation and spatial distribution of recorded structures in the «Felsenkalke» + «Massenkalk» (470.00 m to 548.62 m MD log depth) are shown in Figs. 4-17 to 4-23.

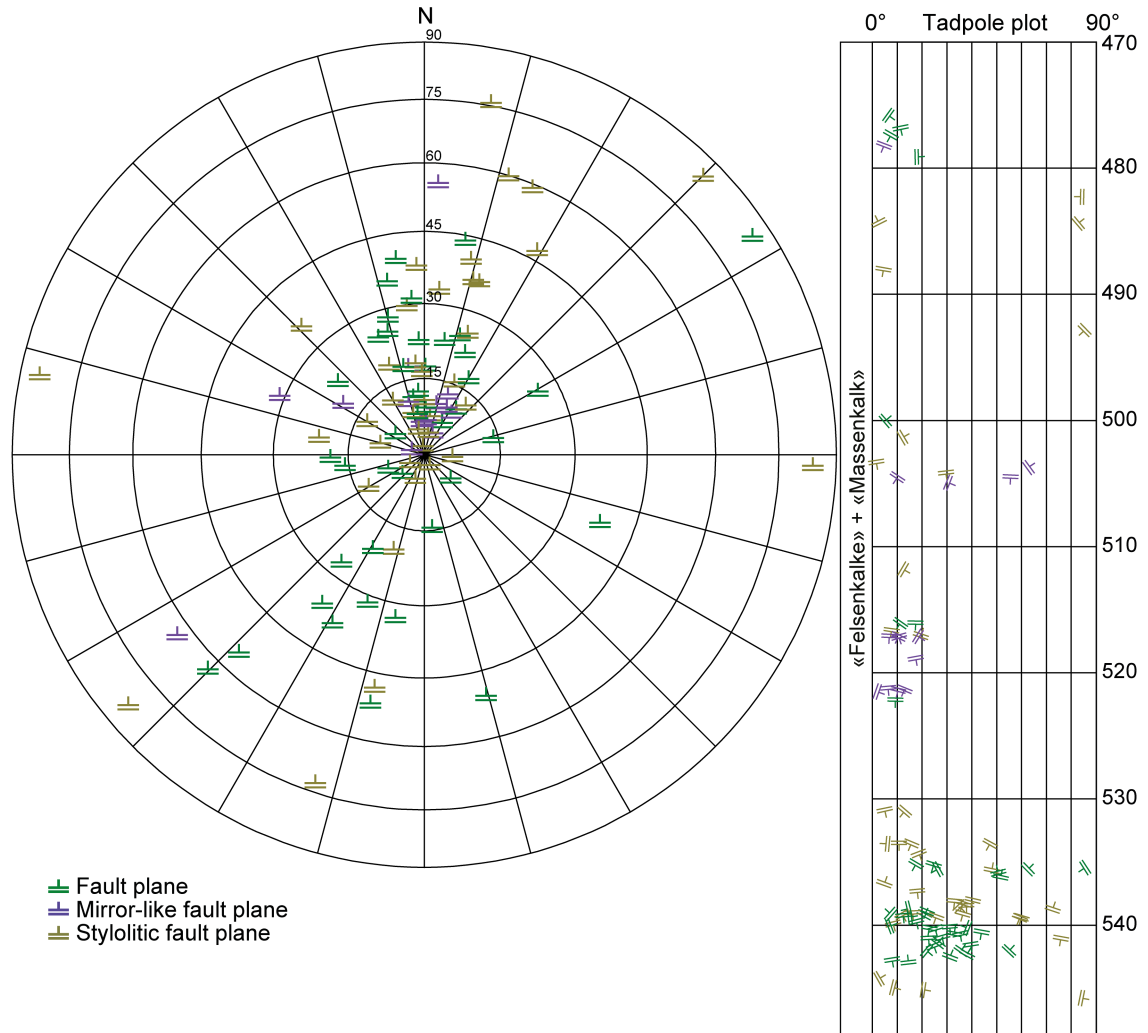


Fig. 4-17: Stereogram and depth plot of fault planes («Felsenkalke» + «Massenkalk») Fault planes (n = 42), mirror-like fault planes (n = 14) and stylolitic fault planes (n = 39).

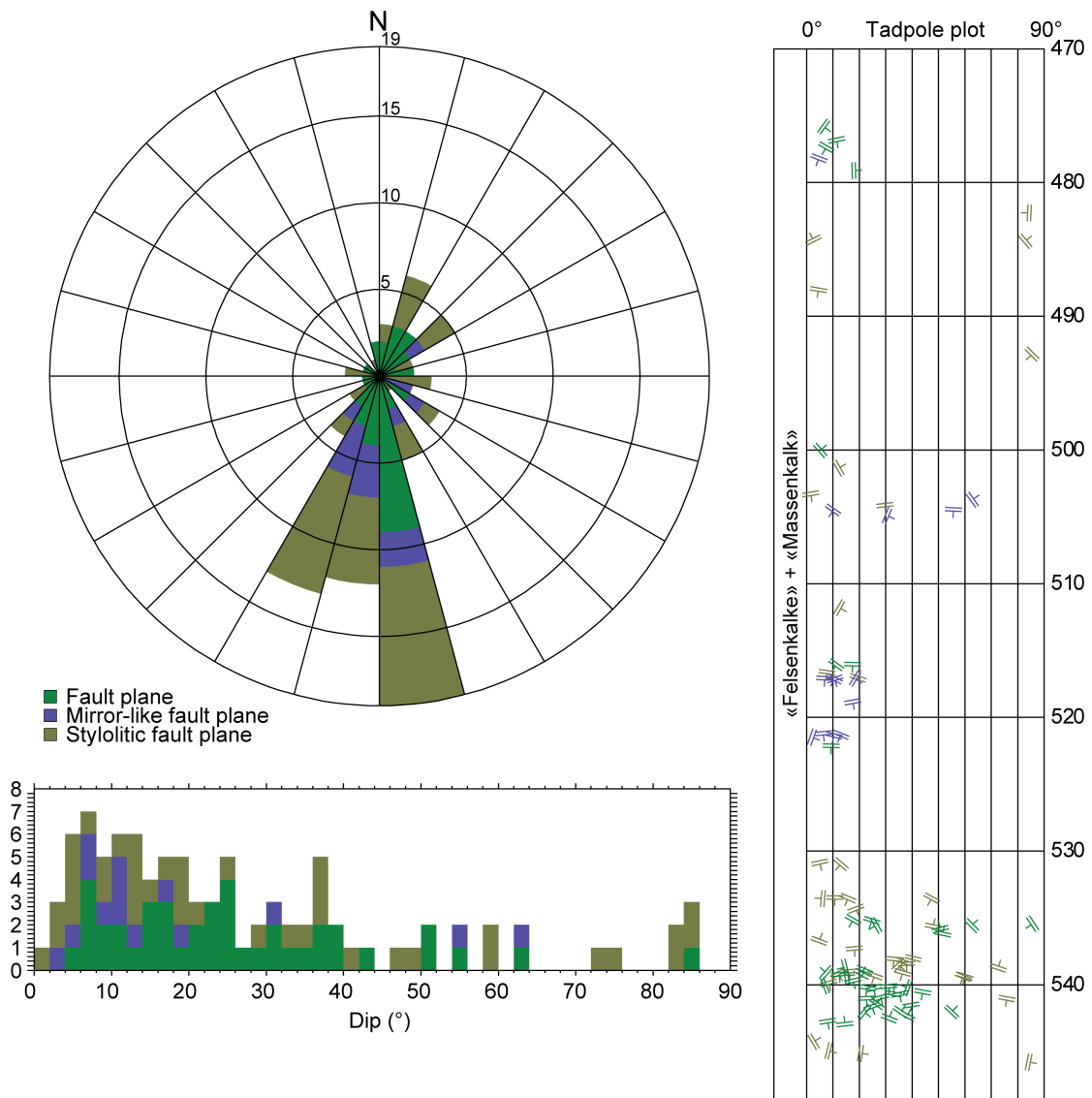


Fig. 4-18: Dip azimuth rose diagram, dip histogram and depth plot of fault planes («Felsenkalk» + «Massenkalk»)

Fault planes (n = 42), mirror-like fault planes (n = 14) and stylolitic fault planes (n = 39).

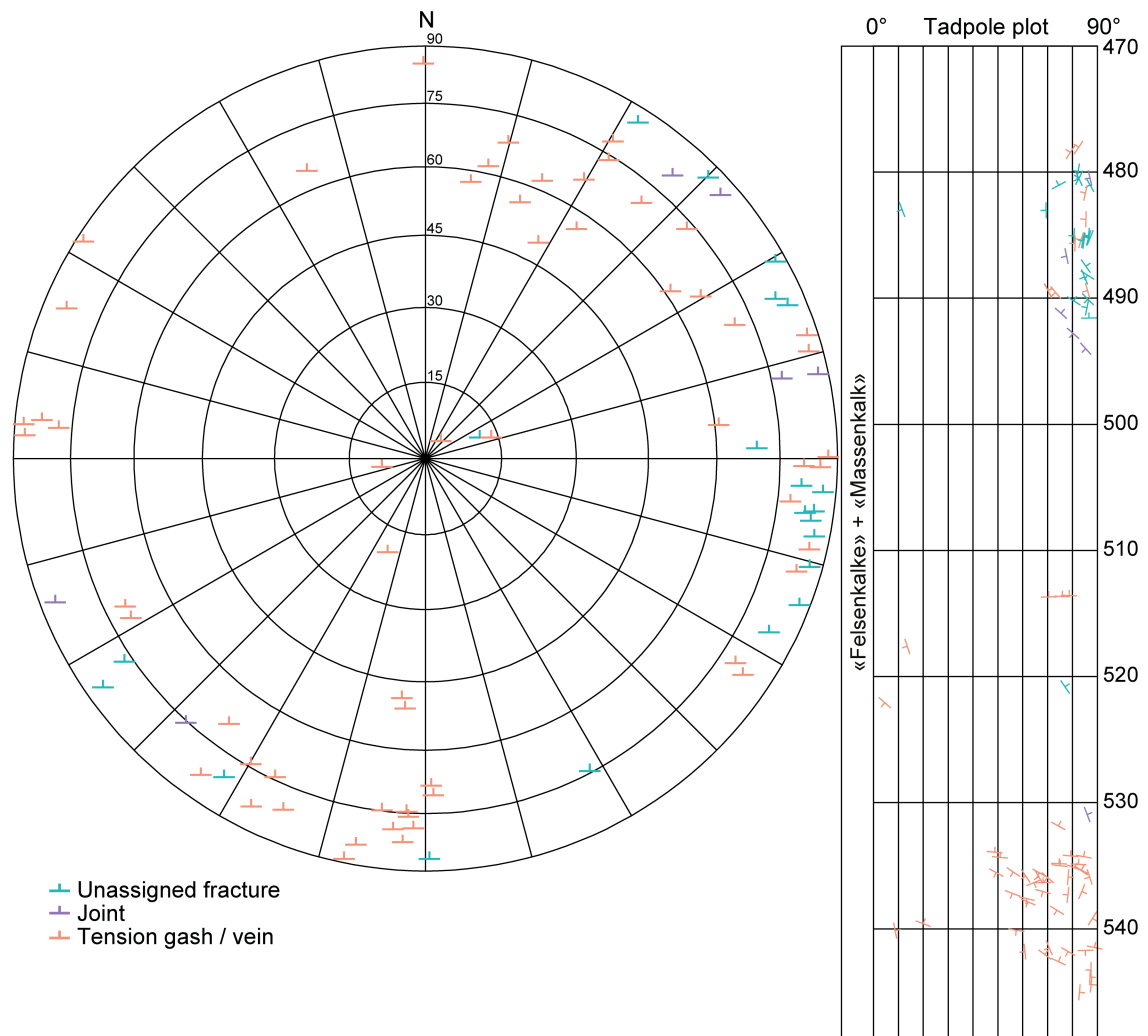


Fig. 4-19: Stereogram and depth plot of tension gashes / veins and unassigned fractures («Felsenkalk» + «Massenkalk»)

Unassigned fractures (n = 21), joints (n = 6) and tension gashes / veins (n = 58).

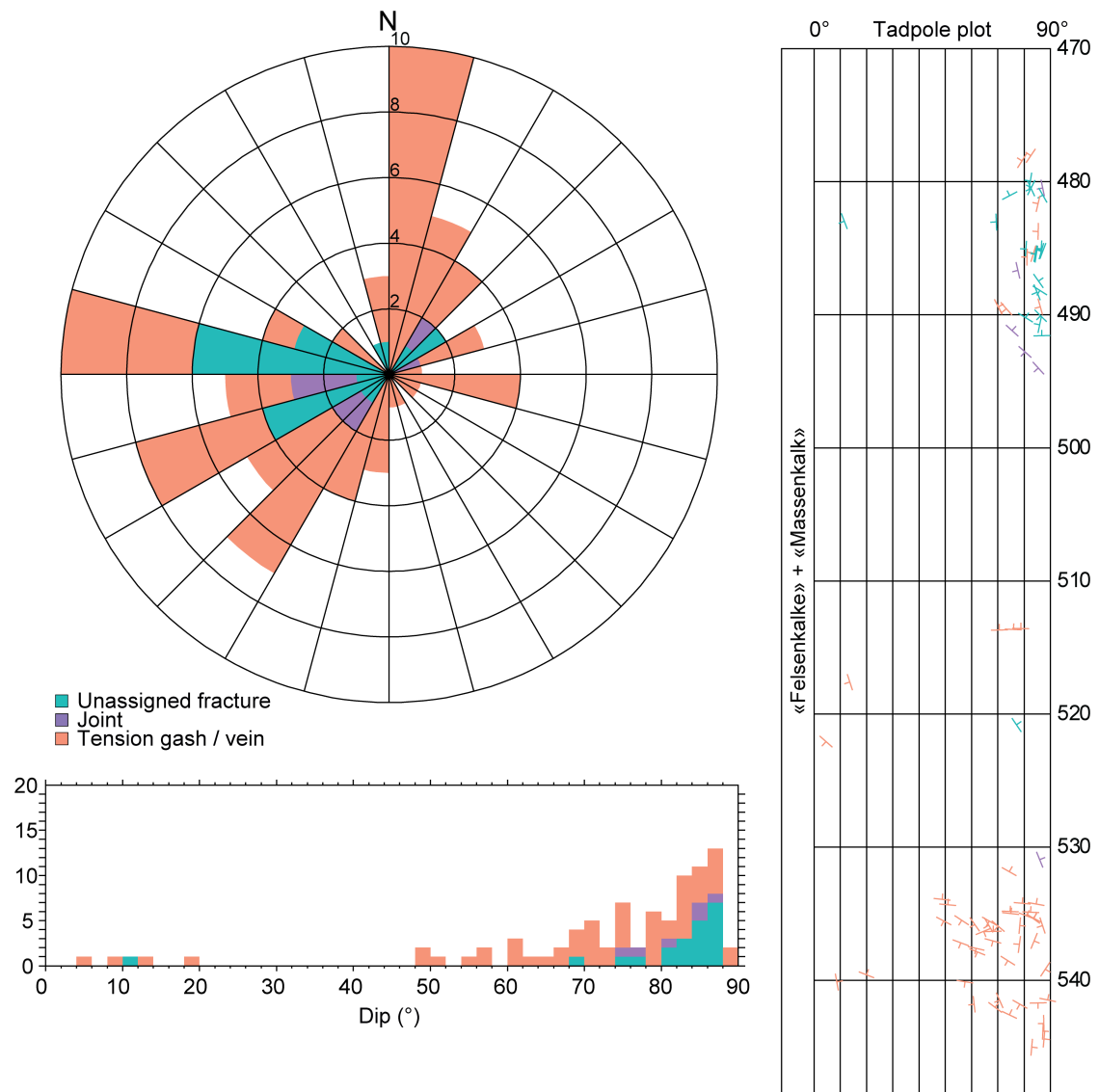


Fig. 4-20: Dip azimuth rose diagram, dip histogram and depth plot of tension gashes / veins, joints and unassigned fractures («Felsenkalke» + «Massenkalk»)

Unassigned fractures (n = 21), joints (n = 6) and tension gashes / veins (n = 58).

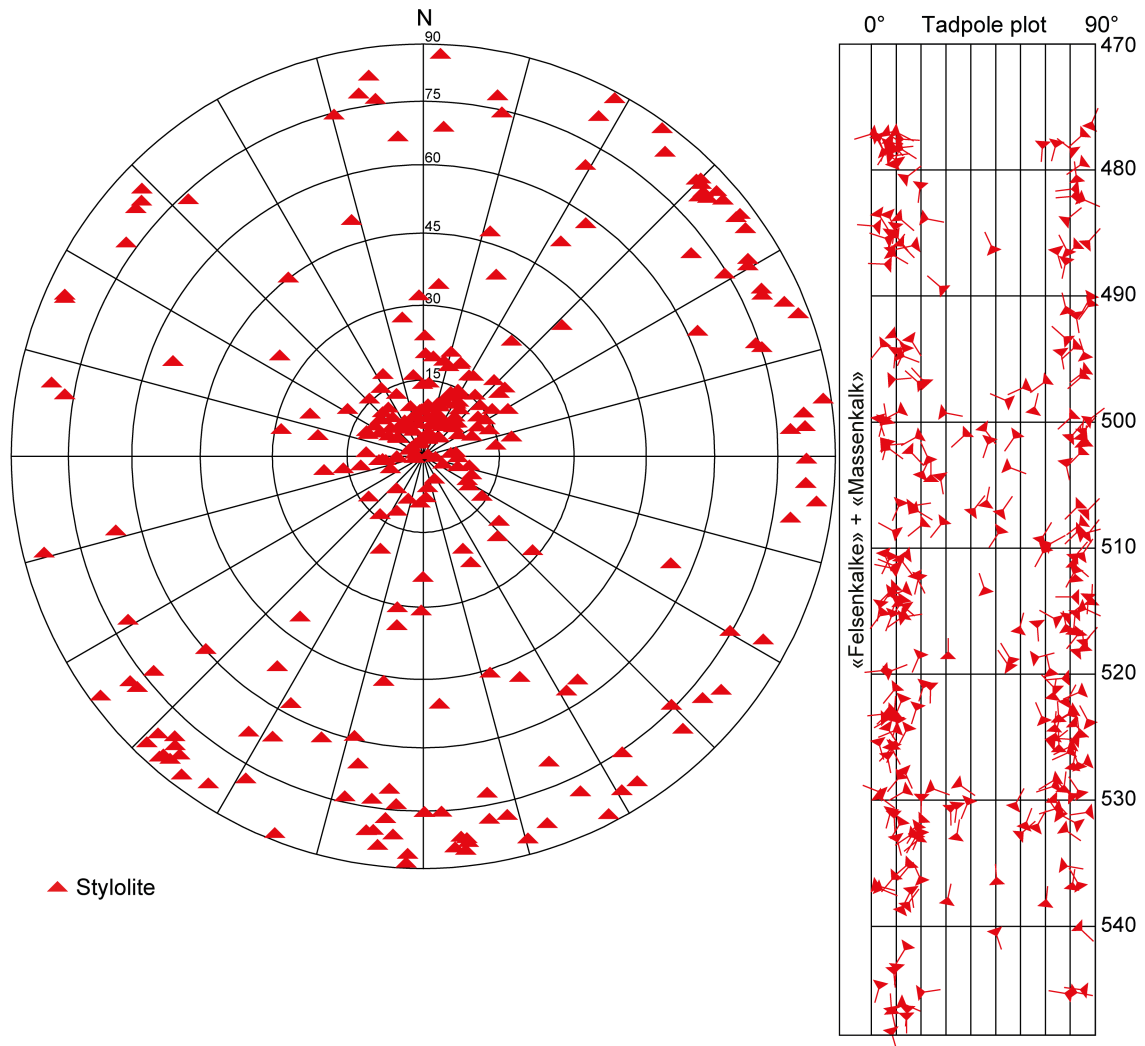


Fig. 4-21: Stereogram and depth plot of stylolites («Felsenkalk» + «Massenkalk»); n = 277)

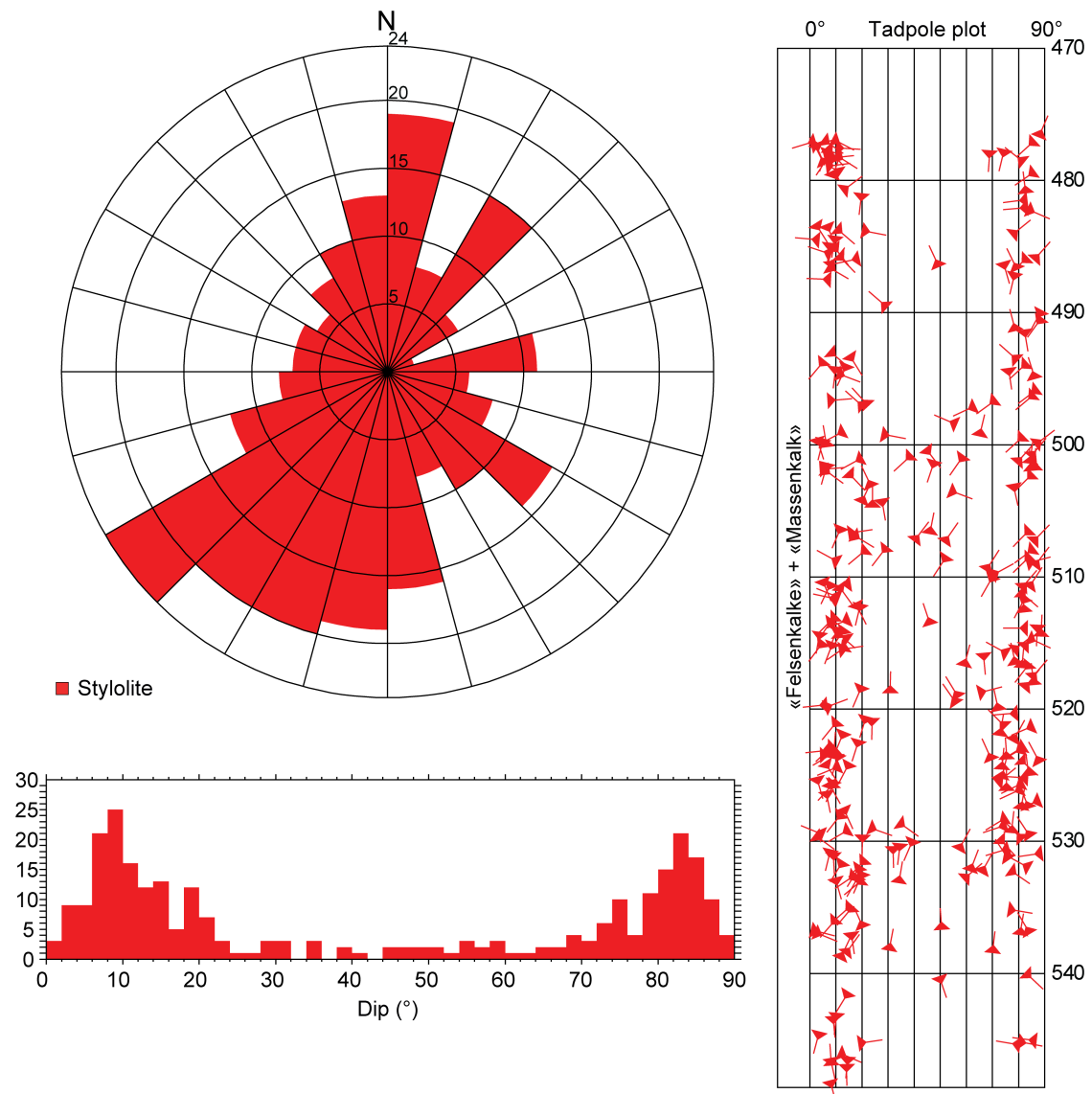


Fig. 4-22: Dip azimuth rose diagram, dip histogram and depth plot of stylolites («Felsenkalk» + «Massenkalk»; n = 277)

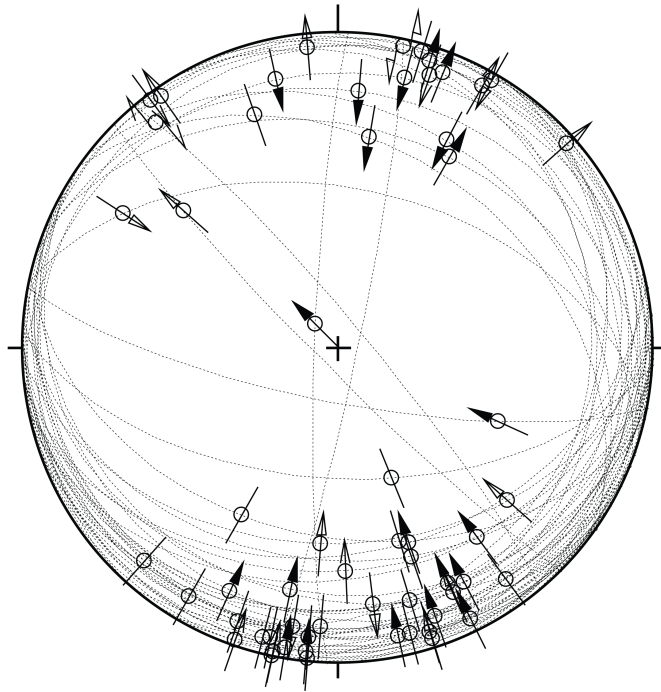


Fig. 4-23: Stereogram with striations on fault planes, including multiple lineations on a single fault plane («Felsenkalke» + «Massenkalk»; n = 60)

4.2.2 Schwarzbach Formation

The orientation and spatial distribution of recorded structures in the Schwarzbach Formation (548.62 m to 575.45 m MD log depth) are shown in Figs. 4-24 to 4-29.

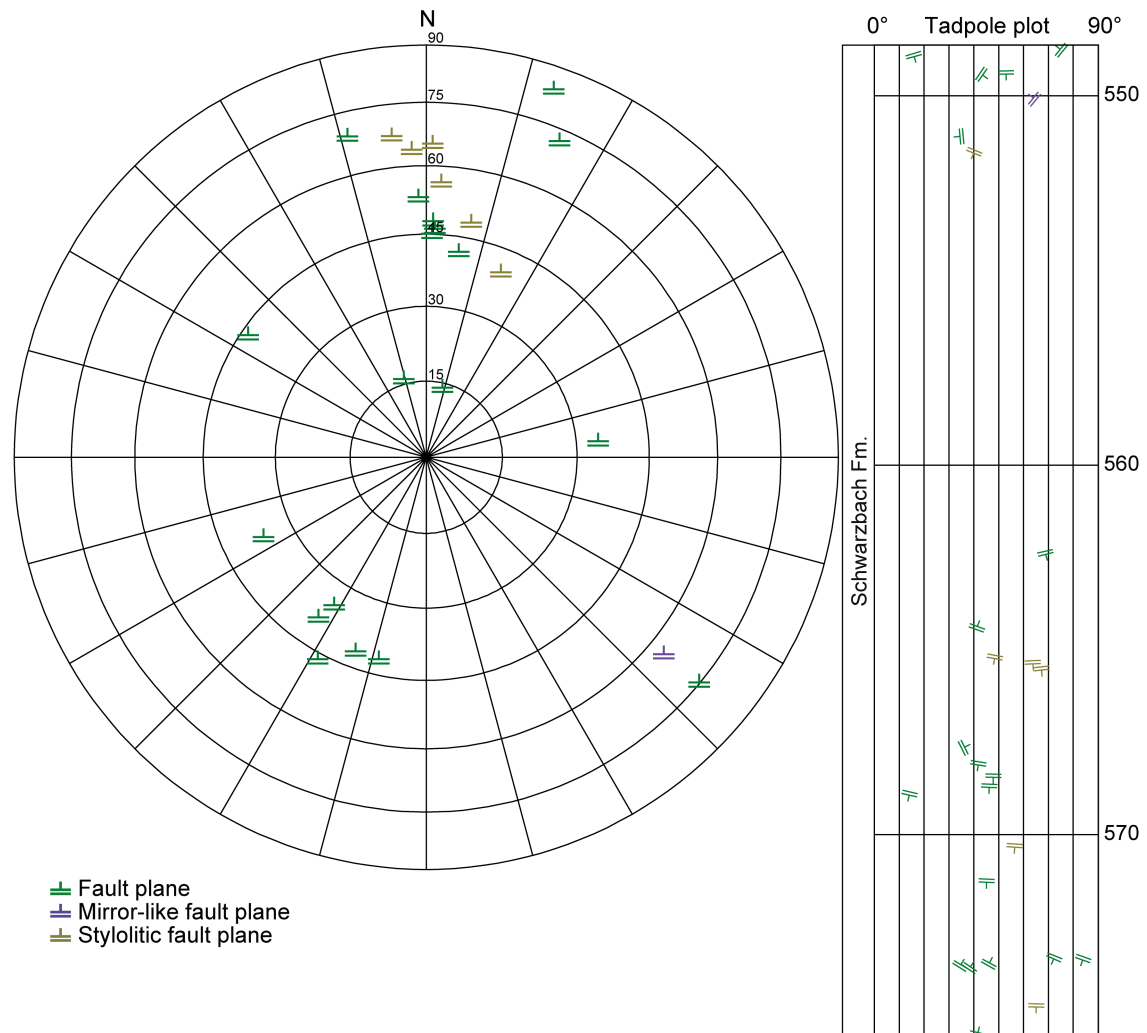


Fig. 4-24: Stereogram and depth plot of fault planes (Schwarzbach Formation)

Fault planes (n = 19), mirror-like fault planes (n = 1) and stylolitic fault planes (n = 6).

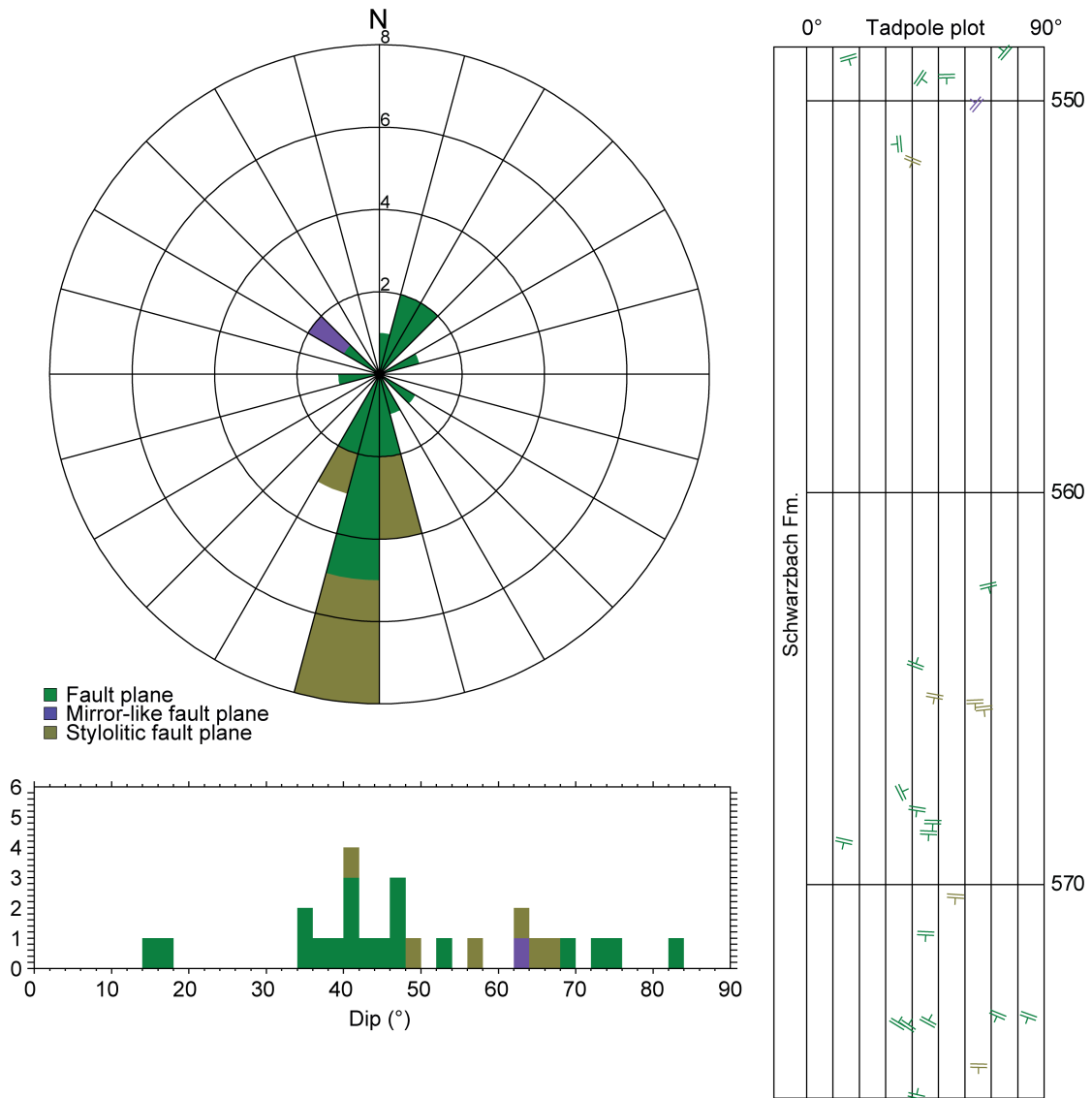


Fig. 4-25: Dip azimuth rose diagram, dip histogram and depth plot of fault planes (Schwarzbach Formation)

Fault planes (n = 19), mirror-like fault planes (n = 1) and stylolitic fault planes (n = 6).

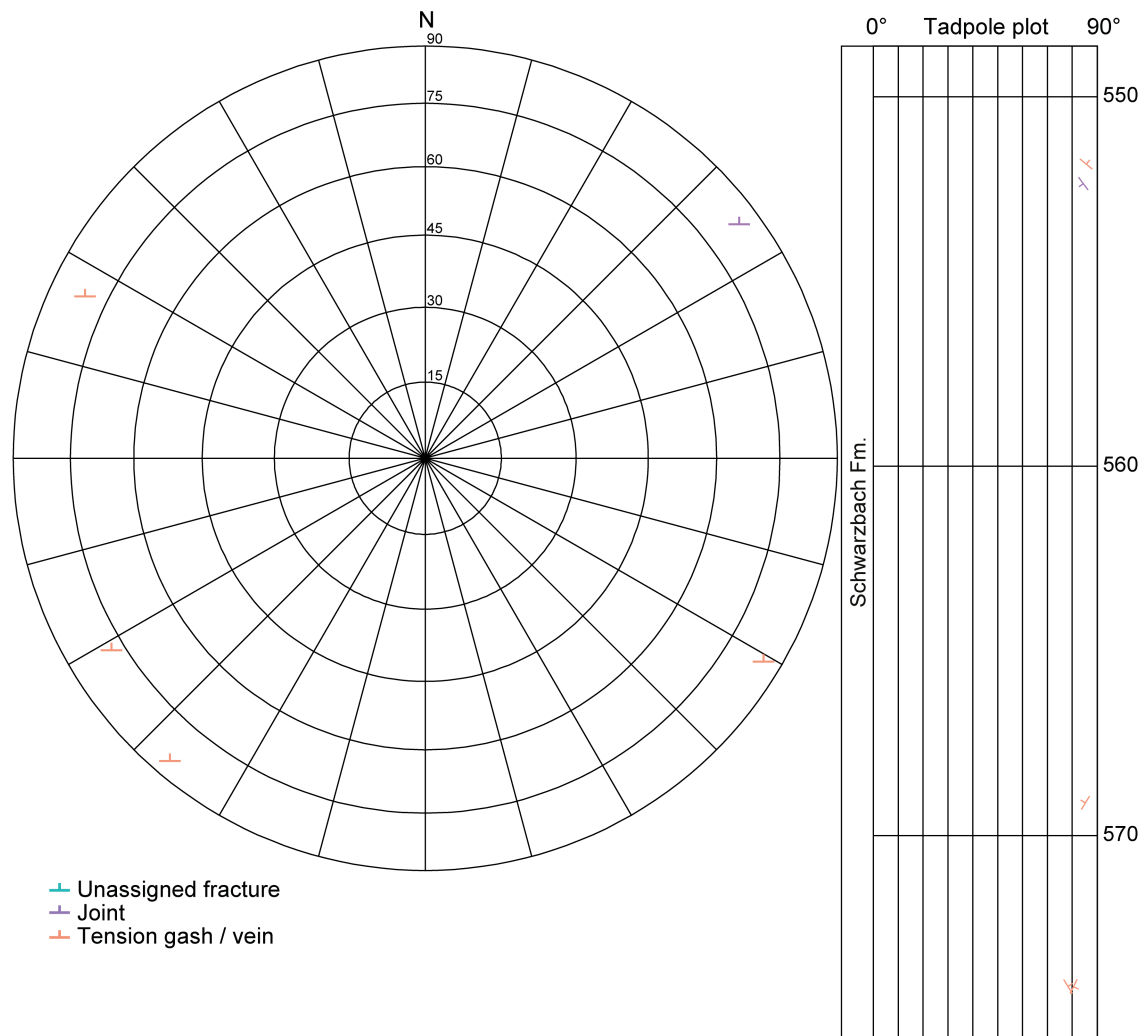


Fig. 4-26: Stereogram and depth plot of tension gashes / veins and unassigned fractures (Schwarzbach Formation)

Joints (n = 1) and tension gashes / veins (n = 4); no unassigned fractures were observed (n = 0).

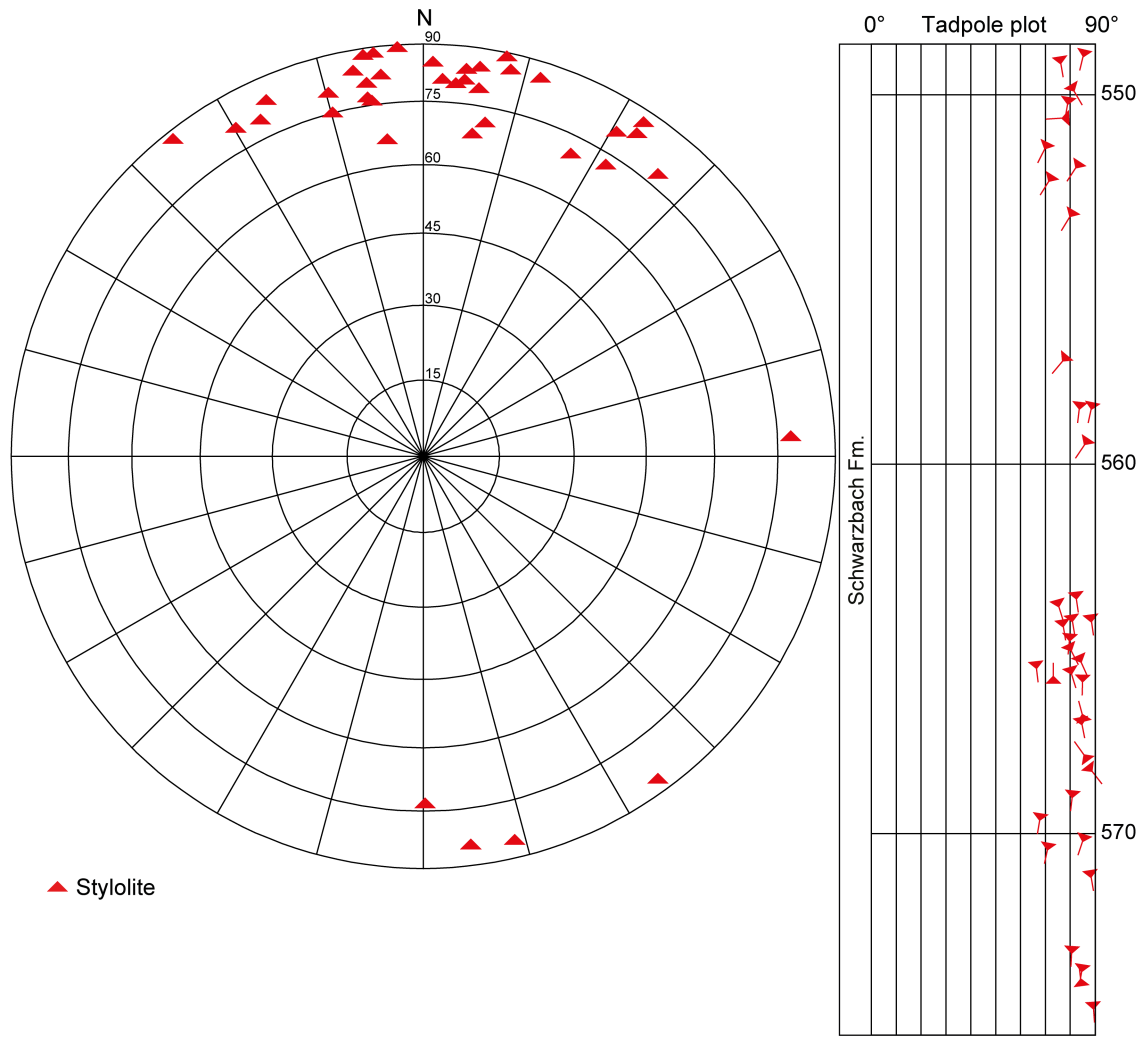


Fig. 4-27: Stereogram and depth plot of stylolites (Schwarzbach Formation; n = 38)

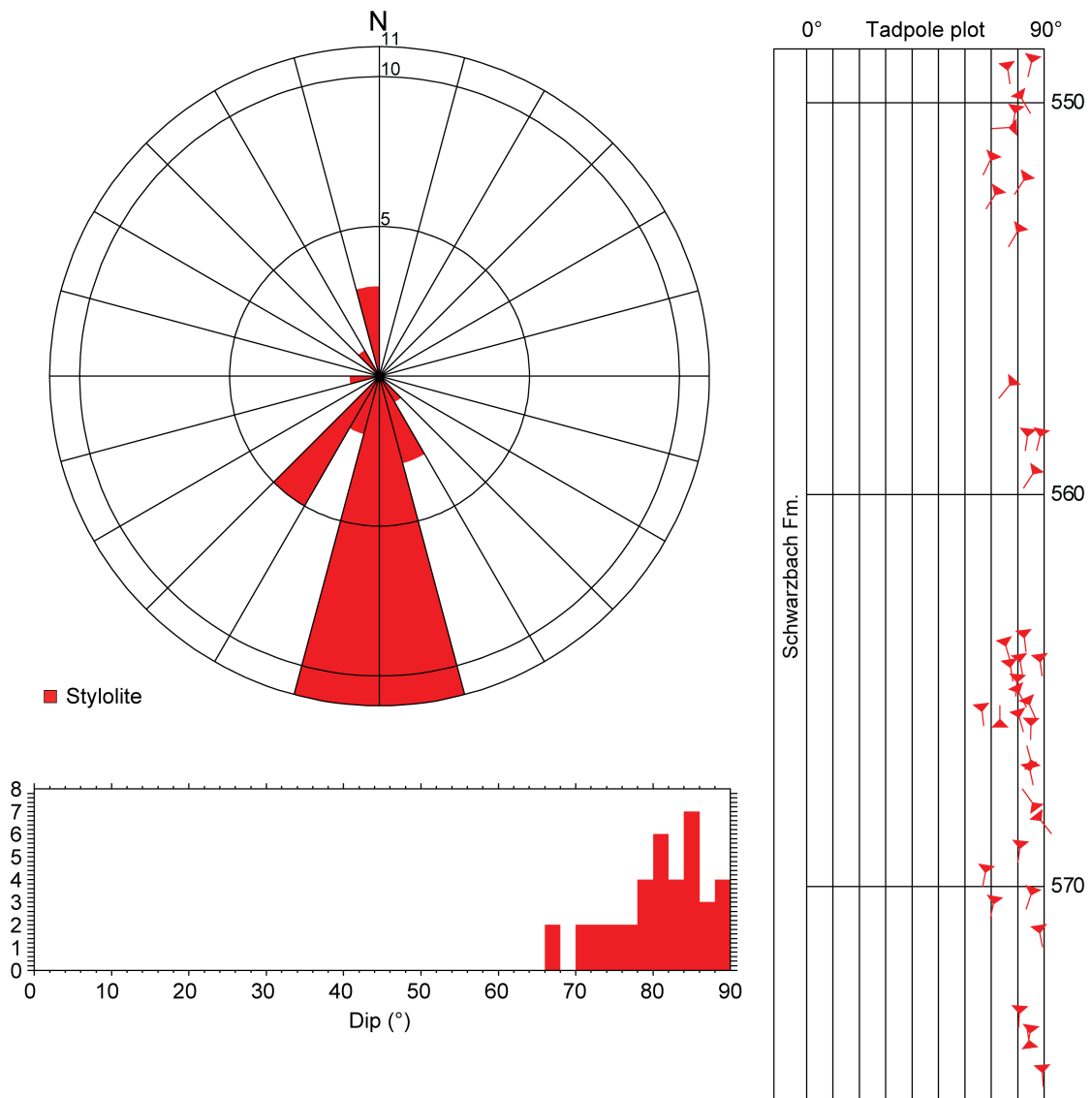


Fig. 4-28: Dip azimuth rose diagram, dip histogram and depth plot of stylolites (Schwarzbach Formation; n = 38)

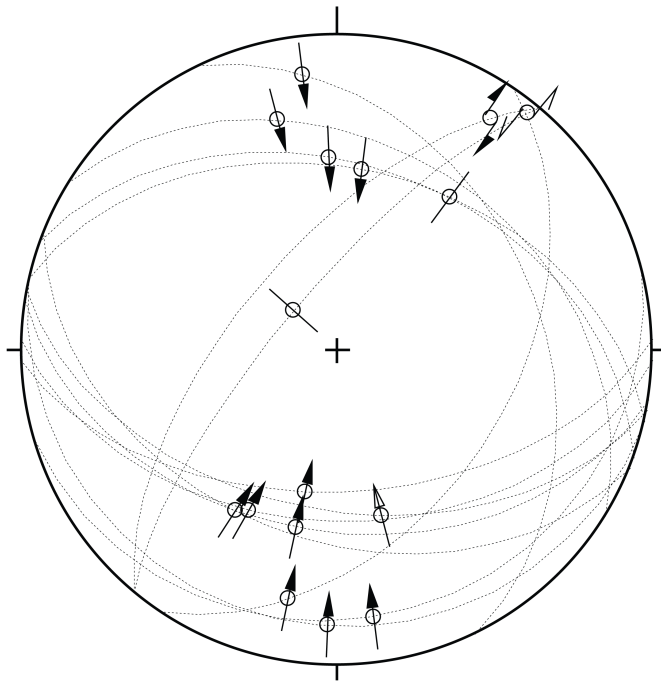


Fig. 4-29: Stereogram of striations on fault planes, including multiple lineations on a single fault plane (Schwarzbach Formation; n = 16)

4.2.3 Villigen Formation

The orientation and spatial distribution of recorded structures in the Villigen Formation (575.45 m to 646.63 m MD log depth) are shown in Figs. 4-30 to 4-36.

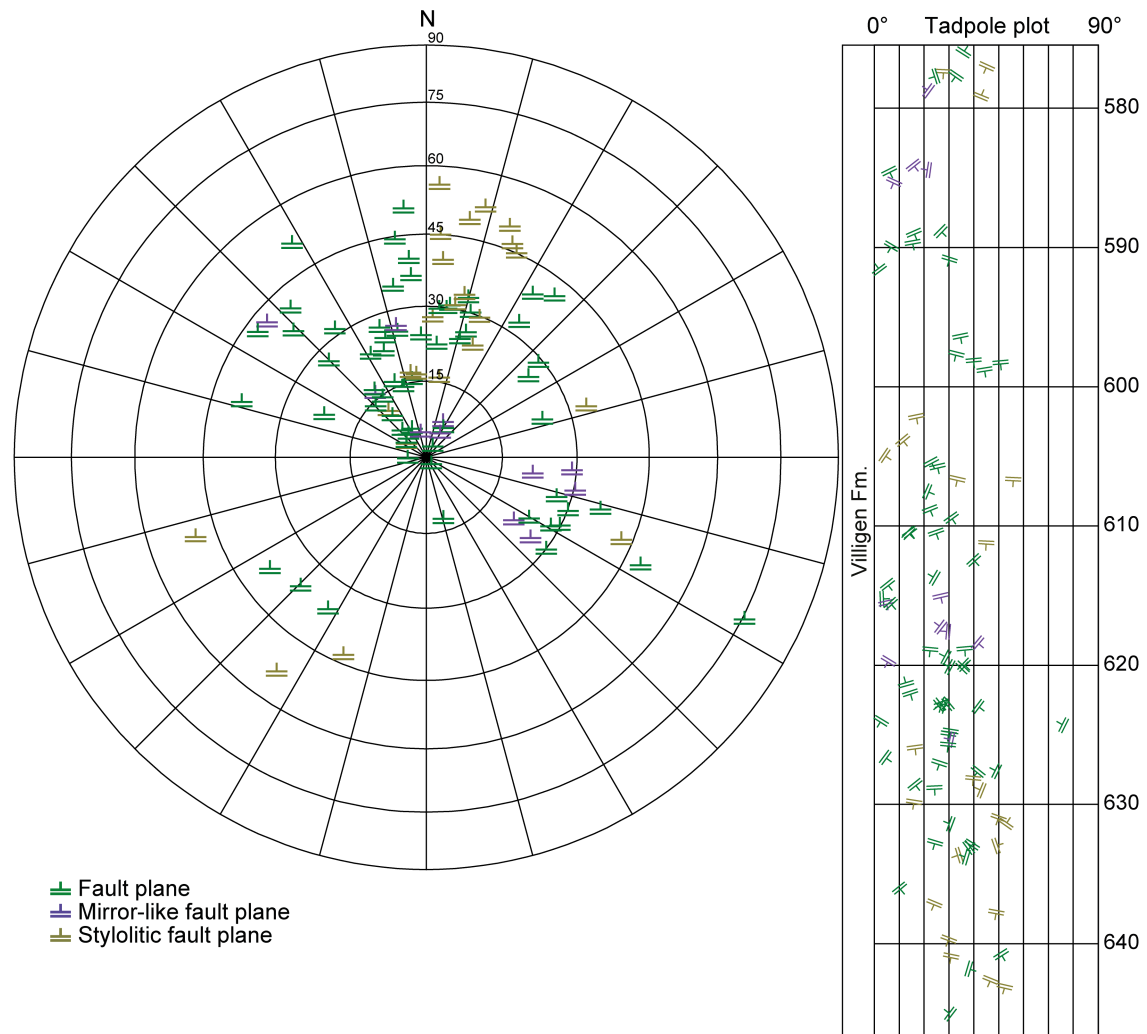


Fig. 4-30: Stereogram and depth plot of fault planes (Villigen Formation)

Fault planes (n = 61), mirror-like fault planes (n = 11) and stylolitic fault planes (n = 23).

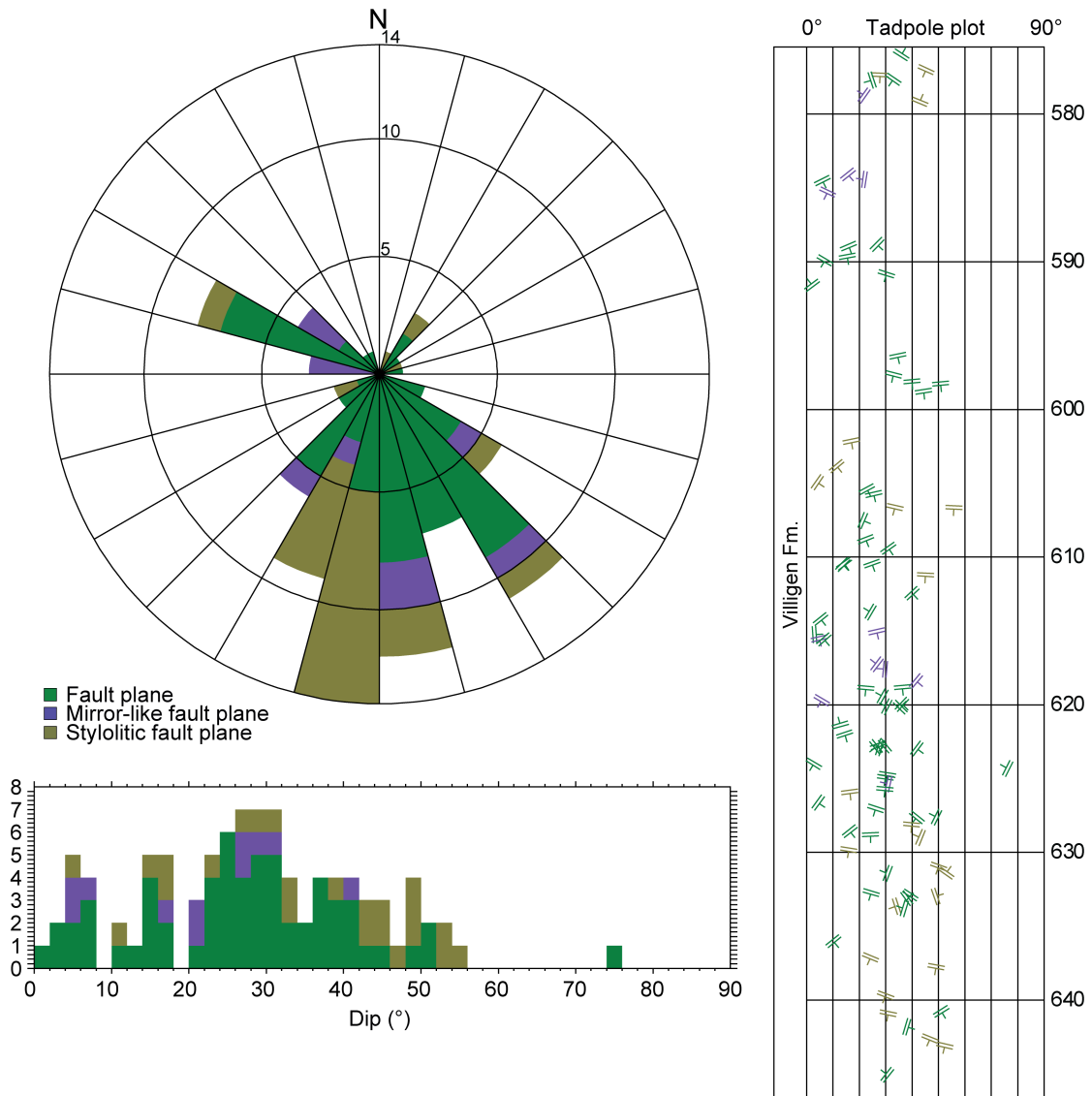


Fig. 4-31: Dip azimuth rose diagram, dip histogram and depth plot of fault planes (Villigen Formation)

Fault planes (n = 61), mirror-like fault planes (n = 11) and stylolitic fault planes (n = 23).

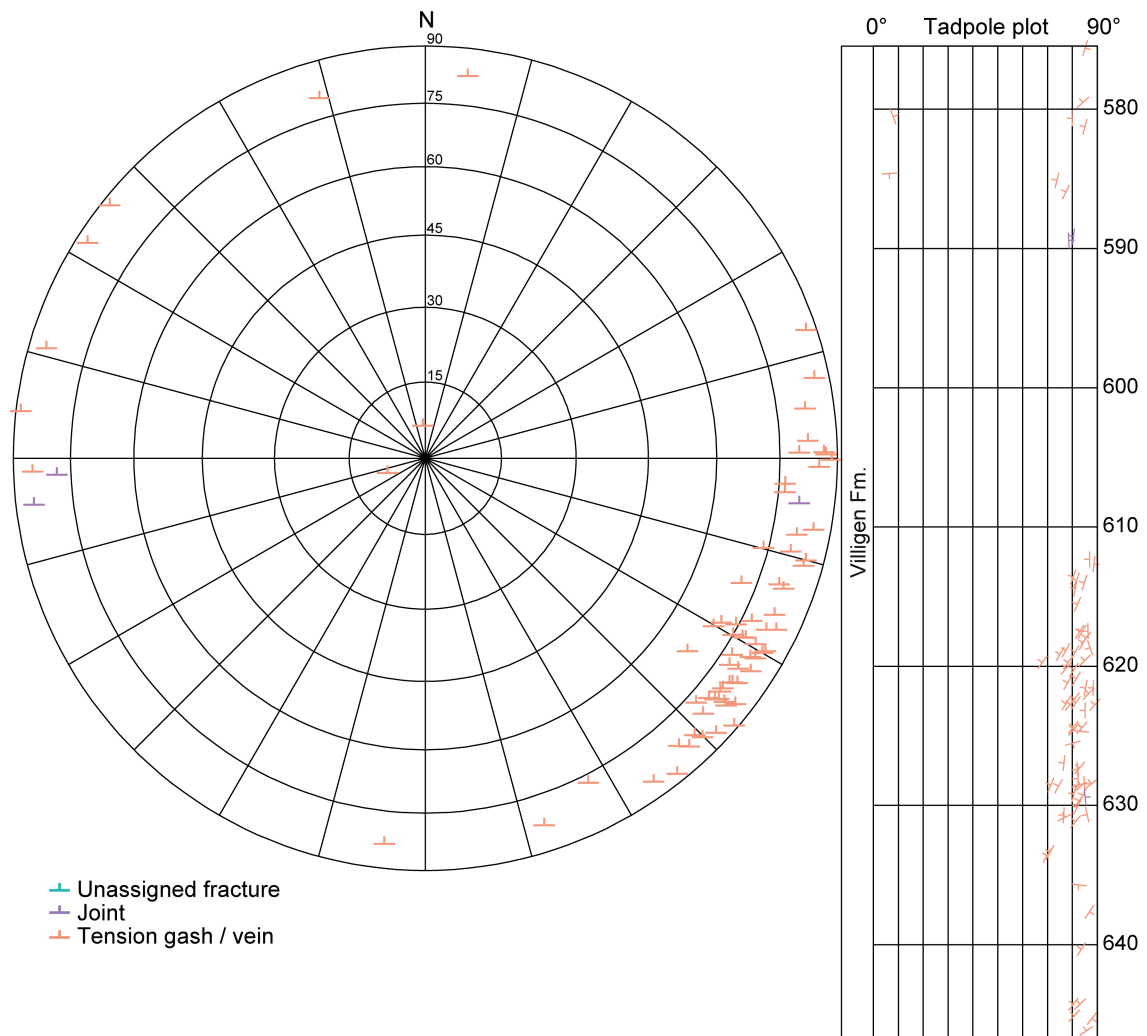


Fig. 4-32: Stereogram and depth plot of tension gashes / veins and unassigned fractures (Villigen Formation)

Joints (n = 3) and tension gashes / veins (n = 73); no unassigned fractures were observed (n = 0).

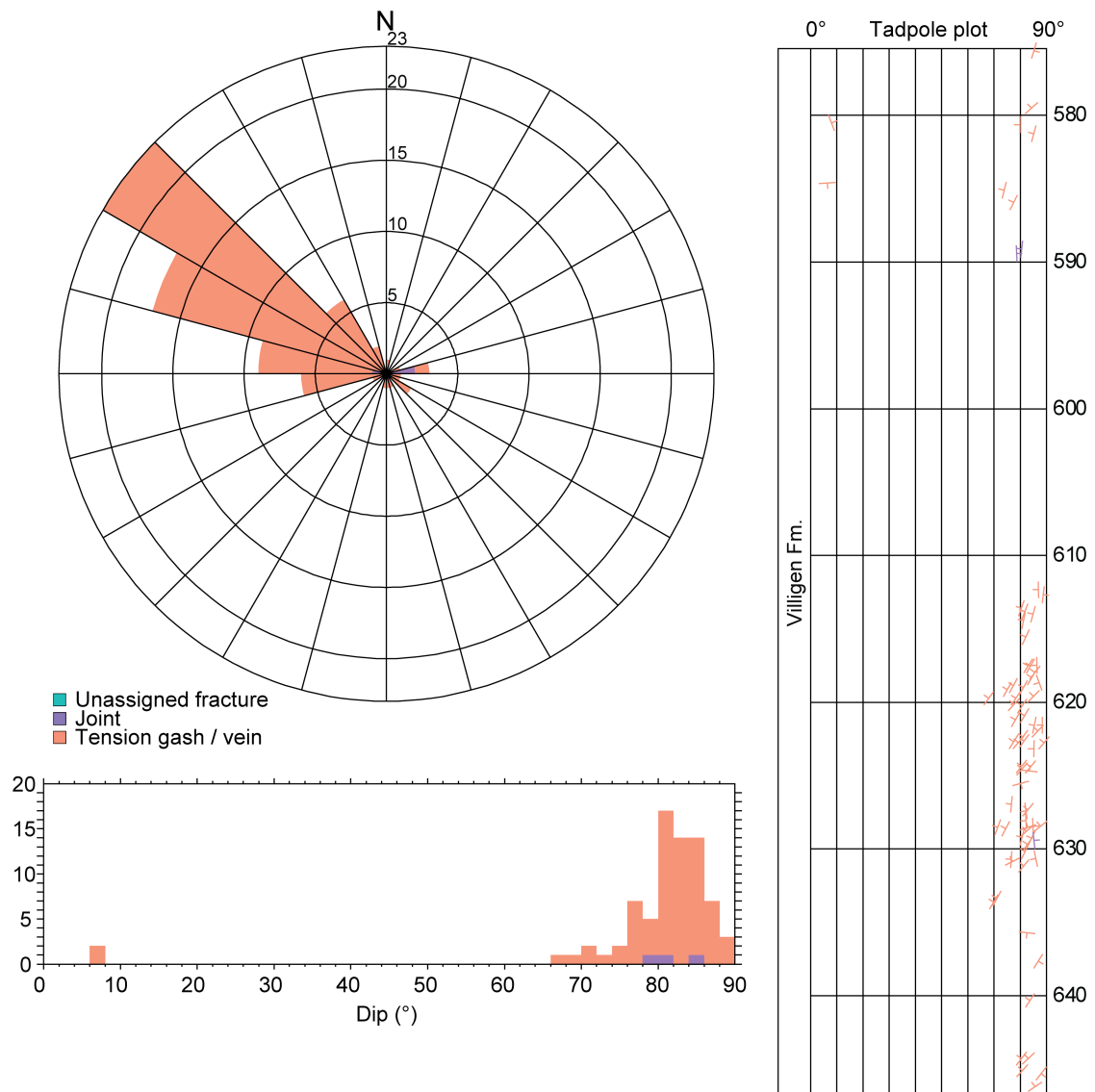


Fig. 4-33: Dip azimuth rose diagram, dip histogram and depth plot of tension gashes / veins, joints and unassigned fractures (Villigen Formation)

Joints (n = 3) and tension gashes / veins (n = 73); no unassigned fractures were observed (n = 0).

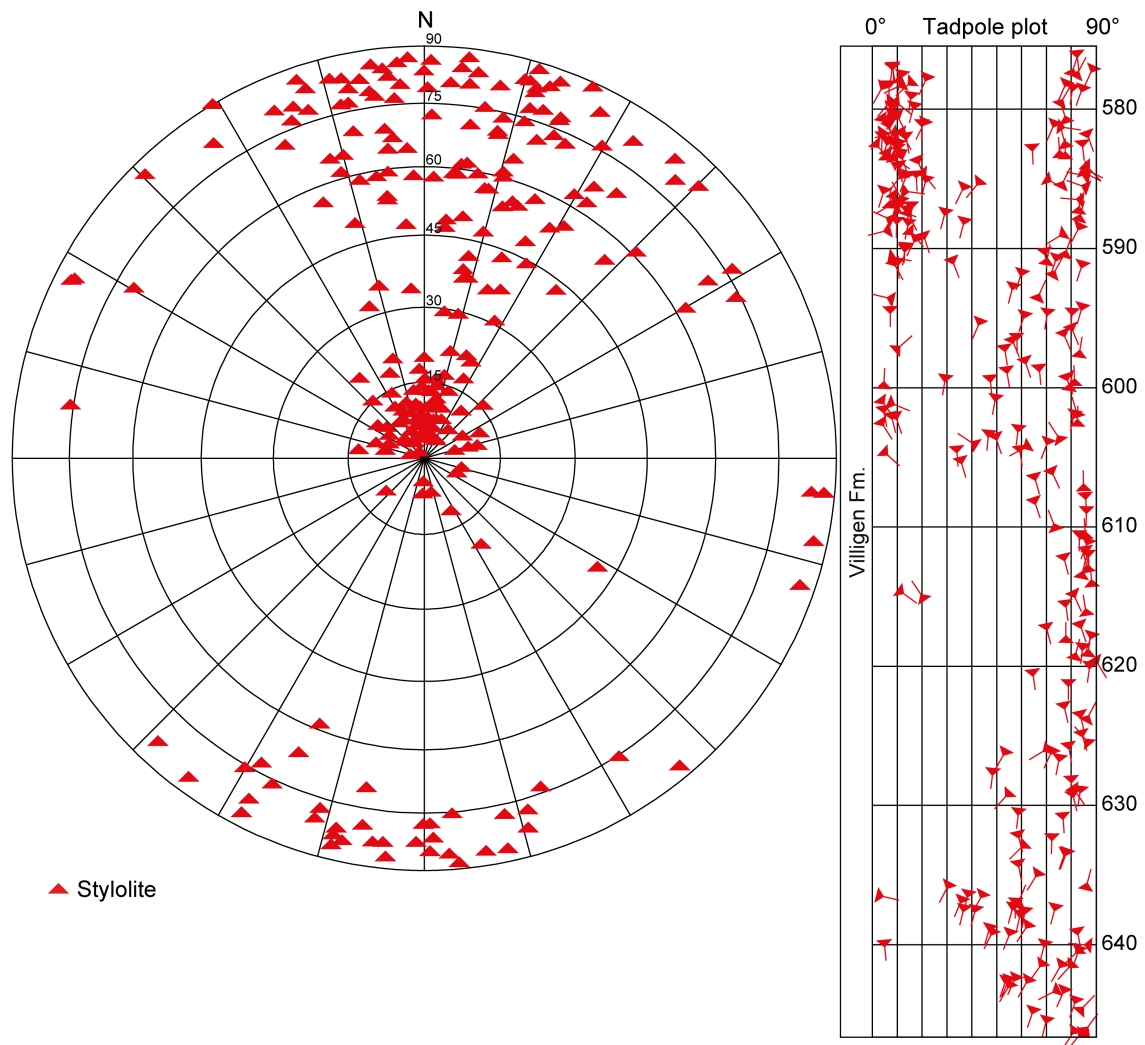


Fig. 4-34: Stereogram and depth plot of stylolites (Villigen Formation; n = 254)

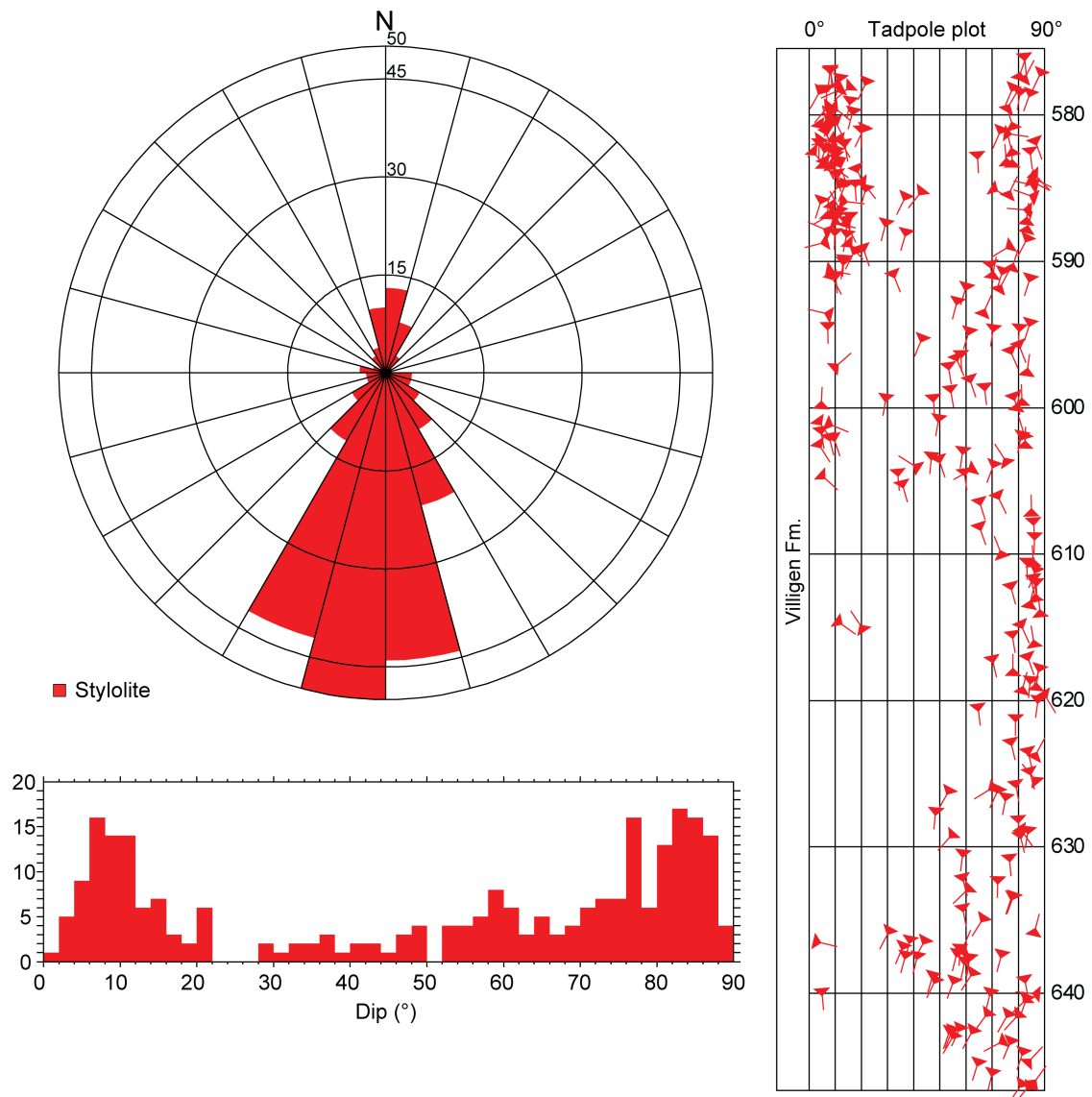


Fig. 4-35: Dip azimuth rose diagram, dip histogram and depth plot of stylolites (Villigen Formation; n = 254)

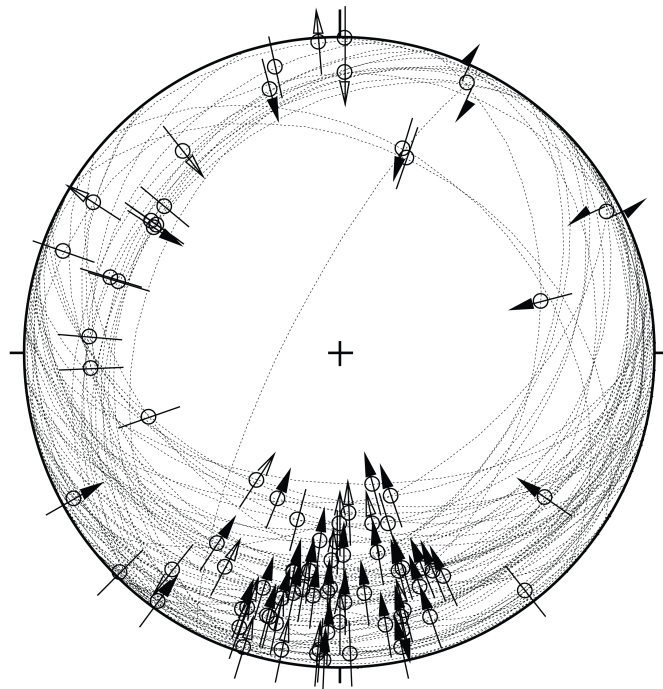


Fig. 4-36: Stereogram of striations on fault planes (including multiple lineations on a single fault plane) (Villigen Formation; n = 82)

4.2.4 Wildegg Formation

The orientation and spatial distribution of recorded structures in the Wildegg Formation (646.63 m to 728.20 m MD log depth) are shown in Figs. 4-37 to 4-43.

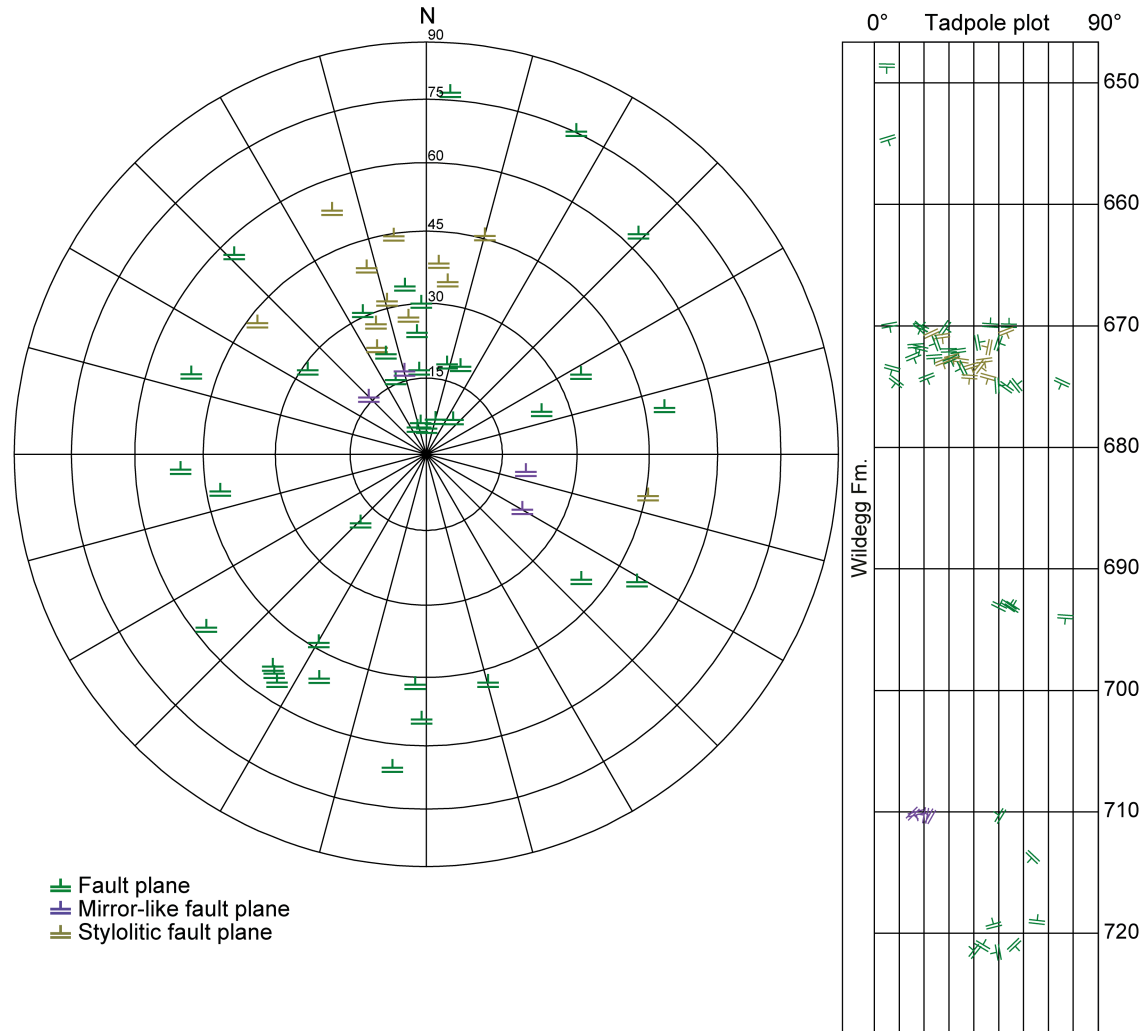


Fig. 4-37: Stereogram and depth plot of fault planes (Wildegg Formation)

Fault planes (n = 38), mirror-like fault planes (n = 4) and stylolitic fault planes (n = 12).

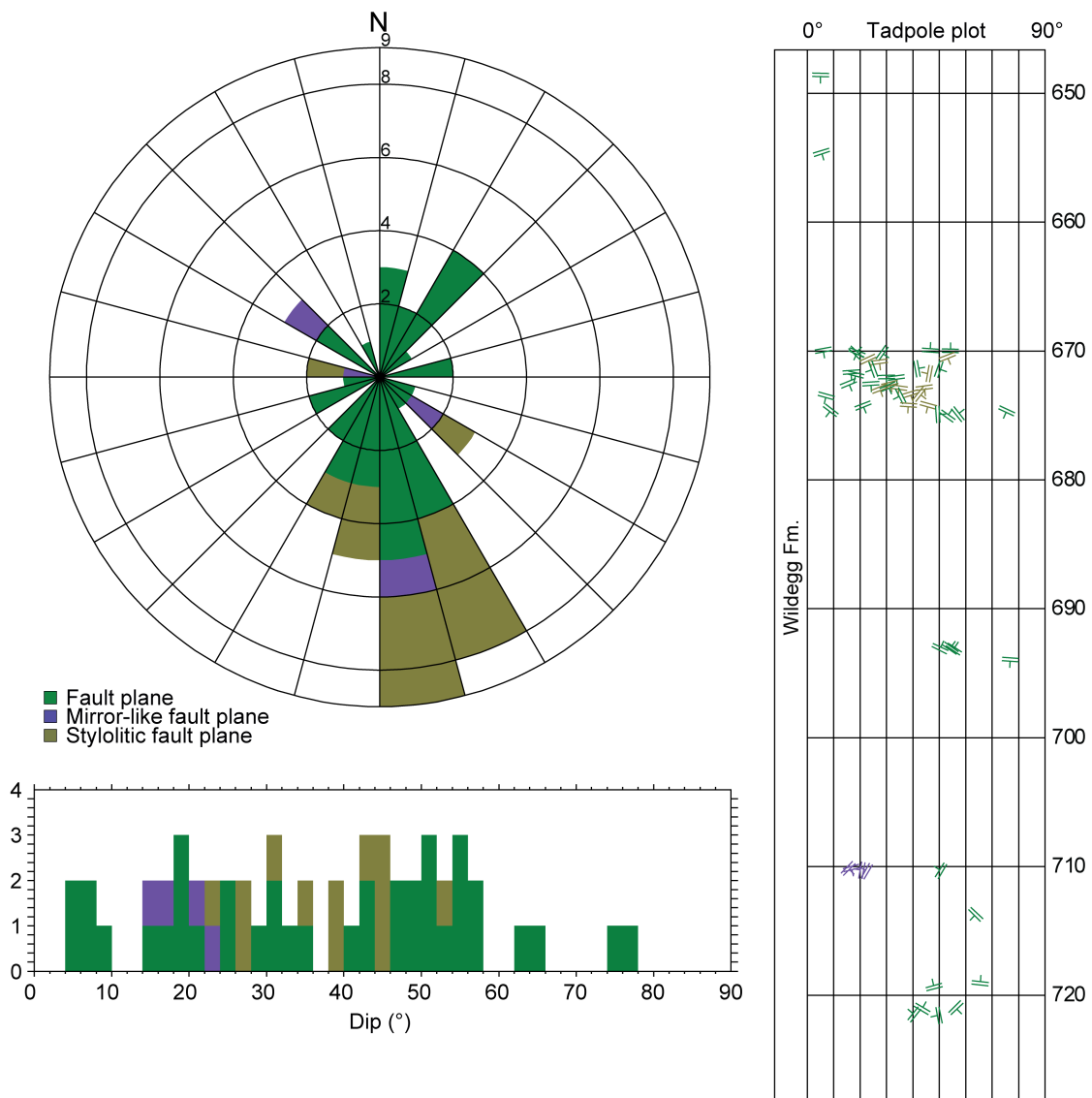


Fig. 4-38: Dip azimuth rose diagram, dip histogram and depth plot of fault planes (Wildegg Formation)

Fault planes (n = 38), mirror-like fault planes (n = 4) and stylolitic fault planes (n = 12).

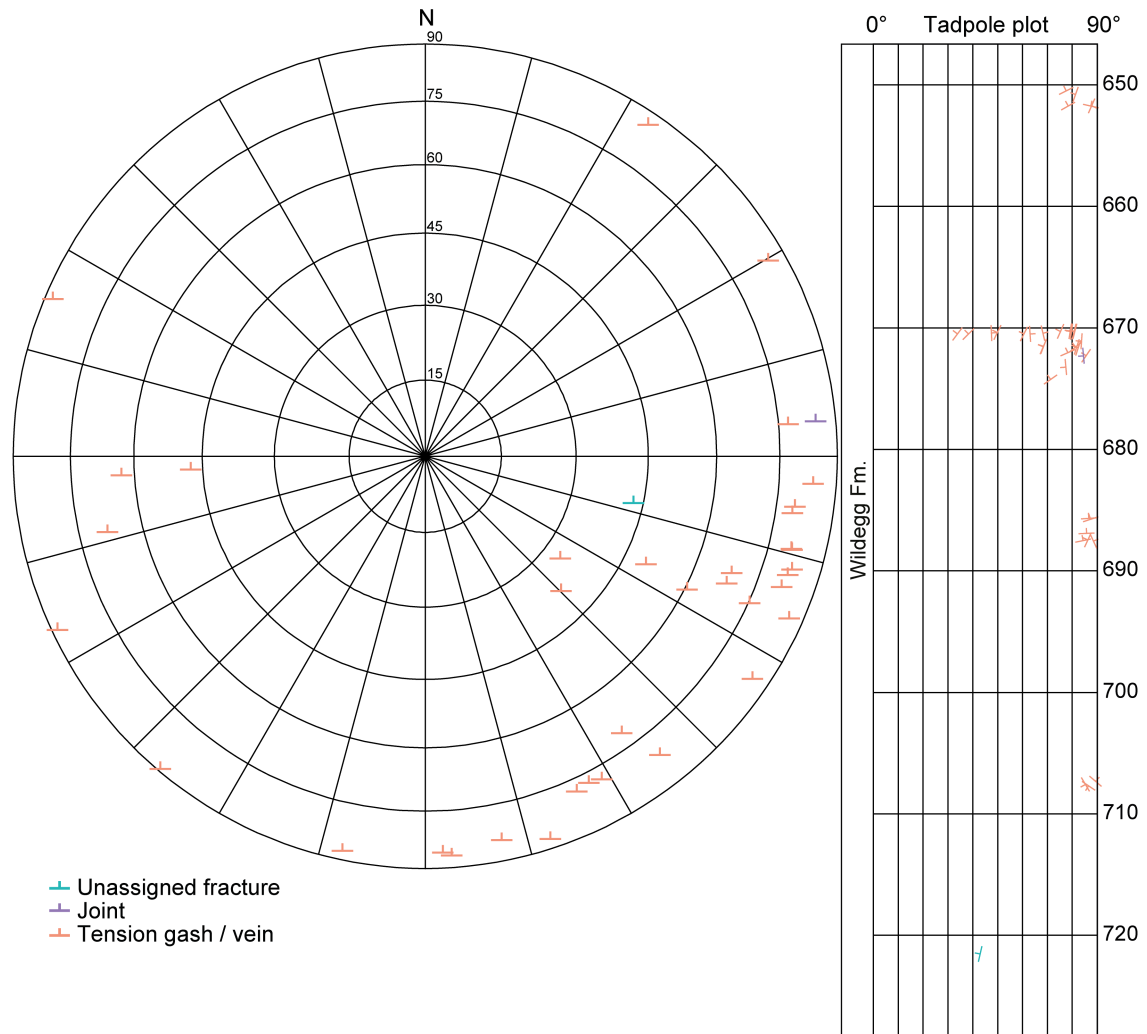


Fig. 4-39: Stereogram and depth plot of tension gashes / veins and unassigned fractures (Wild-egg Formation)

Unassigned fractures (n = 1), joints (n = 1) and tension gashes / veins (n = 36).

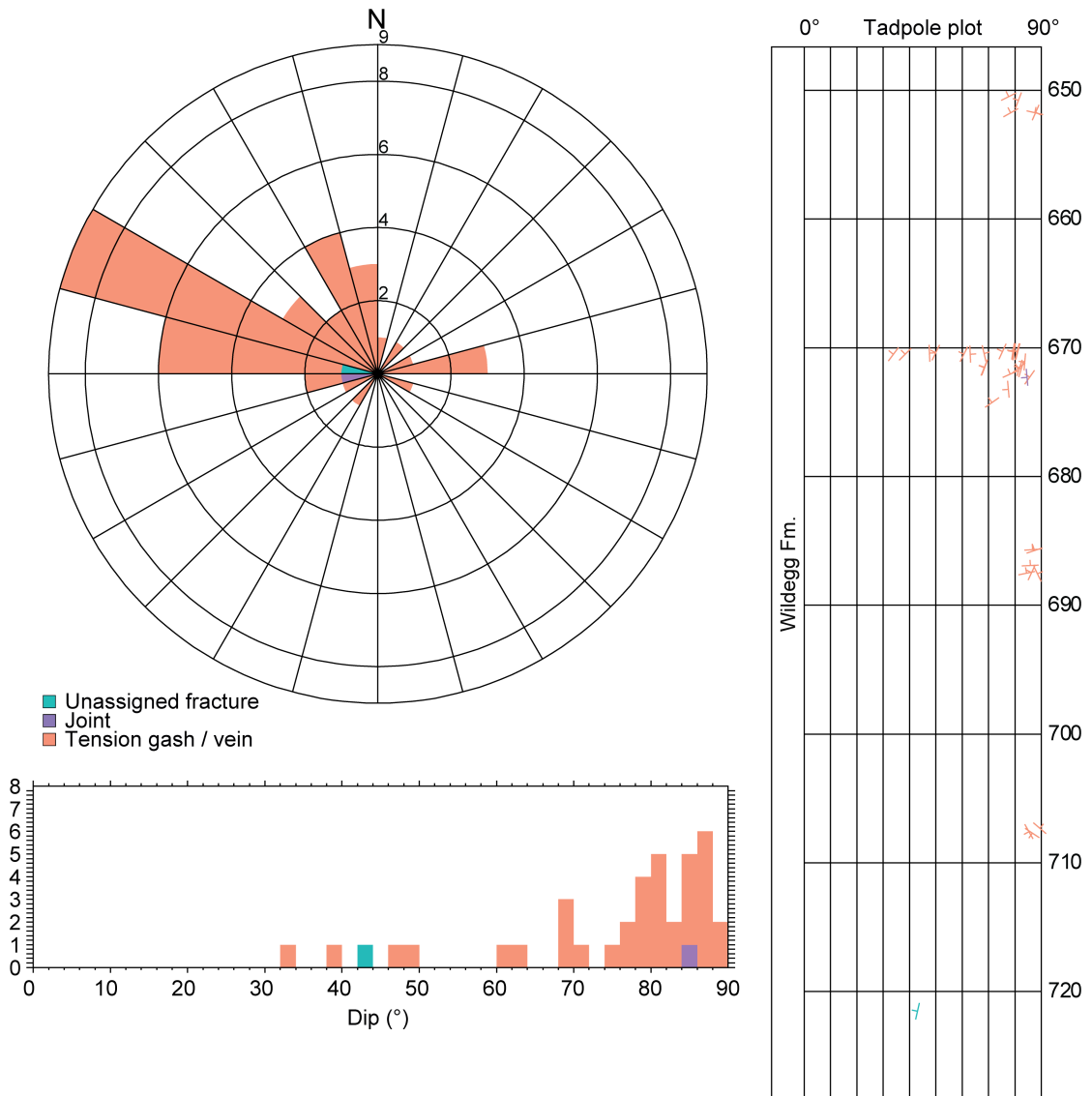


Fig. 4-40: Dip azimuth rose diagram, dip histogram and depth plot of tension gashes / veins, joints and unassigned fractures (Wildegge Formation)

Unassigned fractures (n = 1), joints (n = 1) and tension gashes / veins (n = 36).

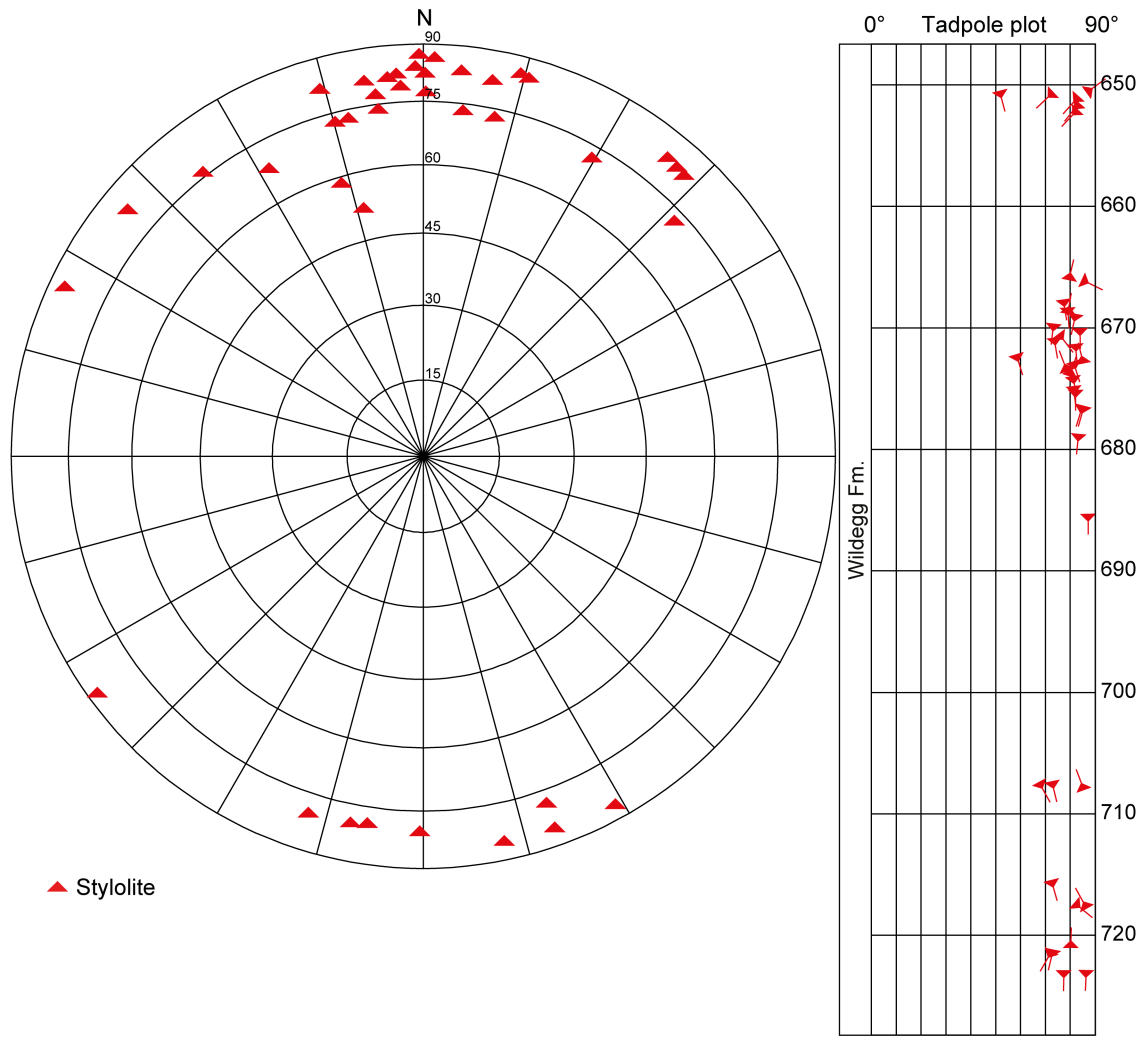


Fig. 4-41: Stereogram and depth plot of stylolites (Wildegg Formation; n = 40)

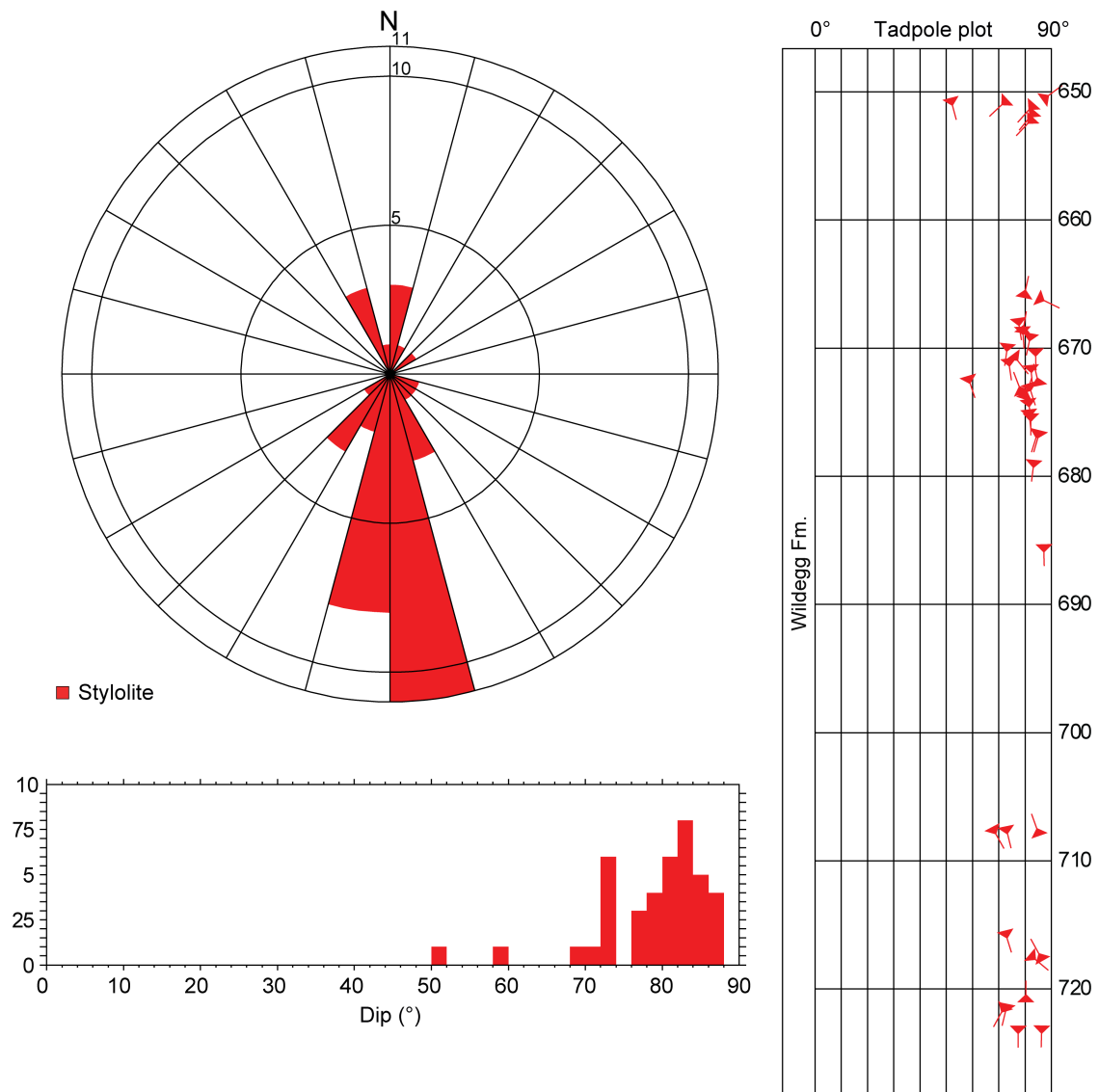


Fig. 4-42: Dip azimuth rose diagram, dip histogram and depth plot of stylolites (Wildegg Formation; n = 40)

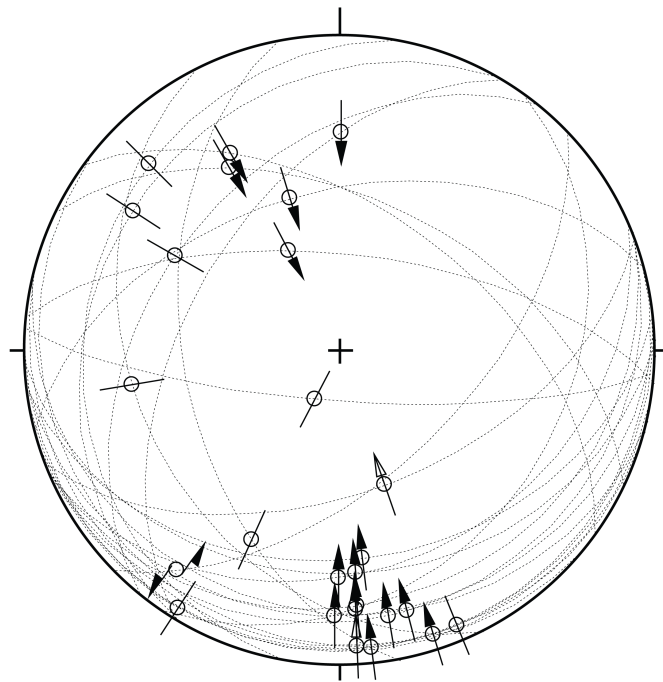


Fig. 4-43: Stereogram of striations on fault planes, including multiple lineations on a single fault plane (Wildegge Formation; n = 26)

4.3 Dogger

For the detailed stereographic evaluation, the Dogger was subdivided into two units: the «Brauner Dogger» and the Opalinus Clay. The orientation and spatial distribution of recorded structures in the Dogger are shown in Figs. 4-44 to 4-56. Only the data from oriented cores are presented.

4.3.1 «Brauner Dogger» (Wutach Formation to «Murchisonae-Oolith Formation»)

The «Brauner Dogger» (728.20 m to 800.67 m MD log depth), an informal lithostratigraphic unit including predominantly claystone-rich lithologies from the Wutach Formation to the «Murchisonae-Oolith Formation», shows a low density of all structure types. All fault types are characterised by varying dip and a preferred dip azimuth towards the SE. Tension gashes / veins, joints and unassigned fractures are generally subvertical with a preferred dip azimuth towards the WNW. The striations plunge predominantly towards the S and reverse faulting dominates. The few stylolites dip steeply towards the S and occur predominantly in the calcareous «Herrenwis Unit».

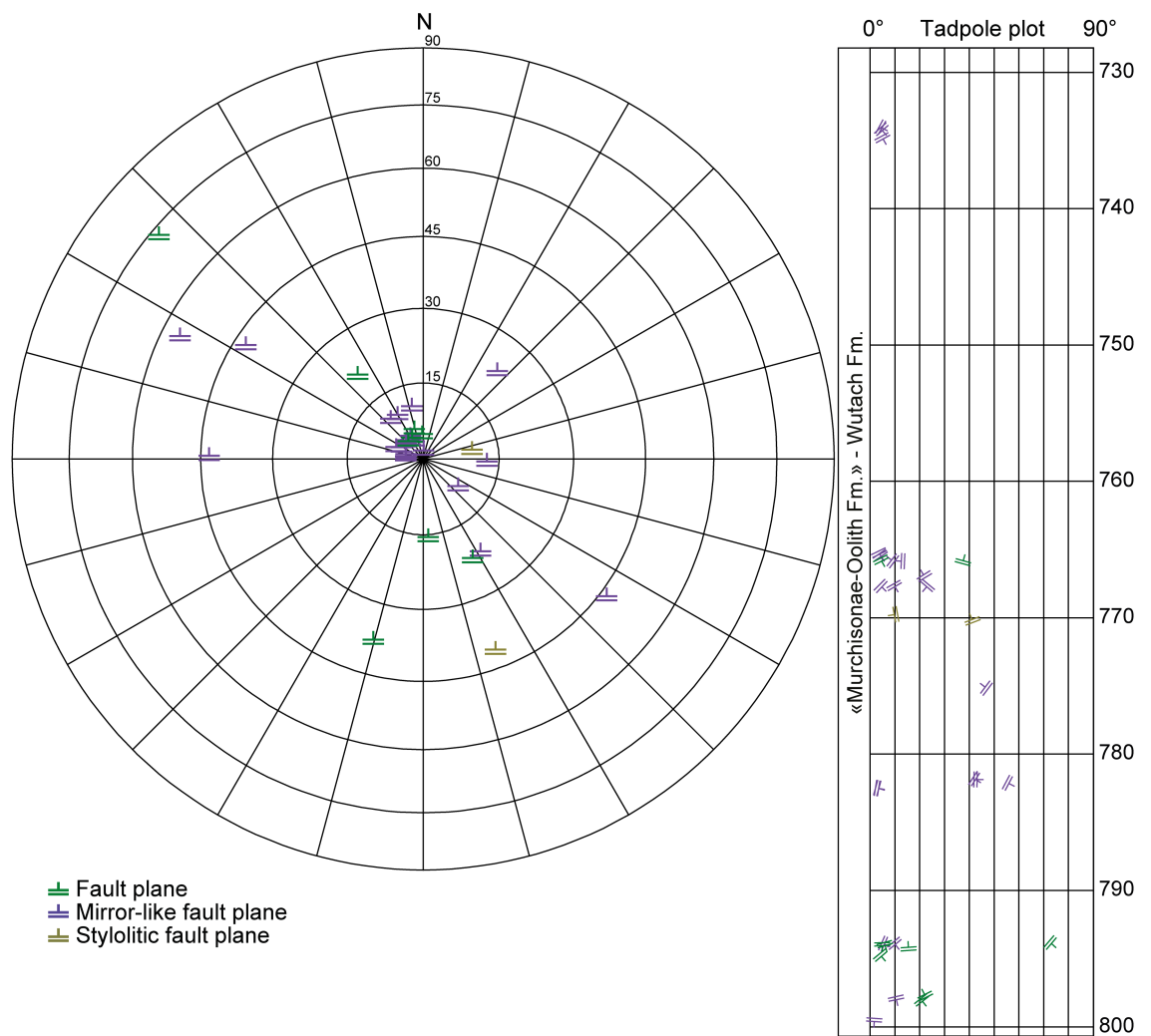


Fig. 4-44: Stereogram and depth plot of fault planes («Brauner Dogger») Fault planes (n = 9), mirror-like fault planes (n = 21) and stylolitic fault planes (n = 2).

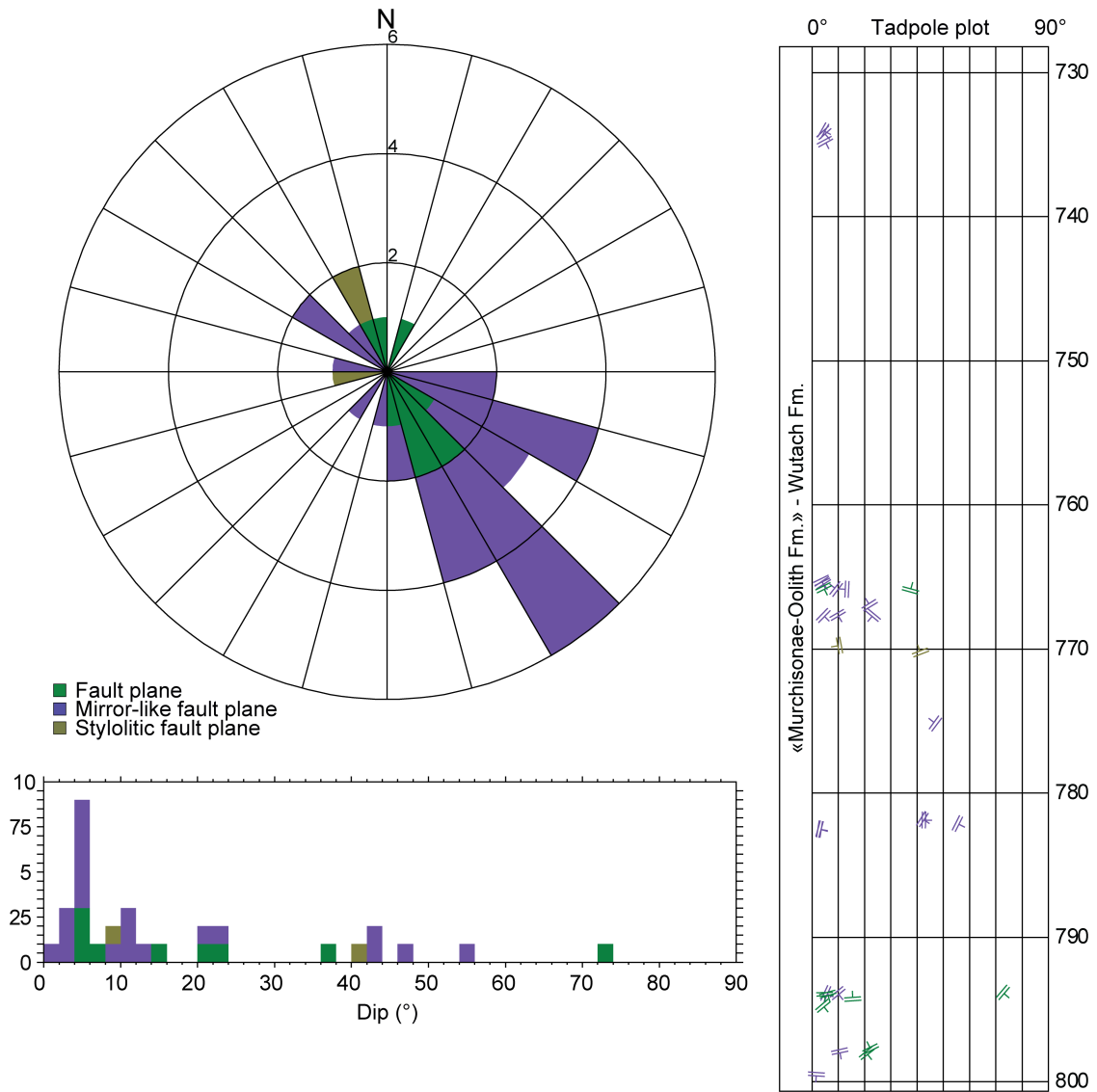


Fig. 4-45: Dip azimuth rose diagram, dip histogram and depth plot of fault planes («Brauner Dogger»)

Fault planes (n = 9), mirror-like fault planes (n = 21) and styloitic fault planes (n = 2).

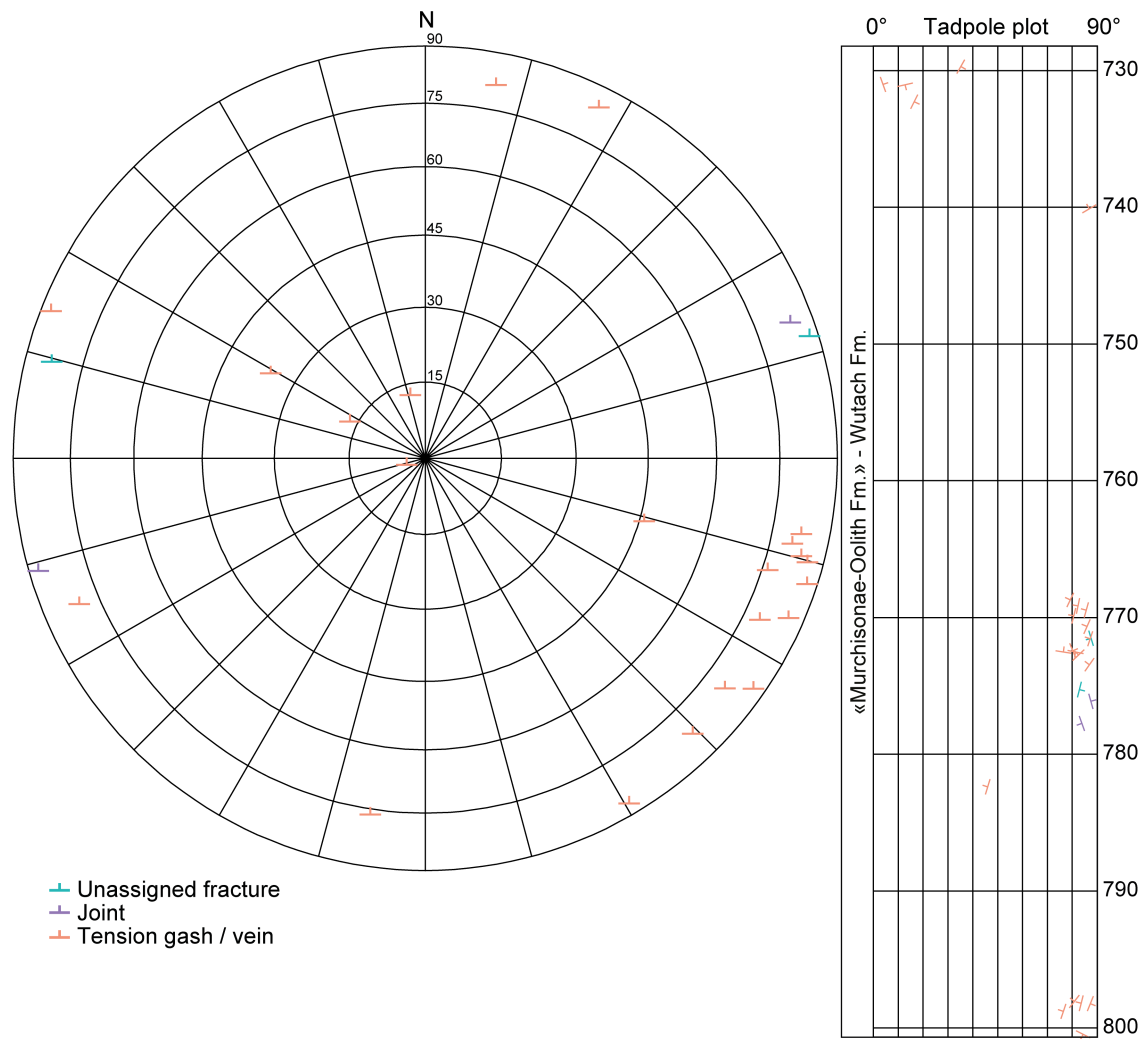


Fig. 4-46: Stereogram and depth plot of tension gashes / veins, joints and unassigned fractures («Brauner Dogger»)

Unassigned fractures (n = 2), joints (n = 2) and tension gashes / veins (n = 22).

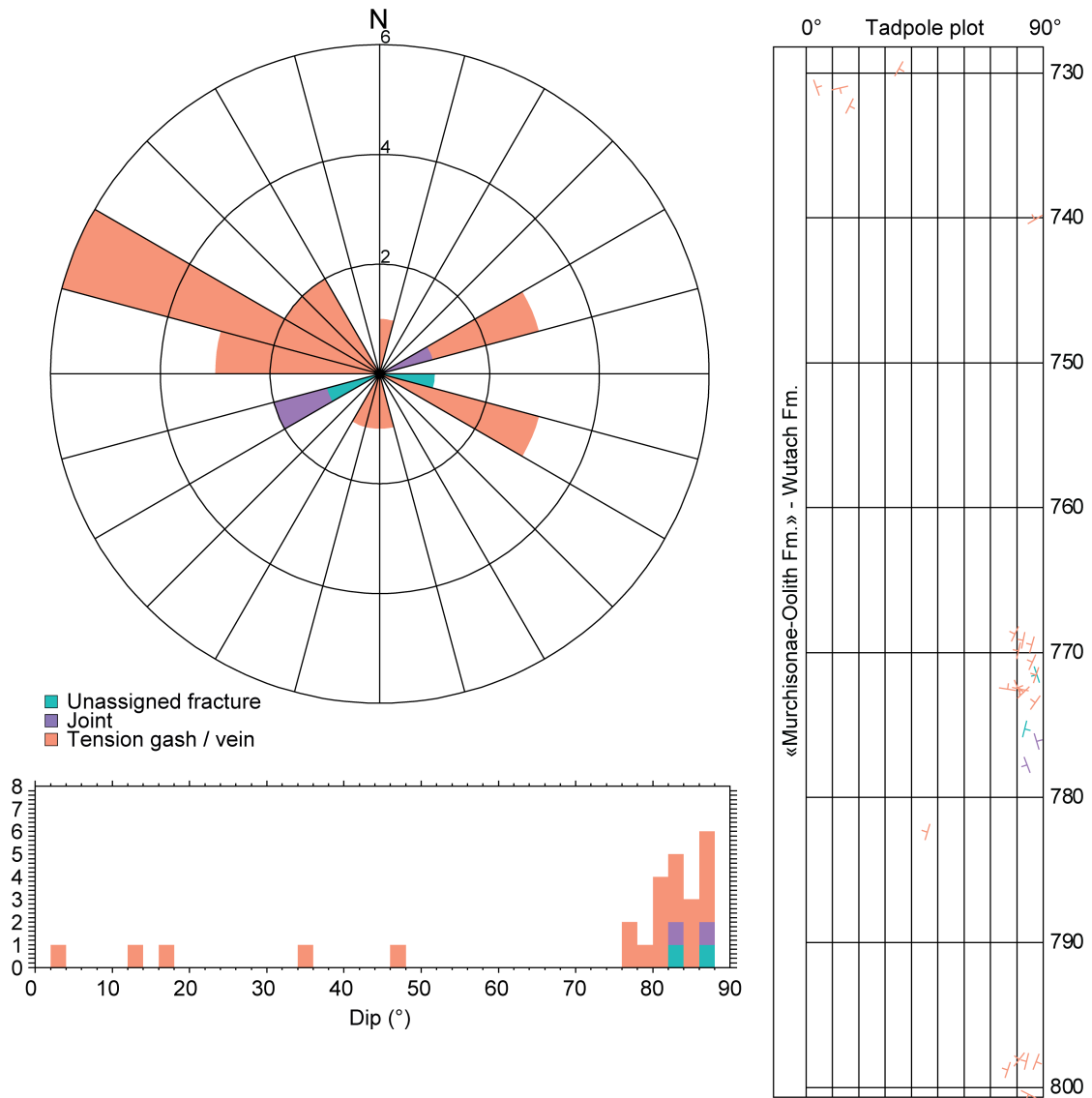


Fig. 4-47: Dip azimuth rose diagram, dip histogram and depth plot of tension gashes / veins, joints and unassigned fractures («Brauner Dogger»)

Unassigned fractures (n = 2), joints (n = 2) and tension gashes / veins (n = 22).

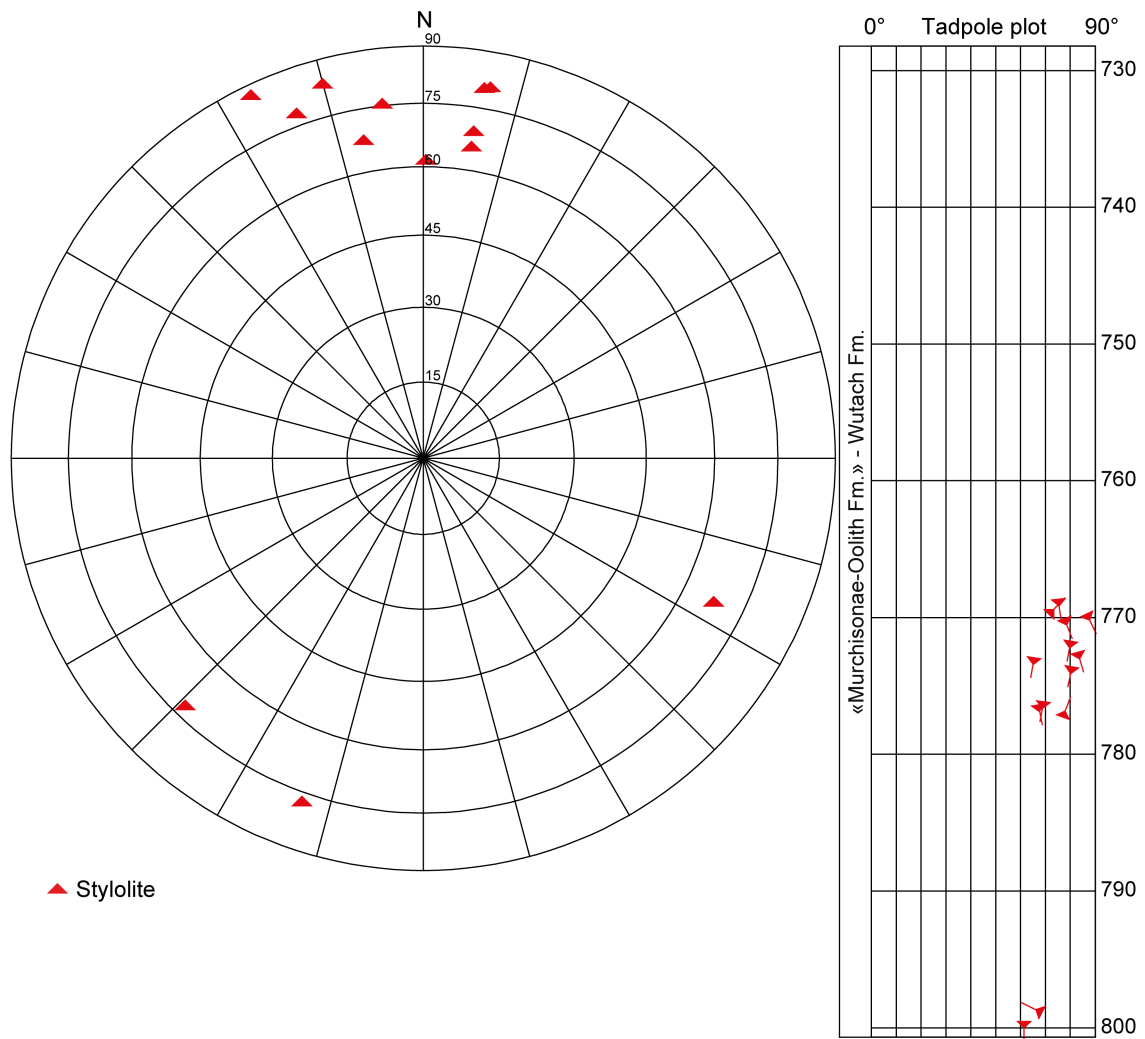


Fig. 4-48: Stereogram and depth plot of stylolites («Brauner Dogger»; n = 13)

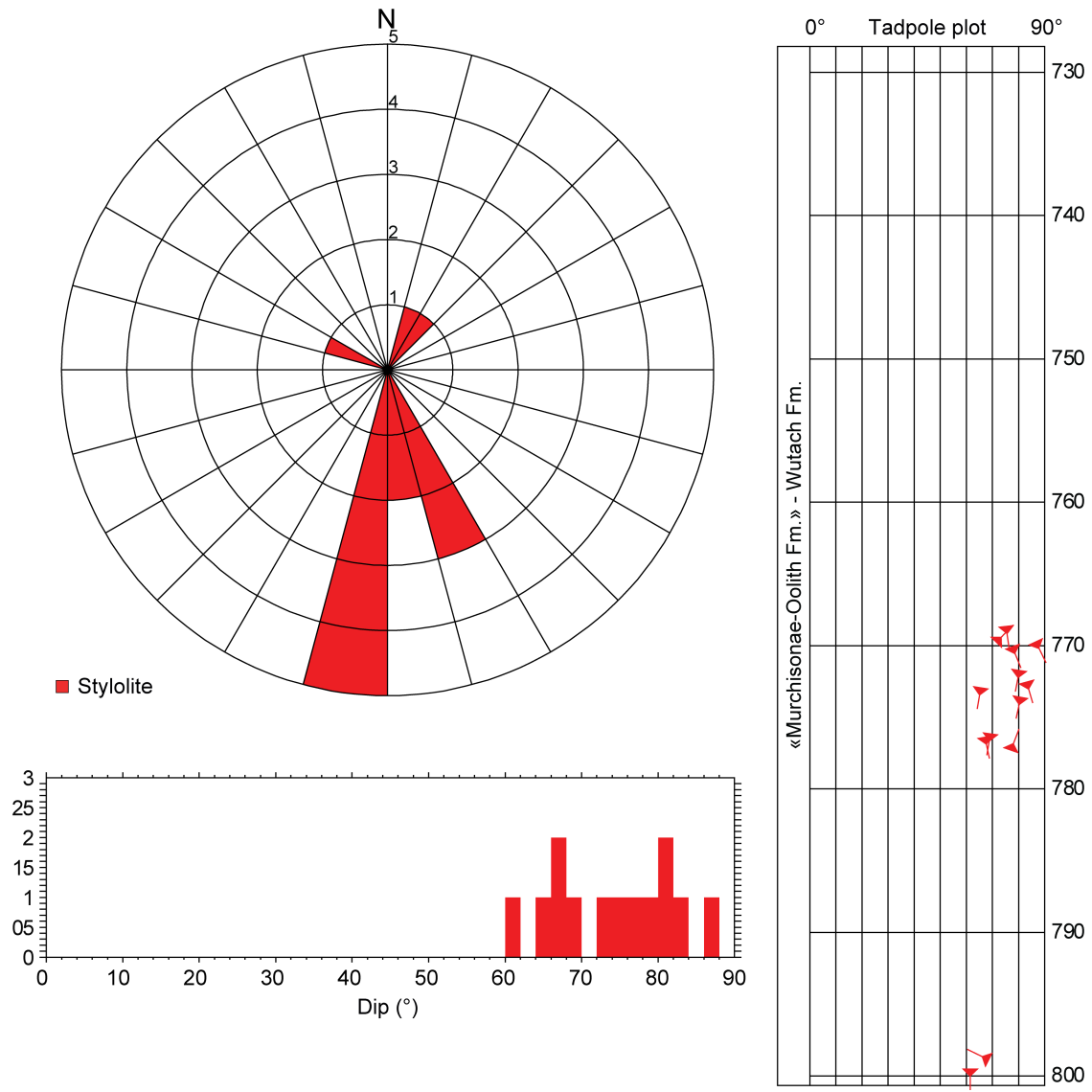


Fig. 4-49: Dip azimuth rose diagram, dip histogram and depth plot of stylolites («Brauner Dogger»; n = 13)

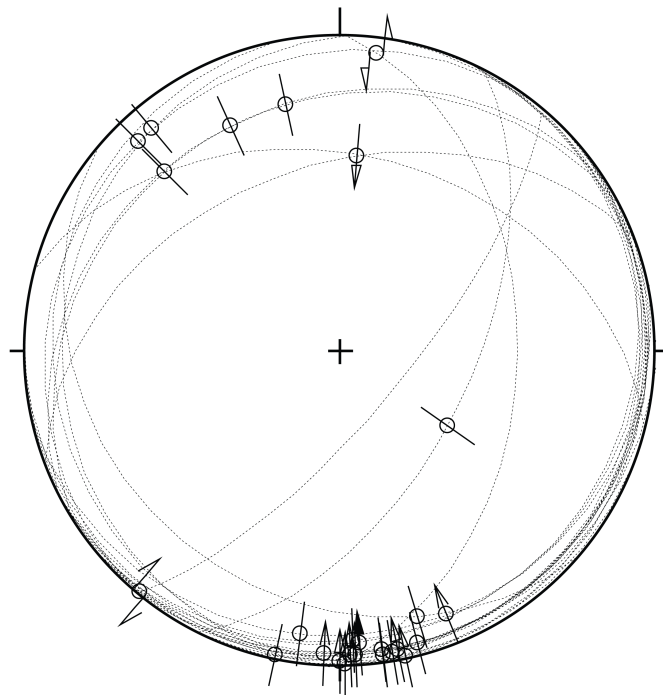


Fig. 4-50: Stereogram of striations on fault planes, including multiple lineations on a single fault plane («Brauner Dogger»; $n = 26$)

4.3.2 Opalinus Clay

The Opalinus Clay (800.67 m to 906.87 m MD log depth) reveals a low density of fault planes, mirror-like fault planes and tension gashes / veins. Stylolitic fault planes, unassigned fractures and joints were not observed. Only one stylolite was found. Most of the fault planes and tension gashes / veins were concentrated within two zones, from 843.35 m to 844.29 m MD (log depth) and from 884.51 m to 890.19 m MD (log depth). Tension gashes / veins often show fibrous calcite mineralisation with mineral grains oriented normal to the fracture plane.

The fault planes and tension gashes / veins show shallow to steep dip angles. Most of the structures reveal dip directions towards the WNW or SE. Only few shear sense indicators were observed. Reverse faulting dominates, with striations predominantly plunging towards the S. Fault planes are often characterised by calcite fillings (synkinematic calcite or fibrous mineralisation normal to the fracture plane), which are commonly less than 1 mm thick.

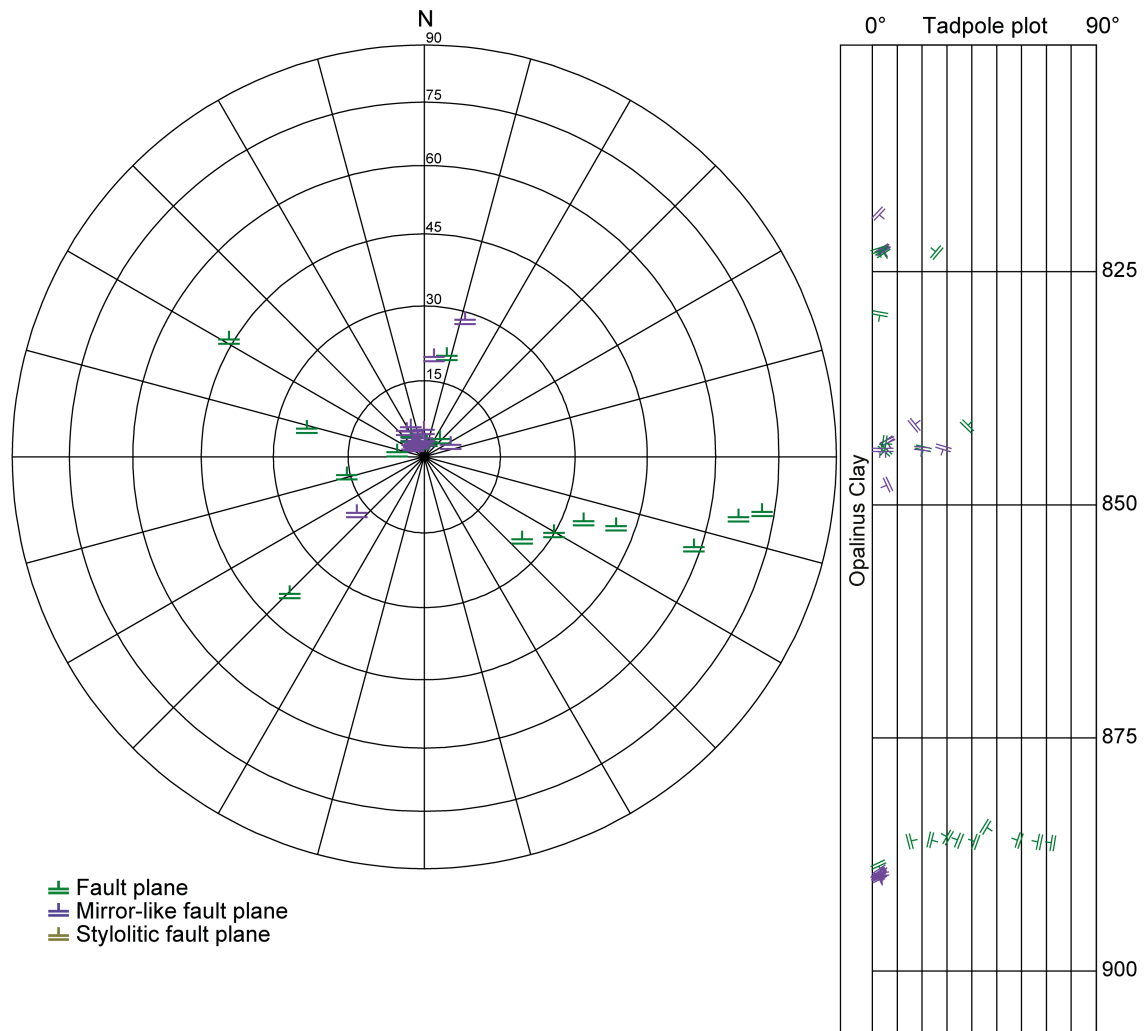


Fig. 4-51: Stereogram and depth plot of fault planes (Opalinus Clay)

Fault planes (n = 18) and mirror-like fault planes (n = 19); no stylolitic fault planes were observed (n = 0).

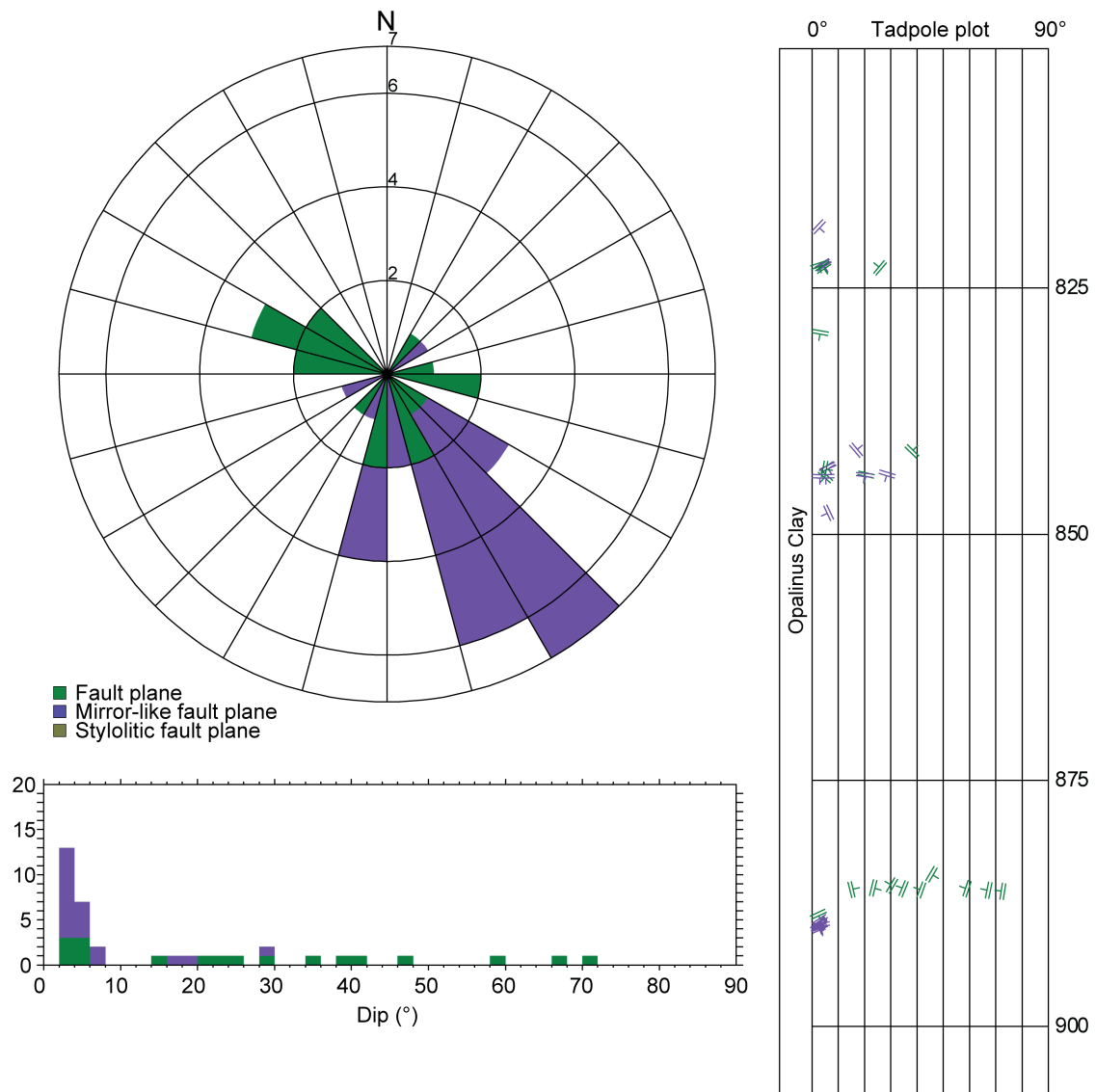


Fig. 4-52: Dip azimuth rose diagram, dip histogram and depth plot of fault planes (Opalinus Clay)

Fault planes (n = 18) and mirror-like fault planes (n = 19); no stylolitic fault planes were observed (n = 0).

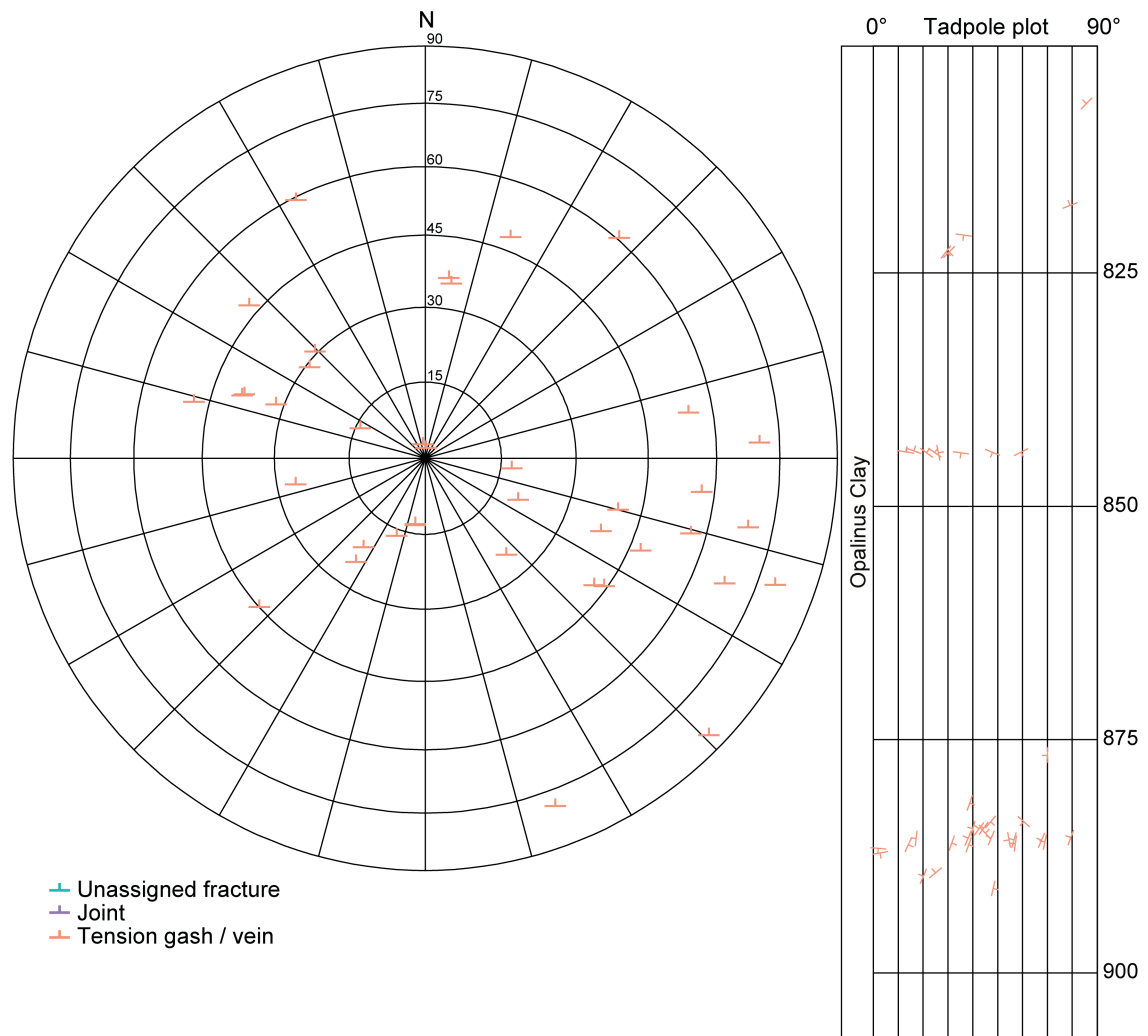


Fig. 4-53: Stereogram and depth plot of tension gashes / veins, joints and unassigned fractures (Opalinus Clay)

Tension gashes / veins (n = 39); no unassigned fractures and joints were observed (n = 0).

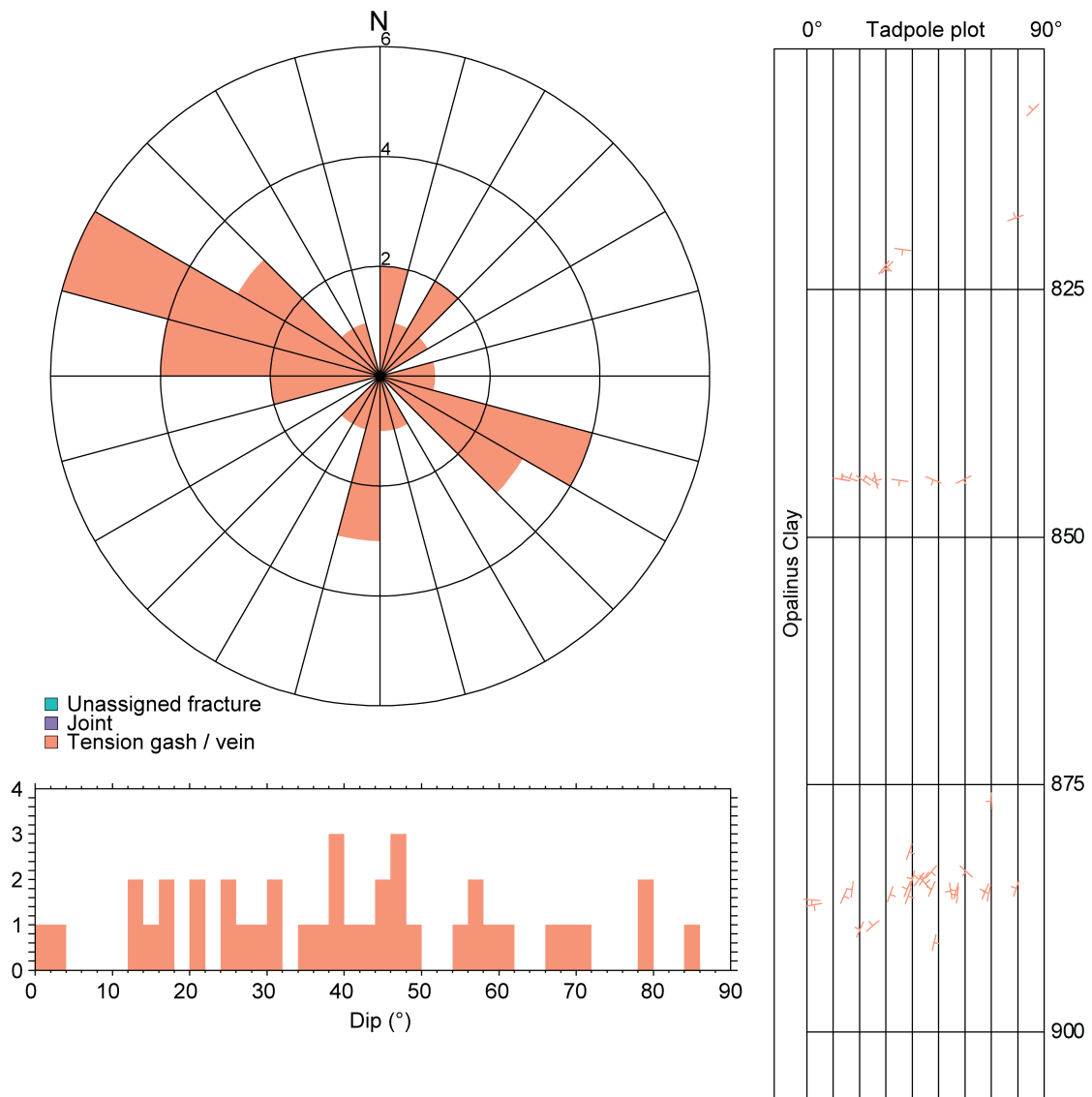


Fig. 4-54: Dip azimuth rose diagram, dip histogram and depth plot of tension gashes / veins, joints and unassigned fractures (Opalinus Clay)

Tension gashes / veins (n = 39); no unassigned fractures and joints were observed (n = 0).

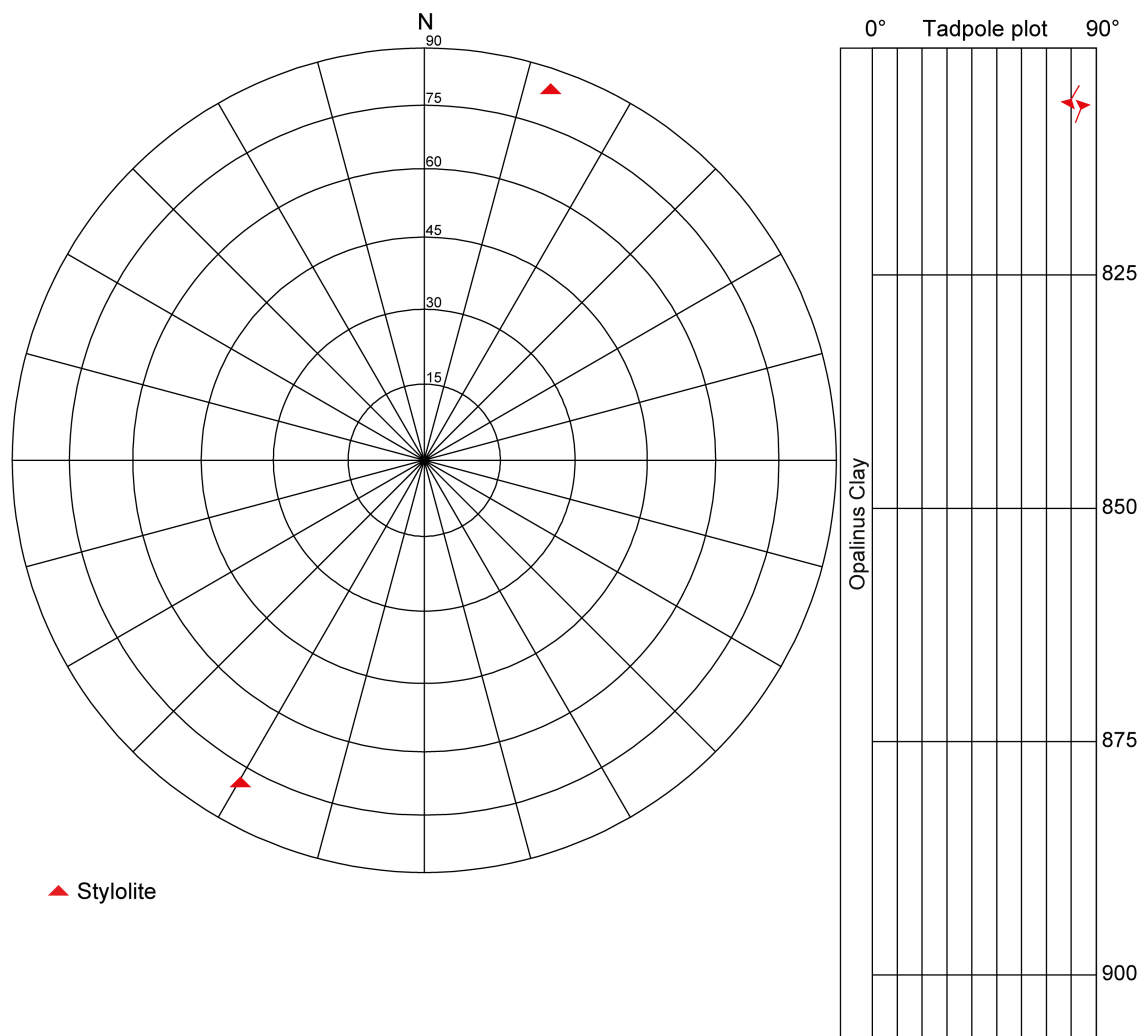


Fig. 4-55: Stereogram and depth plot of stylolites (Opalinus Clay; n = 2)

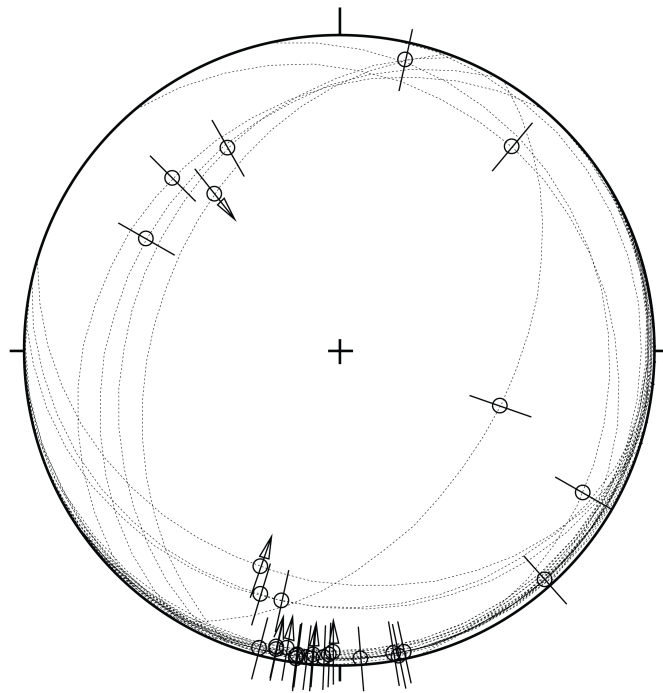


Fig. 4-56: Stereogram of striations on fault planes, including multiple lineations on a single fault plane (Opalinus Clay; $n = 30$)

4.4 Lias (Staffelegg Formation)

As presented in Figs. 4-57 to 4-62, the Lias (906.87 m to 941.42 m MD log depth) is characterised by a low number of structures. However, predominantly subhorizontal mirror-like fault planes and steeply dipping tension gashes were found. Other fault plane types, stylolites and unassigned fractures were rare, while stylolitic fault planes and joints were not observed. Striations plunge mainly towards the south. Only the data from oriented cores are presented.

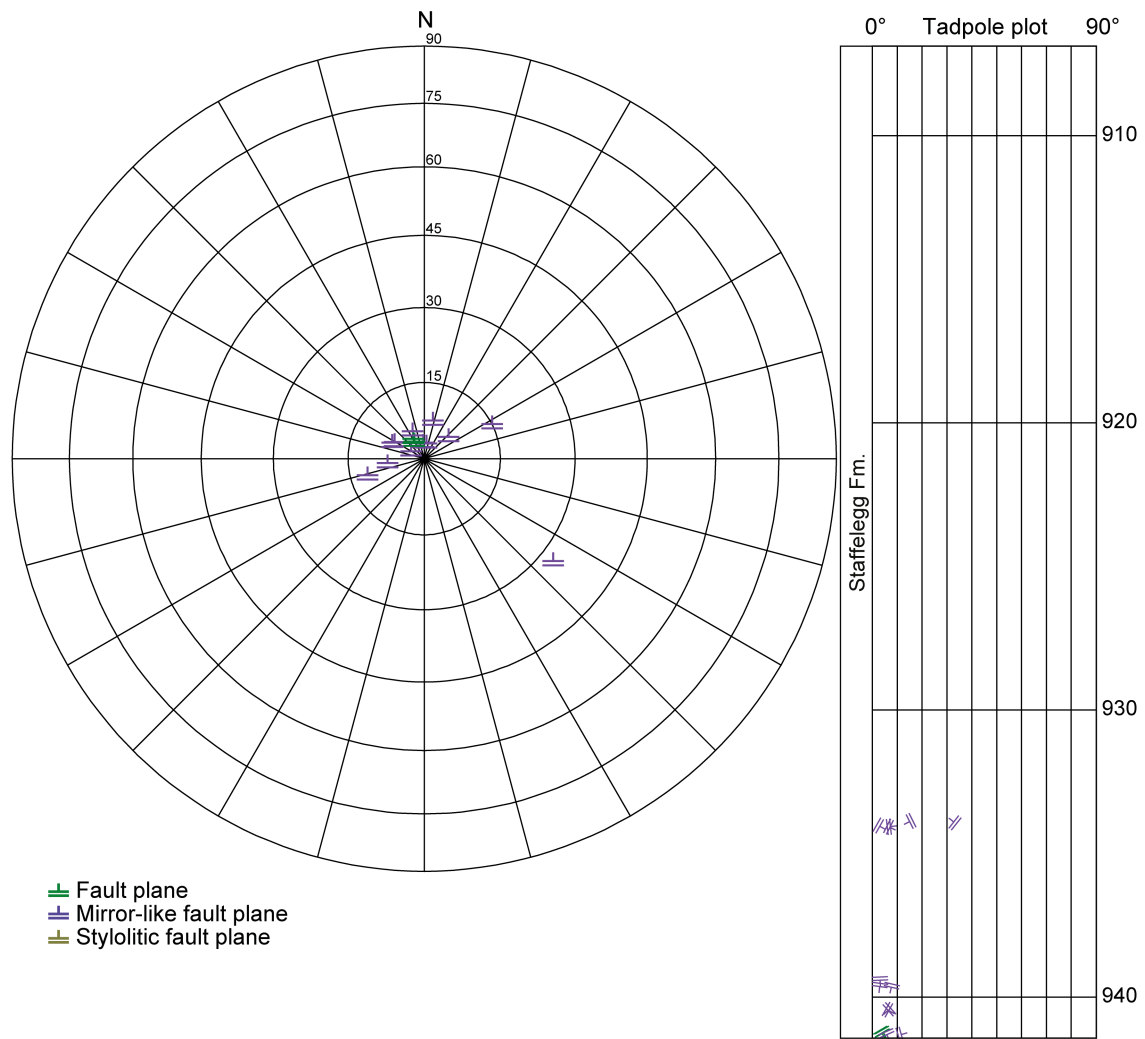


Fig. 4-57: Stereogram and depth plot of fault planes (Lias)

Fault planes (n = 2) and mirror-like fault planes (n = 12); no stylolitic fault planes were observed (n = 0).

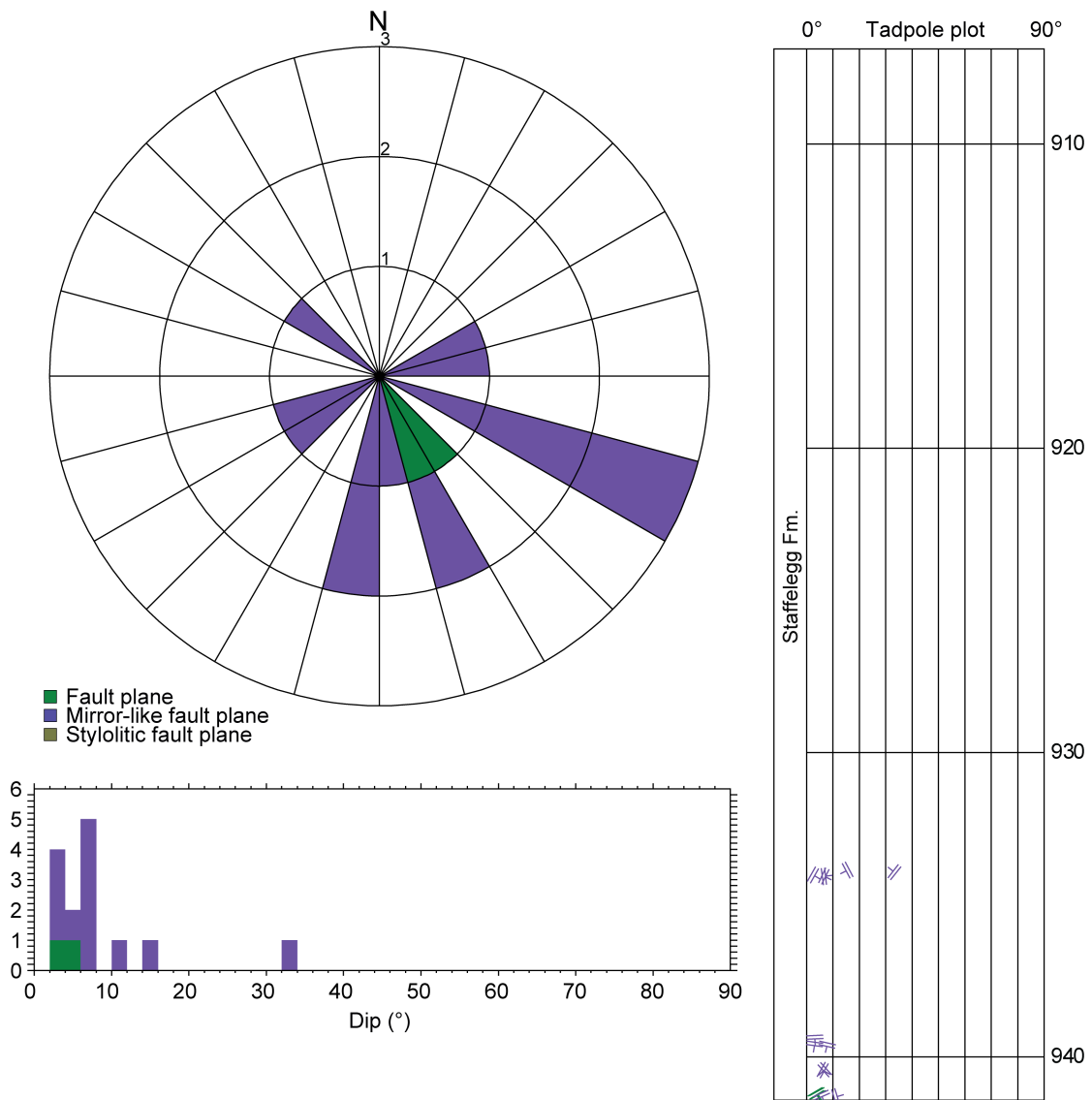


Fig. 4-58: Dip azimuth rose diagram, dip histogram and depth plot of fault planes (Lias)
 Fault planes (n = 2) and mirror-like fault planes (n = 12); no stylolitic fault planes were observed (n = 0).

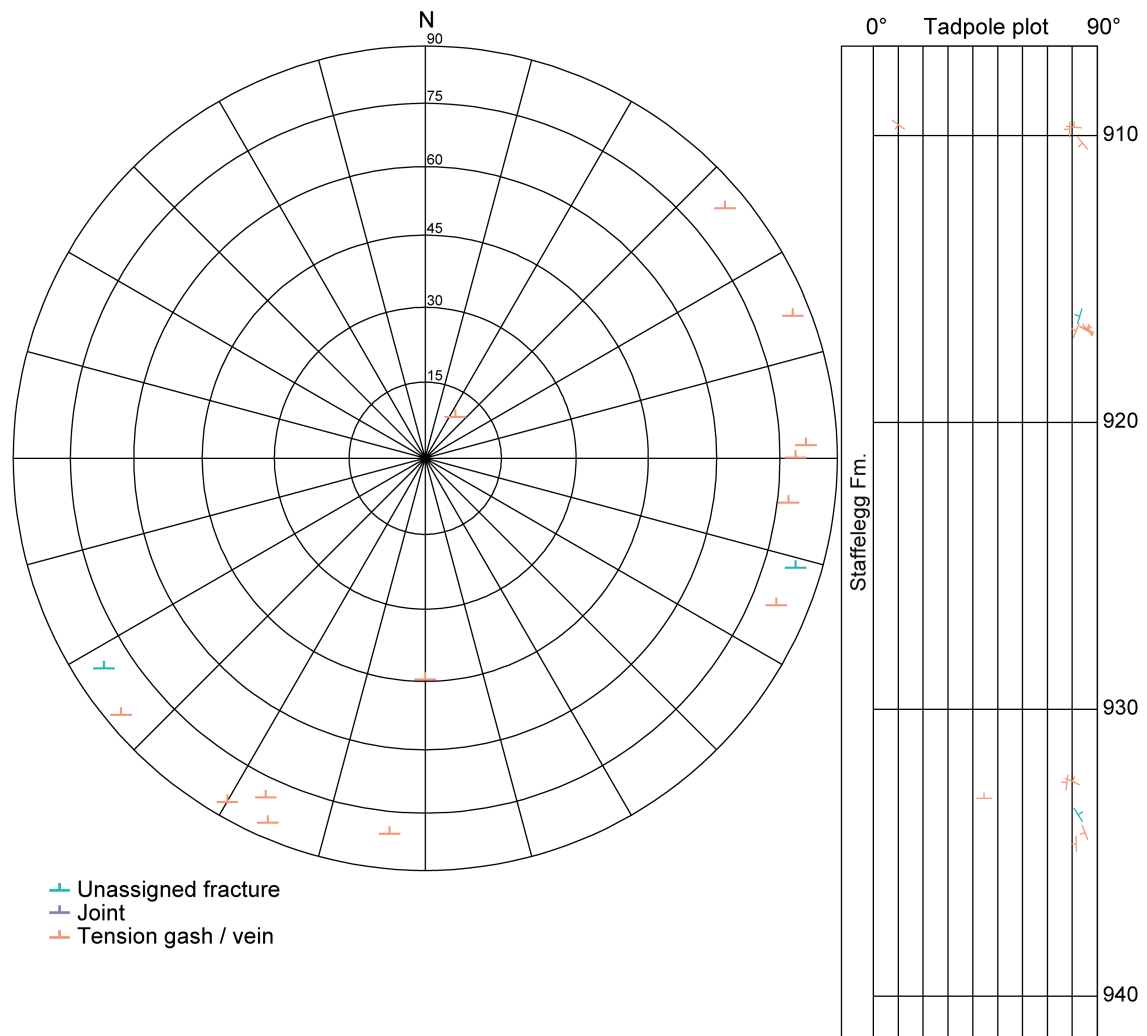


Fig. 4-59: Stereogram and depth plot of tension gashes / veins, joints and unassigned fractures (Lias)

Unassigned fractures (n = 2) and tension gashes / veins (n = 13); no joints were observed (n = 0).

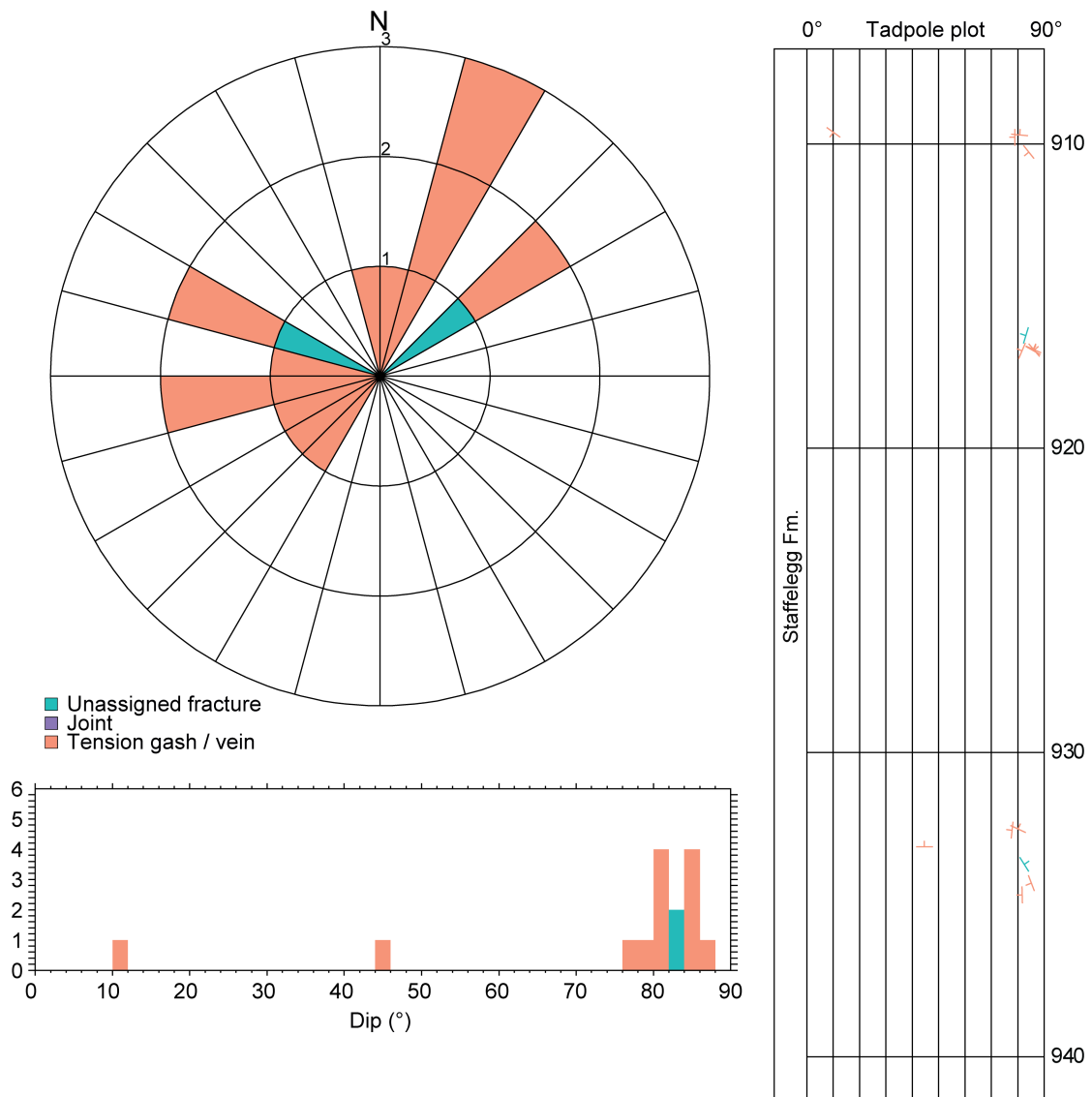


Fig. 4-60: Dip azimuth rose diagram, dip histogram and depth plot of tension gashes / veins, joints and unassigned fractures (Lias)

Unassigned fractures (n = 2) and tension gashes / veins (n = 13); no joints were observed (n = 0).

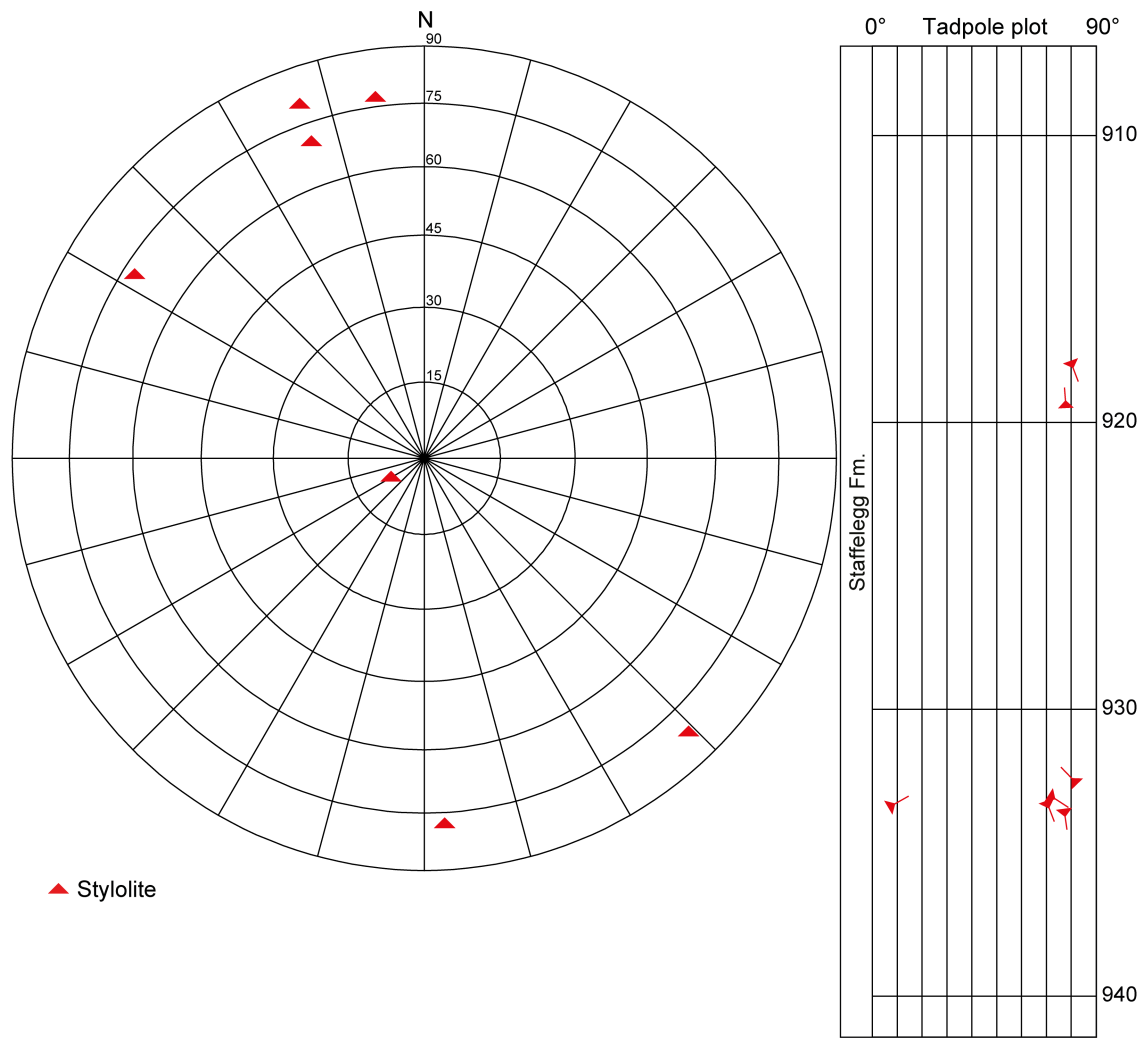


Fig. 4-61: Stereogram and depth plot of stylolites (Lias; n = 7)

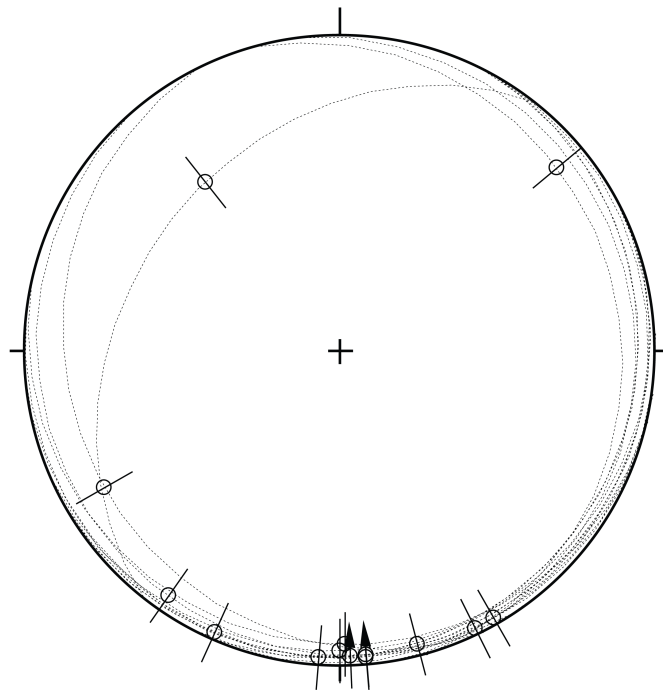


Fig. 4-62: Stereogram of striations on fault planes, including multiple lineations on a single fault plane (Lias; $n = 14$)

4.5 Keuper

The Keuper (941.42 m to 1'043.62 m MD log depth) reveals the highest average fracture density of 4.3 fractures per metre. Mirror-like fault planes and tension gashes / veins prevail. The latter are mainly found within the Bänkerjoch Formation and show random orientations. Only the data from oriented cores are presented.

4.5.1 Klettgau Formation

In the Klettgau Formation (941.42 m to 970.52 m MD log depth), mirror-like fault planes are the dominant fracture type (Figs. 4-63 to 4-66). They are scattered throughout the interval, show more or less random orientations and have mostly shallow to steep (10° to 50°) dip angles. The striations are randomly oriented. Shear sense indicators were generally not recognised. Tension gashes / veins and unassigned fractures are rare. Stylolitic fault planes, joints and stylolites were not observed.

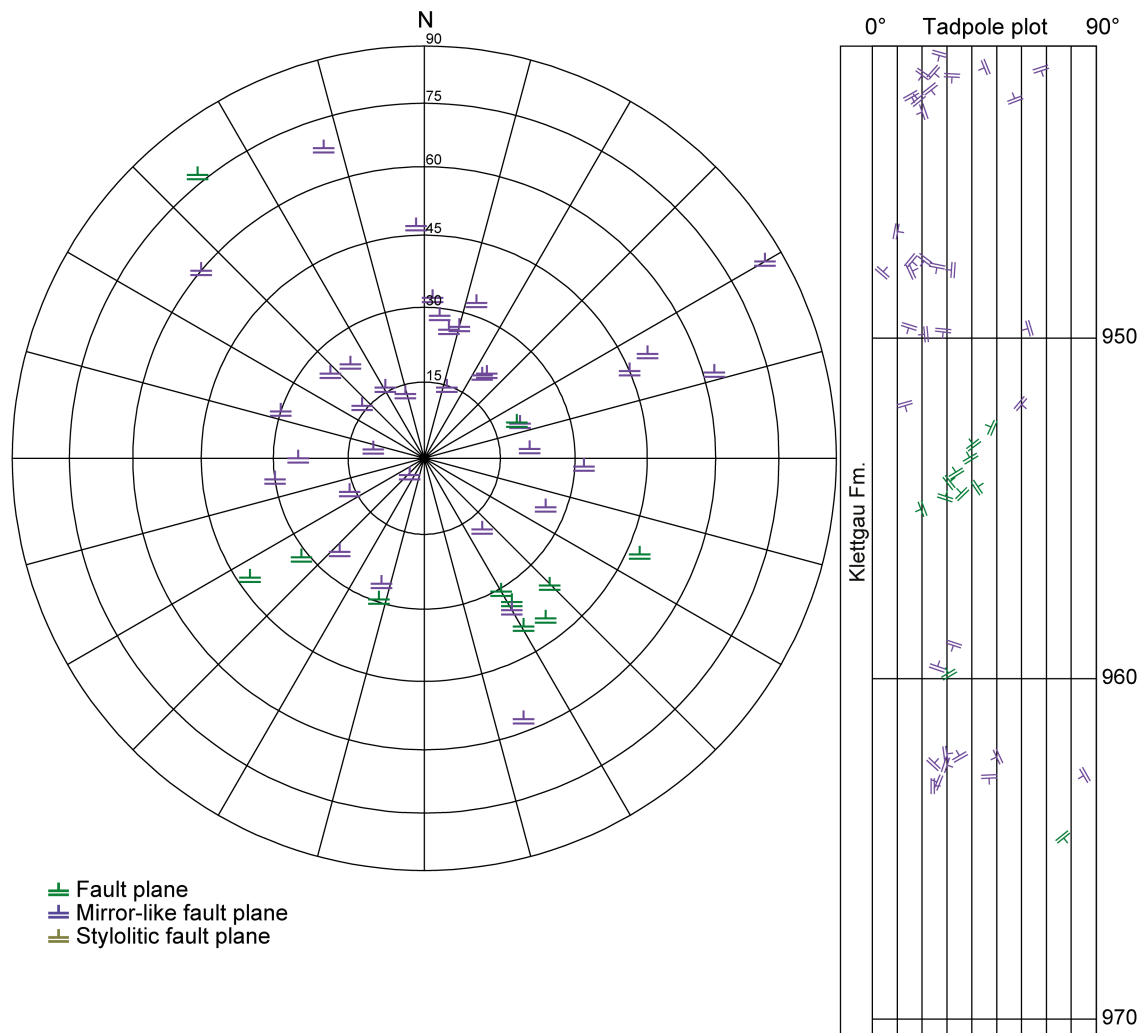


Fig. 4-63: Stereogram and depth plot of faults (Klettgau Formation)

Fault planes (n = 11) and mirror-like fault planes (n = 35); no stylolitic fault planes were observed (n = 0).

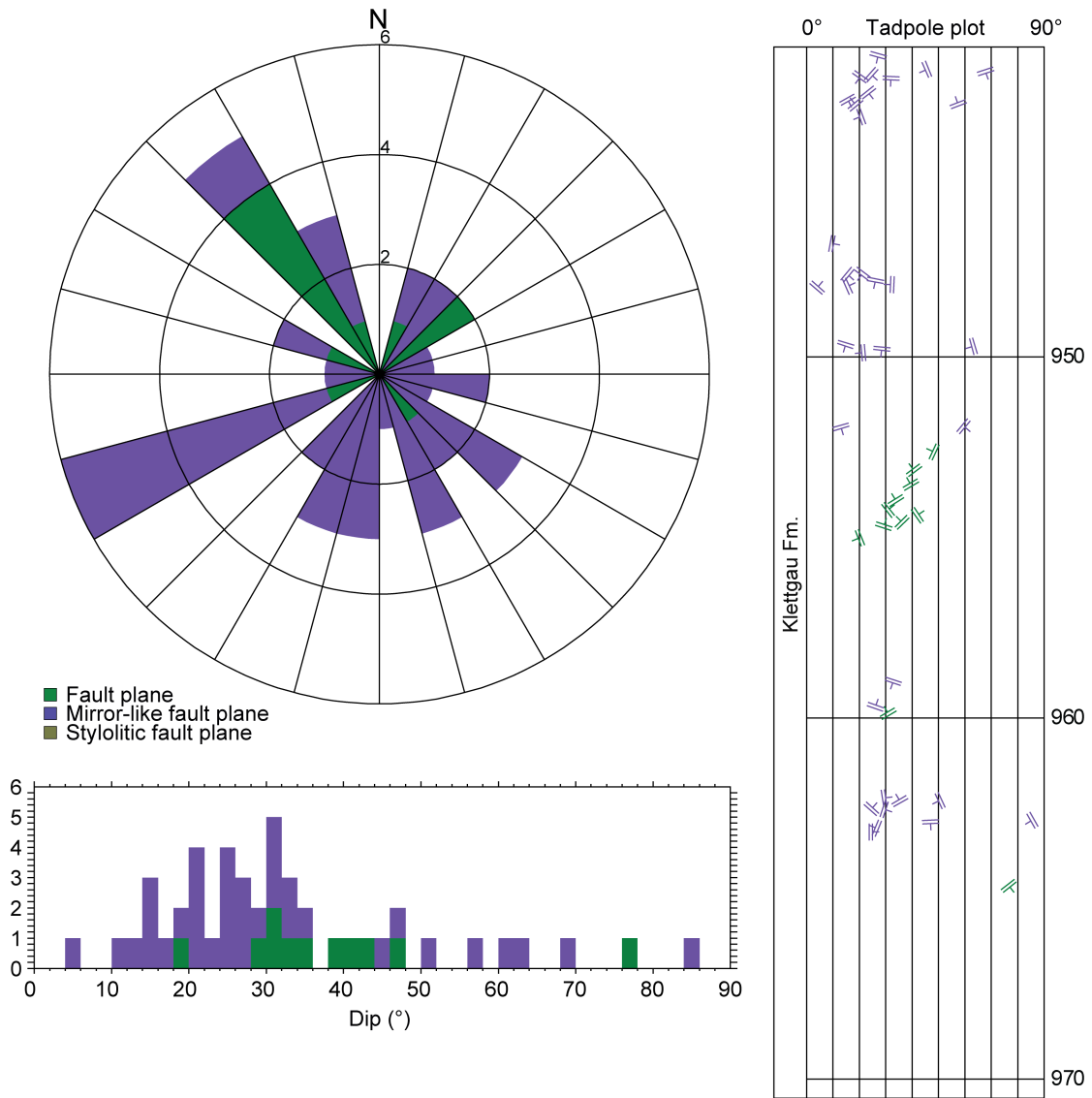


Fig. 4-64: Dip azimuth rose diagram, dip histogram and depth plot of faults (Klettgau Formation)

Fault planes (n = 11) and mirror-like fault planes (n = 35); no stylolitic fault planes were observed (n = 0).

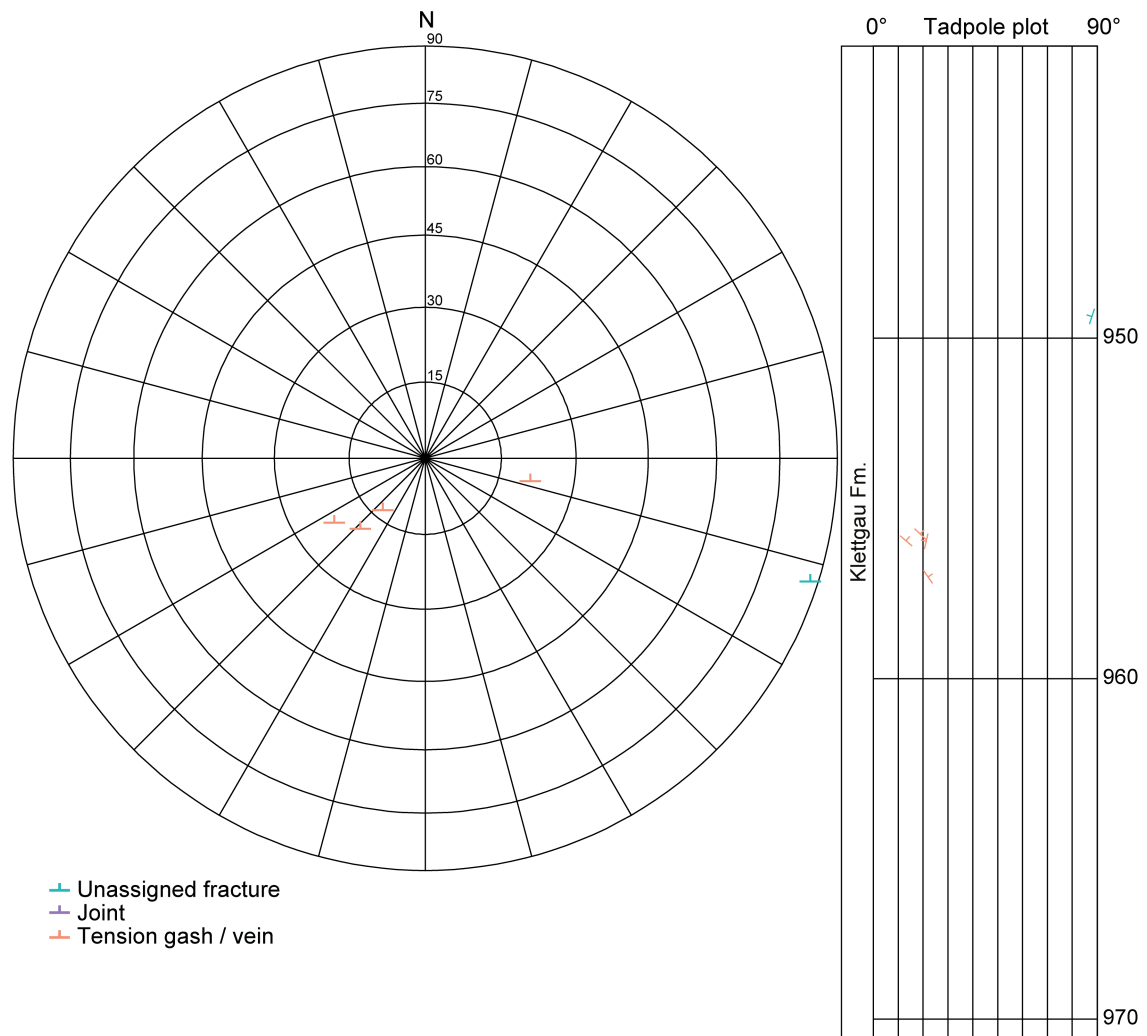


Fig. 4-65: Stereogram and depth plot of tension gashes / veins, joints and unassigned fractures (Klettgau Formation)

Unassigned fractures (n = 1) and tension gashes / veins (n = 4); no joints were observed (n = 0).

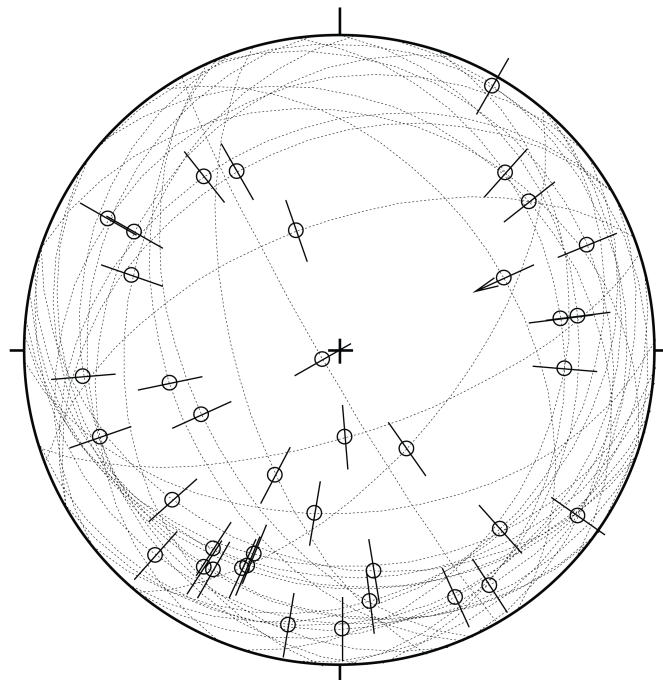


Fig. 4-66: Stereogram of striations on fault planes, including multiple lineations on a single fault plane (Klettgau Formation; $n = 39$)

4.5.2 Bänkerjoch Formation

The orientation and spatial distribution of recorded structures in the Bänkerjoch Formation (970.52 m to 1'043.62 m MD log depth) are shown in Figs. 4-67 to 4-72. Mirror-like fault planes and tension gashes / veins are abundant and evenly distributed above approximately 1'030.00 m MD (log depth). They are rather randomly oriented as well as the associated striations. Shear sense indicators were generally not recognised. Structure types other than the ones mentioned above are rare or absent within this borehole interval.

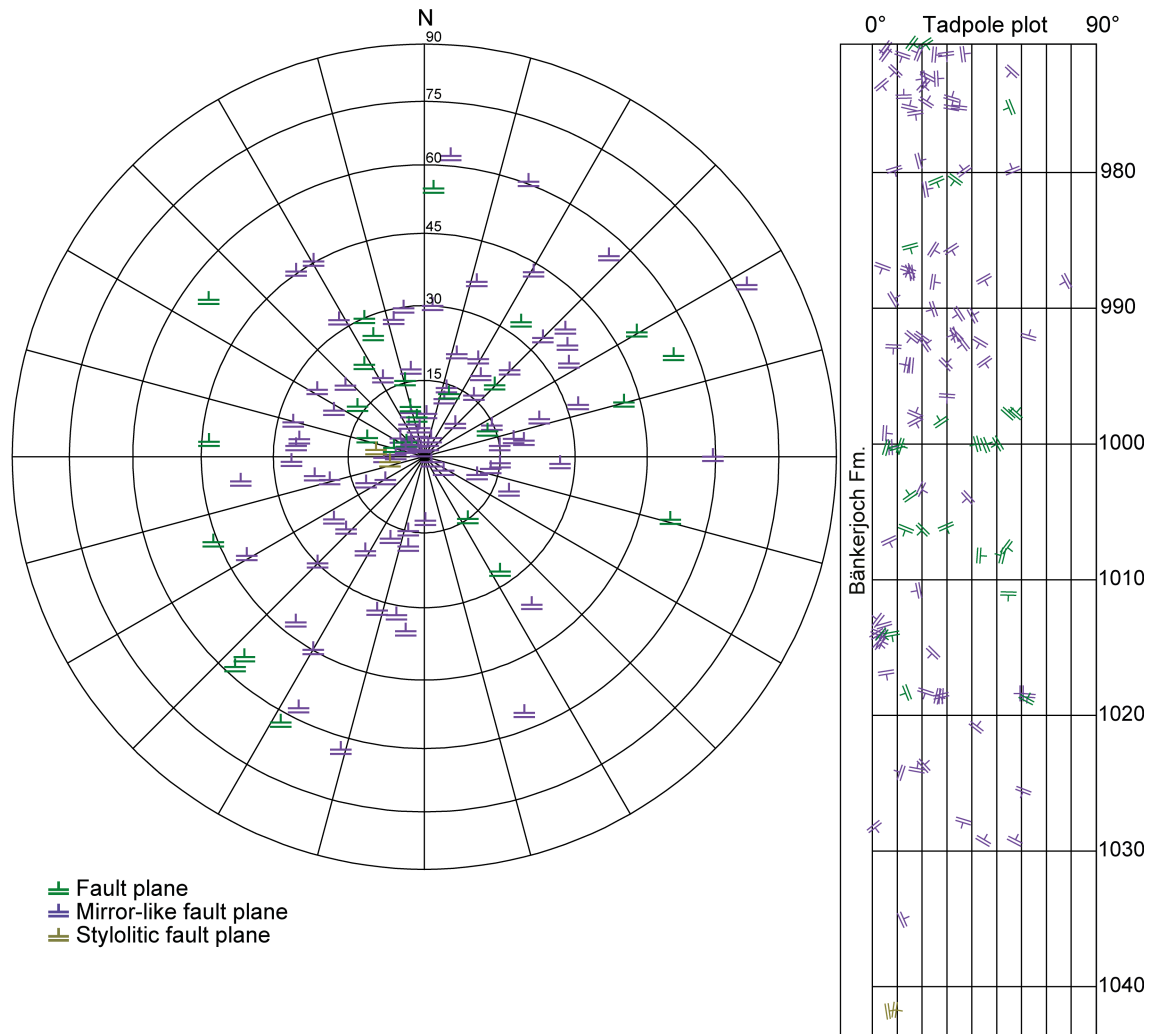


Fig. 4-67: Stereogram and depth plot of faults (Bänkerjoch Formation)

Fault planes (n = 27), mirror-like fault planes (n = 85) and stylolitic fault planes (n = 2).

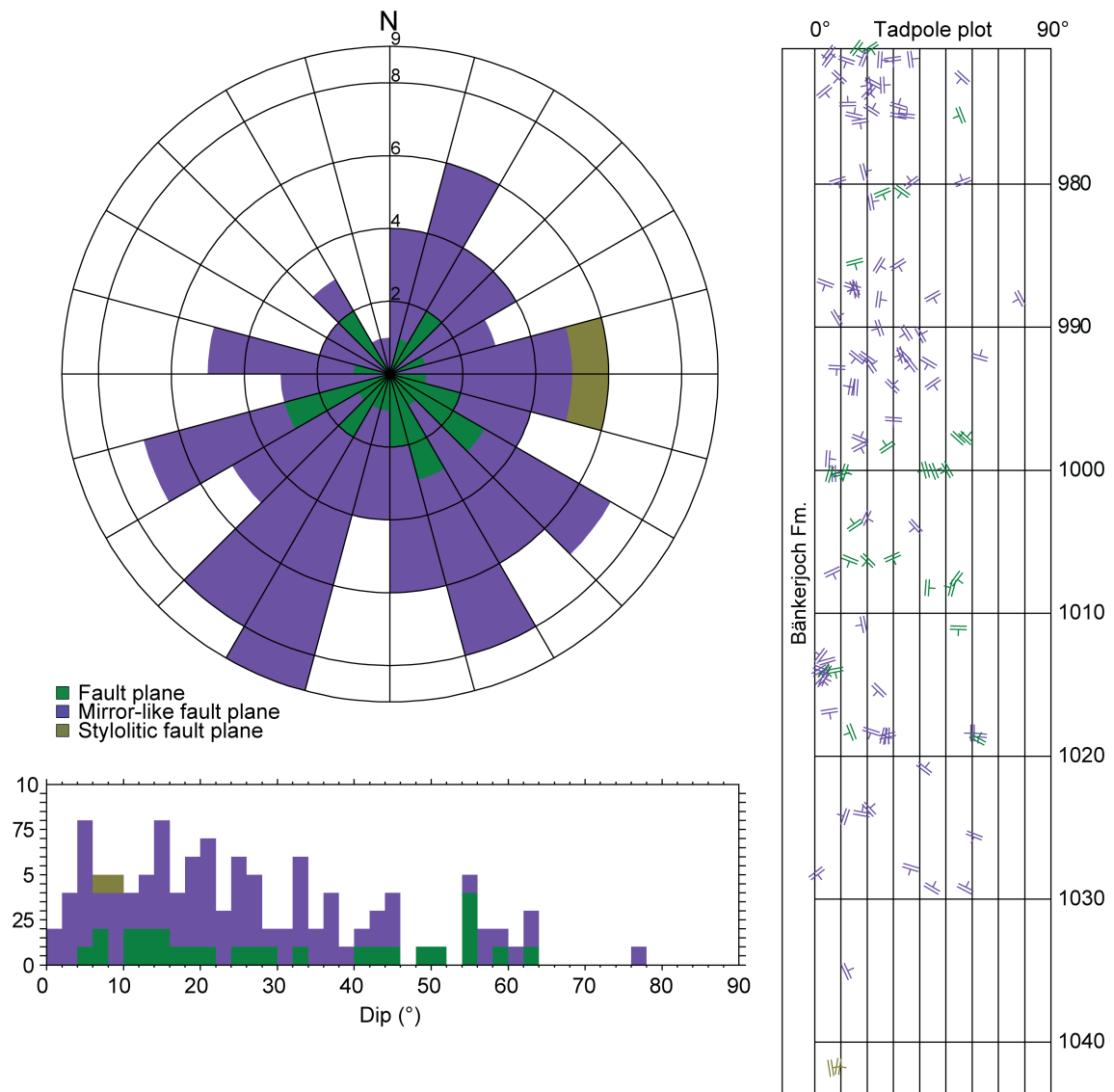


Fig. 4-68: Dip azimuth rose diagram, dip histogram and depth plot of faults (Bänkerjoch Formation)

Fault planes (n = 27), mirror-like fault planes (n = 85) and stylolitic fault planes (n = 2).

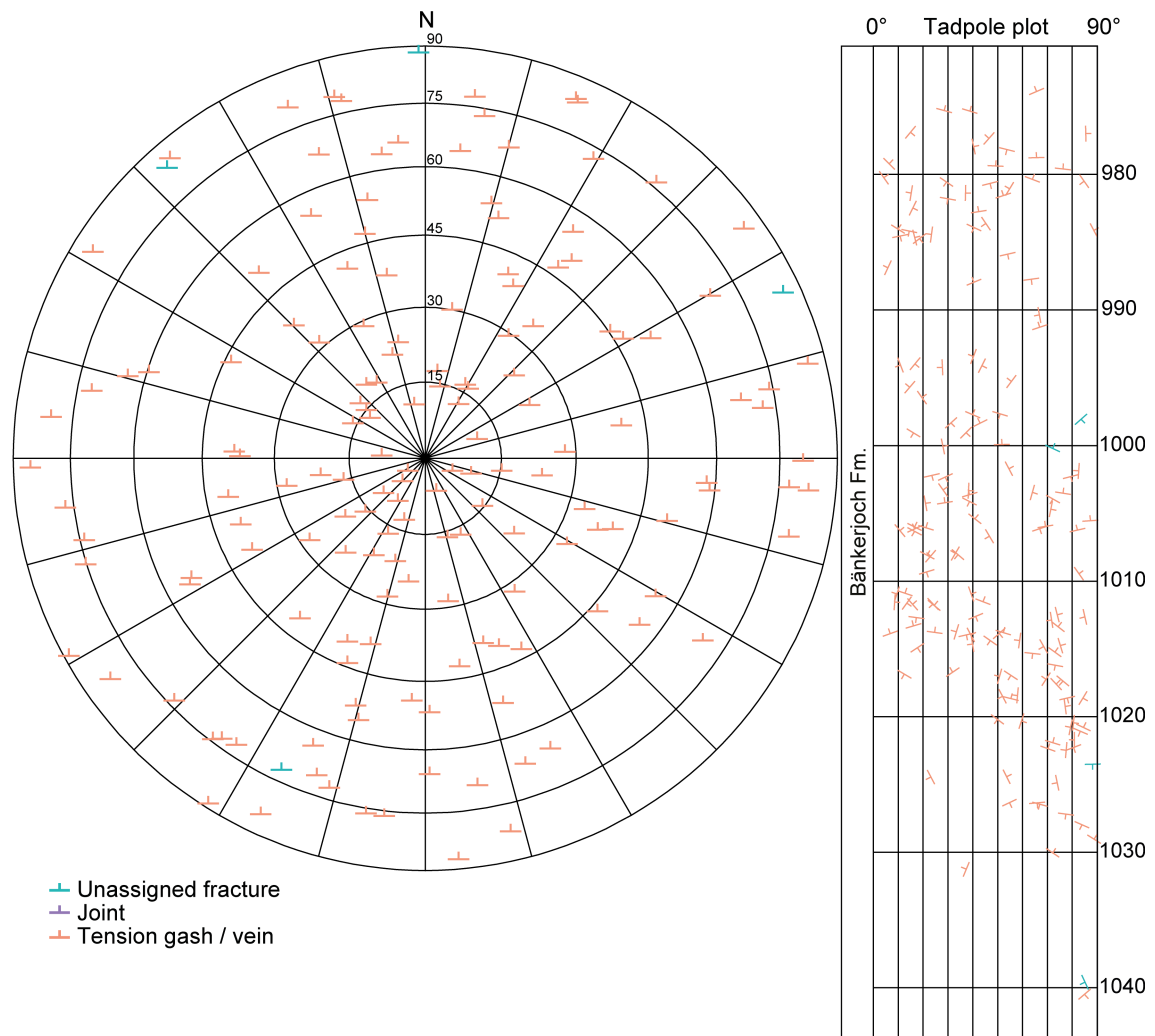


Fig. 4-69: Stereogram and depth plot of tension gashes / veins, joints and unassigned fractures (Bänkerjoch Formation)

Unassigned fractures (n = 4) and tension gashes / veins (n = 155); no joints were observed (n = 0).

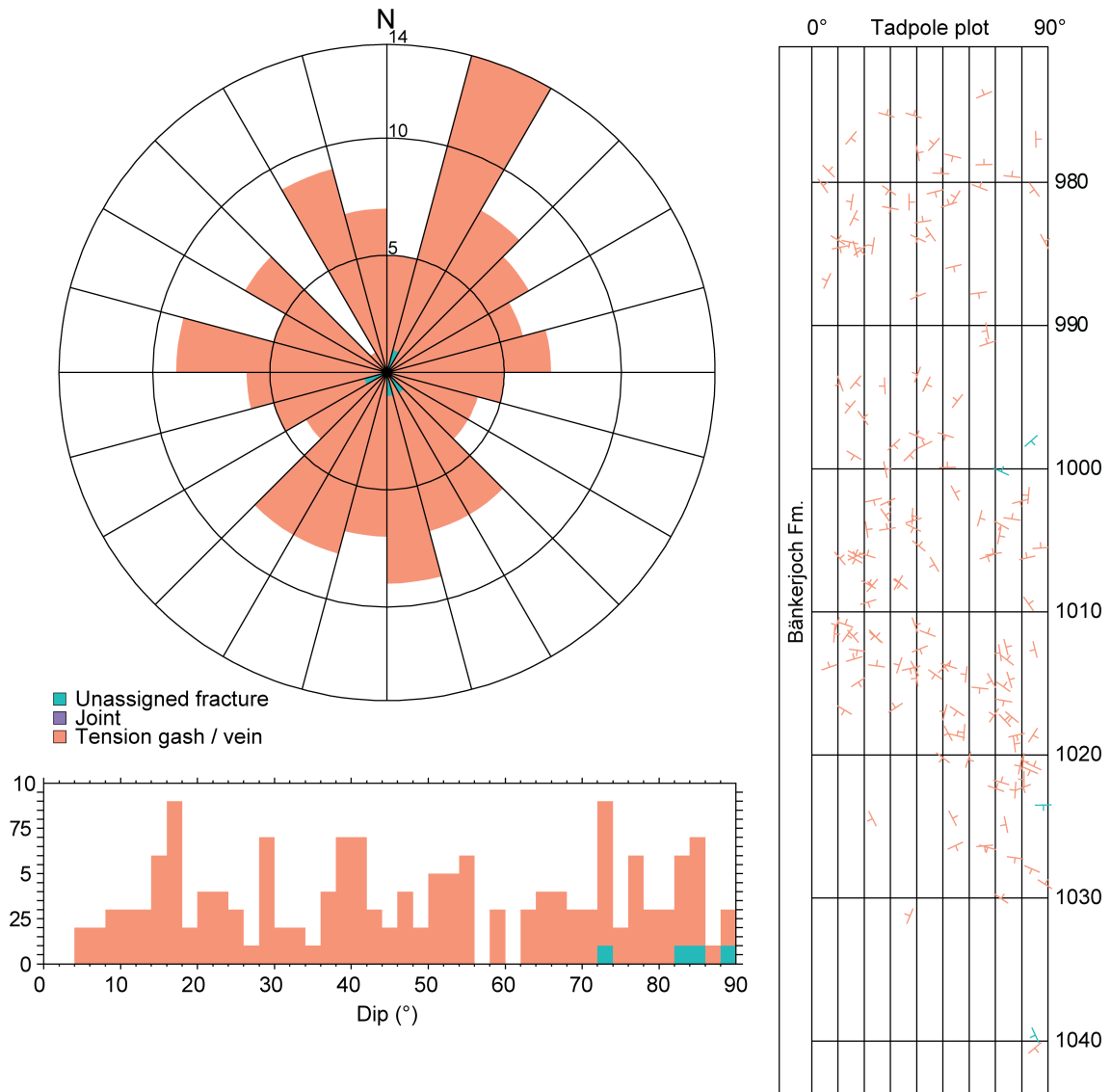


Fig. 4-70: Dip azimuth rose diagram, dip histogram and depth plot of tension gashes / veins, joints and unassigned fractures (Bänkerjoch Formation)

Unassigned fractures (n = 4) and tension gashes / veins (n = 155); no joints were observed (n = 0).

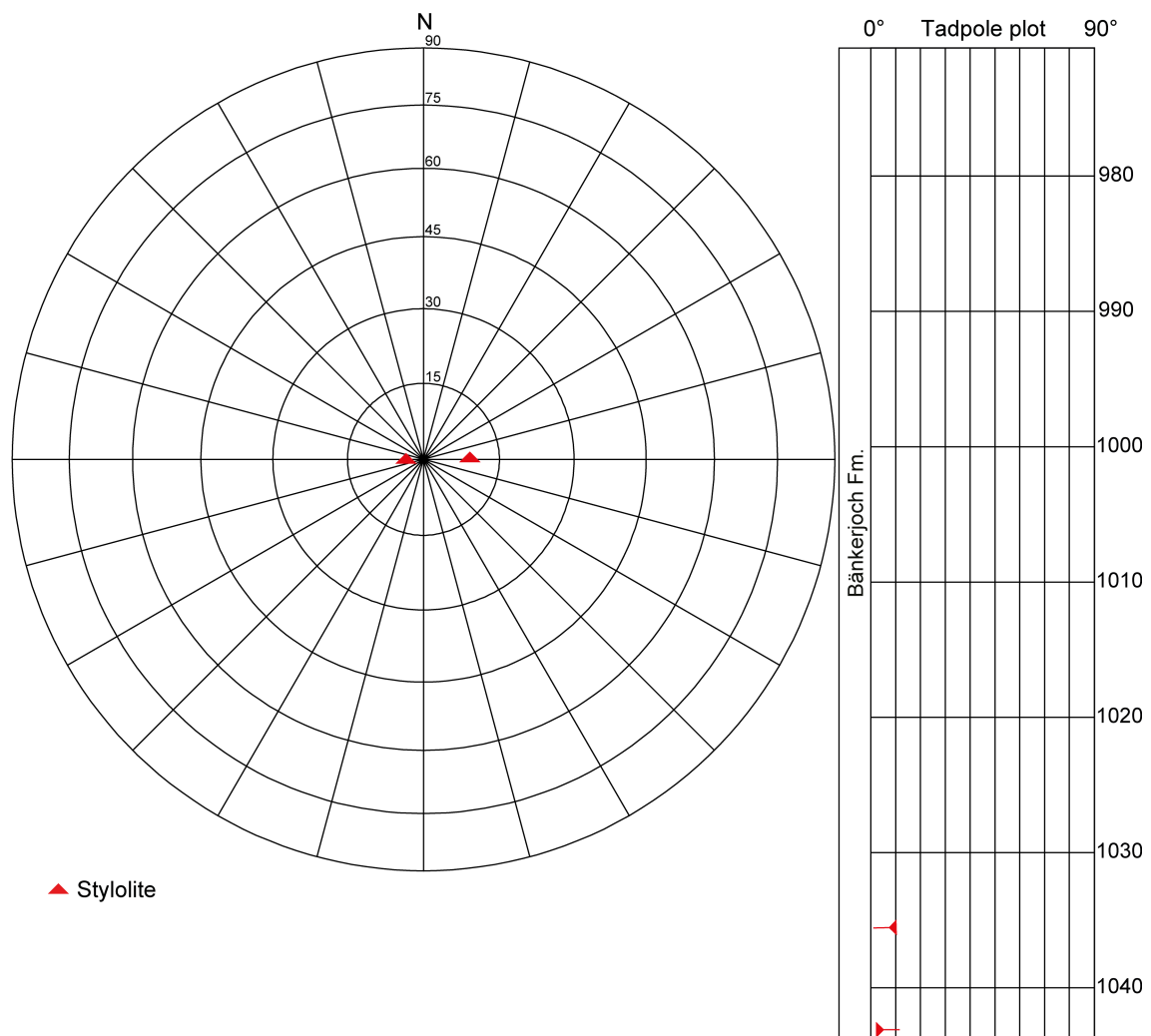


Fig. 4-71: Stereogram and depth plot of stylolites (Bänkerjoch Formation; n = 2)

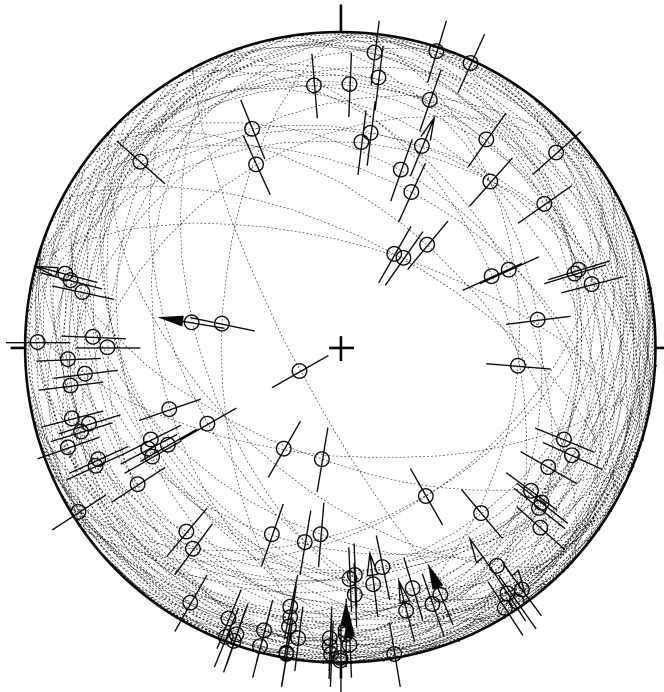


Fig. 4-72: Stereogram of striations on fault planes, including multiple lineations on a single fault plane (Bänkerjoch Formation; $n = 107$)

4.6 Muschelkalk

The Muschelkalk (1'043.62 m to 1'225.07 m MD log depth) shows a low to moderate density of fault planes and tension gashes /veins (1 structure per metre). A high density of stylolites is restricted to the Schinznach Formation. In addition, abundant mm- to cm-sized open pores (vugs) were observed. Only the data from oriented cores are presented.

4.6.1 Schinznach Formation

The orientation and spatial distribution of recorded structures in the Schinznach Formation (1'043.62 m to 1'116.69 m MD log depth) are shown in Figs. 4-73 to 4-78. The Schinznach Formation displays a high density of stylolites and a moderate density of unassigned fractures and joints. The latter occur within the Asp Member at approximately 1'045.00 m MD (log depth) and below approximately 1'080.00 m MD (log depth). In contrast, stylolites are evenly distributed throughout the formation. Joints, unassigned fractures and tension gashes / veins show a predominant subvertical dip directed towards the W. Most stylolites have shallow to subhorizontal dip angles and show a preferred dip direction towards the E to S. A few stylolites have a subvertical dip. Fault planes and tension gashes are rare.

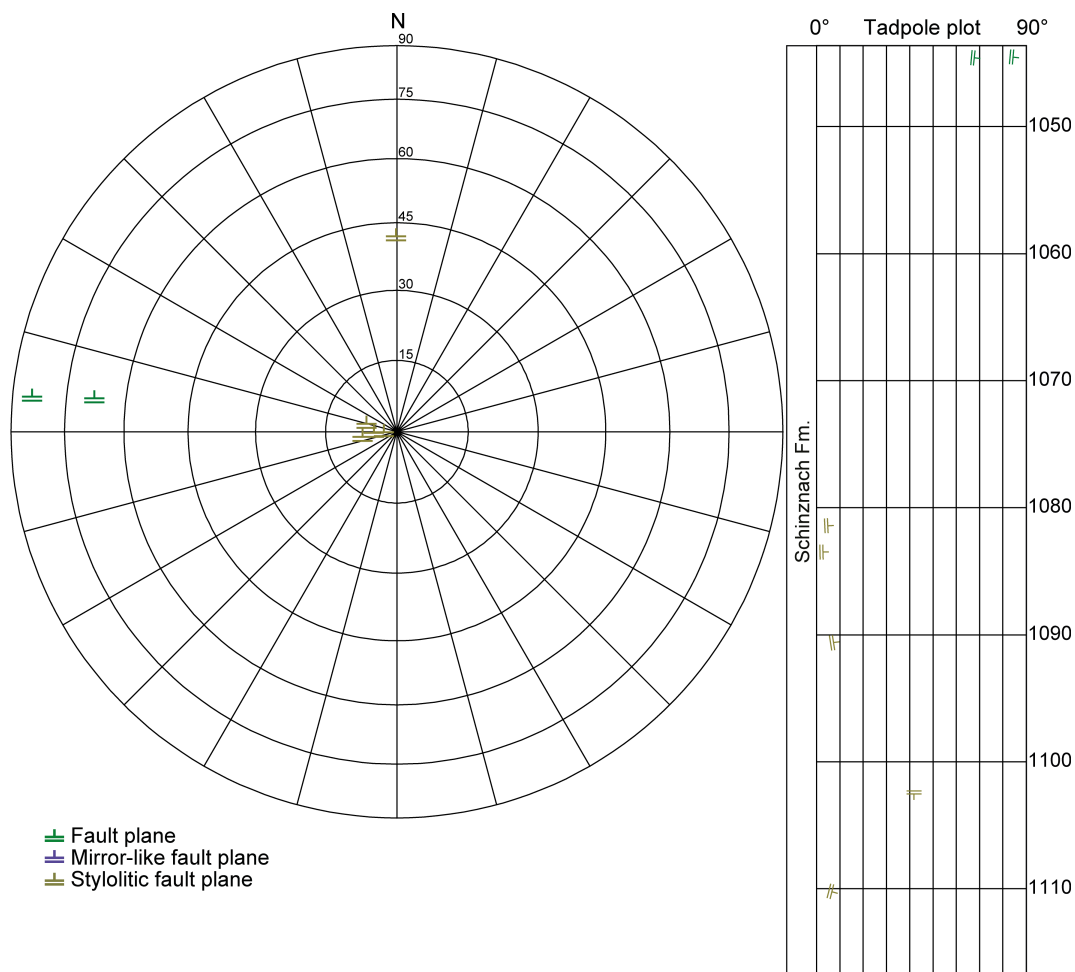


Fig. 4-73: Stereogram and depth plot of fault planes (Schinznach Formation)

Fault planes (n = 2) and stylolitic fault planes (n = 5); no mirror-like fault planes were observed (n = 0).

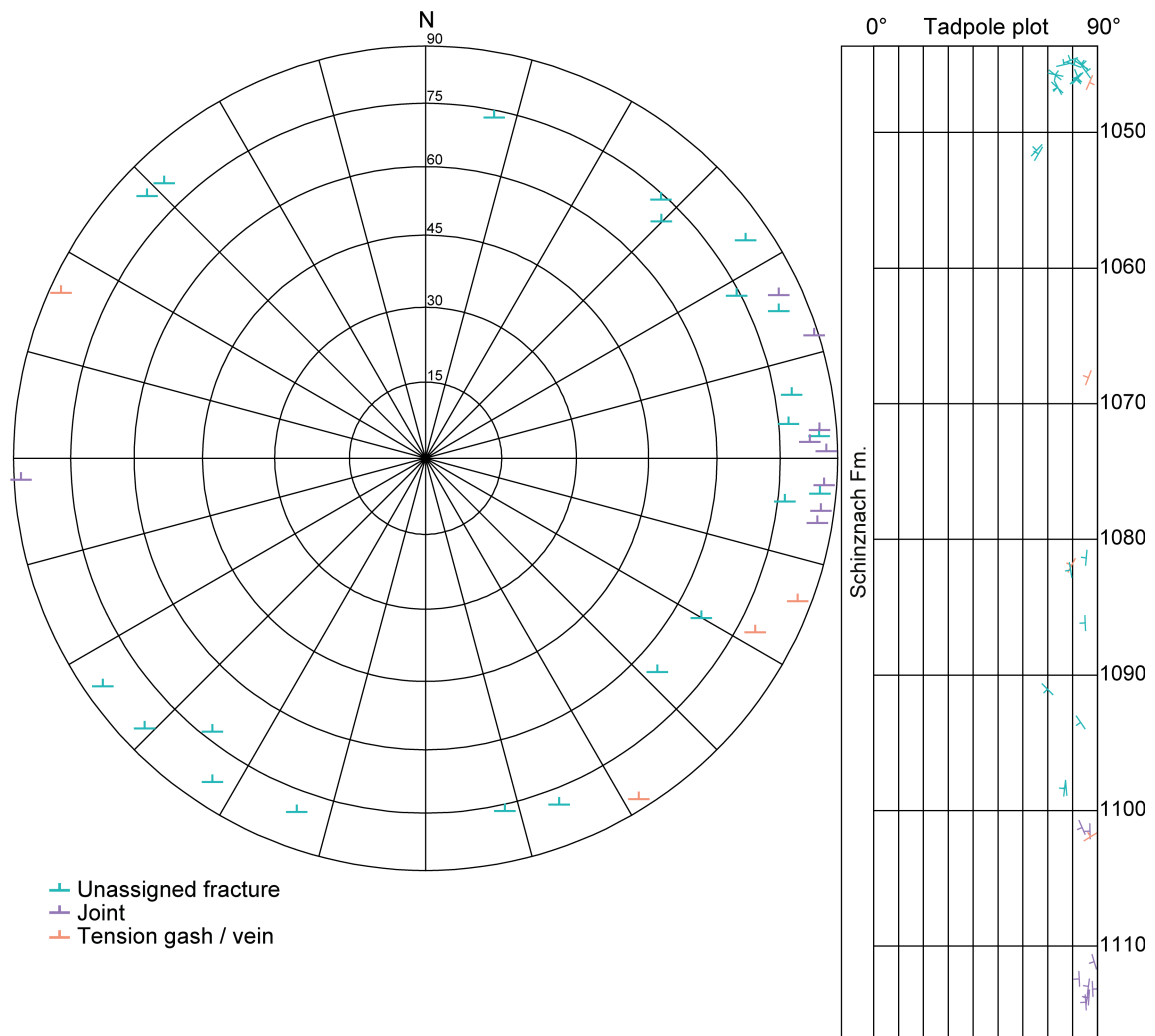


Fig. 4-74: Stereogram and depth plot of tension gashes / veins, joints and unassigned fractures (Schinznach Formation)

Unassigned fractures (n = 22), joints (n = 9) and tension gashes / veins (n = 4).

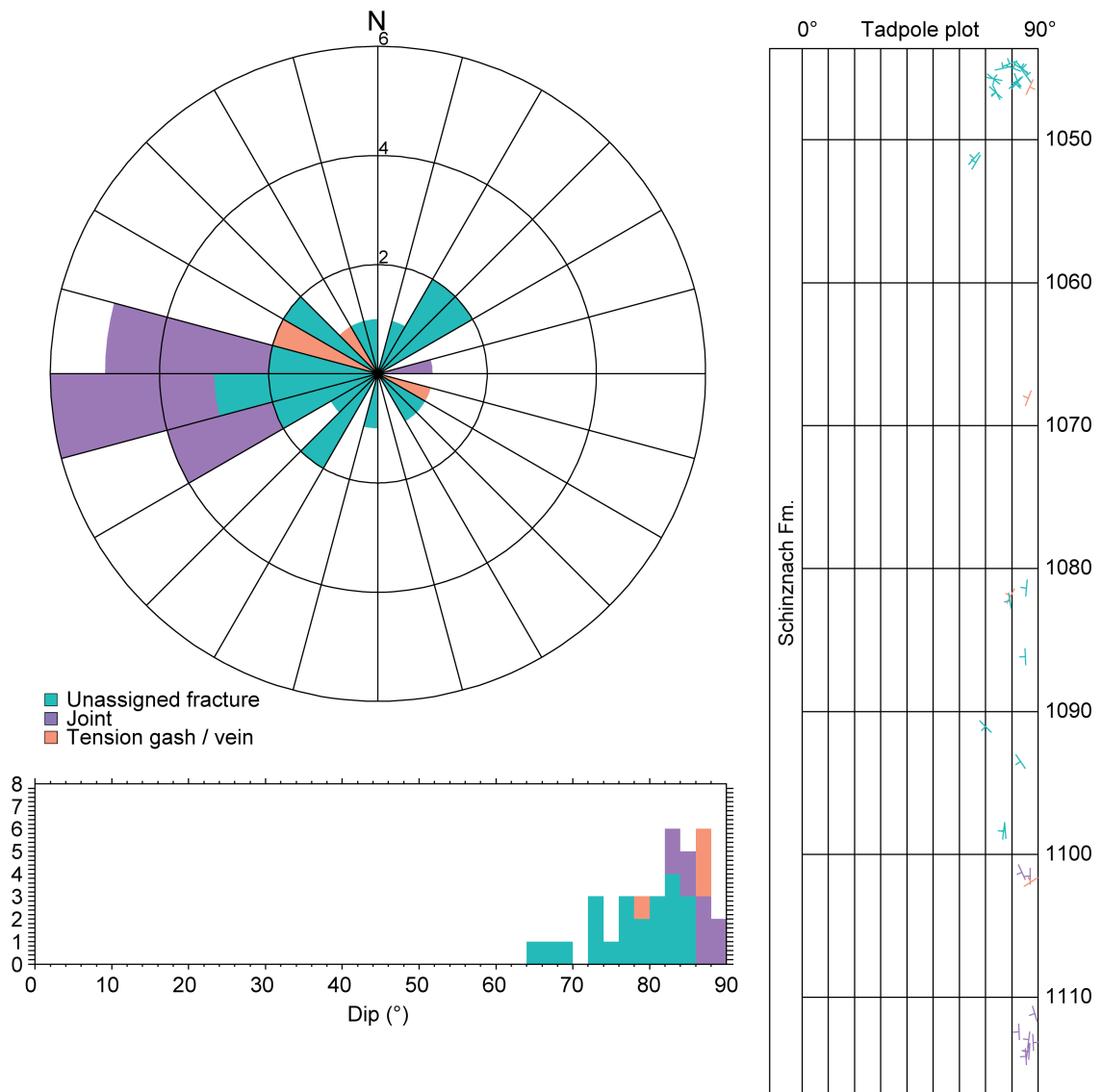


Fig. 4-75: Dip azimuth rose diagram, dip histogram and depth plot of tension gashes / veins, joints and unassigned fractures (Schinznach Formation)

Unassigned fractures (n = 22), joints (n = 9) and tension gashes / veins (n = 4).

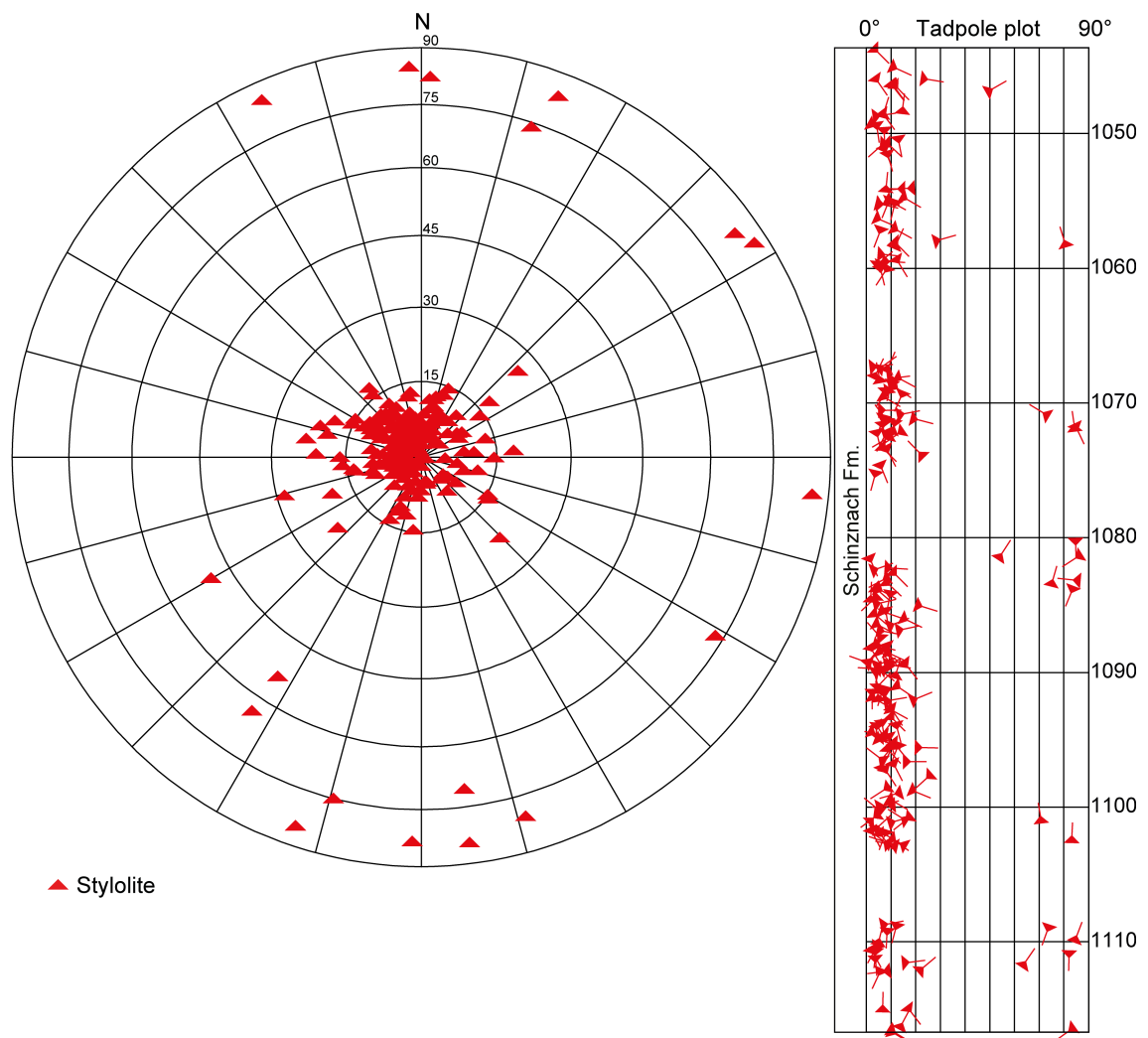


Fig. 4-76: Stereogram and depth plot of stylolites (Schinznach Formation; n = 200)

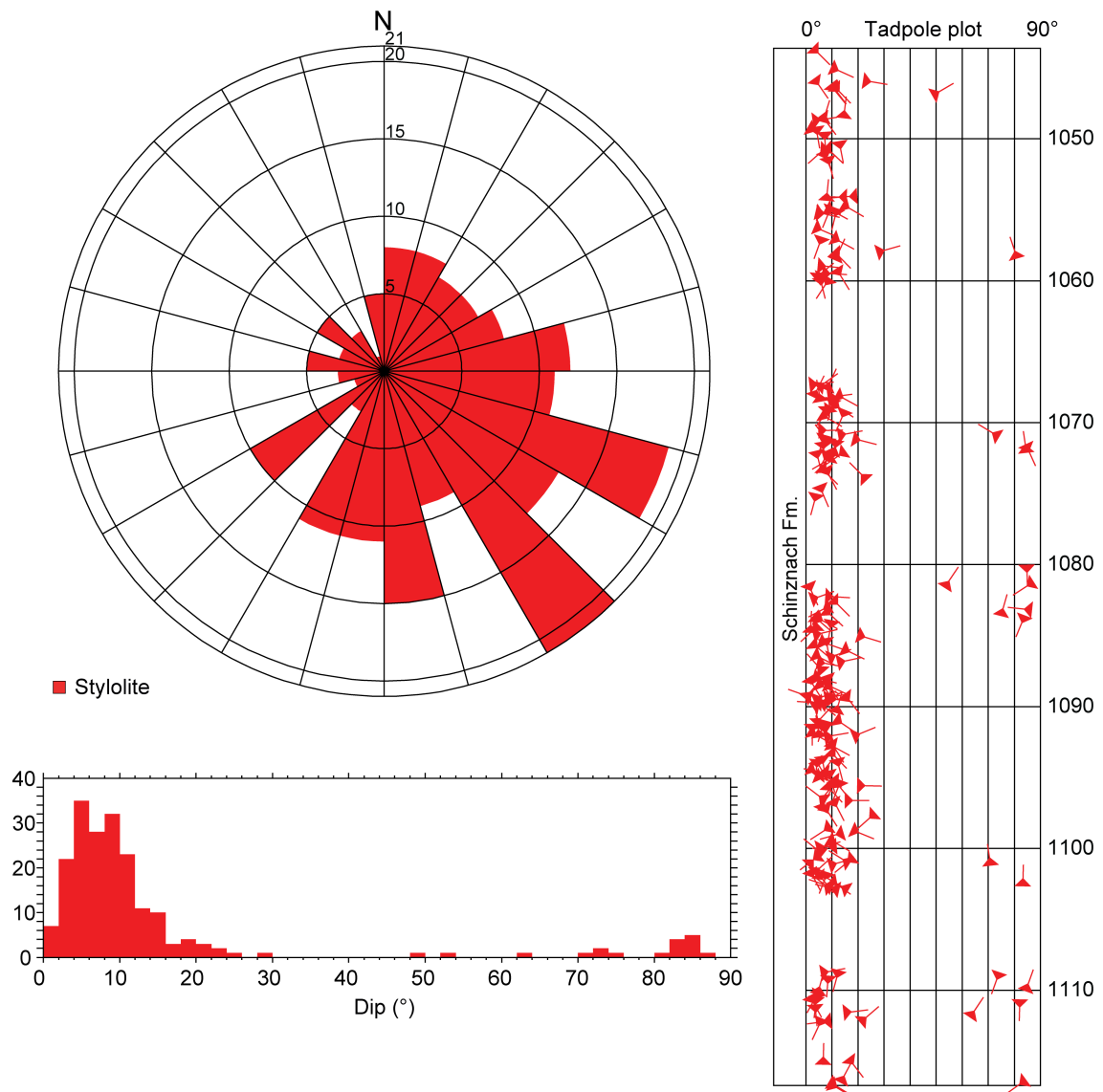


Fig. 4-77: Dip azimuth rose diagram, dip histogram and depth plot of stylolites (Schinznach Formation; n = 200)

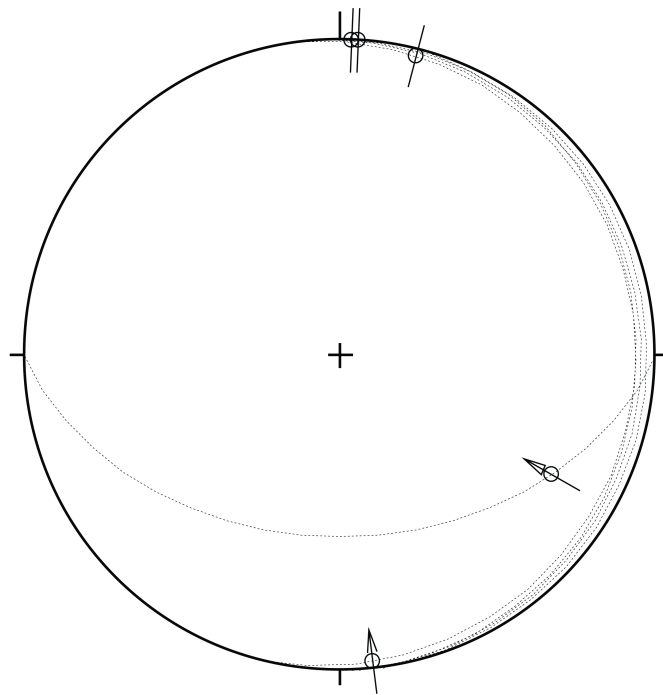


Fig. 4-78: Stereogram of striations on fault planes, including multiple lineations on a single fault plane (Schinznach Formation; $n = 5$)

4.6.2 Zeglingen Formation

The orientation and spatial depth distribution of the recorded structures in the Zeglingen Formation (1'116.69 m to 1'185.42 m MD log depth) are shown in Figs. 4-79 to 4-85. This formation shows a moderate density of fault planes and tension gashes / veins. The structures are distributed throughout the formation and show a slight preference of E to S dip azimuths. The plunge azimuth of the striations is random. The shear sense indicators show no clear dominance of either reverse or normal faulting. Stylolites, unassigned fractures, joints and stylolitic fault planes are rare. The deformation in the salt layers is described in Chapter 6.

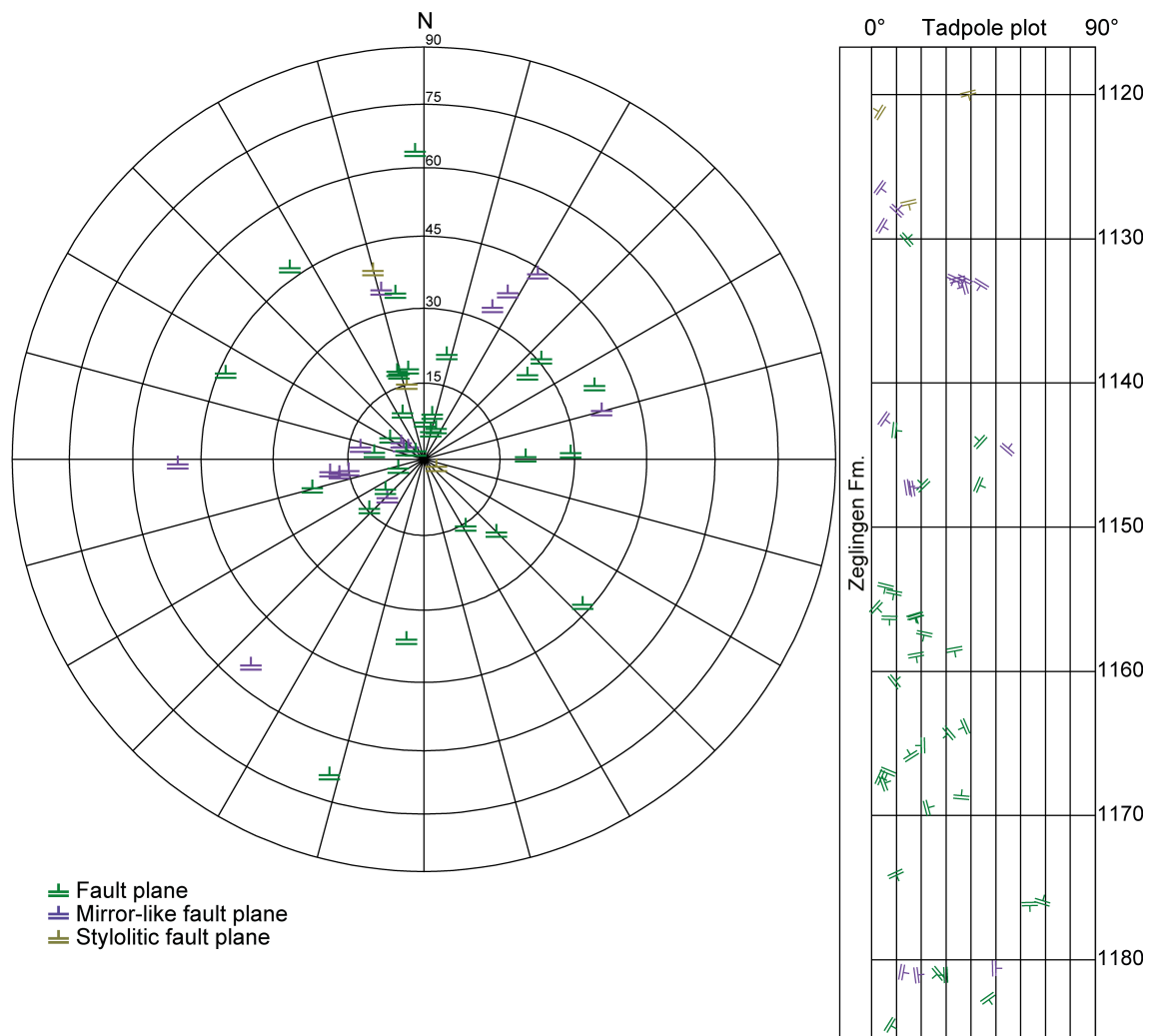


Fig. 4-79: Stereogram and depth plot of fault planes (Zeglingen Formation)

Fault planes / shear bands (n = 31), mirror-like fault planes (n = 15) and stylolitic fault planes (n = 3).

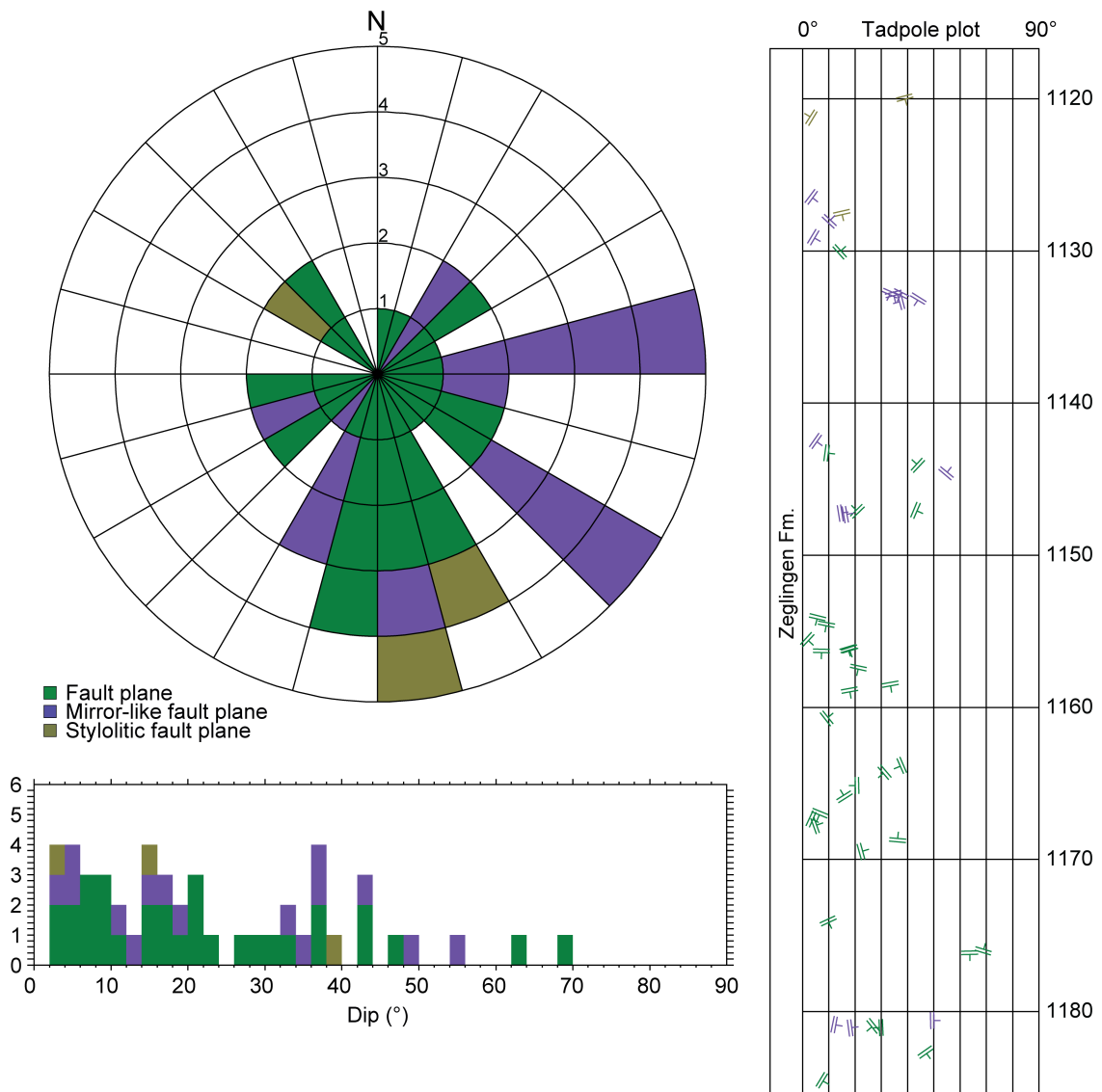


Fig. 4-80: Dip azimuth rose diagram, dip histogram and depth plot of fault planes (Zeglingen Formation)

Fault planes / shear bands (n = 31), mirror-like fault planes (n = 15) and stylolitic fault planes (n = 3).

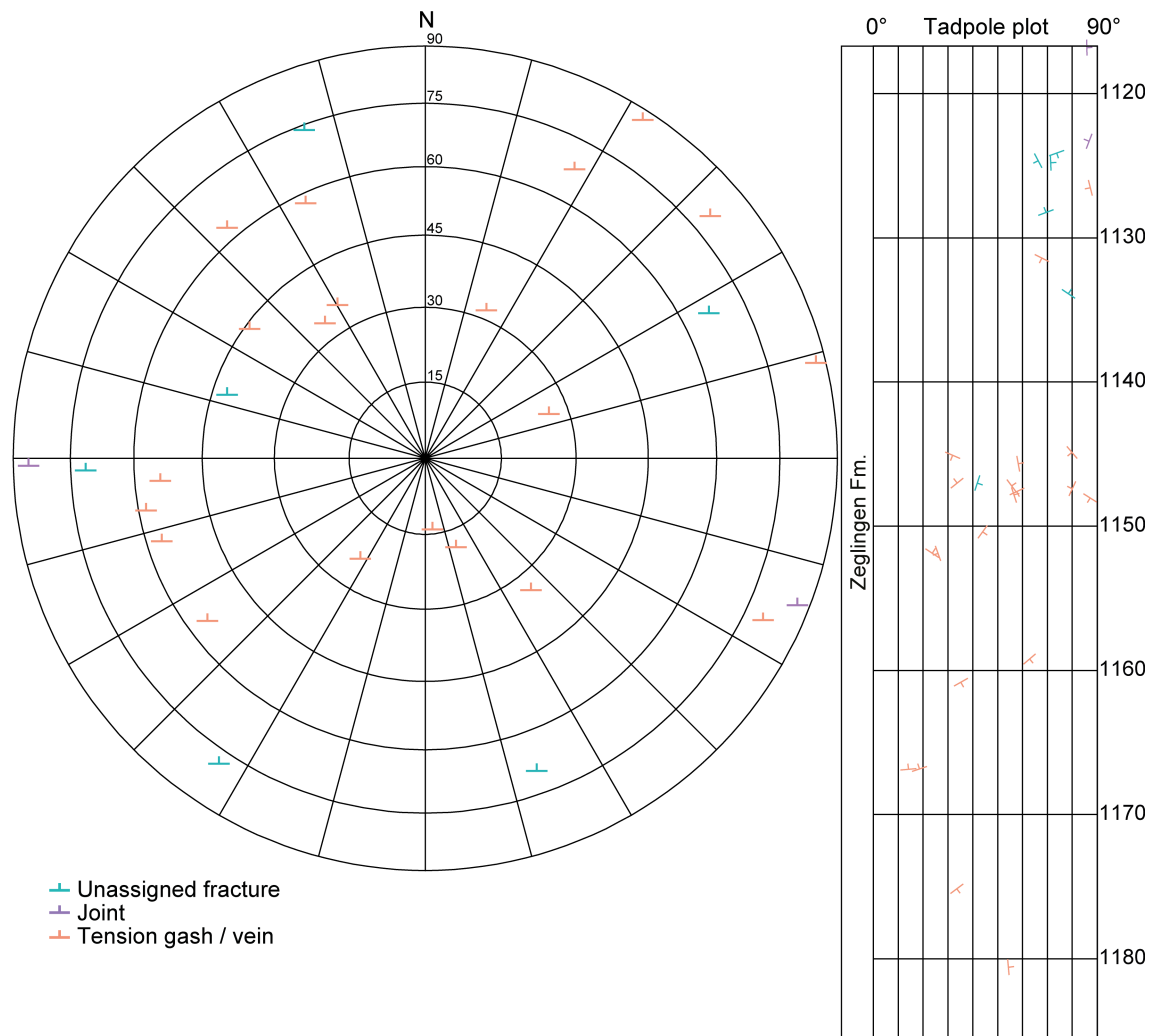


Fig. 4-81: Stereogram and depth plot of tension gashes / veins, joints and unassigned fractures (Zeglingen Formation)

Unassigned fractures (n = 6), joints (n = 2) and tension gashes / veins (n = 20).

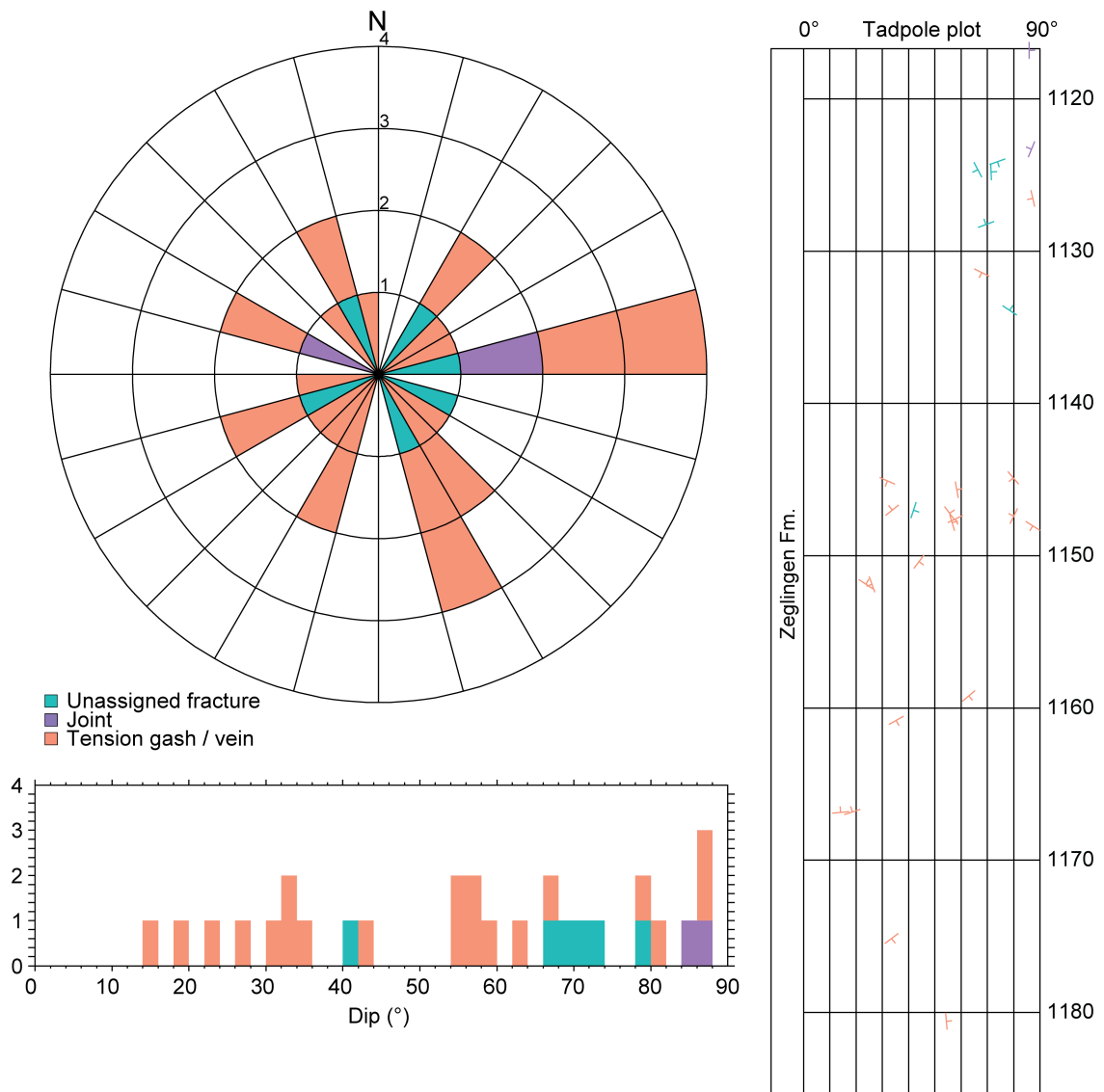


Fig. 4-82: Dip azimuth rose diagram, dip histogram and depth plot of tension gashes / veins, joints and unassigned fractures (Zeglingen Formation)

Unassigned fractures (n = 6), joints (n = 2) and tension gashes / veins (n = 20).

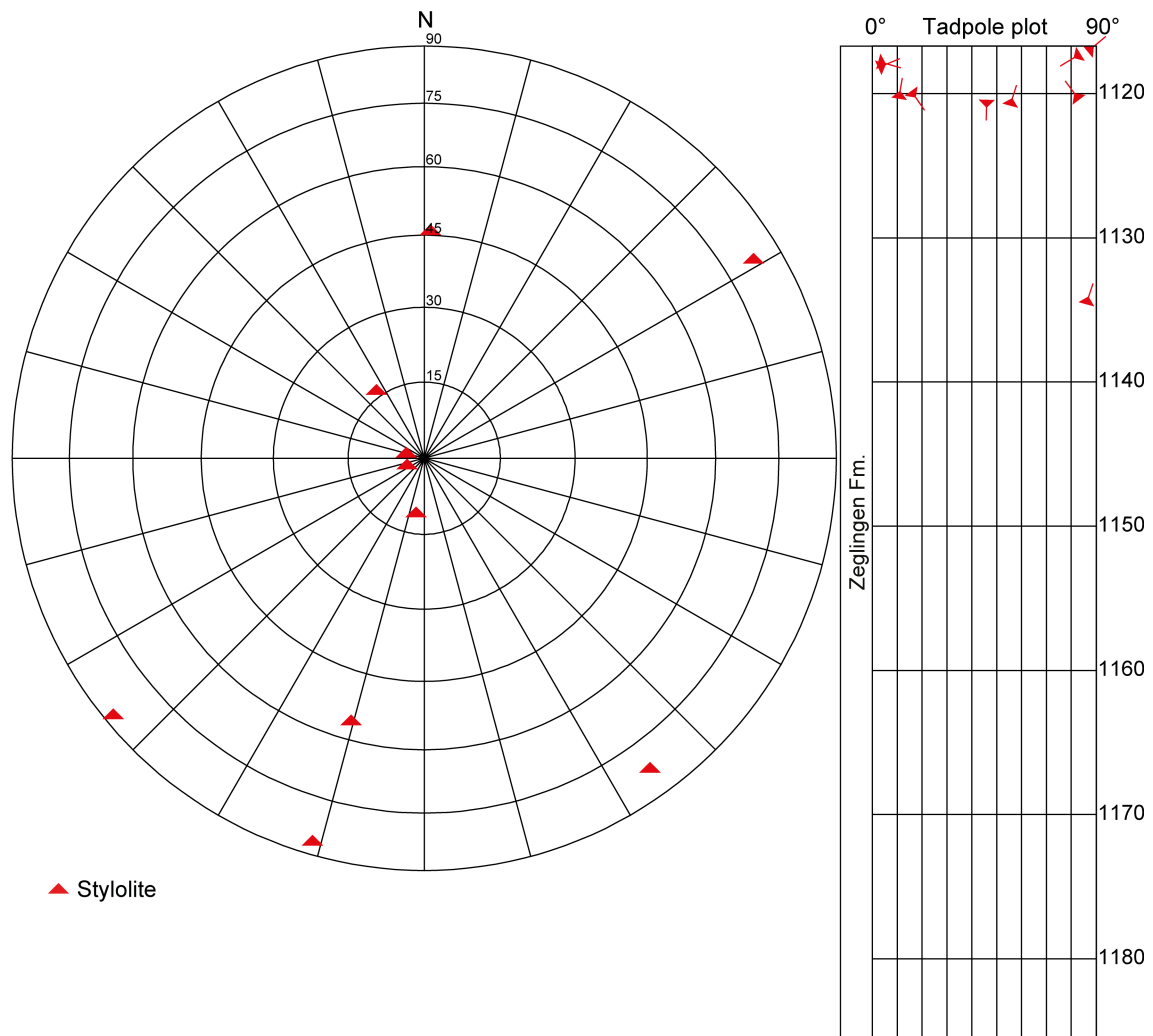


Fig. 4-83: Stereogram and depth plot of stylolites (Zeglingen Formation; n = 10)

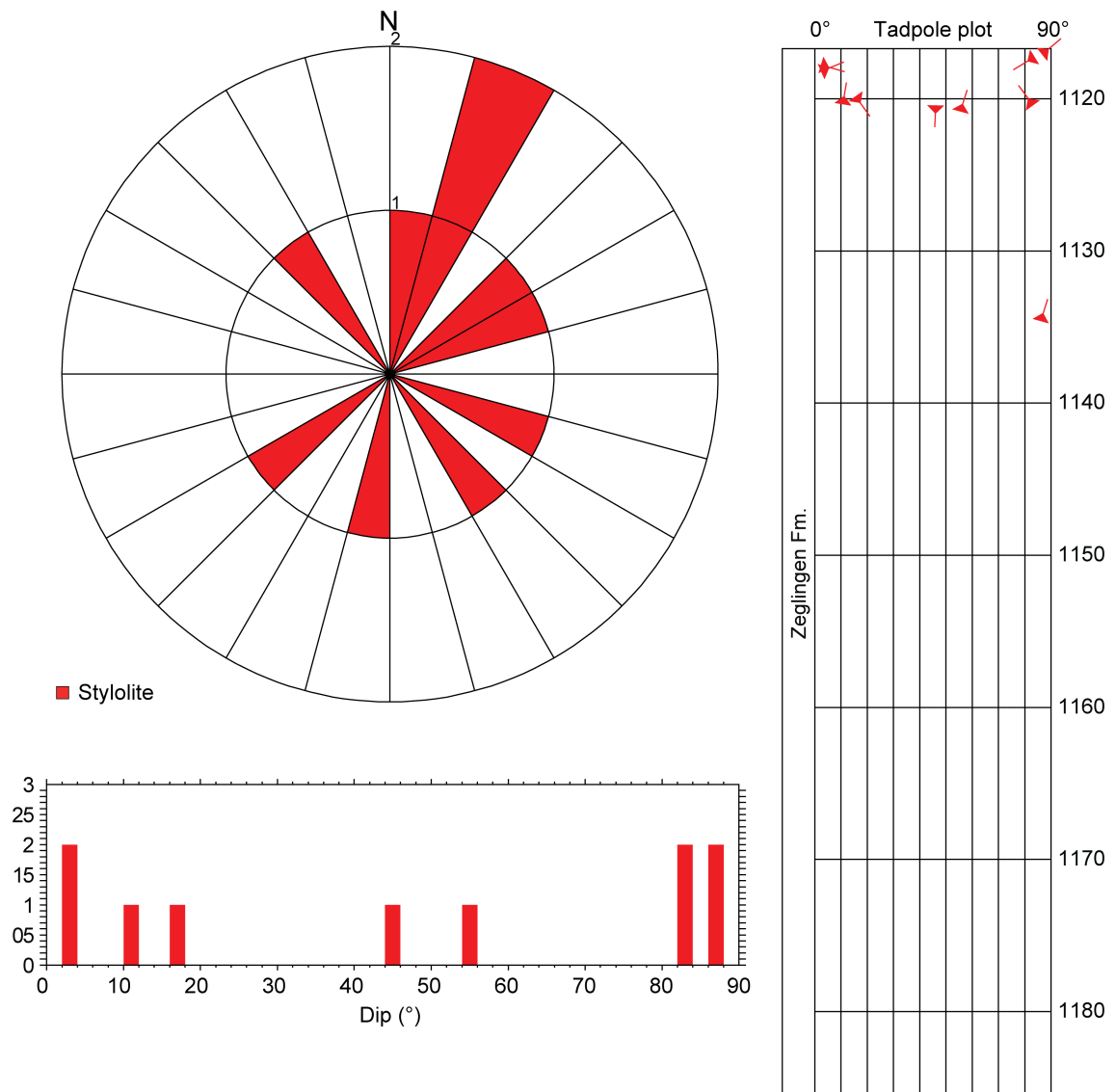


Fig. 4-84: Dip azimuth rose diagram, dip histogram and depth plot of stylolites (Zeglingen Formation; n = 10)

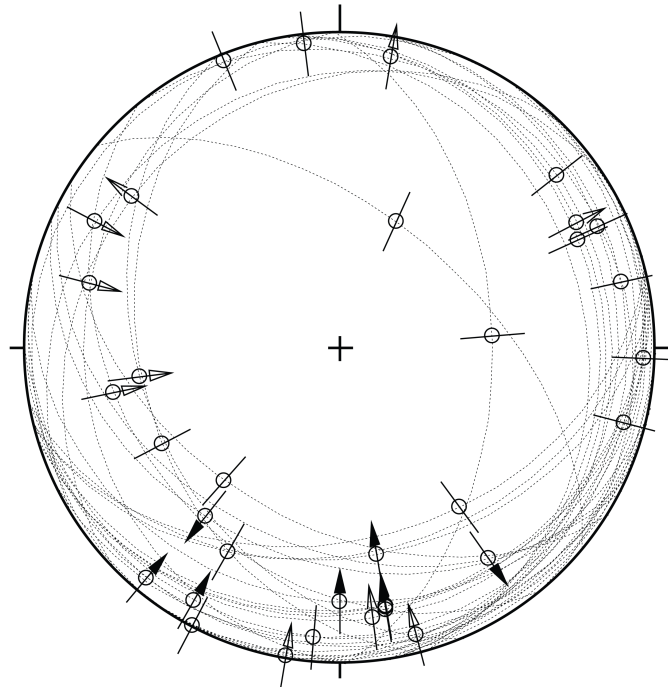


Fig. 4-85: Stereogram of striations on fault planes, including multiple lineations on a single fault plane (Zeglingen Formation; n = 35)

4.6.3 Kaiseraugst Formation

The orientation and spatial depth distribution of recorded structures in the Kaiseraugst Formation (1'185.42 m to 1'225.07 m MD log depth) are shown in Figs. 4-86 to 4-90. The overall density of structures is low. The dominant structures are mirror-like fault planes, which dip gently mainly towards the SE. The plunge azimuths of the striations have a slight preferential orientation towards the south. Shear senses could generally not be defined. All other structure types are rare or absent.

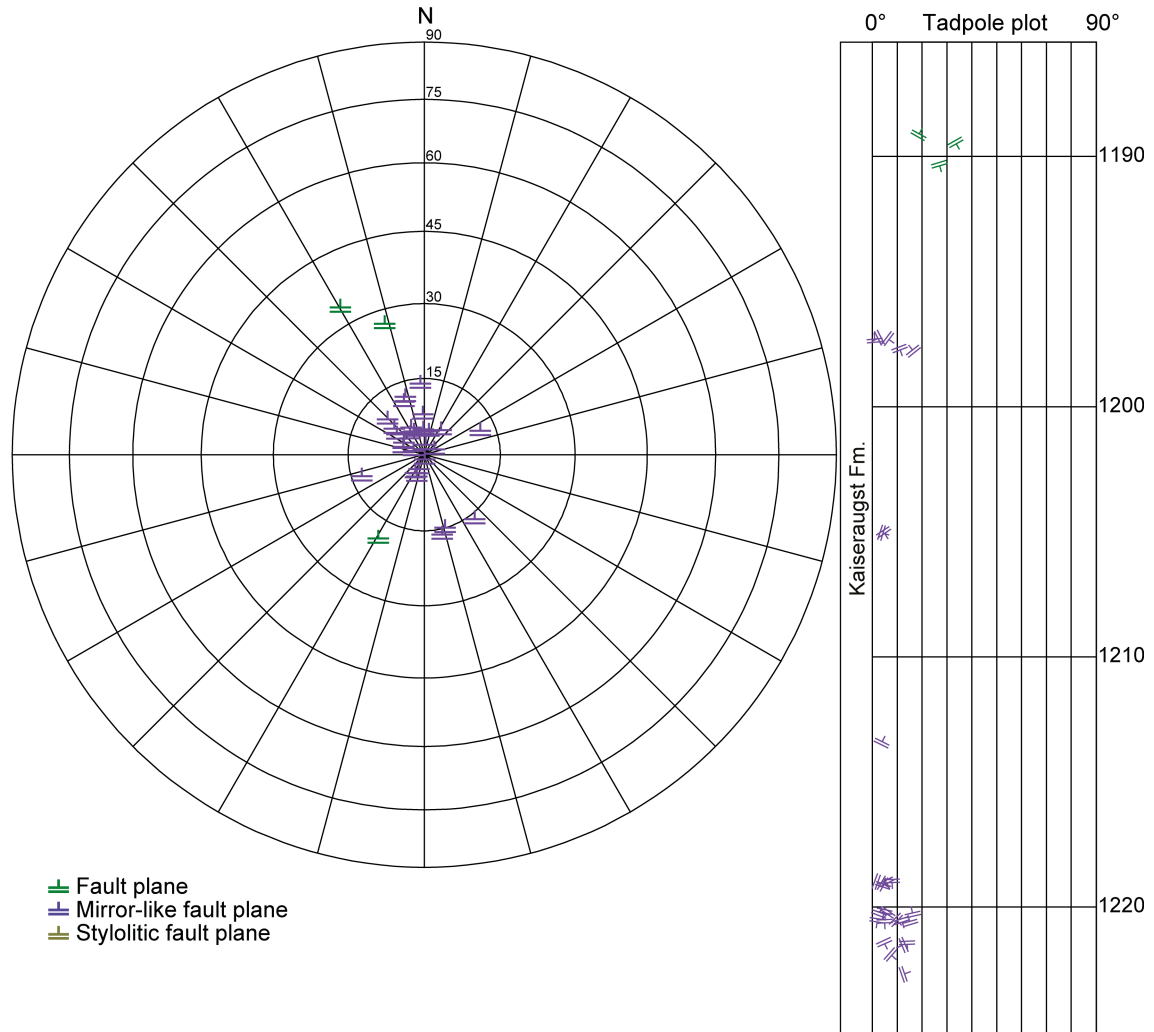


Fig. 4-86: Stereogram and depth plot of fault planes (Kaiseraugst Formation)

Fault planes (n = 3) and mirror-like fault planes (n = 27); no stylolitic fault planes were observed (n = 0).

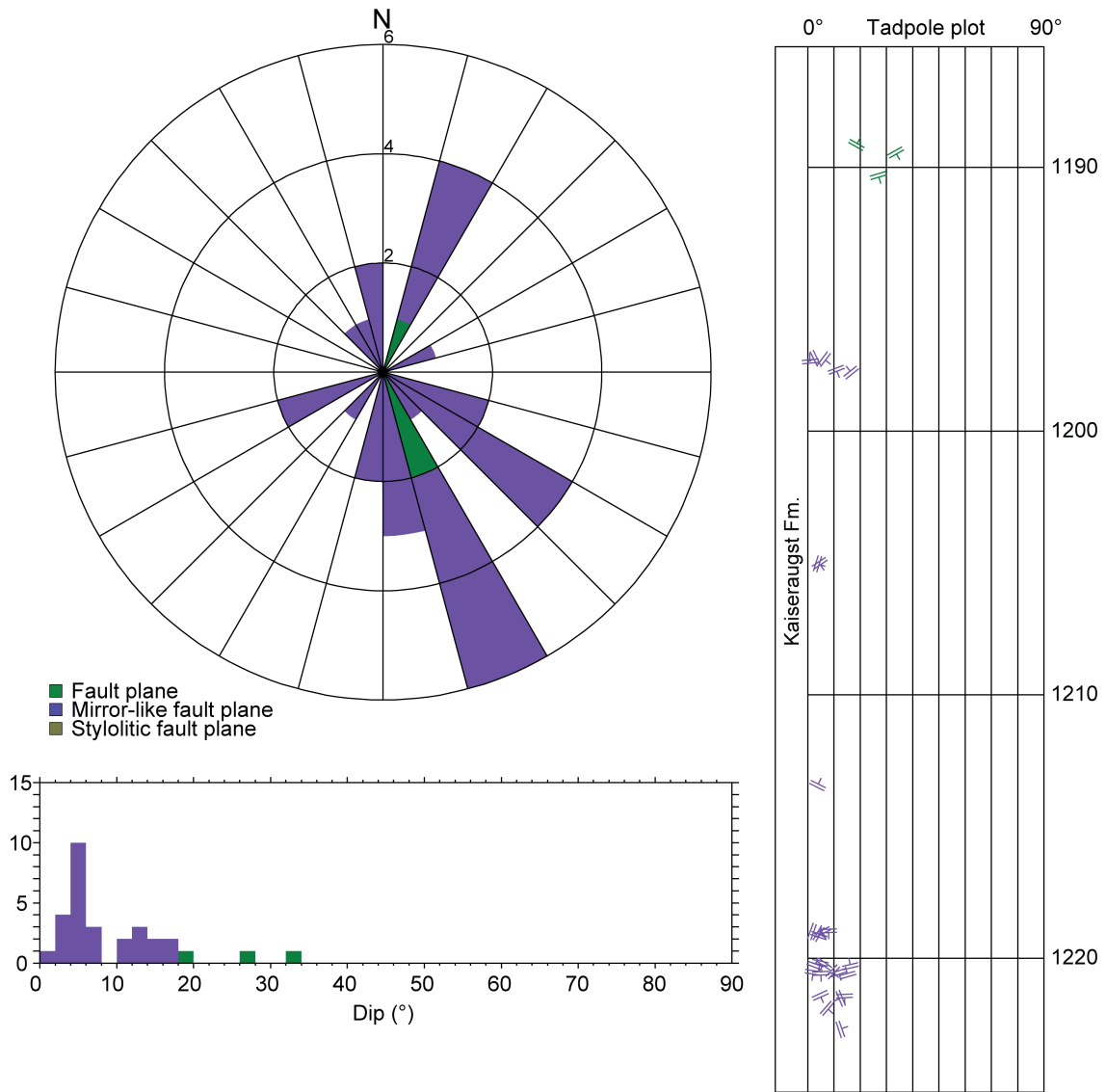


Fig. 4-87: Dip azimuth rose diagram, dip histogram and depth plot of fault planes (Kaiseraugst Formation)

Fault planes (n = 3) and mirror-like fault planes (n = 27); no stylolitic fault planes were observed (n = 0).

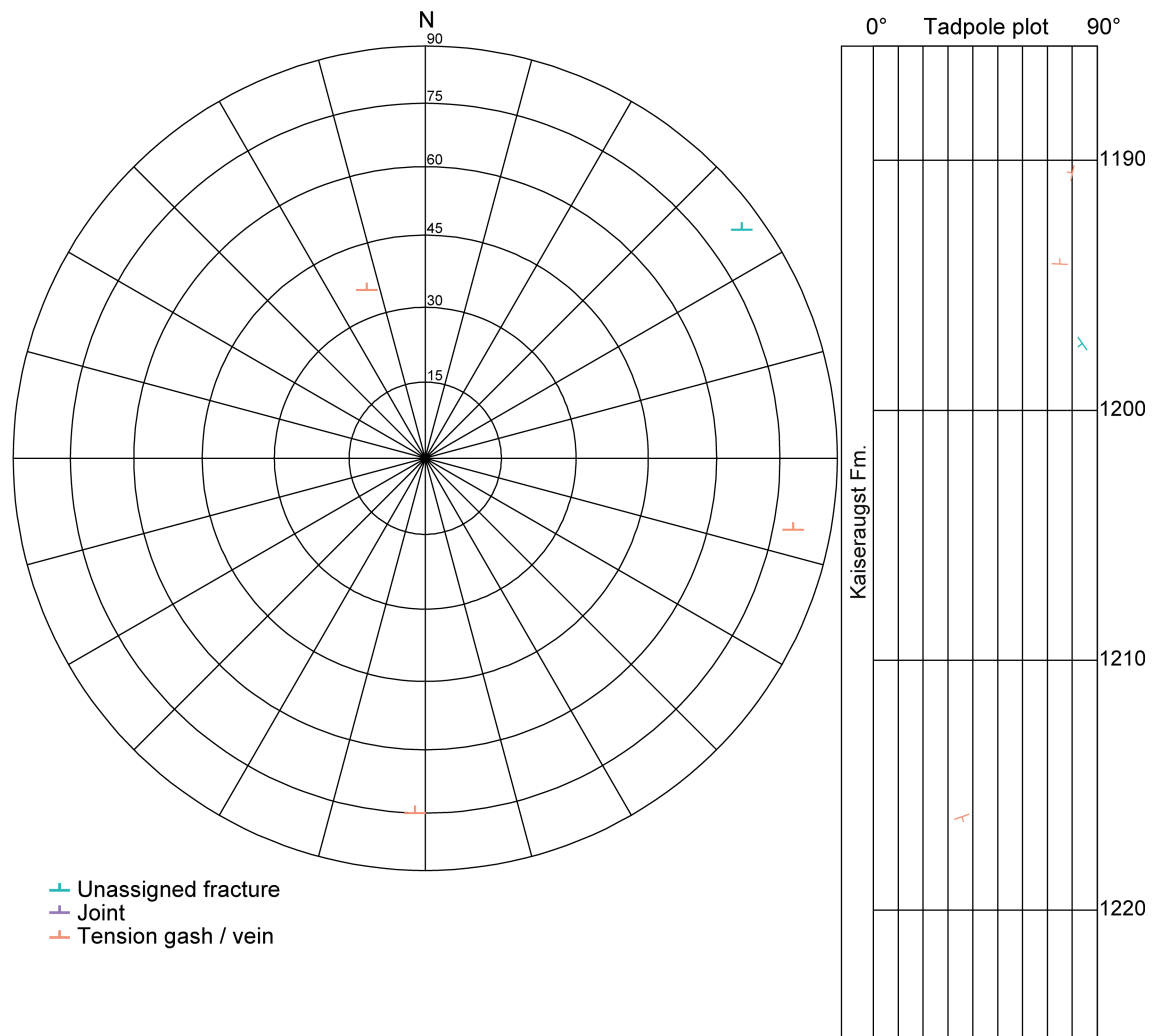


Fig. 4-88: Stereogram and depth plot of tension gashes / veins, joints and unassigned fractures (Kaiseraugst Formation)

Unassigned fractures (n = 1) and tension gashes / veins (n = 3); no joints were observed (n = 0).

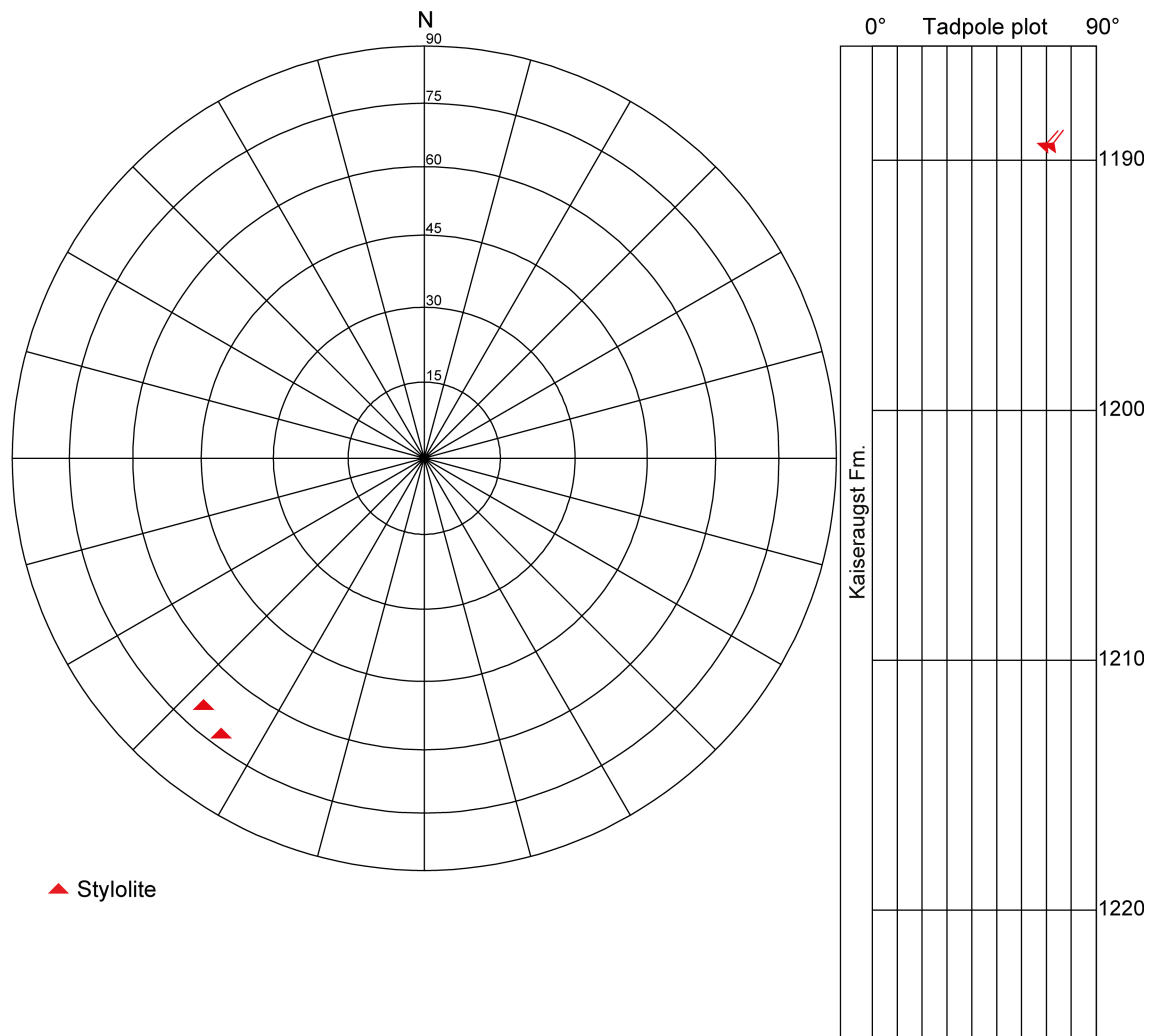


Fig. 4-89: Stereogram and depth plot of stylolites (Kaiseraugst Formation; n = 2)

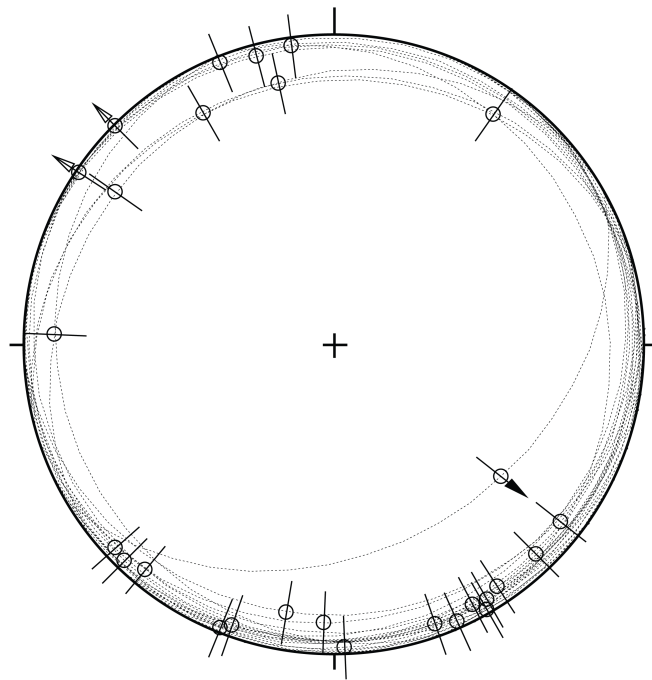


Fig. 4-90: Stereogram of striations on fault planes, including multiple lineations on a single fault plane (Kaiseraugst Formation; $n = 27$)

4.7 Dinkelberg Formation and Weitenau Formation

The orientation and spatial distribution of recorded structures in the Dinkelberg Formation and the Weitenau Formation (1'225.07 to 1'288.87 m MD log depth; base of cored section) are shown in Figs. 4-91 to 4-93. These formations are characterised by a low number of structures. The most common structure type are mirror-like fault planes. They particularly occur between 1'252.00 m and 1'261.00 m MD (log depth) and dip shallowly, mainly towards the NW to N. The striations plunge towards the north. Most shear sense indicators suggest a reverse sense of shear. Stylolites, stylolitic fault planes, tension gashes / veins, unassigned fractures and joints are absent.

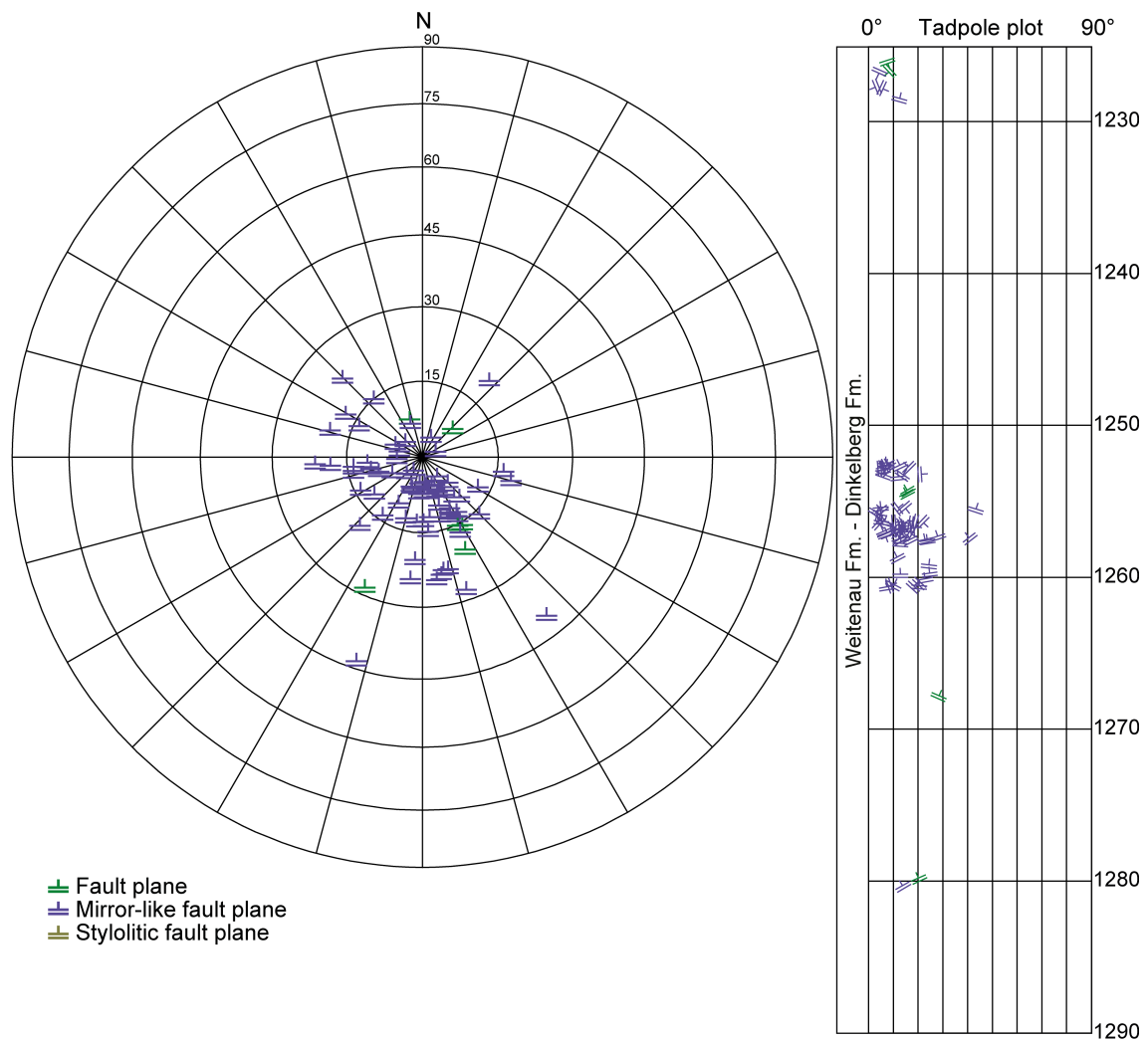


Fig. 4-91: Stereogram and depth plot of fault planes (Dinkelberg Formation and Weitenau Formation)

Fault planes (n = 6) and mirror-like fault planes (n = 69); no stylolitic fault planes were observed (n = 0).

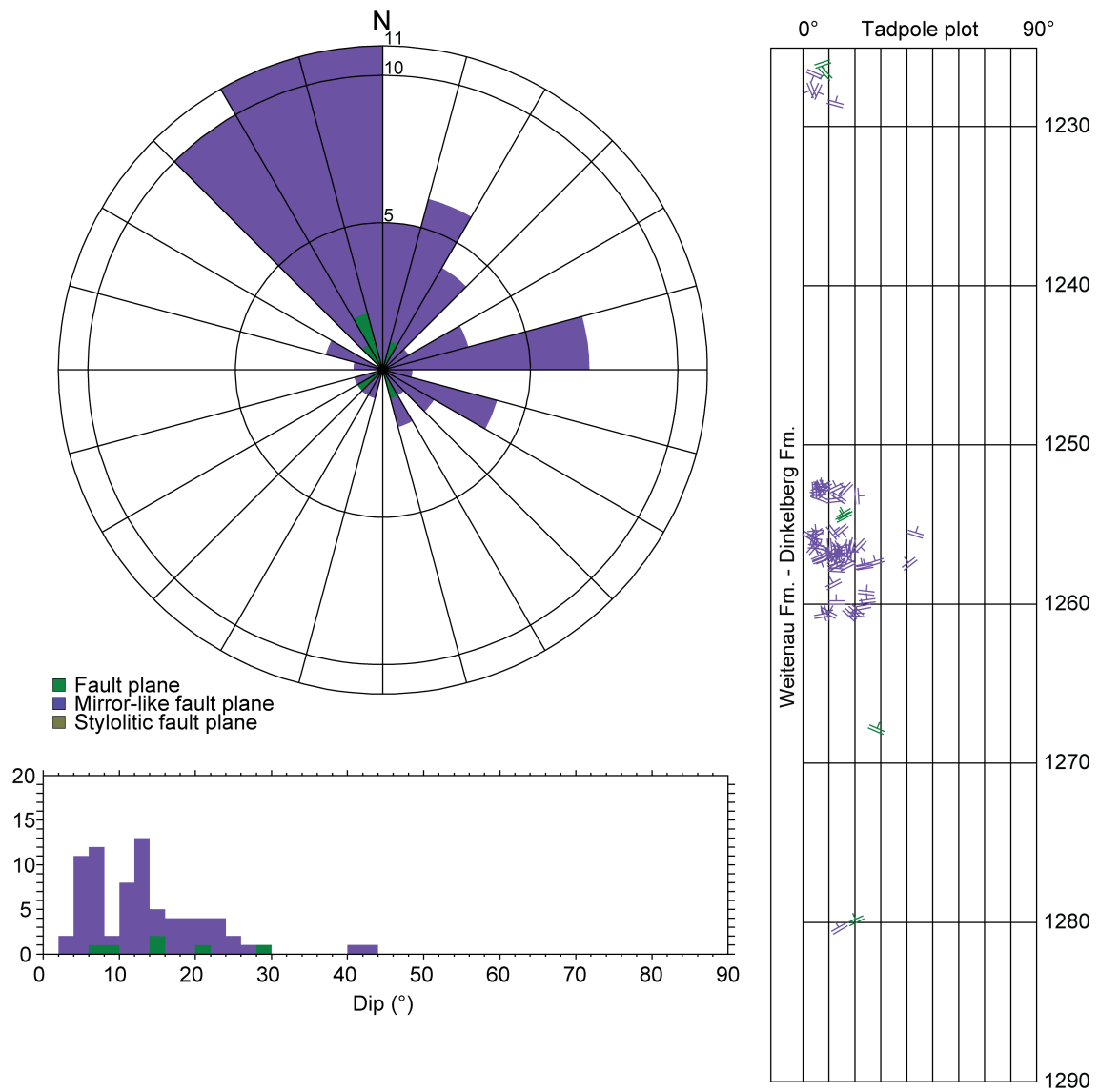


Fig. 4-92: Dip azimuth rose diagram, dip histogram and depth plot of fault planes (Dinkelberg Formation and Weitenau Formation)

Fault planes (n = 6) and mirror-like fault planes (n = 69); no stylolitic fault planes were observed (n = 0).

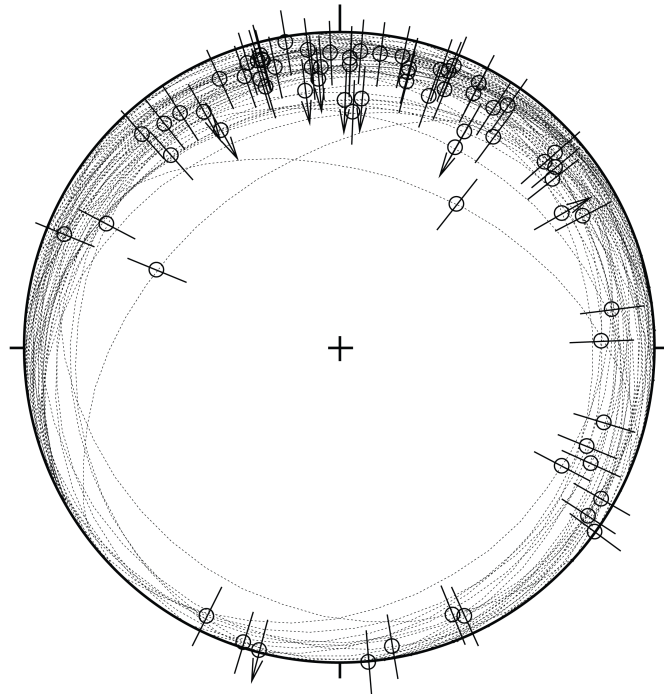


Fig. 4-93: Stereogram of striations on fault planes, including multiple lineations on a single fault plane (Dinkelberg Formation and Weitenau Formation; n = 73)

5 Main structural findings

Among the relevant geological features within the studied interval of the cored section from 470.00 m to 1'288.87 m MD (log depth) presented in Chapters 3 and 4, two prominent deformed intervals deserve a more detailed examination.

5.1 Deformed interval in the Opalinus Clay between 883.78 m and 890.19 m MD (log depth)

A deformed interval occurs in the Opalinus Clay from 883.78 m to 890.19 m MD (log depth). This 6.41 m thick zone is characterised by disturbed bedding, numerous fault planes and tension gashes /veins forming a distinct fault zone from 885.80 m to 886.48 m MD (log depth). Above the deformed interval, the orientation of bedding planes is relatively constant and reveals a main orientation of 145 / 05 (Figs. 5-1, 5-2 and 5-3). The deformed interval is characterised by shallow to inclined (up to 34°) bedding varying in dip azimuth from east to south. The observed changes in dip are mostly linked to soft-sediment deformation.

Fault planes, tension gashes / veins and mirror-like fault planes were encountered in the deformed interval (n = 18; Figs. 5-1, 5-2 and 5-3). All fault planes are mineralised and the filling generally does not exceed 1 mm to 2 mm in thickness. Faults with a thicker mineral filling are clearly visible on the FMI image and appear resistive. Many fault planes were intact and therefore no lineation could be measured. In general, two types of fault planes were observed: These are either mineralised with synkinematic calcite that show a striation and reverse sense of shear (1), or filled with vein-like fibrous calcite and showing striations (2) as shown in Fig. 5-5. Most fault planes dip towards the WNW; a few dip towards the ESE. Dip angles vary between 16° and 72° (Figs. 5-1, 5-2 and 5-3). The few measured striations on the fault planes plunge either towards the SE or the NW. Only one shear sense indicating reverse faulting could be determined (Fig. 5-4).

A series of 8 sub-parallel mirror-like fault planes were observed in a narrow interval from 889.38 m to 890.19 m MD (log depth) in the lower part of the deformed interval (Figs. 5-1, 5-2 and 5-3). They have a homogeneous SW-NE strike with a mean orientation of 153 / 03. The orientation is similar to that of the bedding. All striations plunge towards the S. Only one shear sense indicating reverse faulting could be determined. (Fig. 5-4).

The tension gashes / veins are filled with 0.5 mm to 4 mm thick calcite layers (Fig. 5-7). Some show a fibrous mineralisation (sub-) normal to the fracture plane. Most tension gashes / veins dip towards the WNW; a few dip towards the ESE. Dip angles vary from 2° to 84° (Figs. 5-1, 5-2 and 5-3).

Within the deformed interval, a distinct fault zone was interpreted from 885.80 m to 886.48 m MD (log depth) (Fig. 5-6). This fault zone shows a mean orientation of approximately 280 / 67 and is 0.68 m thick. The fault zone is characterised by a network of fault planes and tension gashes / veins that do not cross-cut the entire drill core nor the few dominant steep fault planes with synkinematic calcite. The latter reveal a similar orientation to the fault zone. Many fault planes and tension gashes / veins are arranged en-echelon or in Riedel shear-like configurations. The disintegration level of the drill core is equivalent to FDC 3.

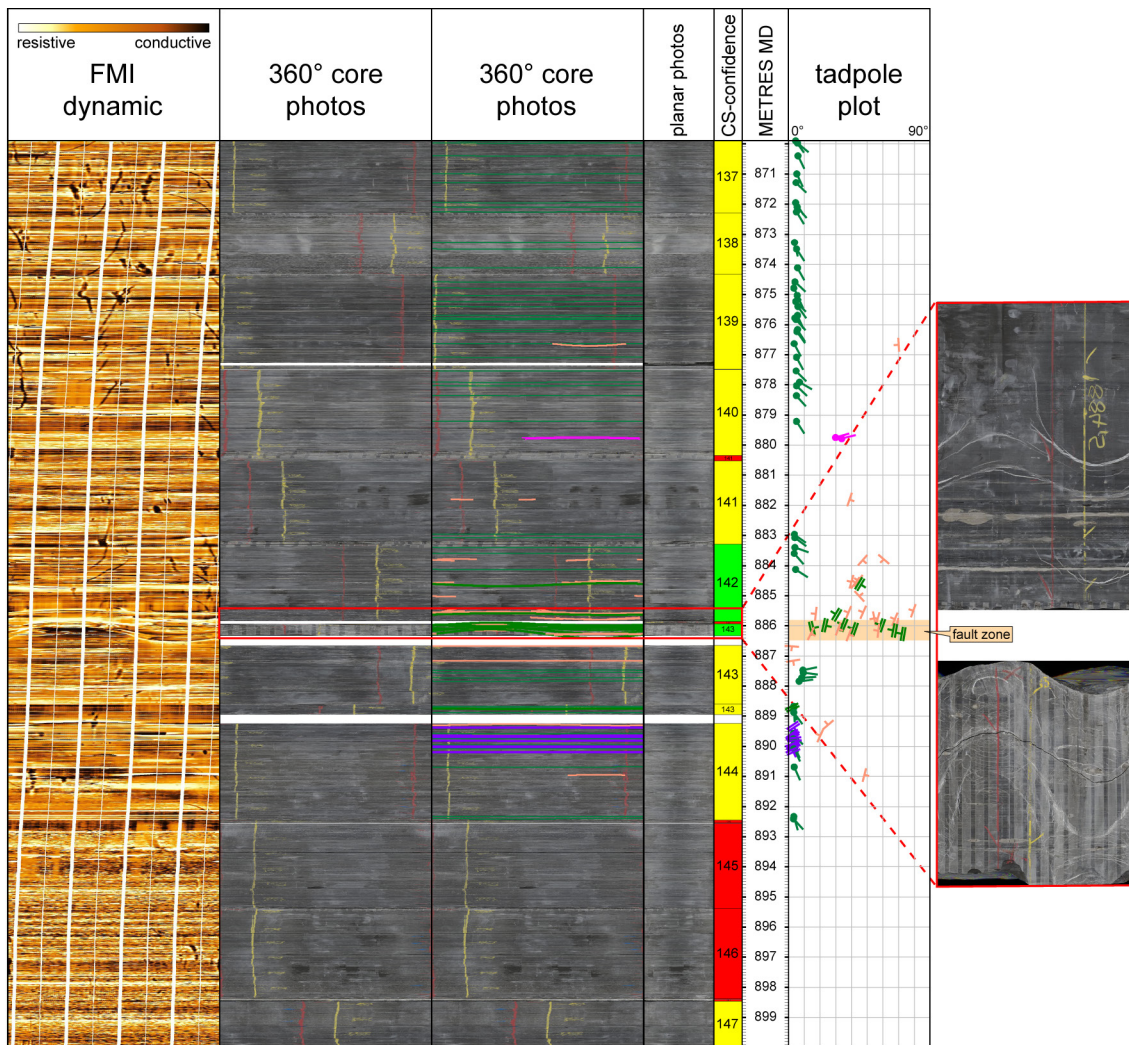


Fig. 5-1: Overview plot of the Opalinus Clay with the deformed interval from 883.78 m to 890.19 m MD (log depth)

The inset on the right is an enlarged image of the interval from 885.40 m MD to 886.40 m MD (log depth).

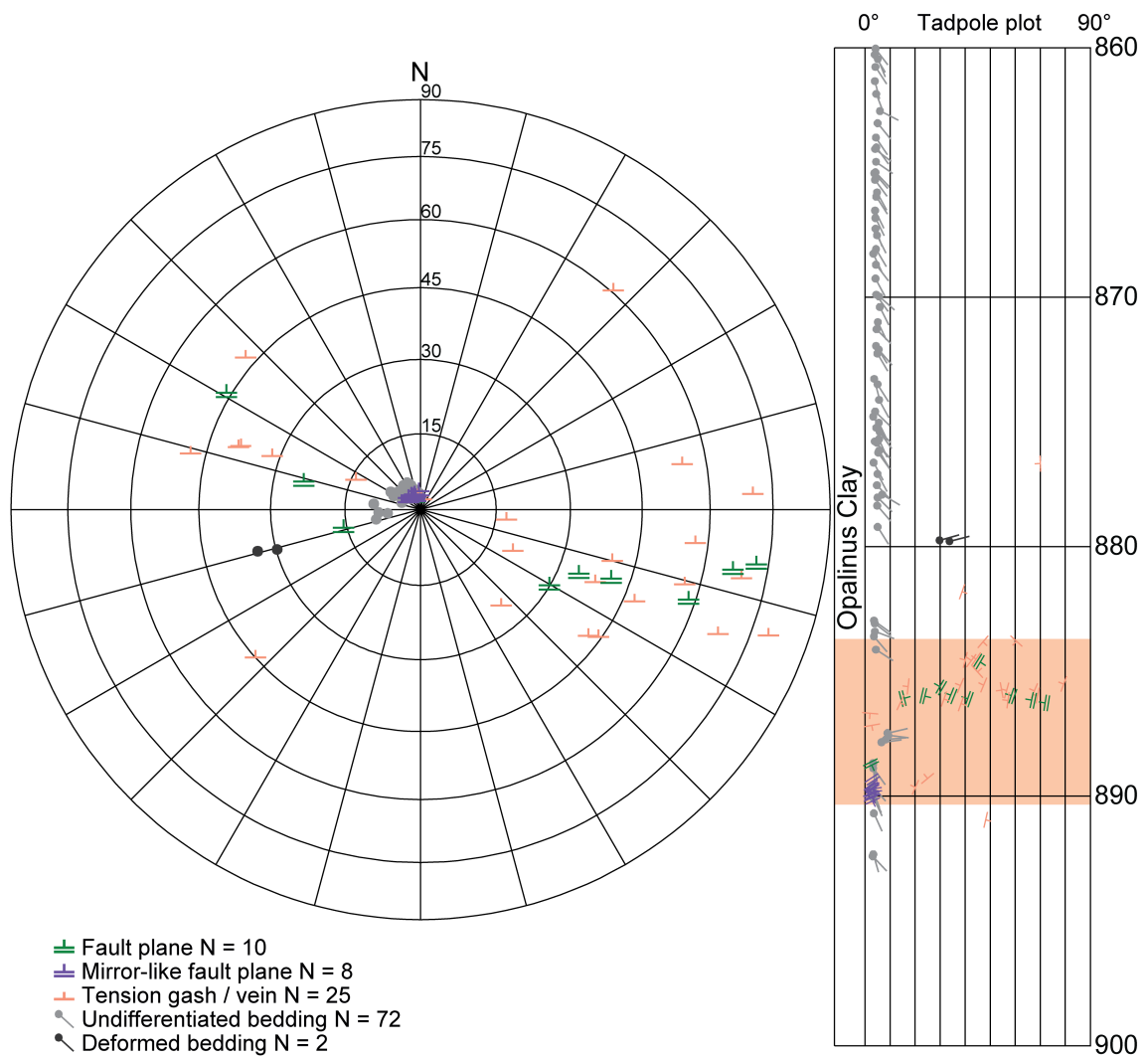


Fig. 5-2: Stereogram and depth plot of fault planes and bedding planes from the depth interval from 883.78 m to 890.19 m MD (log depth)

The deformed interval is indicated by an orange bar.

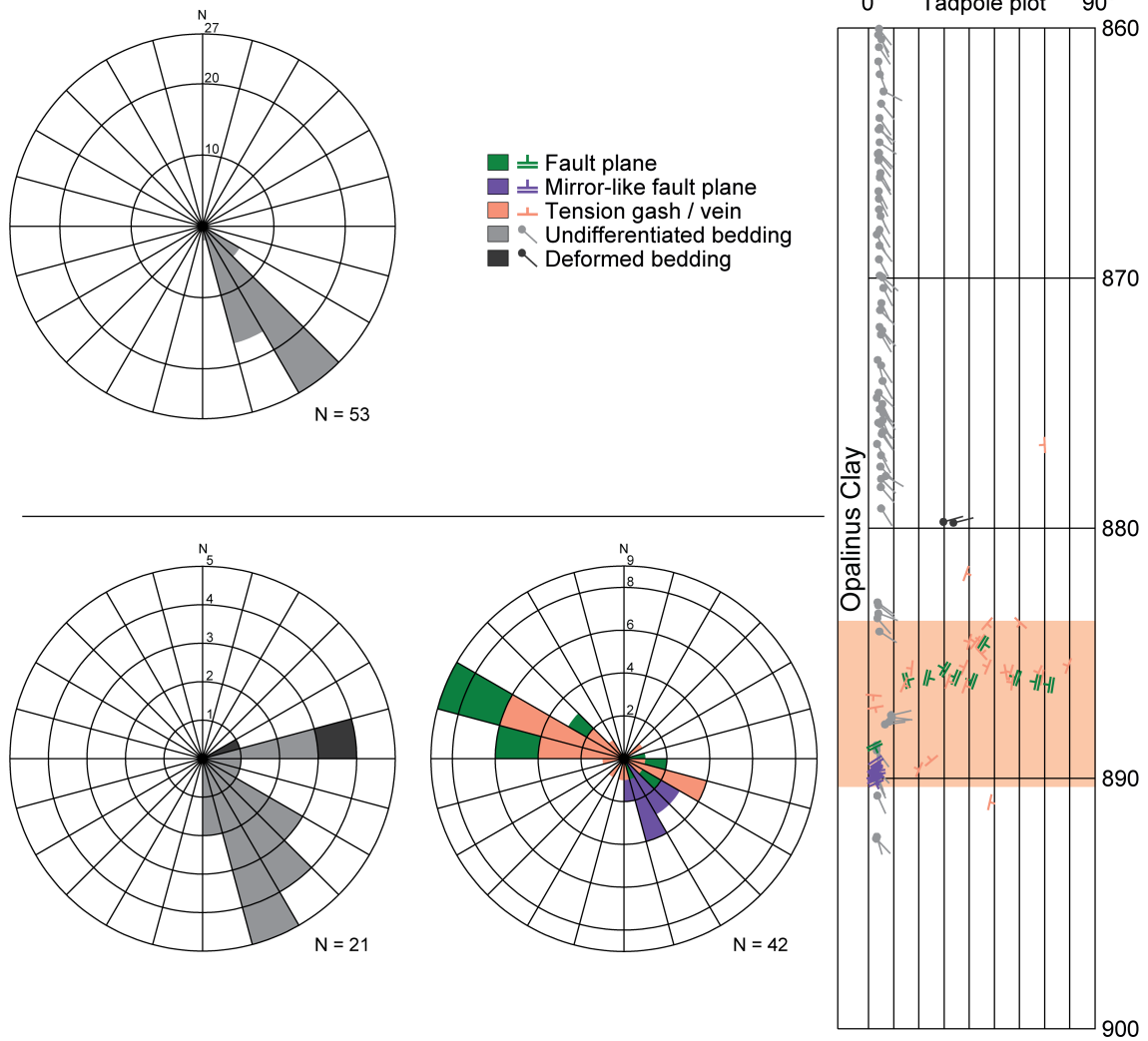


Fig. 5-3: Dip azimuth rose diagrams and depth plot of bedding planes (left) and fault planes (right) from the depth interval from 883.78 m to 890.19 m MD (log depth)
 The rose diagrams are given for the structures above and below 879.50 m MD (log depth).
 The deformed interval is indicated by an orange bar.

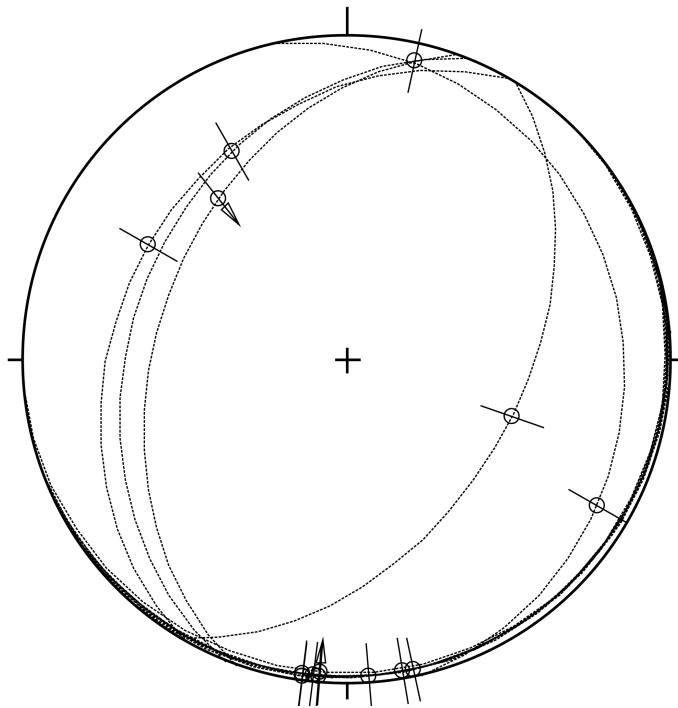


Fig. 5-4: Stereogram of striations on fault planes within the deformed interval
Interval given from 883.78 m to 890.19 m MD (log depth); (n = 15).



Fig. 5-5: Example of a fault plane, depth 855.61 m MD (log depth)

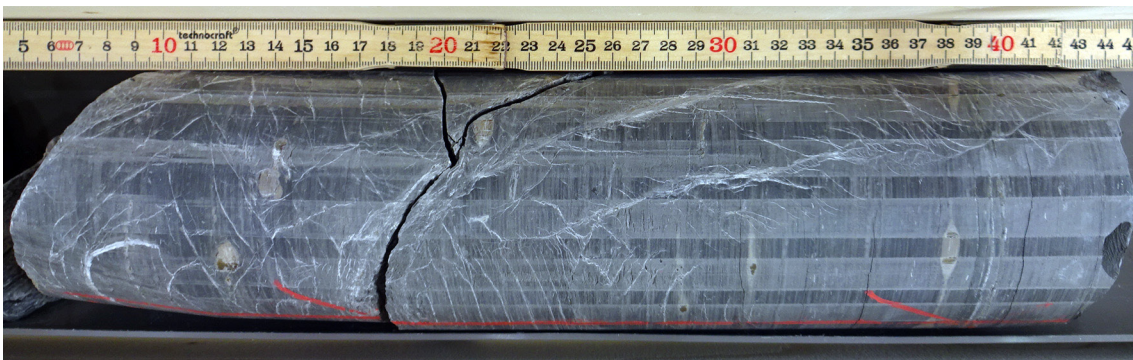


Fig. 5-6: Fault planes and tension gashes/veins in the interval from 885.93 m to 886.33 m MD (log depth)

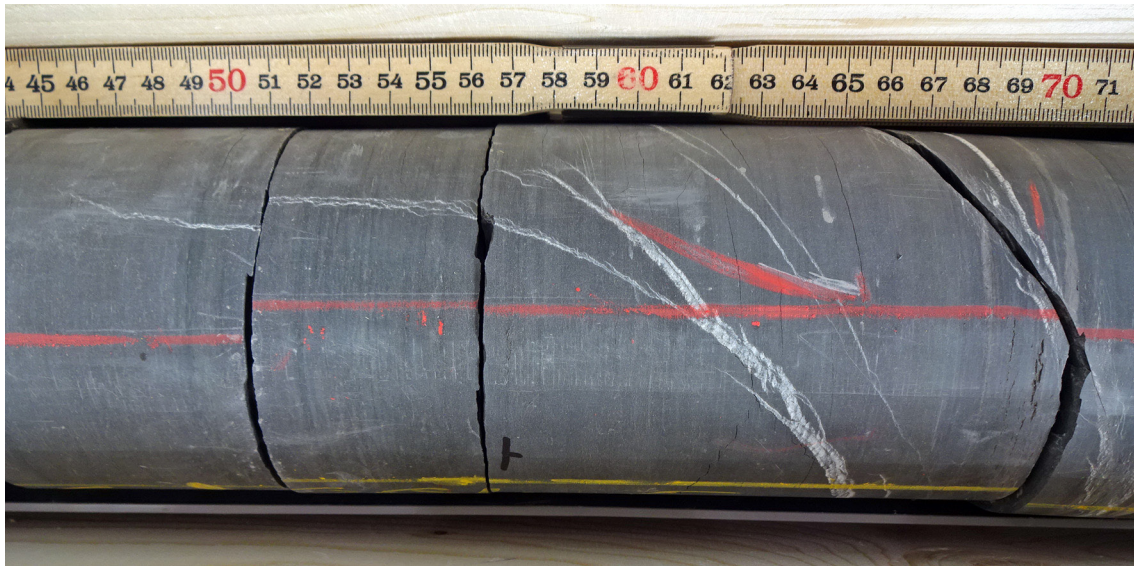


Fig. 5-7: Tension gashes / veins in the interval from 885.38 m to 885.64 m MD (log depth)

5.2 Deformed salt in the Zeglingen Formation from 1'152.02 m to 1'179.58 m MD (log depth)

A deformed interval within the lower part of the Zeglingen Formation («Salzlager») was encountered from 1'154.13 m to 1'174.68 m MD (log depth). This zone mainly consists of thick halite layers and anhydrite with intercalations of claystone, dolostone or marl.

From 1'151.94 m to 1'179.58 m MD (log depth), six thick pure halite layers were observed. From 1'154.06 m to 1'154.26 m MD (log depth), from 1'154.51 m to 1'154.90 m MD (log depth), from 1'157.13 m to 1'159.27 m MD (log depth), from 1'162.52 m to 1'166.72 m MD (log depth), from 1'169.45 m to 1'170.07 m MD (log depth) and from 1'173.82 m to 1'174.69 m MD (log depth), the salt is dynamically recrystallised. In these intervals the salt appears as fine-grained halite with elongated grains alternating with partly recrystallised layers with sigma-clasts. Recrystallised salt is characterised by mm-sized elongated grains with an aspect ratio of 1:2 or 1:3 (short to long axis; Fig. 5-8). The preferred orientation of recrystallised grains and sigma-clasts indicates a reverse sense of shear. The long axes of the recrystallised salt grains plunge towards the S to W (Fig. 5-9). Undeformed halite comprises cm-sized blocky halite crystals.

Anhydrite-rich layers with thin dolomitic intercalations occur between the salt intervals. These mm-thick dolomitic layers are often characterised by boudin-like fabrics (Fig. 5-10) or by networks of tension gashes / veins in an en-echelon arrangement (Fig. 5-11). The observed orientation of the stretching lineations is N – S (Fig. 5-12). The dominant sense of shear is reverse with top to the north.

Apart from the structures mentioned above, only a few additional core cross-cutting tension gashes / veins and fault planes were observed in this interval. They are unevenly distributed.

Within the deformed salt zone, the bedding planes dip predominantly towards the E with dips between 11° and 17° (Fig. 5-13). In contrast, bedding planes above this zone are subhorizontal to shallow (2° to 10°). Below the deformed salt zone, the orientation of the bedding planes is variable. They dip generally towards the east but with generally lower dip angles than in the deformed salt (2° to 26°).

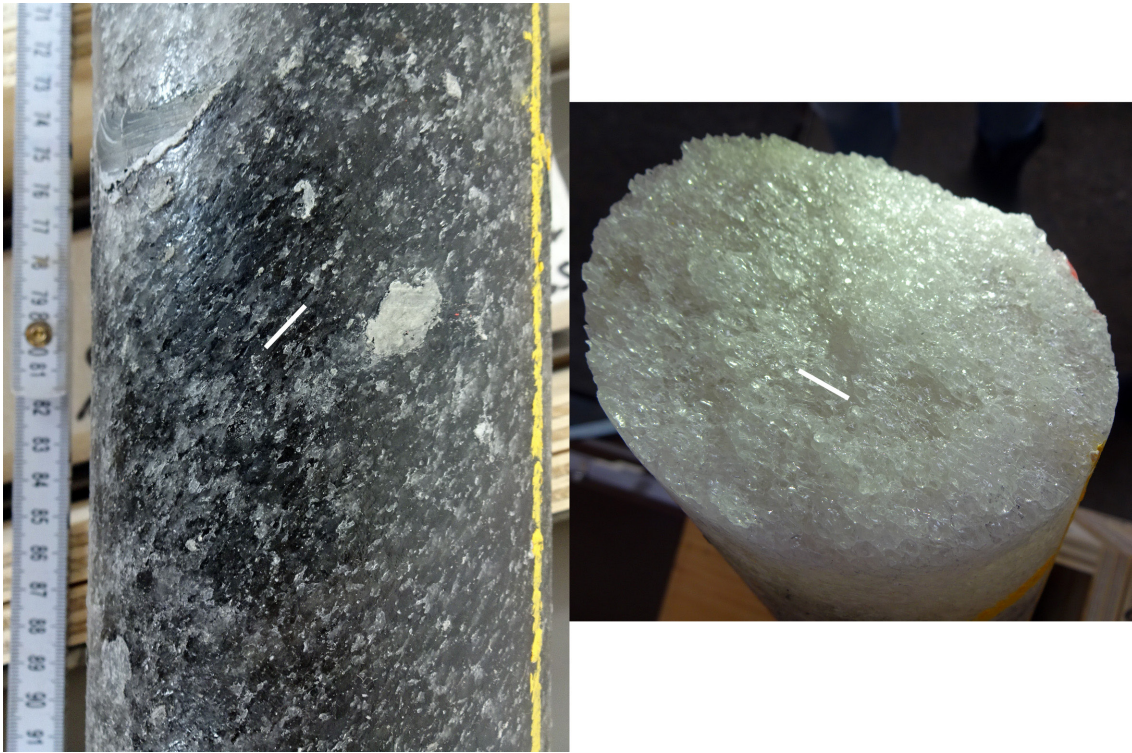


Fig. 5-8: Example of recrystallised halite

The elongation and shape-preferred orientation of salt crystals is well visible and is highlighted by white lines. The left image shows the interval from 1'158.49 m to 1'158.61 m MD (log depth) and the right image corresponds to the depth of 1'164.34 m MD (log depth).

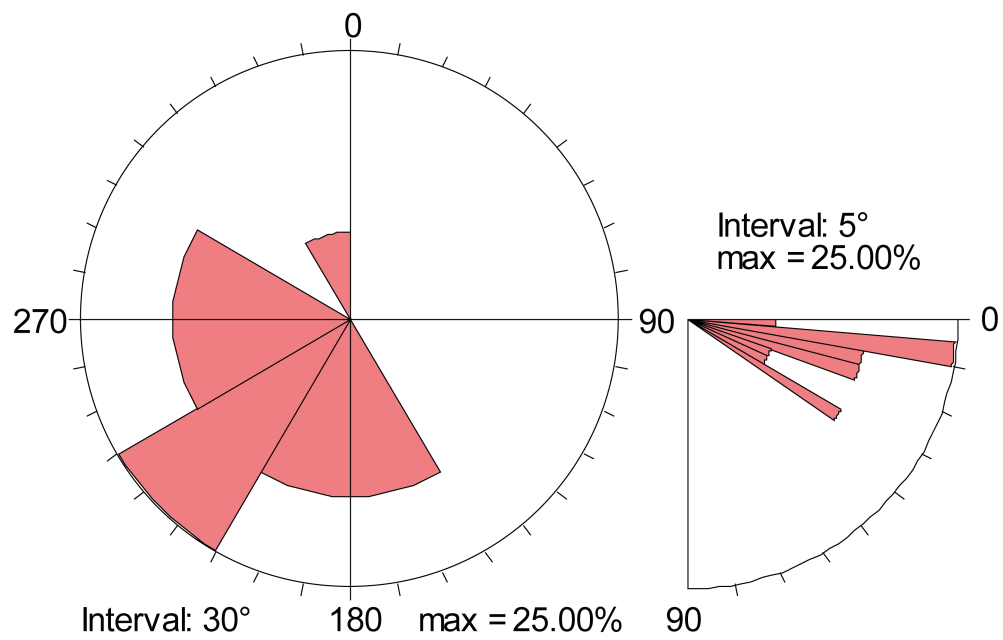


Fig. 5-9: Plunge rose diagram of shape preferred orientation of the long axes of recrystallised salt grains

Data given from the interval between 1'154.13 m and 1'174.68 m MD (log depth); n = 12.

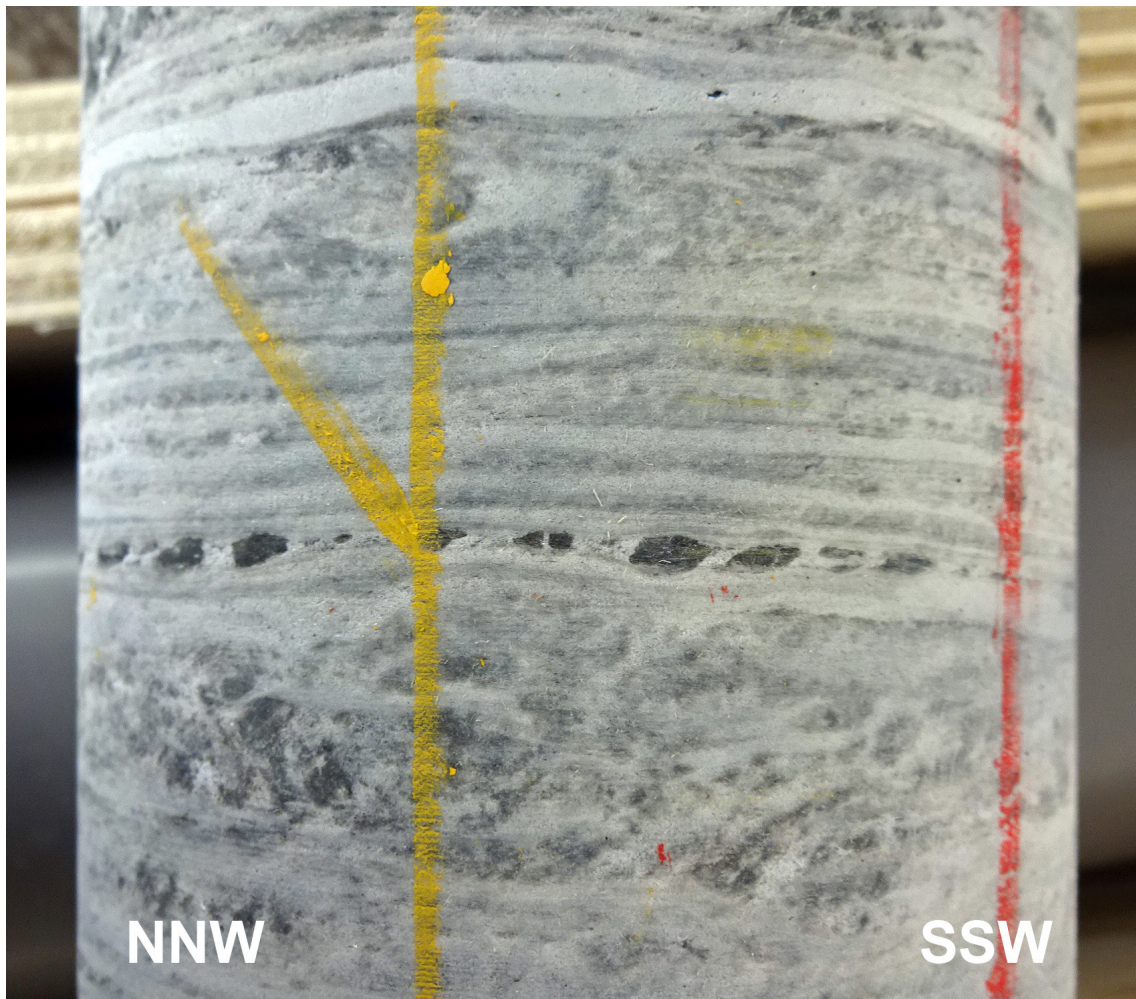


Fig. 5-10: Thin stretched dolomitic layer forming boudins in anhydrite

This dolomitic layer is situated at a depth of 1'167.38 m MD (log depth). Orientation of the image is NNW (left) to SSW (right). The orientation of the layer is 115 / 04.

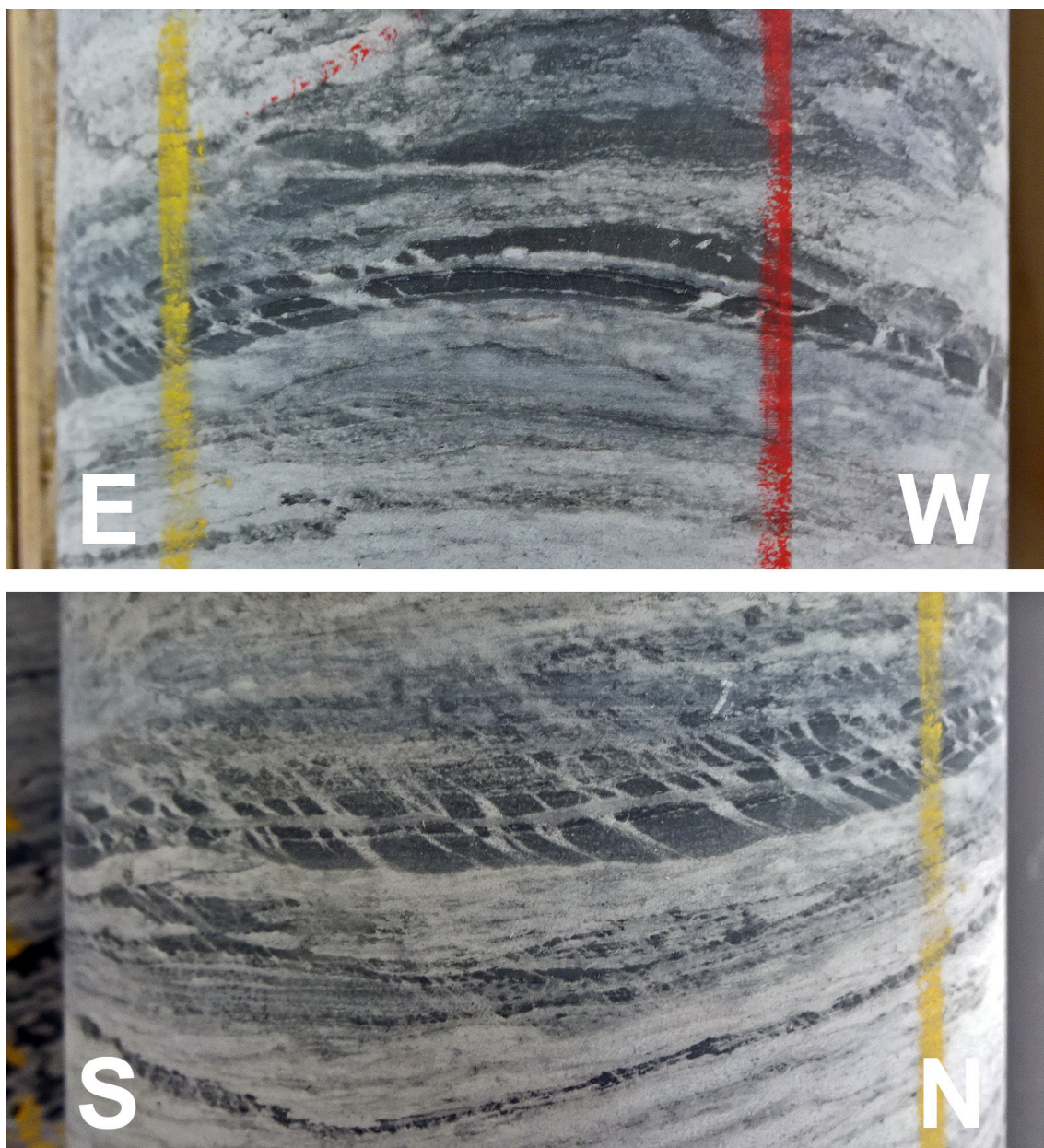


Fig. 5-11: Thin dolomitic layer with a fabric characterised by boudins and tension gashes / veins in an en-echelon arrangement

This dolomitic layer is situated at a depth of 1'156.39 m MD (log depth). The orientation of the layer is 181 / 07, and the stretching lineation has an orientation of 165 / 07.

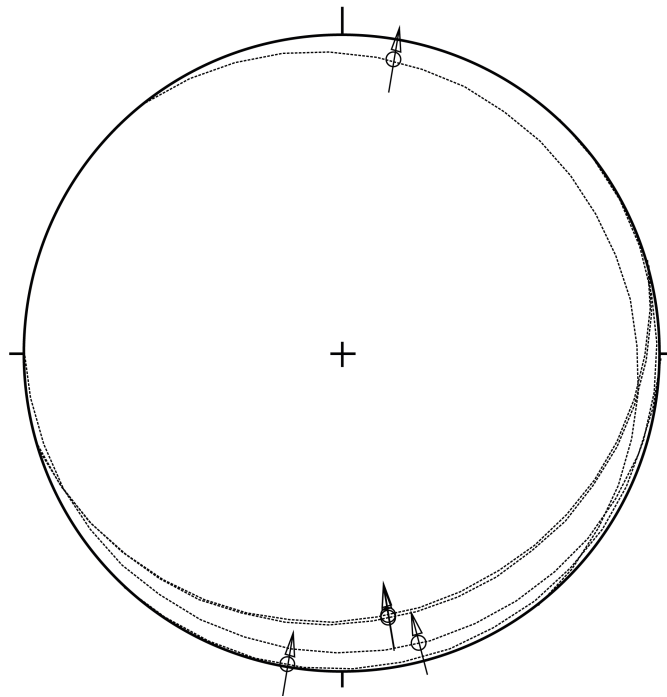


Fig. 5-12: Stereogram of stretching lineations and shear directions indicated within thin dolomitic layers

Data given from the interval 1'154.61 m to 1'160.66 m MD (log depth); $n = 5$.

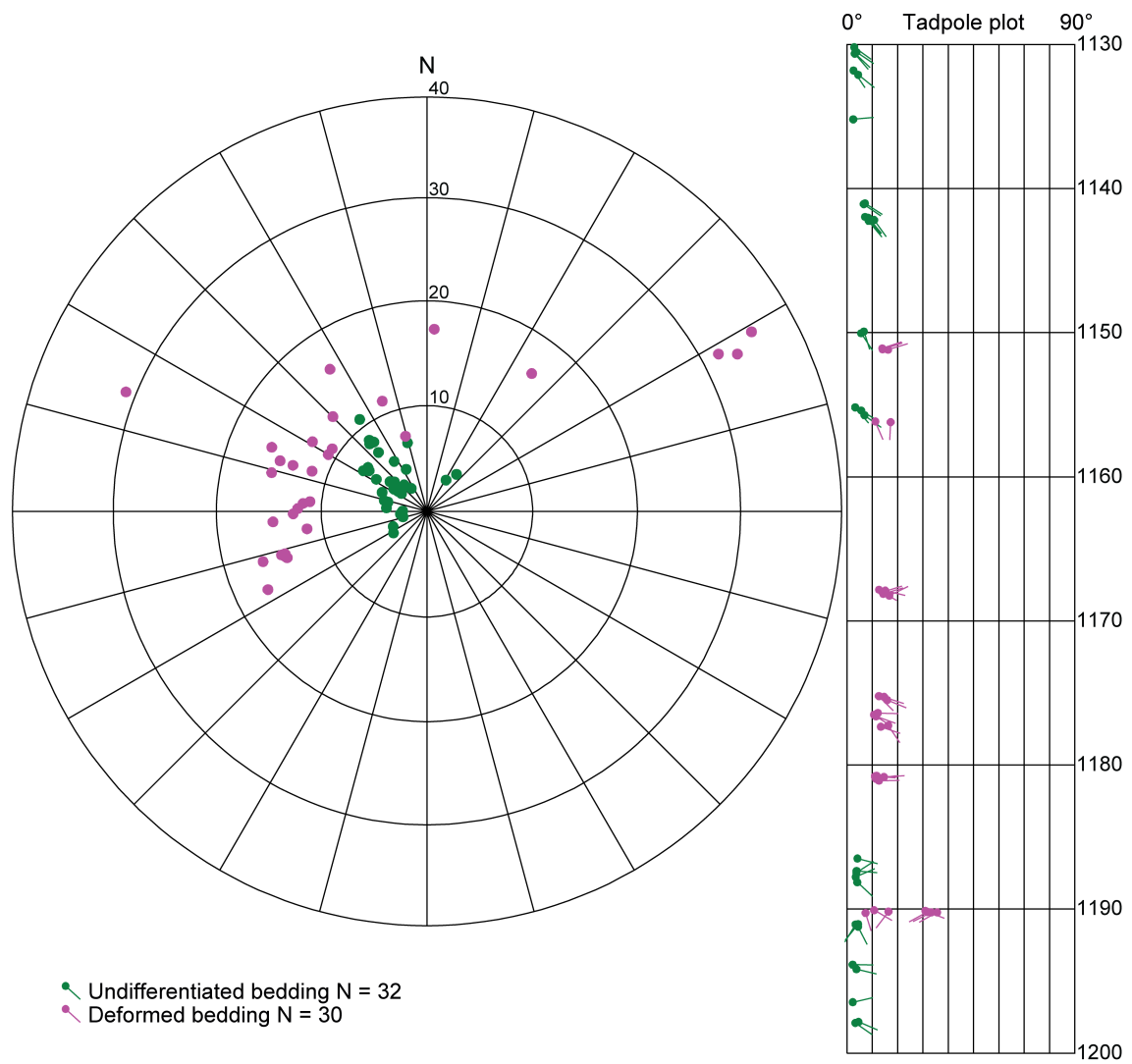


Fig. 5-13: Stereogram and depth plot of bedding

Data given from the interval 1'130 m to 1'200 m MD (log depth); n = 62.

6 References

- Barton, N. (1976): The shear strength of rock and rock joints. *Int. J. Rock. Mech. Min. Sci. & Geomech. Abstr.* 13/9, 255-279.
- Barton, N. & Choubey, V. (1977): The shear strength of rock joints in theory and practice. *Rock mechanics* 10/1-2, 1-54.
- Bauer, H., Schröckenfuchs, T. & Decker, K. (2016): Hydrogeological properties of fault zones in a karstified carbonate aquifer (Northern Calcareous Alps, Austria). *Hydrogeology Journal* 24, 1147-1170.
- Ebert, A. & Decker, K. (2019): Structural Analysis Manual. Nagra Arbeitsbericht NAB 19-12.
- Hancock, P.L. (1985): Brittle microtectonics: principles and practice. *J. Structural Geology* 7/3-4, 437-457.
- Isler, A., Pasquier, F. & Huber, M. (1984): Geologische Karte der zentralen Nordschweiz 1:100'000. Herausgegeben von der Nagra und der Schweiz. Geol. Komm.
- Nagra (2014): SGT Etappe 2: Vorschlag weiter zu untersuchender geologischer Standortgebiete mit zugehörigen Standortarealen für die Oberflächenanlage – Geologische Grundlagen. Dossier II – Sedimentologische und tektonische Verhältnisse. Nagra Technischer Bericht NTB 14-02.
- Passchier, C.W. & Trouw, R.A.J. (1996): *Microtectonics*. Springer, 289 pp.
- Peacock, D.C.P., Nixon, C.W., Rotevatn, A. & Sanderson, D.J. (2016): Glossary of faults and other fracture networks. *J. Structural Geology* 92, 12-29.
- Pietsch, J. & Jordan, P. (2014): Digitales Höhenmodell Basis Quartär der Nordschweiz – Version 2013 (SGT E2) und ausgewählte Auswertungen. Nagra Arbeitsbericht NAB 14-02.